Università degli Studi di Torino
Facoltà di Scienze M.F.N.

Dottorato di Ricerca in Fisica fondamentale, applicata ed astrofisica
XXI Ciclo

Measurement of D^0-$\bar{D}^0$ mixing with a time-dependent amplitude analysis of $D^0 \rightarrow K^+\pi^-\pi^0$

Dr. Mario Pelliccioni

Relatore: **Prof. Diego Gamba**	Controrelatore: **Dott. Daniele Pedrini**
Corelatore: **Dott. Gianluca Cavoto**	Coordinatore del Ciclo: **Prof. Stefano Sciuto**

I would like to thank prof. D. Gamba for his continuous help during my PhD program. Also, doct. G. Cavoto deserves a particular thank; he has had a significant contribution in my work, has guided and supported me in this analysis. I would like to thank prof. F. Bianchi too, for his patience and his commitment in these years.

I am particularly grateful to my family and friends for being always close when it was necessary. In particular, this work is dedicated to Anna, for being the funniest sister in the world.

Contents

List of Figures

List of Tables

Introduction

Flavor mixing of neutral mesons is a long and well known phenomenon in particle physics. Experimental evidence of mixing of the neutral kaon was obtained in 1956, followed in 1987 by the evidence of B_d mixing. In 1974, A. Pais and S. B. Treiman firstly introduced the idea of charm mixing and CP violation. Even though many searches were conducted over time, it was clear that the small scale at which both amplitude and frequency of the oscillation took place made any possible observation challenging. In 2007, both the *BABAR* and *Belle* experiments announced the first evidence of mixing in the charm sector. The analyses concerned the study of a two body decay of the D^0 meson. Few months later, *BABAR* presented the analysis of the decay $D^0 \to K^+\pi^-\pi^0$. This is the main topic of this thesis.

In the first Chapter, we present a general overview of the theoretical aspects of mixing, within and beyond the Standard Model. The current experimental scenario is also shown. The main characteristic of this analysis is the study of the complete amplitude of the decay, which allows to exploit the full interference term to get information on mixing. As this analysis was the first attempt to extract mixing parameters with this procedure, most of the formalism was sorted out by the author. *Belle* previously studies the decay $D^0 \to K_S\pi^+\ \pi^-$; this is a self conjugate final state and the technique used to extract the mixing parameters differs significantly from our case. This is described in Chapter 2, along with detailed information on the Dalitz plot technique and the common parametrizations used to described the resonances contributions to the total amplitude.

In Chapter 3, the *BABAR* experimental apparatus is described. As tracking precision and particle identifications are two key components for this analysis, more detail are given on the detectors responsible for this task. Chapter 4 describes the selection criteria used to select signal events from the *BABAR* dataset (384 fb^{-1}). These criteria were optimized in order to have the highest statistical power on the sample.

To perform a fit to the data sample and obtain the information on the oscillation parameters, the signal yields must be determined. This is described in Chapter 5. The number of signal and background events are determined performing a two-dimensional maximum likelihood fit on the D^0 mass and on the difference in mass between the D^0 and a reconstructed excited state, the D^{*+}. The efficiency of reconstruction of our signal will depend on the kinematic quantities of the particles in the final state. An appropriate Dalitz plot analysis requires a careful momentum-dependent efficiency correction. This is described in Chapter 6.

One of the originalities of this analysis is the use of the clean and abundant $D^0 \to K^-\pi^+\pi^0$ decay to get information to the decay channel we are interested to. It is relevant that part of the amplitude that describes the $D^0 \to K^+\pi^-\pi^0$ decay can be determined by fitting the $D^0 \to K^-\pi^+\pi^0$. This is described in Chapter 7. Information on the signal experimental resolution is needed. Again, the $D^0 \to K^-\pi^+\pi^0$ channel can be used to obtain this information, as it is topologically identical to our signal. More details on this are found in Chapter 8.

Once all these ingredients are sorted out, we describe the signal and background parametrizations in Chapter 9. As this analysis is the first time-dependent fit of this sample, a lot of work was needed to have a detailed study of the background on both the Dalitz plot and the D^0 lifetime. Chapter 10 covers the validation of the probability density function and of the maximum likelihood fit procedure.

In Chapter 11 we report the results of our fit, and the extraction of the mixing parameters from it. As this parametrization of signal was firstly introduced here, a lot of care was needed to determine the correct and most powerful approach to interpret the result. Studies on the systematic uncertainties are reported in Chapter 12. Finally, Chapter 13 describes a possible approach to compare this result with other mixing measurements and an outlook on future experiments on D^0-$\overline{D}^0$ mixing.

Chapter 1

D^0-$\overline{D}^0$ mixing introduction

1.1 $D^0\overline{D}^0$ mixing in the Standard Model

D^0-$\overline{D}^0$ mixing is a quantum oscillation between the eigenstates, $|D^0\rangle$ and $|\overline{D}^0\rangle$, of the Strong and Electromagnetic Interactions. These states do not diagonalize the full Standard Model (SM) Hamiltonian. Given a state that is initially the superposition of D^0 and $\overline{D}^0$, its time evolution is determined by a 2x2 effective Hamiltonian $\mathbf{H}$ that is not hermitian. Any complex matrix, such as $\mathbf{H}$, can be written in term of hermitian matrices as

$$\mathbf{H} = \mathbf{M} - \frac{i}{2}\mathbf{\Gamma}. \tag{1.1}$$

$\mathbf{M}$ and $\mathbf{\Gamma}$ are associated with $(D^0,\overline{D}^0) \leftrightarrow (\overline{D}^0,D^0)$ transitions via on-shell and off-shell intermediate states. Diagonal elements of $\mathbf{M}$ and $\mathbf{\Gamma}$ are associated with flavor-conserving transitions, while off-diagonal elements are associated with flavor-changing transitions $D^0 \leftrightarrow \overline{D}^0$. Note that CPT invariance requires $M_{11} = M_{22}$ and $\Gamma_{11} = \Gamma_{22}$.

The time evolution of this system is described by the Schroedinger equation

$$i\frac{\partial}{\partial t}\left(\begin{array}{c} D^0(t) \\ \overline{D}^0(t) \end{array}\right) = \left(\mathbf{M} - \frac{i}{2}\mathbf{\Gamma}\right)\left(\begin{array}{c} D^0(t) \\ \overline{D}^0(t) \end{array}\right), \tag{1.2}$$

The eigenvectors of $\mathbf{H}$ have well defined masses and decay widths. They can be expressed in terms of the above eigenstates as

$$|D_{1,2}\rangle = p|D^0\rangle \pm q|\overline{D}^0\rangle \tag{1.3}$$

where p and q are complex numbers. We use the phase convention $CP\ |D^0\rangle = -|\overline{D}^0\rangle$ and $CP\ |\overline{D}^0\rangle = -|D^0\rangle$. If CP is an exact symmetry, then $|\frac{p}{q}| = 1$ and D_1 is CP-odd, D_2 is CP-even.

Two physical parameters that characterize D^0-$\overline{D}^0$ mixing are

$$x = 2\frac{m_2 - m_1}{\Gamma_1 + \Gamma_2} \quad \text{and} \quad y = \frac{\Gamma_2 - \Gamma_1}{\Gamma_1 + \Gamma_2} \tag{1.4}$$

where $m_{1,2}$ ($\Gamma_{1,2}$) are the mass (width) parameters for the $D_{1,2}$ eigenstates.

Since we don't know which between $|D_1\rangle$ and $|D_2\rangle$ is the most massive state, there is an ambiguity in this definition of x and y. Where needed, we resolve this ambiguity by choosing $|D_2\rangle$ as the state with higher mass, so x is positive by construction. Most of the formalism and results presented herein are independent of this particular convention, and it is noted when this convention is applied.

CP violation might be observed in an experimental search for D^0-$\overline{D}^0$ mixing. As in other cases, such as the B^0-$\overline{B}^0$ or K^0-$\overline{K}^0$ systems, it could appear in any of three ways. The first way would be a modification of the mixing rate because $p \neq q$ in Equation 1.3 above. The second and third ways would be modifications of either the decay rates of D^0 with respect to the $\overline{D}^0$ or the interference between mixing and decay for the particular decay channels chosen in an analysis. As explained below, an observation of *CP* violation would be the most suggestive sign of New Physics (NP) in this system.

1.2 Origin of the contributions to mixing parameters

In the SM, the mixing rate in the D^0-$\overline{D}^0$ system is expected on general grounds to be very small, but precise predictions are hard to make because of significant contributions from long distance effects of hadronic interactions. This theoretical uncertainty relative to the non-perturbative regime limits, but does not eliminate, the potential for identifying signs of NP.

One can easily show that x may be sensitive to the quark-level ("short range") contributions on mixing, while y can only be affected by hadron level effects ("long range"). As shown in Equation 1.1, mixing arises from $\Delta C = 2$ interactions generating off-diagonal terms in the mass matrix $\mathbf{M}$. The expansion of the off-diagonal terms of $\mathbf{M}$ to the second order of perturbation theory is

$$\left(\mathbf{M} - \frac{i}{2}\mathbf{\Gamma}\right)_{12} = \frac{1}{2M_{D^0}}\langle\overline{D}^0|\mathcal{H}_{\mathcal{W}}^{\Delta C=2}|D^0\rangle + \frac{1}{2M_D^0}\sum_n \frac{\langle\overline{D}^0|\mathcal{H}_{\mathcal{W}}^{\Delta C=1}|n\rangle\langle n|\mathcal{H}_{\mathcal{W}}^{\Delta C=1}|\overline{D}^0\rangle}{M_D^0 - E_n + i\varepsilon} \tag{1.5}$$

where $\mathcal{H}_{\mathcal{W}}^{\Delta C=1,2}$ is the effective $\Delta C = 1, 2$ hamiltonian and $|n\rangle$ is the intermediate state that is eigenstate of the strong interaction. The first term of Equation 1.5 sums the $\Delta C = 2$ contributions that are local at the mass pole. So it contributes to the M_{12} part of the mixing matrix, and not to the Γ_{12}. For this reason, x is believed to be more sensitive to the short range contributions. Note that $\mathcal{H}_{\mathcal{W}}^{\Delta C=2}$ may also include NP contributions. The second term of Equation 1.5 arises from the insertion of two $\Delta C = 1$ operators in the Lagrangian, and it contributes to both M_{12} and Γ_{12}. It is dominated by SM even if NP would be present.

At small distances, neutral-meson mixing proceeds via flavor-changing neutral currents (FCNC). Since there are no tree-level FCNC contributions in the SM, processes such as mixing occur at the quark level primarily via box diagrams, as shown in Figure 1.1. In the B^0-$\overline{B}^0$ or K^0-$\overline{K}^0$ systems, the mesons comprise down-type quarks. In the D^0-$\overline{D}^0$ system, it involves up-type quarks. D mixing is therefore sensitive to the contributions of virtual down-type quarks coupled to the Weak Interaction, making it a process that might reveal physics not seen in the B or K systems. One immediate result of this difference is that there is no contribution from heavy quarks in the D-mixing box diagram. This particular type of contribution breaks the Glashow-Iliopoulos-Maiani (GIM) [3] cancellation in the B or K systems[1] and allows sizable mixing rates. The heaviest quark in the D-mixing box diagram is the b-quark. Because the suppression from Cabibbo-Kobayashi-Maskawa (CKM) [1], [2] mixing factors $V_{cb}V_{ub}^*$ outweighs the potential contribution of the b-quark in the box, the b-quark does not significantly affect the D-mixing rate [4],[5].

Thus, the short distance contribution to x comes primarily from transitions to d- and s-quarks, and this is estimated to be:

$$x_{box} \approx \mathcal{O}(10^{-6}) - \mathcal{O}(10^{-5}). \tag{1.6}$$

Short distance contributions to y are further suppressed by the absence of $\Delta C = 2$ contributions to $\mathbf{\Gamma}$.

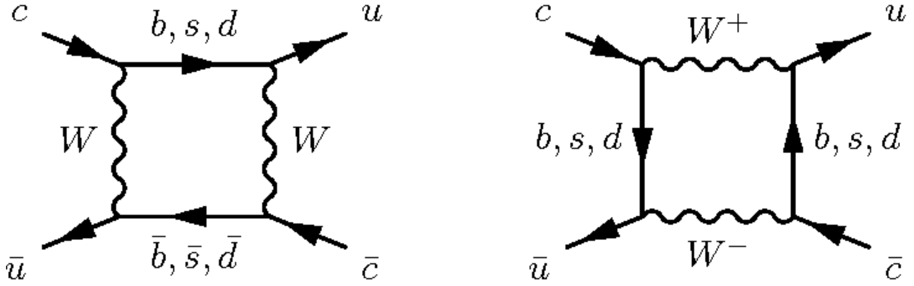

Figure 1.1: Standard-Model box diagrams of flavor-changing neutral currents contributing to D^0-$\overline{D}^0$ mixing at the quark level

Long distance contributions to D mixing are expected to be dominant, but these contributions are non-perturbative and cannot be calculated from first principles. They come from transitions to real final states $|f\rangle$ that are accessible to both $|D^0\rangle$ and $|\overline{D}^0\rangle$. This appears in the second term of Equation 1.5. For example, a contribution to mixing comes from transitions to two pseudoscalars.

---

[1] In K mixing, it is $m_c^2 - m_u^2$ that is relevant; in B mixing, it is $m_t^2 - m_c^2$.

1.3 Theoretical predictions on the mixing parameters

As shown in Section 1.6, the present results on the search of D^0-$\overline{D}^0$ mixing bound x and y to be of the order of 10^{-2}. These results are expected to improve significantly in the coming years. To discern possible new physics contributions from the SM contributions to mixing, precise predictions on the x and y value are needed. It has been shown [7] that x and y are generated only at second order in flavor $SU(3)_F$ breaking in the SM, so schematically

$$x \quad , y \quad \sim \sin^2\theta_C \times [SU(3)_F \quad breaking]^2, \tag{1.7}$$

where $\sin\theta_C$ is the Cabibbo angle. The problem is then shifted to the estimation of the $SU(3)_F$ breaking. Although y is expected to be determined by SM processes, its value affects significantly the sensitivity of D mixing to NP.

Because D mixing only involves the first two quark generations, *CP* violation from SM sources is very small on general grounds. Observing *CP* violation in a search for D mixing would be a clear sign of NP.

There is a vast literature on estimating x and y within and beyond the SM, and the results span many orders of magnitudes. Roughly speaking, there are two approaches to estimate the $SU(3)_F$ breaking, neither of which is very reliable, because m_c is in some sense between heavy and light.

Another significant problem in the theoretical calculation of the mixing parameters is that nobody knows the phase between the SM contribution and a possible NP contribution to mixing. For this reason, given any estimation of mixing, the true value of x and y will be in the limits of the constructive and destructive interference.

To give a pictorial view of the several orders which the predictions on the mixing parameters span, in Figure 1.2 we report the expected values of x and y in the SM for several theoretical calculations [5].

1.3.1 The inclusive approach

The inclusive approach is based on the operator product expansion (OPE) [7]. In the $m_c >> \Lambda$ limit, where Λ is a scale characteristic of the strong interactions, ΔM and $\Delta\Gamma$ in Equation 1.5 can be expanded in terms of matrix elements of local operators [7]. For example, one can consider the width difference between the two mass eigenstates:

$$\Gamma_{12} = \frac{1}{2M_D^0}\Im\langle\overline{D}^0|i\int d^4x\, T\{\mathcal{H}_W^{\Delta C=1}(x)\mathcal{H}_W^{\delta C=1}(0)\}|\overline{D}^0\rangle \tag{1.8}$$

In this approach, the time ordered product in Equation 1.8 is expanded in local oper-

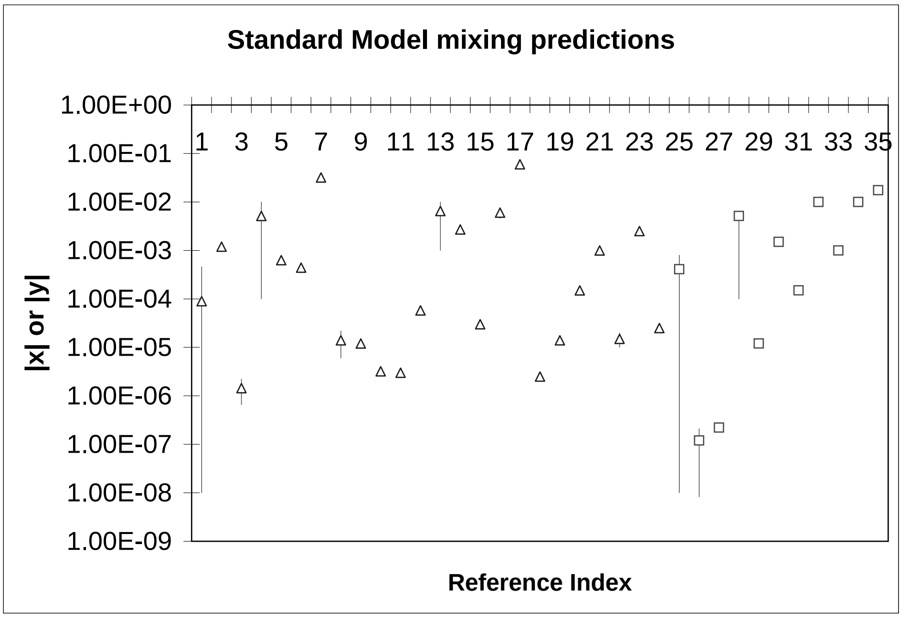

Figure 1.2: Theoretical predictions on the $|x|$ (open triangles) and $|y|$ (open squares) mixing parameters. Horizontal line references are presented in Table 5 of [6].

ators of increasing dimension. The higher dimension operators are suppressed by powers of Λ/m_c.

The use of OPE relies on local quark-hadron duality [7] (i.e. the duality between the partonic rate and the sum over the hadronic final states) and on Λ/m_c being small enough to allow the truncation of the series after the first few terms. However, the charm mass may not be large enough for these to be good approximations for nonleptonic D decays. The result of this type of approach is a prediction of

$$x \sim y \sim 10^{-3} \; . \tag{1.9}$$

A generic feature of OPE based analyses is that $x > y$, which seems to be disfavored by the recent experimental results. It is important to note that at present time these methods are useful for understanding the order of magnitude of x and y, but not for obtaining reliable results.

1.3.2 Exclusive approach

One may question if the OPE approach described in Section 1.3.1 can correctly describe the D mixing phenomenology. A purely long distance analysis of D mixing is complementary to the OPE, and seems favored by data in the present experimental scenario. Instead of assuming that the D meson is heavy enough, one explicitly examines certain exclusive decays. This is particularly interesting for studying $\Delta\Gamma$, which depends on real final states. On the other hand, the usual recipe to compute ΔM is to first calculate

$\Delta\Gamma$ and then use a dispersion relation to obtain the mass difference (like Equation 49 in [7]). This is appropriate, as the contributions from b quarks (a short distance effect, so it appears in ΔM but not in $\Delta\Gamma$) is negligible.

Unfortunately, D decays are not dominated by a small number of final states. Moreover, the D^0 meson is not light enough to approximate its decays into a purely two-body process. Since there are cancellations between states within a given $SU(3)_F$ multiplet, one needs to know the contribution of each state with high precision. While most studies find x , $y \sim 10^{-3}$, it has also been argued that $SU(3)_F$ violation is of the order of unity and so x , $y \sim 10^{-2}$ is possible [8].

Two different exclusive approaches are particularly interesting, as they shed more light on the mixing phenomenology. They involve the estimation of the $SU(3)_F$ breaking from Phase Space (PS) calculations and the inclusion of narrow resonances effects.

Phase Space determination of y

In this case y is estimated considering the on-shell final states. Every decay common to D^0 and $\overline{D}^0$ contributes to the $D_{1,2}$ width difference. If $SU(3)_F$ were an exact symmetry, the sum of all the different contributions over the $SU(3)_F$ multiplets would cancel, giving a zero y value. These cancellations are present both in the decay matrix and in the phase space characterizing the final state. With some simple assumptions, it is possible to calculate the $SU(3)_F$ violation in the phase space. It has been proved that values of y of the order of the percent can be obtained solely from the phase space symmetry breaking [7].

From Equation 1.5 one can derive that for final states common to D^0 and $\overline{D}^0$ y is

$$y = \frac{1}{\Gamma}\sum_n \int [\mathrm{PS}]_n \, \langle \overline{D}^0|\mathcal{H}_\mathcal{W}|n\rangle\langle n|\mathcal{H}_\mathcal{W}\rangle \tag{1.10}$$

in which the sum is over distinct final states and the integral is over the phase space for the state n.

If one considers the sum over the final states F belonging to the same $SU(3)_F$ multiplet R, one ends up with a contribution to y like

$$\frac{1}{\Gamma}\langle \overline{D}^0|\mathcal{H}_\mathcal{W}\left[\eta_{CP}(F_R)\sum_{n\in F_R}|n\rangle\rho_n\langle n|\right]\mathcal{H}_\mathcal{W}|\overline{D}^0\rangle \tag{1.11}$$

where η_{CP} is the eigenvalue of the CP transformation, and is always properly defined within the same $SU(3)_F$ multiplet. ρ_n is the phase space available to the state n. In the $SU(3)_F$ limit, all the quantities in square bracket in Equation 1.11 are equal within the same F_r. Since the ρ_n depend on the masses of the particles in the final state only, it is the place where the symmetry breaking manifests itself, and is the origin of this contribution to y.

If one neglects *CP* violation in the charm sector, a relation is known between $\langle \overline{D}^0|\mathcal{H}_\mathcal{W}|n\rangle$ and $\langle D^0|\mathcal{H}_\mathcal{W}|\bar{n}\rangle$. Since $|n\rangle$ and $|\bar{n}\rangle$ are in the same $SU(3)_F$ multiplet, they are determined by the same effective hamiltonian. As a consequence, it is possible to compute the quantity

$$y_{F,R} = \frac{\sum_{n\in F_R}\langle \overline{D}^0|\mathcal{H}_\mathcal{W}|n\rangle\rho_n\langle D^0|\mathcal{H}_\mathcal{W}|n\rangle}{\sum_{n\in F_R}\langle D^0|\mathcal{H}_\mathcal{W}|n\rangle\rho_n\langle D^0|\mathcal{H}_\mathcal{W}|n\rangle} = \frac{\sum_{n\in F_R}\langle \overline{D}^0|\mathcal{H}_\mathcal{W}|n\rangle\rho_n\langle D^0|\mathcal{H}_\mathcal{W}|n\rangle}{\sum_{n\in F_R}\Gamma(D^0\to n)} \tag{1.12}$$

which represents the value of y if the particles belonging to F_R were the only possible D^0 decay.

Besides the need of assuming *CP* conservation, this approach has other disadvantages. Firstly, to have the true contribution of $y_{F,R}$ to y, one must rescale $y_{F,R}$ to the total branching ratio to all states in F_R. This is difficult, as a final state can frequently be decomposed into a sum over more than one multiplet F_R. Moreover, there are other sources of $SU(3)_F$ symmetry breaking besides the phase space. These are the matrix elements and the final state interactions.

Determination of y using nearby resonances

One can also exploit the fact that there are several excited mesons with masses near the D^0 mass. In particular, K resonances play an important role in the D^0 decays. It is possible to give an estimation of those resonances contributions to mixing.

In this approach, processes like $D^0 \to R \to \overline{D}^0$ are considered. The resonance R, with mass m_R and width Γ_R, is considered to be spinless [2]. It is possible to demonstrate that the contribution of R to the mixing parameters is:

$$x_R \equiv \eta_R\frac{2|H_R|^2}{\Gamma m_D^0}\frac{m_{D^0}^2-m_R^2}{(m_{D^0}^2-m_R^2)^2+m_{D^0}^2\Gamma_R^2} \tag{1.13}$$

$$y_R \equiv \eta_R\frac{|H_R|^2}{\Gamma}\frac{\Gamma_R}{(m_{D^0}^2-m_R^2)^2+m_{D^0}^2\Gamma_R^2} \tag{1.14}$$

with $H_R \equiv \langle \overline{D}^0|\mathcal{H}_\mathcal{W}|R\rangle\langle R|\mathcal{H}_\mathcal{W}|D^0\rangle$ being the coupling of R to D^0 and $\overline{D}^0$, and η_R being the *CP* eigenvalue for the $SU(3)_F$ multiplet to which R belongs. Again, ignoring direct *CP* violation, a relation can be found between $\langle \overline{D}^0|\mathcal{H}_\mathcal{W}|R\rangle$ and $\langle R|\mathcal{H}_\mathcal{W}|D^0\rangle$. We can consider the ratio:

$$\frac{x_R}{y_R} = \frac{2(m_{D^0}^2-m_R^2)}{m_D^0\Gamma_R} \tag{1.15}$$

---

[2] One can demonstrate that only spin zero resonances are relevant to this calculation.

If D mixing is mediated by a resonance, then we can expect that x and y are of the same size, as in most of the cases $m_{D^0}^2 - m_R^2 \sim m_D^0 \Gamma_R$. This scenario seems to be favored by the current experimental results.

1.4 New Physics contributions to D mixing

As far as NP is concerned, the variable which contains more information is x. As explained in Section 1.2, x is more sensitive than y to short range contributions. As any NP effect would be far off-shell at the D^0 mass energy region, non-SM phenomena are visible in the short distance only. Even though a value of x much greater than y may not be an indication of NP, knowing it at a high level of precision is very useful to tune the theoretical modelling and rule out some scenarios. In many cases, theorists have suppressed the FCNC contributions to K and B decays with mechanisms that enhance the mass difference between the D^0 and $\overline{D}^0$. The most evident case in which this happens is the SUSY extension of the SM.

1.4.1 x in the Minimal Supersymmetric Standard Model

The SUSY extension of the SM was firstly introduce to solve the hierarchy problem [10]. Its minimal supersymmetric (MSSM) extension requires the doubling of the particle spectrum by considering all the SM fermions in chiral supermultiplets and all the SM bosons in vector supermultiplets. In this way, many new parameters are introduced. In general, fermion superpartners (sfermions) masses are not related to the fermion masses at all. For example, if we choose to rotate the squark fields with the same matrices that diagonalize the quark mass matrices, the squark mass matrices are not diagonal. In this basis, one can expand the squark propagators so that non-diagonal terms in the mass matrix result as mass insertions that change the squark flavor.

One can parametrize in a model-independent way the mass insertions:

$$(\delta_{ij}^u)_{\lambda\lambda'} = \frac{(M_{ij}^u)^2_{\lambda\lambda'}}{M_{\tilde{q}}^2} \tag{1.16}$$

where $i \neq j$ are the generation indices, λ, λ' indicate the chirality, $(M_{ij}^u)_{\lambda\lambda'}$ are the off-diagonal elements of the up-type squark mass and $M_{\tilde{q}}$ is the average squark mass. For the down quark sector, the constraints for FCNC in the K and B sectors have lead to very small values for the mass insertions. This leads to an increase in the up sector mass insertions values for the soft breaking mechanism to hold.

It has been shown [11] that in several MSSM scenarios the current experimental knowledge of the mixing parameters (along with the constraints on CP violation in the D sector) can lead to constraint on the lower limits of the masses of squarks and gluinos up to 2 TeV/c^2.

1.5 *CP* violation

Within the SM, *CP* violation in the D sector is expected to be negligible with respect to the K and B sector. Any observable effect of *CP* violation in the charm system with the current experimental scenario would be a sign of NP. In this section we consider some general features of *CP* violation in the SM and beyond.

1.5.1 *CP* violation in the decay

In the SM, *CP* violation is originated from a weak phase in the Cabibbo-Kobayashi-Maskawa (CKM) matrix. The most efficient way to measure this effect experimentally is to look at a decay that proceeds both with a *CP* conserving contribution ("spectator" amplitude) and with a *CP* violating contribution ("penguin" amplitude). In this way, in the interference term of the total amplitude, information on the weak phase is accessible. This typically happens in singly Cabibbo-suppressed decay, where a strong phase is also present. One can demonstrate that the size of the *CP* violation in the SM is in this case

$$A_{CP} \simeq \frac{\Im[V_{cd}V_{ud}^{*}V_{cs}V_{us}^{*}]}{\lambda^2}\sin\delta_s\frac{P}{S} \simeq 10^{-3} \tag{1.17}$$

where δ_s is the strong relative phase between the spectator (S) and the penguin (P) amplitudes. Several calculations for A_{CP} were made [9] in the $D^0 \to KK$, $\pi\pi$ cases as well as in several three-body decay modes. All estimations yield to values of A_{CP} similar to that reported in Equation 1.17. NP effects could enhance the penguin amplitude, increasing the value of A_{CP} up to 1%.

On the other hand, CF and DCS decays do not present two amplitudes with different weak phases, so no *CP* violation is expected within the SM. Nevertheless, several NP scenarios introduce a weak phase difference in the CF processes.

1.5.2 *CP* violation in mixing

Another way in which *CP* violation could manifest itself is in the mixing of D^0 and $\overline{D}^0$. In this case one can demonstrate that

$$A_{CP} \sim -2\sin\frac{\Im[V_{cd}V_{ud}^{*}V_{cs}V_{us}^{*}]}{2\lambda^2}(x\cos\delta_s + y\sin\delta_s)(\Gamma t) \tag{1.18}$$

So NP in x could induce a larger A_{CP}. So even if x would be much smaller than y, *CP* violation could be visible if the strong phase between the final states is significantly large.

1.6 Current experimental status

Evidence of D^0-$\overline{D}^0$ has been claimed by the *BABAR* and *Belle* experiments [12],[13]. The first in the study of the $D^0 \to K^+\pi^-$ decays, the latter in a lifetime ratio analysis. Later, also the *CDF* collaboration claimed an evidence in the same channel as *BABAR* [16]. *BABAR* also claimed the evidence of mixing in a lifetime ratio [14] and in a time-dependent amplitude analysis of $D^0 \to K^+\pi^-\pi^0$ [15]. The second one is the analysis described in this thesis. All the different measurements agree in providing values of x and y of the order of 10^{-2}, within some of the SM predictions. Since a positive value of y is favored by data, the *CP*-even state is short lived, as in the K^0-$\overline{K}^0$ system. However, since x also appears to be positive, the *CP*-even state is heavier, unlike the K^0-$\overline{K}^0$ system.

The study of $D^0 \to K^+ \pi^-$ has for long been considered the *golden mode* for mixing observation. The main advantages of this analysis are a clean signal and the ability to compare the signal distributions to the high statistics $D^0 \to K^- \pi^+$ sample, eliminating many sources of systematic bias. The main disadvantage is that this analysis is not sensitive to x and y, but rather to x' and y', which are related to the mixing parameters by an unknown strong phase. Moreover, this analysis is not sensitive to the sign of x'.

The study of D^0 decays into final states that are *CP* eigenstates (also known as lifetime ratio analysis) exploits the feature that if mixing exists, the mean lifetime of $D^0 \to CP$ is distorted by a factor proportional to y. Historically, the variable measured is called y_{CP}, and corresponds to y if *CP* is conserved. It is not possible to extract any information on x from this analysis. The two channels where both *BABAR* and *Belle* found evidence of mixing are $D^0 \to K^+ K^-$ and $D^0 \to \pi^+ \pi^-$. The advantages of this decays is that the samples obtained are very pure, and that the measurement of the D^0 lifetime is quite straightforward.

One can also analyze the semileptonic decays of the D^0. This has been done by *BABAR* [17] and *Belle* [18], but no signal for mixing has been found. The main problem with this analysis is the high level of background in the sample, due to the unreconstructed neutrino in the event. Also, this analysis is sensitive to the value of $\frac{x^2+y^2}{2}$ only.

The description of the three-body decay analyses is given in detail in Section 2.2. That section focuses on the three body decays which are not self-conjugate. A notable exception is the study of a three body decay which is a *CP*-conjugate final state. In this case, the strong phase of any chosen *CP* component of the amplitude can be fixed. In such a scenario, the mixing parameters can be determined without the problem of the unknown strong phase rotation that affects most of the other mixing analyses. *Belle* presented the study of the $D^0 \to K^0_S \pi^+ \pi^-$ decay [19], which showed no evidence for mixing. Even so, this represents the only direct constraint to x to date.

Lastly, one possible way to measure charm mixing is by studying the coherent production of D^0-$\overline{D}^0$. This can be done exploiting for example the decay of the $\psi(3770)$. Being in a quantum-coherent state, it is possible to fix the strong phase of the D^0 decay analyzed and have a direct measurement of x and y. This has been done by CLEO [20]. There is a main drawback in this technique: the D mesons produced from the ψ decay have a low momentum spectrum, because the mass of the ψ is relatively small. For this

Observable	**Value**	**Comment**
y_{CP}	$(1.132 \pm 0.266)\%$	WA $D^0 \to K^+ K^- / \pi^+ \pi^-$ results [22]
A_Γ	$(0.123 \pm 0.248)\%$	
x (no CPV)	$(0.811 \pm 0.334)\%$	No CPV: WA $D^0 \to K^0_S \pi^+ \pi^-$ results [22]
y (no CPV)	$(0.309 \pm 0.281)\%$	
$\|q/p\|$ (no direct CPV)	$0.95 \pm 0.22^{+0.10}_{-0.09}$	
ϕ (no direct CPV)	$(-0.035 \pm 0.19 \pm 0.09)$ rad	
x	$(0.81 \pm 0.30^{+0.13}_{-0.17})\%$	CPV-allowed: Belle $D^0 \to K^0_S \pi^+ \pi^-$ results.
y	$(0.37 \pm 0.25^{+0.10}_{-0.15})\%$	
$\|q/p\|$	$0.86 \pm 0.30^{+0.10}_{-0.09}$	
ϕ	$(-0.244 \pm 0.31 \pm 0.09)$ rad	
R_M	$(0.0173 \pm 0.0387)\%$	WA $D^0 \to K^+ l^- \nu$ results [22]
R_M	$(0.019 \pm 0.0161)\%$	*BaBar* $D^0 \to K^+ \pi^- \pi^+ \pi^+$ result.
R_M	$(0.199 \pm 0.173 \pm 0.0)\%$	CLEOc results from "double-tagged" branching fractions $\psi(3770) \to DD$ decays. The only external input are branching fractions.
y	$(-5.207 \pm 5.571 \pm 2.737)\%$	
R_D	$(-2.395 \pm 1.739 \pm 0.938)\%$	
$\sqrt{R_D} \cos\delta$	$(8.878 \pm 3.369 \pm 1.579)\%$	
x'^{2+}	$(-0.024 \pm 0.052)\%$	*BaBar* $D^0 \to K^+ \pi^-$ results.
y'^{+}	$(0.98 \pm 0.78)\%$	
x'^{2-}	$(-0.020 \pm 0.050)\%$	*BaBar* $\overline{D}^0 \to K^- \pi^+$ results.
y'^{-}	$(0.96 \pm 0.75)\%$	
x'^{2+}	$(0.032 \pm 0.037)\%$	*Belle* $D^0 \to K^+ \pi^-$ results.
y'^{+}	$(-0.12 \pm 0.58)\%$	
x'^{2-}	$(0.006 \pm 0.034)\%$	*Belle* $\overline{D}^0 \to K^- \pi^+$ results.
y'^{-}	$(0.20 \pm 0.54)\%$	

Table 1.1: Summary of the experimental measurements of the charm mixing parameters.

reason, it is impossible to perform a time-dependent measurement with the experimental resolution feasible at this date. One alternative would be to study the D^0-$\overline{D}^0$ coherent production from the decay of the Υ resonances [21]. In this case, the momentum spectra of the D^0 s would match the experimental capabilities. Unfortunately, because of the low rate of this process, this analysis would only be possible at a high-statistics flavor factory.

In Table 1.1, a summary of the up-to-date experimental measurements is reported.

Chapter 2

Analysis strategy

In this chapter, we present the main features of D^0-$\overline{D}^0$ mixing in a multibody decay. In particular, we show the formalism to be considered in a three body decay. We obtain the formulas by extending the case of a decay of a D meson into two particles. Detailed information on the parametrization of the amplitudes involved in the process is provided. The Dalitz plot technique is described too. Finally, we try to visualize the mixing effects over the Dalitz plot by looking at the change in average D^0 lifetime.

A search for mixing attempts to identify the process[1] $|D^0\rangle \rightarrow |\overline{D}^0\rangle$ by analyzing the decay products of a particle known to be created as a $|D^0\rangle$. In practice, this means reconstructing the state $|\bar{f}\rangle$ in an attempt to observe the transition

$$|D^0\rangle \rightarrow |\overline{D}^0\rangle \rightarrow |\bar{f}\rangle. \tag{2.1}$$

The difficulty comes from the fact that for nonleptonic final states, the decay

$$|D^0\rangle \rightarrow |\bar{f}\rangle \tag{2.2}$$

can occur directly, without any mixing at all. Distinguishing the process 2.1 from 2.2 is the primary goal of this analysis, and it relies on the fact that the decay-time distribution of the final state $|\bar{f}\rangle$ is different for the two processes. The highest sensitivity to mixing will be found when the amplitude for the process 2.2 is as small as possible, and therefore doubly Cabibbo-suppressed (DCS) decays are preferred for this type of analysis. DCS decays have very small branching fractions relative to the CF decays, on the order of

$$|\sin^2(\theta_C)|^2 \approx 0.0023 \tag{2.3}$$

---

[1] Charge conjugation is implied except where otherwise stated.

where θ_C is the Cabibbo angle. To the extent that Process 2.2 has a smaller amplitude for a particular decay compared to others, it will yield more sensitivity to the observation of mixing.

2.1 The two-body decay scenario

To derive the mixing formalism for this analysis, it is easier to firstly consider a simpler case: the decay of a D^0 to a two-body final state that is not a *CP* eigenstate. Most of the formulas derived in this section can be applied to a multi-body decay with some simple caveats.

Following from Equation 1.2, and ignoring the possibility of direct *CP* violation[2], one can derive the time-dependent solutions:

$$\begin{aligned} |D^0(t)\rangle &= a_+(t)|D^0\rangle + a_-(t)|\overline{D}^0\rangle && (2.4)\\ |\overline{D}^0(t)\rangle &= a_-(t)|D^0\rangle + a_+(t)|\overline{D}^0\rangle, && (2.5)\end{aligned}$$

where

$$\begin{aligned} a_+(t) &= \frac{1}{2}(e^{-im_1t-\frac{1}{2}\Gamma_1 t} + e^{-im_2t-\frac{1}{2}\Gamma_2 t}) && (2.6)\\ a_-(t) &= \frac{1}{2}(e^{-im_1t-\frac{1}{2}\Gamma_1 t} - e^{-im_2t-\frac{1}{2}\Gamma_2 t}). && (2.7)\end{aligned}$$

We are interested in the measurable, time-dependent rate:

$$\begin{aligned} \Gamma_{\bar{f}}(t) &= |\langle\bar{f}|\mathcal{H}|D^0(t)\rangle|^2 \\ &= \left(|A_{\bar{f}}|^2|a_+(t)|^2 + A_{\bar{f}}\bar{A}^*_{\bar{f}}a_+(t)a^*_-(t) + \bar{A}_{\bar{f}}A^*_{\bar{f}}a_-(t)a^*_+(t) + |\bar{A}_{\bar{f}}|^2|a_-(t)|^2\right) && (2.8)\end{aligned}$$

where

$$\begin{aligned} A_{\bar{f}} &= \langle\bar{f}|\mathcal{H}|D^0\rangle && (2.9)\\ \bar{A}_{\bar{f}} &= \langle\bar{f}|\mathcal{H}|\overline{D}^0\rangle. && (2.10)\end{aligned}$$

Here, $\mathcal{H}$ is the hamiltonian described in Equation 1.1.

---

[2] *CP* violation in the charm sector is strongly suppressed within the SM, especially in CF and DCS decays [23].

In general, there is a phase difference between $A_{\bar{f}}$ and $\bar{A}_{\bar{f}}$ arising from the Strong Interaction. To understand this, consider the set of strong eigenstates $|n\rangle$ that can scatter into the final state $|\bar{f}\rangle$. Similar to Equations 2.9–2.10, we can write the amplitudes for decay into these eigenstates:

$$A_n = \langle n|\mathcal{H}|D^0\rangle = b_n e^{i\delta_n} \tag{2.11}$$

$$\bar{A}_n = \langle n|\mathcal{H}|\overline{D}^0\rangle = \bar{b}_n e^{i\delta_n}, \tag{2.12}$$

where $b_n, \bar{b}_n$ are real numbers. In terms of these eigenstates,

$$A_{\bar{f}} = \textstyle\sum_n \langle \bar{f}|n\rangle\langle n|\mathcal{H}|D^0\rangle = \sum_n c_n b_n e^{i\delta_n} \tag{2.13}$$

$$\bar{A}_{\bar{f}} = \textstyle\sum_n \langle \bar{f}|n\rangle\langle n|\mathcal{H}|\overline{D}^0\rangle = \sum_n c_n \bar{b}_n e^{i\delta_n}. \tag{2.14}$$

In the general case,

$$b_n = k_n \bar{b}_n \tag{2.15}$$

$$k_n \neq k_m \text{ for } n \neq m, \tag{2.16}$$

where k_n are constants. Unless there is a unique k such that $k_n = k$ for all n, then there is a phase shift between $A_{\bar{f}}$ and $\bar{A}_{\bar{f}}$. Therefore, we can write

$$A_{\bar{f}} \bar{A}^*_{\bar{f}} = |A_{\bar{f}}||\bar{A}_{\bar{f}}|e^{-i\delta}, \tag{2.17}$$

where δ is the strong phase difference. We can simplify Equation 2.8 under the assumptions

$$|A_{\bar{f}}| \ll |\bar{A}_{\bar{f}}|, \qquad |x|, |y| \ll 1 \tag{2.18}$$

and we have

$$|A_{\bar{f}}|^2|a_+(t)|^2 = |A_{\bar{f}}|^2 \frac{e^{-\Gamma t}}{2}[\cosh(y\Gamma t) + \cos(x\Gamma t)] \approx |A_{\bar{f}}|^2 e^{-\Gamma t} \tag{2.19}$$

$$|\bar{A}_{\bar{f}}|^2|a_-(t)|^2 = |\bar{A}_{\bar{f}}|^2 \frac{e^{-\Gamma t}}{2}[\cosh(y\Gamma t) - \cos(x\Gamma t)] \approx |\bar{A}_{\bar{f}}|^2 e^{-\Gamma t}\left(\frac{x^2+y^2}{4}\right)(\Gamma t)^2 \tag{2.20}$$

$$\begin{aligned} & A_{\bar{f}}\bar{A}^*_{\bar{f}} a_+(t) a^*_-(t) + \bar{A}_{\bar{f}} A^*_{\bar{f}} a_-(t) a^*_+(t) = \\ &= |A_{\bar{f}}||\bar{A}_{\bar{f}}| \frac{e^{-\Gamma t}}{2}\left(e^{-i\delta}(\sinh(y\Gamma t) - i\sin(x\Gamma t)) + e^{i\delta}(\sinh(y\Gamma t) + i\sin(x\Gamma t))\right) \\ &\approx |A_{\bar{f}}||\bar{A}_{\bar{f}}| e^{-\Gamma t}\,(y\cos\delta - x\sin\delta)\,(\Gamma t) \end{aligned} \tag{2.21}$$

where $\Gamma = \frac{\Gamma_1+\Gamma_2}{2}$.

In this way, we can obtain the standard form of the time-dependent decay rate, including D mixing:

$$\Gamma_{\bar{f}}(t) = e^{-\Gamma t}\left(|A_{\bar{f}}|^2 + |A_{\bar{f}}||\bar{A}_{\bar{f}}|\left(y\cos\delta - x\sin\delta\right)(\Gamma t) + \frac{x^2+y^2}{4}|\bar{A}_{\bar{f}}|^2(\Gamma t)^2\right). \tag{2.22}$$

As shown, D mixing is characterized in the decay rate by a deviation from a pure exponential. In order to have the highest sensitivity to x and y, a decay channel for which $|A_{\bar{f}}|^2$ is relatively small is desired. The analysis technique benefits from the ability to compare the signal distribution, given by Equation 2.22, to the Cabibbo-favored decay distribution, which may be treated as a pure exponential. In this way, systematic bias is significantly limited.

One quantity which is often quoted, as it is the only one accessible to the mixing analysis of semileptonic decays, is the time-integrated mixing rate:

$$R_{mix} = \frac{x^2+y^2}{2}. \tag{2.23}$$

2.2 The three-body decay scenario

2.2.1 The Dalitz plot

In the case of a multi-body decay, the amplitudes describing the CF and DCS transitions vary according to the kinematic configurations of the final states. Given a three-body decay $D \to 123$, in Dalitz plot two independent kinematic quantities of the process are represented. This method was firstly developed by Richard Dalitz to analyze the decay of $K^+ \to \pi^+\,\pi^+\,\pi^-$ [32]. The axes on the two dimensional plane correspond to the invariant mass of two of the three possible pairs one can construct. Let us consider for instance:

$$\begin{aligned} m_{12} &= (p_1+p_2)^2 \\ m_{13} &= (p_1+p_3)^2 \end{aligned} \tag{2.24}$$

where $p^2 = E^2 + \vec{p}^{\,2}$. Here $p_{1,2,3}$ are the four-momenta of the particles in the final state. For a generic process, the region of the Dalitz plot that will be populated is constrained by the four-momentum conservation.

For a three-body final state of a scalar resonance, the decay rate is known to be[3]:

---

[3] This formula is correct if one ignores the particle-antiparticle mixing of the parent meson. If one includes the mixing phenomenon, $d\Gamma$ will also depend on the decay time, similarly to Equation 2.26.

$$\Gamma = \frac{1}{(2\pi)^3 32\sqrt{s^3}}|\mathcal{M}|^2 dm_{12}^2 dm_{13}^2 \tag{2.25}$$

If $\mathcal{M}$ is constant, the Dalitz plot will be uniformly populated. This is generally not the case: the dynamics of the strong interactions generate resonances structures along the Dalitz plot.

For this analysis, we choose the invariant masses $m^2_{K\pi}$ and $m^2_{K\pi^0}$ to describe the Dalitz plot.

2.2.2 Mixing in a three-body decay

In a three-body process, such as $D^0 \to K^+\pi^-\pi^0$, the decay rate described in Equation 2.22 will become a function of the invariant masses of the resonances involved in the decay.

One strategy may be to consider the decay rate integrated over a particular Dalitz plot region. This was previously done by *BABAR* [24], but no mixing signal was observed. Although this technique avoids the study of the complete Dalitz plot of the decay, it is sensitive to y' and the time-integrated rate R_{mix} only. Moreover, by considering only a small fraction of the phase-space, one gives up the extreme richness that the interference term may come up with if all the possible contributions to the final states are considered. As the interference term is linear in the mixing parameters, the harder path of doing an amplitude analysis may reward with a larger statistical power in characterizing mixing.

In our case the decay rate described in Equation 2.22 becomes:

$$\begin{aligned}\Gamma_{\bar f}(m_{12}, m_{13}, t) &= e^{-\Gamma t}[|A_{\bar f}(m_{12}, m_{13})|^2 + |A_{\bar f}(m_{12}, m_{13})||\bar A_{\bar f}(m_{12}, m_{13})| \cdot \\ &\cdot \left(y \cos\delta_{\bar f}(m_{12}, m_{13}) - x \sin\delta_{\bar f}(m_{12}, m_{13})\right)(\Gamma t) \\ &+ \frac{x^2+y^2}{4}|\bar A_{\bar f}(m_{12}, m_{13})|^2 (\Gamma t)^2].\end{aligned} \tag{2.26}$$

where

$$\delta_{\bar f}(m_{12}, m_{13}) = arg(A^*_{\bar f}(m_{12}, m_{13})\bar A_{\bar f}(m_{12}, m_{13})) \tag{2.27}$$

and $\bar f = K^+\pi^-\pi^0$.

Note that this equation is valid for intermediate resonances which are not *CP* eigenstates. Here, the Dalitz plot variables are m_{12}, m_{13} and the amplitudes and strong phase difference are explicit functions of the location on the Dalitz Plot.

The CF amplitude $\bar A_{\bar f}(m_{12}, m_{13})$ can be determined up to an overall phase in a time-independent Dalitz Plot analysis of a CF decay to the same final state, with one reference resonance given an arbitrary amplitude. Likewise, in the Dalitz plot analysis of the DCS amplitude, one reference resonance is fixed. The interference between the CF and DCS amplitudes, parametrized with $\delta_{\bar{f}}(m_{12}, m_{13})$, can be determined up to a phase in a time-dependent analysis using Equation 2.26 as long as there are at least two well-measured DCS resonances in the Dalitz plot.

Because both $\bar{A}_{\bar{f}}(m_{12}, m_{13})$ and $A_{\bar{f}}(m_{12}, m_{13})$ now appear in the same Dalitz plot, one of the two arbitrary amplitudes can be determined with respect to the other. We define

$$\begin{aligned} A_{\bar{f}}(m_{12}, m_{13}) &= r_0 A_{\bar{f}}^{DCS}(m_{12}, m_{13}) && (2.28)\\ \bar{A}_{\bar{f}}(m_{12}, m_{13}) &= \bar{A}_{\bar{f}}^{CF}(m_{12}, m_{13}) && (2.29) \end{aligned}$$

In this way the module and the phase of the reference resonance for the DCS amplitude can be set to a fixed value. The arbitrary phase between the CF reference and the DCS reference resonances, δ_0, cannot be extracted from the fit [4]. To better understand the physical meaning of r_0 and δ_0, one should consider that the ratio of the DCS and the CF amplitudes is a global complex number. r_0 is the module of that complex number, while δ_0 is the phase.

Using the Euler's relations in order to expand $\delta_{\bar{f}}(m_{12}, m_{13})$, we find

$$\begin{aligned} \Gamma_{\bar{f}}(m_{12}, m_{13}, t) = {} & e^{-\Gamma t}[r_0^2 |A_{\bar{f}}^{DCS}(m_{12}, m_{13})|^2 + r_0(y^{'}\Re(A^{*DCS}_{\bar{f}}(m_{12}, m_{13})\bar{A}_{\bar{f}}^{CF}(m_{12}, m_{13}))\\ & -x^{'}\Im(A^{*DCS}_{\bar{f}}(m_{12}, m_{13})\bar{A}_{\bar{f}}^{CF}(m_{12}, m_{13})))(\Gamma t)\\ & +\frac{x^2+y^2}{4}|\bar{A}_{\bar{f}}^{CF}(m_{12}, m_{13})|^2(\Gamma t)^2]. \qquad (2.30) \end{aligned}$$

where

$$\begin{aligned} y^{'} &= y\sin(\delta_0) - x\cos(\delta_0)\\ x^{'} &= -y\cos(\delta_0) + x\sin(\delta_0) \end{aligned}$$

The δ_0 phase cannot be determined within this analysis. Nevertheless, fitting the WS Dalitz plot allows to extract x' and y'. Note that in general this phase is different from the equivalent δ in the $D^0 \to K^+ \pi^-$ analysis.

A convention must be adopted to define δ_0. We consider it as the phase difference between the $D^0 \to K^- \rho^+$ and the $D^0 \to K^+ \rho^-$ amplitudes.

---

[4] Note that this phase could not have been parametrized inside the $A_{\bar{f}}^{DCS}$ amplitude and extracted from a fit; Equation 2.26 has no predictive power on δ_0.

2.3 D mixing analysis of $D^0 \to K^+\pi^-\pi^0$

This analysis considers the decay $D^{*+} \to D^0\pi^+$, $D^0 \to K^+\pi^-\pi^0$, indicated in the following as "Wrong sign" (WS) decay. The charge of the pion from the D^* decay tags the initial flavor of the D^0, while the charge of the kaon form the D^0 defines the flavor at decay. If one ignores the mixing contribution, the final state we consider is reached through a DCS transition. If we also include the mixing effect, a further contribution comes from the CF $\overline{D}^0$ decays that undergo a mixing transition. We thus expect to have an interference term arising from the sum of the two contributions. These are the second and third terms in Equation 2.30.

We can have a parametrization of the CF amplitude by fitting separately the process $D^0 \to K^-\pi^+\pi^0$, indicated in the following as "Right Sign" (RS) decay. We can assume that the only contribution to this process is a CF transition, since the DCS amplitude could only intervene through mixing[5].

Our goal is to fully analyze the Dalitz plot structure of both the RS and WS decays. In this way we will be able to measure x' and y' separately.

2.4 $|\mathcal{M}|^2$ parametrization: the *Isobar* model

In order to specify the matrix element $|\mathcal{M}|^2$ defined in Section 2.2.1, an *Isobar* model approach is adopted [33, 34]. The basic idea in this model is that the original three-body decay (in our case the D^0 decay) can be considered as a two steps phenomenon: the D^0 decays into a long living particle (typically a pion or a kaon) and into a resonance. The resonance then decays into two particles. This is pictorially shown in Figure 2.1. Each vertex of the process includes a spin factor that in Figure 2.1 is indicated as ϵ_λ. This differs if one considers scalars, vectors or tensors in the final state.

The matrix element is written in terms of a sum of resonant terms plus a non-resonant contribution:

$$\mathcal{M} = \sum_i a_i e^{i\delta_i} A_i(m_{12}^2, m_{13}^2) + a_0 e^{i\delta_0} \tag{2.31}$$

where a_i and δ_i are the strong amplitudes and phases of the ith resonance. Generally, the A_i are parametrized with relativistic Breit-Wigner functions, which contain a kinetic term and an angular function describing the spin dynamics of the decay. We follow this tradition in order to describe the vectorial and tensorial components of our process. As shown in Section 2.5, the scalar part of the process will be treated differently.

The amplitude for the decay $D^0 \to 123$ with an intermediate spin 1 resonance (12) is:

---

[5] Given that mixing has a rate of the order 10^{-2} and that the ratio between the DCS amplitude and the CF amplitude is of the order 10^{-3}, we expect approximately 1 mixing event every 100,000 CF events in the RS sample

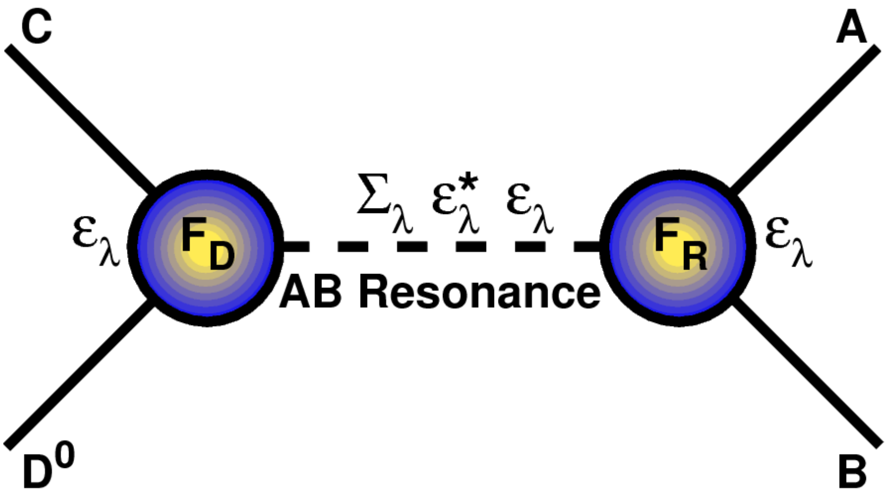

Figure 2.1: Pictorial view of the *Isobar* model for the decay $D^0 \rightarrow$ ABC

$$A = F_r F_D (p_{D^0} + p_3)_\mu \frac{\sum_\lambda \epsilon_\lambda^{\mu *} \epsilon_\lambda^\nu}{m_r^2 - m_{12}^2 - i m_r \Gamma_{12}} (p_1 + p_2)_\nu \tag{2.32}$$

where m_r is the nominal mass of the resonance. If instead one considers a tensorial resonance:

$$A = F_r F_D (p_{D^0} + p_3)_\mu (p_{D^0} + p_3)_\nu \frac{\sum_\lambda \epsilon_\lambda^{\mu\nu *} \epsilon_\lambda^{\alpha\beta}}{m_r^2 - m_{12}^2 - i m_r \Gamma_{12}} (p_1 + p_2)_\alpha (p_1 + p_2)_\beta \tag{2.33}$$

Here F_D and F_r are form factors that quantify the finite nature of the decaying meson and of the intermediate resonance. They will be described in more detail in Section 2.4.2. The rest of the numerator is the angular contribution to the amplitude and will be described in Section 2.4.1.

The denominator of both Equations 2.32 and 2.33 is the relativistic propagator. It is generally accepted to consider a good approximation of the propagator the standard Breit-Wigner function used here:

$$\text{Breit-Wigner} = \frac{1}{m_r^2 - m_{12}^2 - i m_r \Gamma_{12}} \tag{2.34}$$

This approximation holds particularly well if the resonance is narrow. Here, Γ_{12} is a function of the reconstructed mass m_{12}, the momentum p_{12} of either daughter in the (12) rest frame, the momentum p_r of either daughter in the resonance rest frame, the spin J of the resonance, and the width Γ_r of the resonance. The explicit expression is

$$\Gamma_{12} = \Gamma_r \left(\frac{p_{12}}{p_r}\right)^{2J+1} \left(\frac{m_r}{m_{12}}\right) F_r^2. \tag{2.35}$$

2.4.1 Spin dynamics

If the resonance has a non zero spin, it is necessary to provide the amplitude with a description of the angular distribution. In order to determine the angular properties, we start from the spin-sum rule. For a vector resonance, the numerator of Equation 2.32 is:

$$\sum_{\lambda} \epsilon_{\lambda}^{\mu *} \epsilon_{\lambda}^{\nu} = -g^{\mu\nu} + \frac{p_{12}^{\mu} p_{12}^{\nu}}{m_{12}^{2}} \tag{2.36}$$

with λ being the helicity state. Note that in the denominator of the second term of the Equation, we consider the reconstructed invariant mass of the resonance instead of a constant value. This enforces a spin 1 current in the process ($\epsilon_{\lambda}^{\mu}(p_{12}^{\mu}) = 0$). This assumption is generally called Zemach tensor formalism. On the opposite, using a constant in the denominator is the assumption on the base of the helicity model. If the W is near the on-shell region, it is characterized by a spinless component. On the contrary, if the W is far off-shell, it has an effective spin 0 component into its current, and the helicity formalism is more appropriate. It is not established, and is still controversial, where exactly in the mass spectrum one of the two formalisms becomes more appropriate than the other.

2.4.2 Blatt-Weisskopf penetration factors

The coefficients F_D and F_r in Equations 2.32 and 2.33 are the form factors which attempt to model the underlying quark structure of the D^0 meson and the intermediate resonances. To parametrize them, we use the Blatt-Weisskopf penetration form factors with the same convention used by the *CLEO* experiment [34]. In Table 2.1 the parametrization of the form factors is given[6]. Note that they depend on the parameter R, which can be thought of as the effective radius of the meson. To be consistent with the previous Dalitz plot analyses, we choose the D meson to have $R = 5\,\mathrm{GeV}^{-1}$ and all the intermediate resonances to have $R = 1.5\,\mathrm{GeV}^{-1}$.

2.4.3 Final parametrization for vector and tensor resonances

Using the information in the previous sections, we can rewrite the formulas in Equations 2.32 and 2.33 in their final form. For a spin 1 resonance AB we can describe the amplitude as

$$\mathcal{A}_1(ABC|r) = F_D F_r \frac{m_{BC}^2 - m_{AC}^2 + \frac{(m_D^2 - m_C^2)(m_A^2 - m_B^2)}{m_r^2}}{m_r^2 - m_{AB}^2 - i m_r \Gamma_{AB}}. \tag{2.37}$$

---

[6] The basic assumptions behind this parametrization is that the potential for a finite size particle can be derived from the spherical well potential. The solution of the spherical well problem are the Hankel spherical functions. The Blatt-Weisskopf barrier penetration factors are given by the logarithmic derivative of the Hankel wave functions evaluated at R.

Spin	Form Factor
0	1
1	$\frac{\sqrt{1+R^2p_r^2}}{\sqrt{1+R^2+p_{AB}^2}}$
2	$\frac{\sqrt{9+3R^2p_r^2+R^4p_r^4}}{\sqrt{9+3R^2+p_{AB}^2+R^4p_{AB}^4}}$

Table 2.1: The Blatt-Weisskopf penetration form factors parametrization. p_r is the momentum of the meson calculated using the nominal mass value. p_{AB} is the momentum of the meson using the reconstructed mass.

Similar expressions hold for tensor particles:

$$\mathcal{A}_2(ABC|r) = \frac{F_D F_r}{m_r^2 - m_{AB}^2 - i\Gamma_{AB} m_r} \left[\left(m_{BC}^2 - m_{AC}^2 + \frac{(m_D^2 - m_C^2)(m_A^2 - m_B^2)}{m_r^2} \right)^2 \right.$$
$$\left. -\frac{1}{3} \left(m_{AB}^2 - 2m_D^2 - 2m_C^2 + \frac{(m_D^2 - m_C^2)^2}{m_r^2} \right) \left(m_{AB}^2 - 2m_A^2 - 2m_B^2 + \frac{(m_A^2 - m_B^2)^2}{m_r^2} \right) \right]. \tag{2.38}$$

2.5 LASS parametrization for scalar resonances

For scalar particles, a different parametrization is used. For the $K\pi$ S-wave component of the model we use a parametrization extracted in a scattering experiment (LASS,[35])[7]. It consists of a $K_0^*(1430)$ resonance together with an effective range non-resonant component:

$$\mathcal{A}_0 = F \sin\delta_F e^{i\delta_F} + R \sin\delta_R e^{i\delta_R} e^{i2\delta_F} \tag{2.39}$$

where

$$\delta_F = \phi_F + ctg^{-1}(1/(ap_{AB}) + (rp_{AB})/2) \tag{2.40}$$
$$\delta_R = \phi_R + tg^{-1}\left(\frac{M \cdot \Gamma}{M^2 - m_{K\pi}^2}\right) \tag{2.41}$$

---

[7] In the early 1990's, the LASS experiment at SLAC studied the scattering process K^- $p \rightarrow$ K^- π^+ n at 11 GeV of energy to study the $K\pi$ system. They found a scalar resonance, the K^* (1430), with a broad width, that was not possible to describe with the usual Breit-Wigner lineshape.

The first term represents a non-resonant contribution, while the second term represents a resonant contribution. The phases δ_F and δ_R depend on the $K\pi$ invariant mass, while the parameters F, ϕ_F, R and ϕ_R are constants and left floating in the nominal fit. Since the LASS parametrization already includes a non-resonant term, there is no need of further including a global non-resonant contribution.

The central values of the LASS parameters may depend on whether they are measured in a scattering or in a production experiment. In order to illustrate the differences between scattering and production experiments we show in Figure 2.2 the modulus of transition amplitude for the E791 analysis of the $D^+ \to K^- \pi^+ \pi^+$ decay [25] and the LASS scattering data. The reader should be made aware that in the LASS case, the 1/2 isospin component only is represented, while in the E791 case the amplitude in the figure represents a superposition of 1/2 and 3/2 isospin amplitudes. The FOCUS experiment analyzed the separate 1/2 and 3/2 isospin components of the amplitude, and proved that the 1/2 isospin contribution is consistent with the LASS scattering production [26]. As shown in Table 7.3, our parameters differ from the LASS findings. Nevertheless, the large correlation among the parameters in our fit makes any comparison hard.

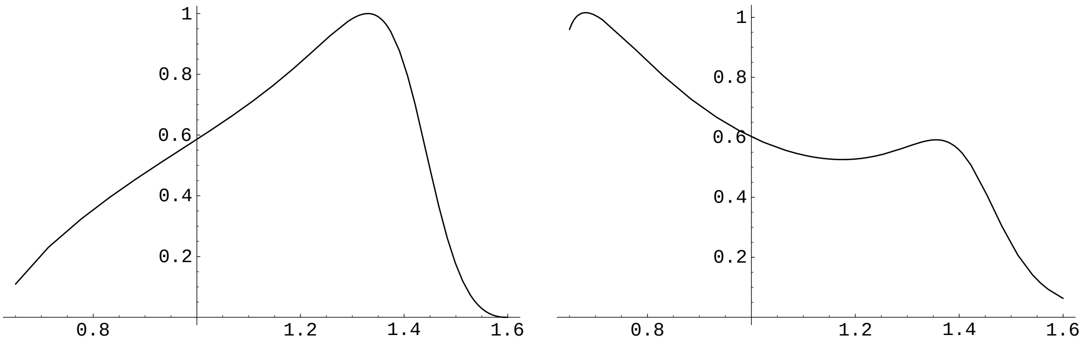

Figure 2.2: Modulus of transition amplitude as a function of $m_{K\pi}$ for LASS (left) and the E791 analysis of $D^+ \to K^- \pi^+ \pi^+$ (right). The parameters used in these plots are given in Table 2.2.

Parameter	E791	LASS
Mass MeV/c^2	1428 +/- 16	1435 +/- 5
Width MeV/c^2	266 +/- 28	279 +/- 6
a	5.73 +/- 0.78	1.95 +/- 0.09
r	-1.32 +/- 0.38	1.76 +/- 0.36
F	-0.96 +/- 0.06	1.0
ϕ_F[deg]	-71.1 +/- 0.1	0.0
R	0.57 +/- 0.04	1.0
ϕ_R[deg]	13.4 +/- 0.3	0.0

Table 2.2: Parameters of LASS K_0^* model as extracted in LASS data and the E791 $D^{*+} \to K^- \pi^+ \pi^-$.

The strategy we adopt in this analysis is to determine the values of the LASS parameters by fitting the $D^0 \to K^-\pi^+\pi^0$ sample, and then use these values as a parametrization of the S-wave in the $D^0 \to K^+\pi^-\pi^0$ fit.

2.6 Average lifetime over the Dalitz plot

This analysis is particularly sensitive to mixing in the interference term, because the second term of Equation 2.30 is linear in the mixing parameters. Mixing varies the average D^0 lifetime, increasing or decreasing its value if the interference is constructive or destructive respectively. Therefore we expect to see a variation of the average lifetime over the Dalitz plot. In order to test this statement, and to see which parts of the Dalitz plot are more sensitive to mixing, we plot the average lifetime in two different mixing scenarios. Each bin of these figures is represented with a box whose dimensions are proportional to the statistics for that bin. This helps in understanding not only which bins vary with the mixing, but also which ones have the higher statistical sensitivity.

For each scenario we perform a MC generation of the Dalitz plot variables and the D^0 lifetime for the signal PDF, using for the Dalitz plot the model obtained from the blind fit described in Section 10.1. We divide the Dalitz plot in bins, and in each bin we calculate the average lifetime. The value of the lifetime used for the generation is the PDG central value of 0.4101 ps [37].

In Figure 2.3 we show the plot of the average lifetime for the no-mixing scenario. As expected, the average is the same all over the Dalitz plot, and is within the range expected given the generated value of the lifetime.

In Figure 2.4 we show the plot of the average lifetime for the scenario where $x' = 0.8\%$ and $y' = 1\%$. This is the preferred scenario looking at the 2008 averages of the HFAG group [22]. It appears from this plot that in the regions where the statistics is higher, the average lifetime is generally higher. An exception seems the region of the interference between the K^{*0} (892) and the $\rho(770)$: on one side of the interference lobe the average lifetime is lower than the generated value. There is also a central region of the Dalitz plot where the statistic is low and the average lifetime is lower than the PDG central value.

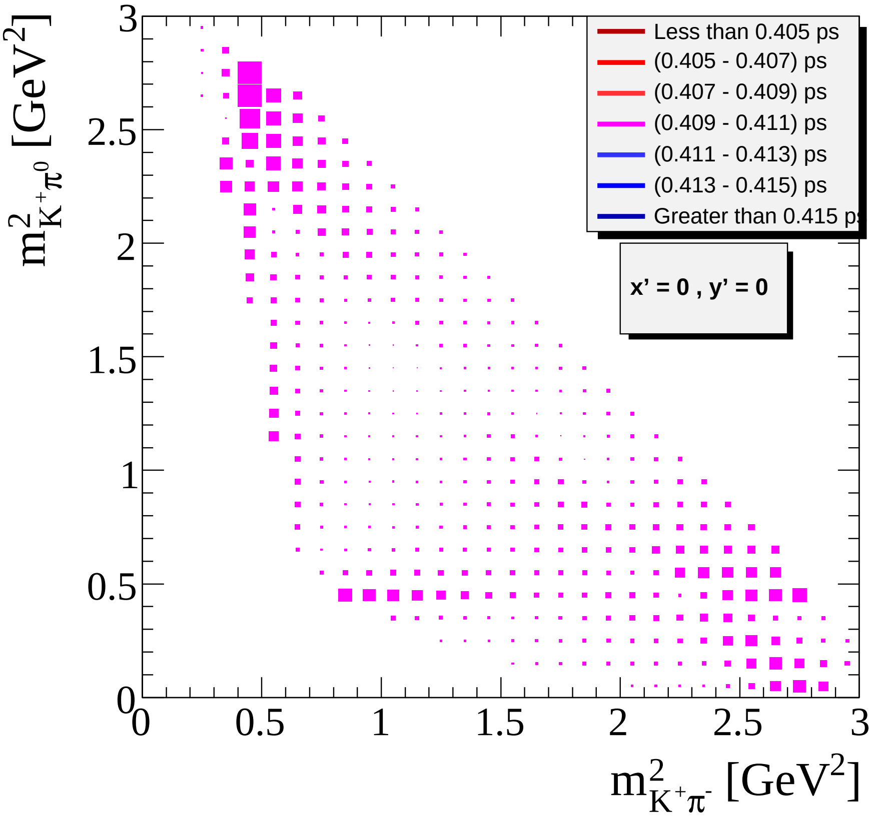

Figure 2.3: Average D^0 lifetime over the Dalitz plot for the no-mixing scenario.

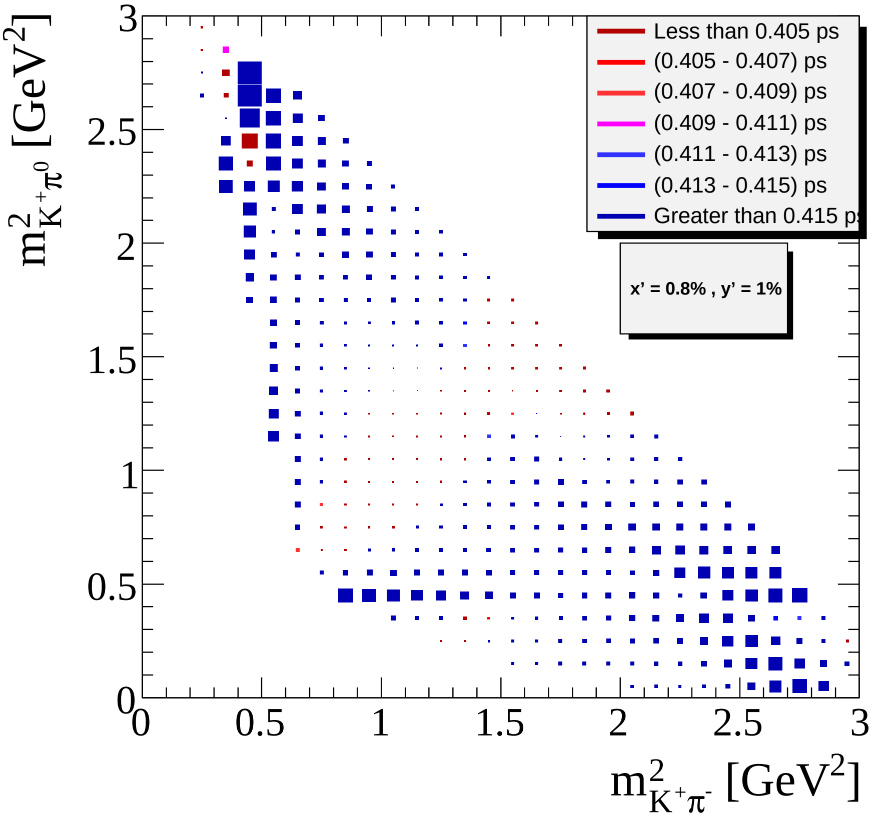

Figure 2.4: Average D^0 lifetime over the Dalitz plot for the scenario $x' = 0.8\%$ and $y' = 1\%$.

Chapter 3

The *BABAR* experiment

3.1 Introduction

The design of *BABAR* detector [27] was planned to allow studies of *CP* violation, together with the study of several B and D meson decays. The PEP-II B factory is a high luminosity e^+e^- collider, which operates at the center-of-mass (CM) energy of 10.58 GeV on the $\Upsilon(4S)$ resonance.

While the main purpose of *BABAR* is the study of B decays from the $\Upsilon(4S)$ resonance, the cross section of $e^+e^- \to c\bar{c}$ events is of the same order of magnitude as the one of $e^+e^- \to b\bar{b}$ events (see Table 3.2). Therefore, high statistics D meson samples are expected.

In PEP-II the electron beam of 9 GeV collides head-on with the positron beam of 3.1 GeV, thus resulting in a Lorentz boost of the $\Upsilon(4S)$ resonance of $\beta\gamma = 0.56$ in the laboratory frame. Many analyses in the B sector require a knowledge of the time interval between the two B decays Δt. If the B momenta are known, Δt can be obtained by measuring the decay point distance Δz. Using a symmetric e^+e^- collider operating at the $\Upsilon(4S)$ resonance, the two B are created almost at rest and the decay point distance would be calculated considering the small phase space left once B masses have been subtracted from the $\Upsilon(4S)$ mass

$$E_{\Upsilon(4S)} = 10.580 \text{ GeV} \quad \to \quad E_B = \frac{E_{\Upsilon(4S)}}{2} = 5.290 \text{ GeV}.$$

Given the total energy of each B, the kinetic energy is

$$\sqrt{E_B^2 - m_B^2} = p = m_B\beta\gamma = 0.341 \text{ GeV}$$

getting:

$$\beta\gamma = 0.065 \sim \beta$$

with the approximation of $\gamma \sim 1$ (the system is non-relativistic). The B decay length would then be

$$\lambda_B = \beta\tau c = 0.065 \cdot 468\ \mu m \simeq 30.42\ \mu m$$

which is a quite small value with respect to a typical vertex detector resolution ($\sim 50\,\mu m$). If a boost is applied along the z-axis, it results in a larger value of $\beta\gamma$ so that the average B meson decay distance Δz is increased to values within the detector resolution. Notice that the typical decay length of a D^0 is approximately $\lambda_D = 23.22\mu m$. This makes its lifetime measurement challenging in the *BABAR* experimental environment.

The very small branching ratios of B meson to *CP* eigenstates, typically of the order of 10^{-4}, the need for full reconstruction of final states with two or more charged particles and several π^0 and the need of tagging the second neutral B place stringent requirements on the detector, which should have:

- a large and uniform acceptance down to small polar angle, relative to the boost direction (forward);
- excellent reconstruction efficiency for charged particles down to momenta of 60 MeV/c and for photons of energy down to 20 MeV;
- very good momentum resolution to separate small signals from background;
- excellent energy and angular resolution for photons detection from π^0 and η^0 decays, and from radiative decays in the range of energy from 20 MeV to 4 GeV;
- very good vertex resolution, both transverse and parallel to beam direction;
- efficient electron and muon identification. This feature is crucial for tagging the B and D flavor, for reconstruction of charmonium states, and for studies of decays with leptons;
- efficient and accurate identification of hadrons over a wide range of momenta for B and D flavor tagging and for exclusive states reconstruction.

Figure 3.1 (top) shows a longitudinal view of the detector, while an end view is shown in Figure 3.1 (bottom). A conventional right-handed coordinate system is defined: the z-axis coincides with the principal axis of the *DCH*, oriented toward the positron direction, while the x-axis points upward. The polar angle coverage extends down to 0.35 mrad in the forward direction and to 0.4 mrad in the backward region. These limits are determined by the permanent dipole (B1) and permanent quadrupoles (Q1) magnets of PEP-II. In order to improve the coverage in the forward region, the whole detector is offset relative to the interaction point (IP) by 37 cm in the forward direction.

In the following, a detailed presentation of design, construction and performance of the main components of the *BABAR* detector is provided.

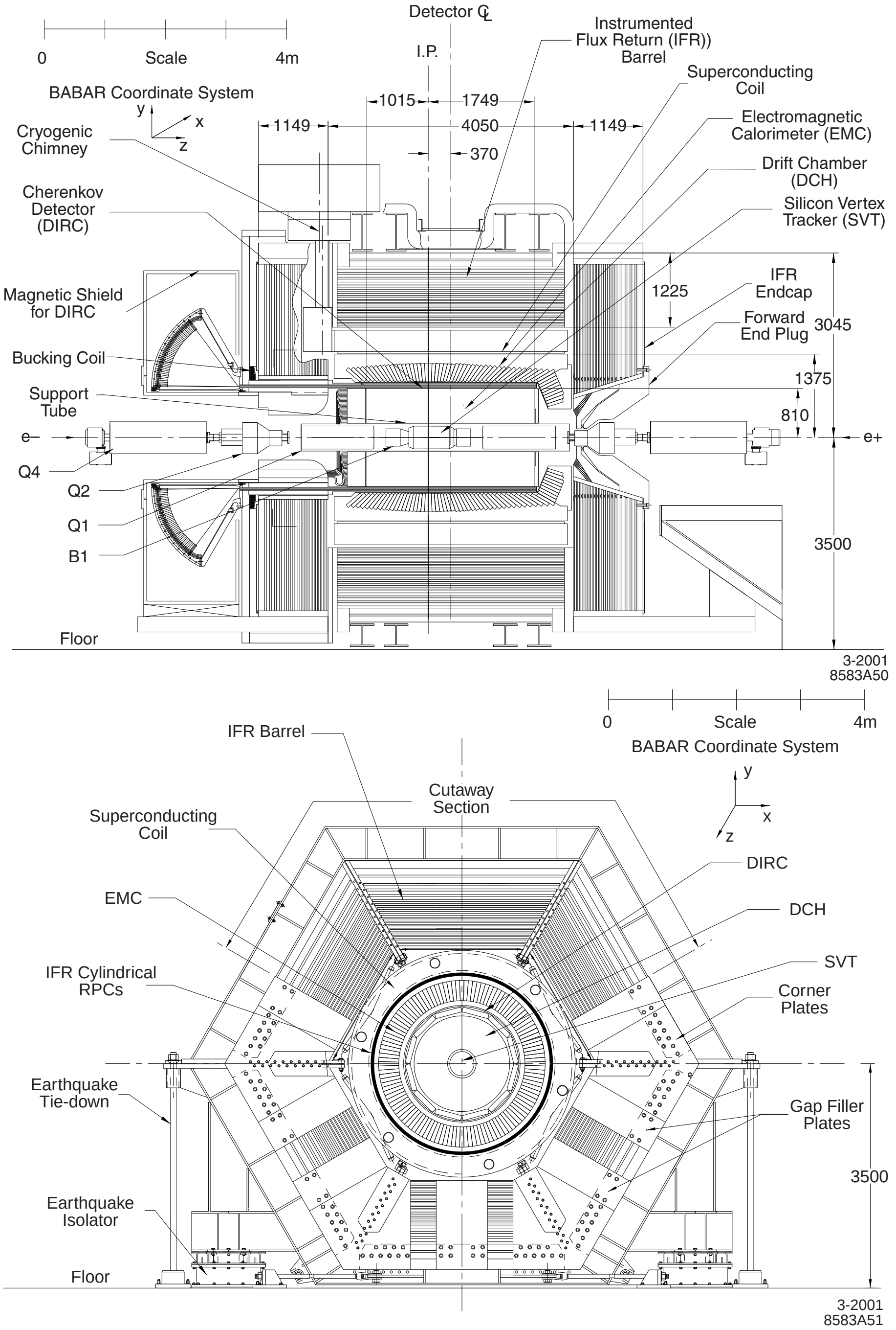

Figure 3.1: Longitudinal (top) and end (bottom) views of the *BABAR* detector. Units are mm

3.2 The PEP-II B Factory

PEP-II is an e^+e^- storage ring system, designed to operate at a CM energy equal to the $\Upsilon(4S)$ resonance mass, 10.58 GeV. Design parameters of PEP-II are presented in Tab. 2-1. Instant luminosity and daily integrated luminosity exceed the project values, having achieved the peak value of $1.2 \cdot 10^{34} cm^{-2}s^{-1}$ and a daily integrated luminosity of 891 pb^{-1} before the end of the data taking.

Parameters	Design	Typical
Energy HER/LER (GeV)	9.0/3.1	9.0/3.1
Current HER/LER (A)	0.75/2.15	0.7/1.3
# of bunches	1658	553-829
Bunch spacing (ns)	4.2	6.3-10.5
$\sigma_{Lx}(\mu m)$	110	120
$\sigma_{Ly}(\mu m)$	3.3	5.6
σ_{Lz} (mm)	9	9
Luminosity $(10^{33} cm^{-2}s^{-1})$	3	10
Luminosity (pb^{-1}/d)	135	700

Table 3.1: PEP-II beam parameters. Values are given both for the design and for typical colliding beam operation. HER and LER refer to the high energy e^- and low energy e^+ ring, respectively. σ_{Lx},σ_{Ly} and σ_{Lz} refer to the horizontal, vertical and longitudinal RMS size of the luminous region.

Data are collected mostly at $\Upsilon(4S)$ peak; they are referred to as *on-resonance* data. The main processes active at the $\Upsilon(4S)$ are summarized in Table 3.2; *light* (u, d, s) and *charm quark pairs* production is usually referred to as *continuum production*. While most of the data are recorded at peak, about 10% are taken at a CM energy 40 MeV lower than $\Upsilon(4S)$ resonance, to allow studies of *continuum*, and are called *off-resonance* data. In addition, in 2008 BABAR undertook a data taking at different Y excited states energy, nominally the $\Upsilon(2S)$, the $\Upsilon(3S)$ and an energy scan between the $\Upsilon(4S)$ and the $\Upsilon(6S)$ mass. These datasets are not considered in the present analysis.

3.2.1 Luminosity

The luminosity $\mathcal{L}$ of the machine depends on the careful tuning of several parameters. This dependence is expressed as:

$$\mathcal{L} = \frac{nfN_1N_2}{A}$$

where n is the number of bunches in a ring, f is the bunch crossing frequency, $N_{1,2}$ are the number of particles in each bunch, and A is their overlap section.

The machine has surpassed the design performances, reaching a peak luminosity of $L = 1.2 \cdot 10^{34}$ $\text{cm}^{-2}\text{s}^{-1}$, with a significantly lower number of bunches.

$e^+e^- \rightarrow$	Cross-section (nb)
$b\bar{b}$	1.05
$c\bar{c}$	1.30
$s\bar{s}$	0.35
$u\bar{u}$	1.39
$d\bar{d}$	0.35
$\tau^+\tau^-$	0.94
$\mu^+\mu^-$	1.16
e^+e^-	~ 40

Table 3.2: Production cross-sections at $\sqrt{s} = M(\Upsilon(4S))$. The e^+e^- cross-section is the effective cross-section, expected within the experimental acceptance.

Figure 3.2.1 shows the integrated luminosity provided by PEP-II collider in the period October 1999 - April 2008, along with the integrated luminosity recorded by the *BABAR* detector, that is 432.89 fb^{-1} collected at the $\Upsilon(4S)$ resonance, plus 53.85 fb^{-1} *off-resonance*, 14.45 fb^{-1} at the $\Upsilon(2S)$ resonance and 30.23 fb^{-1} collected at the $\Upsilon(3S)$ resonance. This analysis uses a subsample of 384 fb^{-1}.

3.2.2 Machine background

Beam-generated background causes high single-counting rates, data acquisition dead times, high currents and radiation damage of both detector components and electronics. This resulted in lower data quality and may have limited the lifetime of the apparatus. For this reason the background generated by PEP-II was studied in detail and the interaction region was carefully designed. Furthermore, background rates were continuously monitored during data acquisition to prevent critical operation conditions for the detector.

The primary sources of machine-generated background are:

- *synchrotron radiation* in the proximity of the interaction region. A strong source of background (many kW of power) is due to beam deflections in the interaction region. This component is limited by channeling the radiation out of *BABAR* acceptance with a proper design of the interaction region and the beam orbits, and placing absorbing masks before the detector components;

- *interaction* between *beam particles* and *residual gas* in either ring. This can have two different origins: beam gas bremsstrahlung and Coulomb scattering. Both types of interaction cause an escape of beam particles from their orbit. This background represents the primary source of radiation damage for the inner vertex detector and the principal background for the other detector components;

- *electromagnetic showers generated by beam-beam collisions.* These showers are due to energy degraded e^+e^- produced by radiative Bhabha scattering and hitting the beam pipe within a few meters of the IP. This background is proportional to the

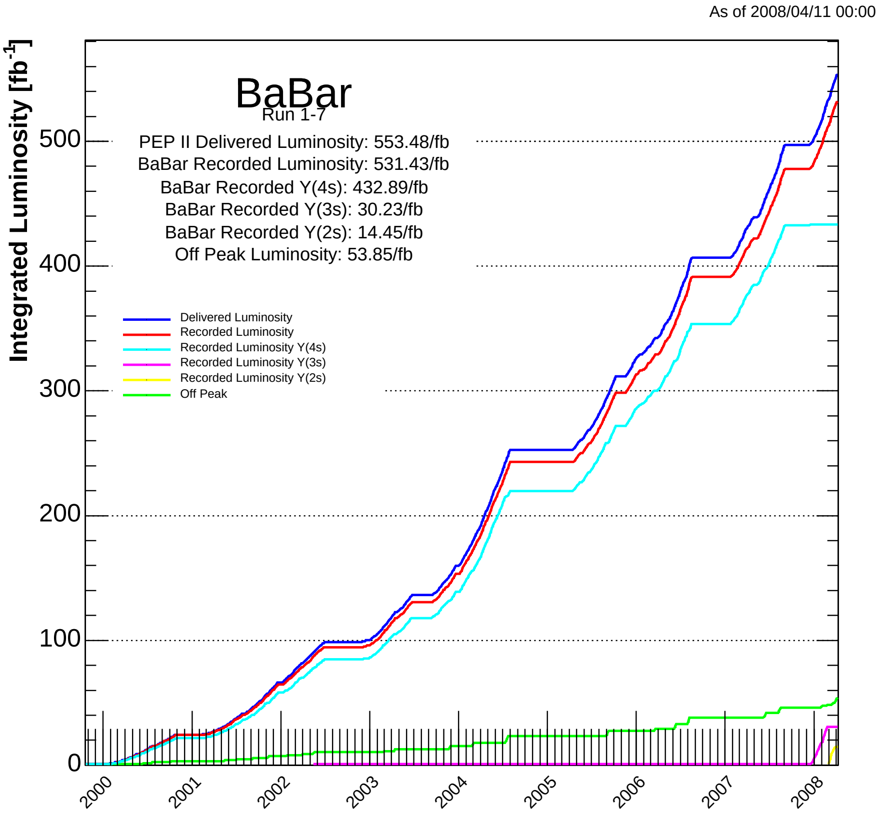

Figure 3.2: PEP-II delivered and *BABAR* recorded luminosity in the whole data taking period.

luminosity of the machine and whereas now is under control, is expected to increase in case of higher operation values.

3.2.3 Detector Overview

The *BABAR* detector was designed and constructed in such a way to fulfill all the above requirements. A cutaway picture of the detector is shown in Figure 3.1. The main subsystems are:

1. the *Silicon Vertex Tracker* (*SVT*), which provides very accurate position information for charged tracks. In addition, it is the only tracking device for charged particles with very low transverse momentum, down to transverse momenta of $p_\perp \sim 50\,\mathrm{MeV}/c$. This is especially important to reconstruct $D^* \rightarrow D^0\ \pi_s^\pm$ decays, where the 'slow' pion $\pi_s^\pm$ has very low energies;
2. the *Drift Chamber* (*DCH*), surrounding the vertex detector, has a helium-based gas mixture in order to minimize multiple scattering. It provides the main momentum measurements for charged particles. In addition, the specific ionization measurements ($\mathrm{d}E/\mathrm{d}x$) are used for identification of low momentum particles;
3. the *Detector of Internally Reflected* Čerenkov *light* (*DIRC*) is a novel device designed for charged hadron particle identification;
4. the *Electromagnetic Calorimeter* (*EMC*), which consists of Cesium Iodide crystals, is the most important detector for electron identification (by means of the ratio $\frac{E}{p}$ of the deposited energy E and measured momentum p). It has a forward endcap to take into account the laboratory frame boost which the decay products are affected of. In addition, its measurements of neutral particles are crucial for the determination of the distributions of interest in many decays;
5. a superconducting *solenoid* surrounds the detector and produces a 1.5 T axial magnetic field;
6. the *Instrumented Flux Return* (*IFR*) which provides muon and neutral hadron identification.

The next few sections will describe the individual detector components.

3.3 Tracking System

The charged particle detection and track parameter determination system consists of two components: the Silicon Vertex Tracker (*SVT*) and the Drift Chamber (*DCH*). In particular, angles and positions, measured by the *SVT*, are used to determine the B and D meson decay vertices, whereas the track curvature, in the *DCH*, gives momentum determination. Tracks reconstructed in *SVT* and *DCH* are also extrapolated to the other detector components (*DIRC*, *EMC* and *IFR*). Since the average momentum of charged particles is less than 1 GeV/c , the precision of the measured track parameters is mostly affected by multiple Coulomb scattering in the detector material. Thus a special attention is devoted to the components design in order to limit the overall amount of active material in the tracking region. The global coordinate system is defined by the *DCH* position. Because of either seismic activity or local deformation due to magnet quenches or detector access, the *SVT* modules move with respect to the *DCH*. The alignment procedure is performed using tracks from $e^+e^- \to \mu^+\mu^-$ events and cosmic rays.

3.3.1 Silicon Vertex Tracker

The charged particle tracking system is made of two components, the *SVT* and the *DCH*, and its principal purpose is the efficient detection of charged particles and the measurement of their momentum and angles with high precision.

The *SVT* [28] has been designed to provide precise reconstruction of charged particle trajectories and decay vertices near the interaction region for the measurement of the time-dependent *CP* asymmetry, which requires a vertex resolution along the z-axis better than $80\,\mu$m. A resolution of $\sim 100\,\mu$m in the plane perpendicular to the beam line is achieved. Many of the decay products of B and D mesons have low p_T. The *SVT* also gives stand-alone tracking for particles with transverse momentum less than 120 MeV/c, the minimum that can be measured reliably in the *DCH* alone. This feature is fundamental for the identification of slow pions from D^* decays: a tracking efficiency of 70% or more is achieved for tracks with a transverse momentum in the range 50-120 MeV, with respect to an efficiency of $\sim$ 95% for $p_T > 300$ MeV/c. The *SVT* is composed of five layers of detectors (see Figure 3.3) that are assembled with modules with readout at each end, thus reducing the inactive material in the acceptance volume.

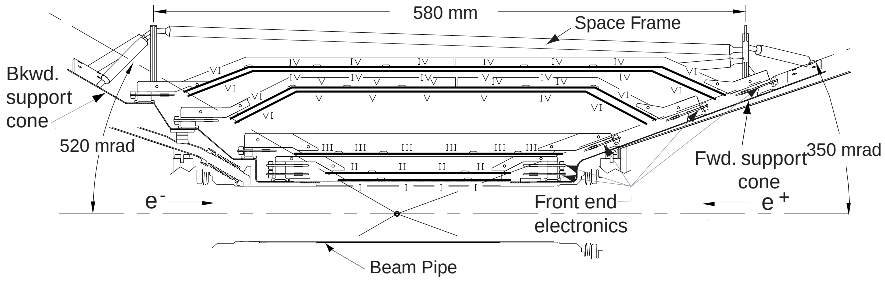

Figure 3.3: Schematic view of the *SVT*: longitudinal section

The inner three layers provide position and angle information for vertices and are mounted as close to the beryllium beam pipe as practical (first layer at a radius $r = 3.2$ cm), thus minimizing the impact of multiple scattering in the beam pipe. The outer two layers are at much larger radius (fourth layer at $r = 12.4$ cm), providing the coordinate and angle measurements needed to link *SVT* and *DCH* track segments (see Figure 3.4).

To fulfill the physics requirements, the spatial resolution, for perpendicular tracks, must be 10–15 μm in the three inner layers and about 40 μm in the two outer layers. The inner three layers perform the impact parameter measurements, while the outer layers are necessary for pattern recognition and low p_T tracking, give redundant information to inner modules and allow track association between *SVT* and *DCH*. The five layers of double-sided silicon strip sensors, which form the *SVT* detector, are organized in 6, 6, 6, 16, and 18 modules, respectively. The modules of the inner three layers are straight, while the modules of layers 4 and 5 are *arch*-shaped (see Figure 3.3 and 3.4). This arch design was chosen to minimize the amount of silicon required to cover the solid angle, while increasing the crossing angle for particles near the edges of acceptance. In order to minimize the material in the acceptance region, the readout electronics are mounted entirely outside the active detector volume. The total active silicon area is 0.96 m^2 and the material traversed by particles is $\sim 4\%$ of a radiation length. The geometrical acceptance of *SVT* is 90% of the solid angle in the CM system, and typically the 86% is used in charged particle tracking.

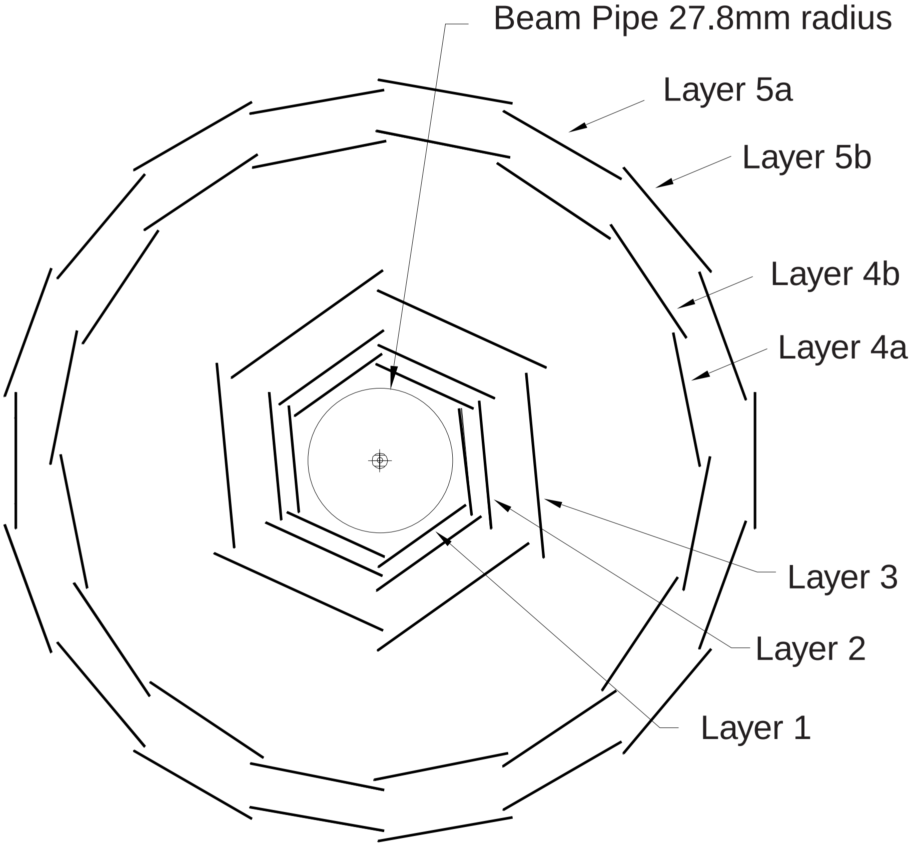

Figure 3.4: Schematic view of the *SVT*: transverse section

The spatial resolution is determined by measuring the distance (in the plane of the sensor) between the track trajectory and the hit, using high-momentum tracks in two prong events. The *SVT* hit resolution for z and ϕ side hits as a function of track incident angle for each of the five layers is shown in Figure 3.5.

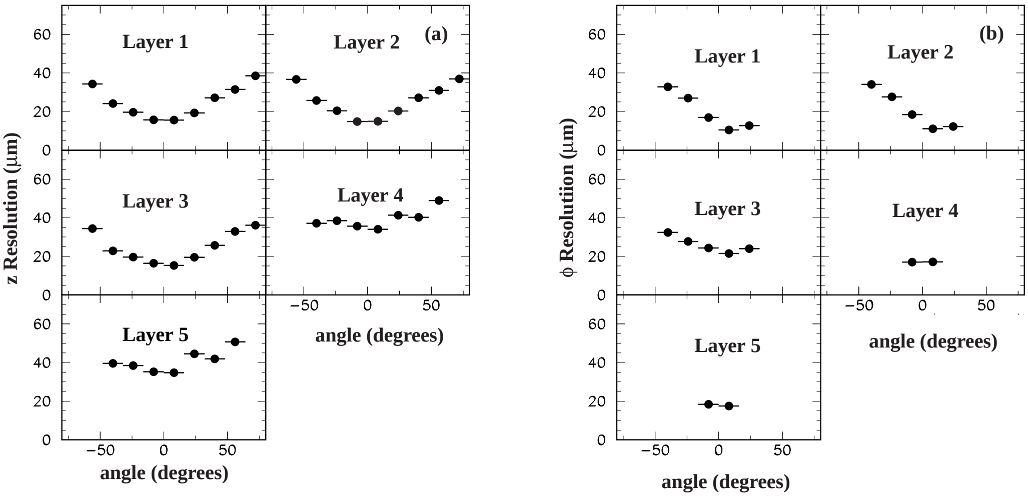

Figure 3.5: *SVT* hit resolution in the z (left) and ϕ (right) coordinates, plotted as a function of track incident angle. Each plot shows a different layer of the *SVT*. The plots in the ϕ coordinate for layers 1-3 are asymmetric around $\phi = 0$ because of the "pinwheel" design of the inner layers.

The measured resolutions are in excellent agreement with expectations from Monte Carlo simulations. The double-sided sensors provide up to ten measurements per track of $\mathrm{d}E/\mathrm{d}x$. For every track with signals from at least four sensors in the *SVT*, the $\mathrm{d}E/\mathrm{d}x$ mean is calculated. For minimum ionizing particles (MIPs), the resolution on $\mathrm{d}E/\mathrm{d}x$ is approximately 14%. A 2σ separation between kaons and pions can be achieved up to momenta of 500 MeV/c and between kaons and protons beyond 1 GeV/c.

3.3.2 Drift Chamber

The Drift Chamber, or *DCH*, is the *BABAR* main tracking device. It supplies high precision measurements of charged particle momenta and angles, through measurements of track curvature inside the 1.5 T magnetic field and it contributes also to particle identification (PID) process by measuring the energy loss due to ionization ($\mathrm{d}E/\mathrm{d}x$); a resolution of about 7.5% allows a π/K discrimination in the momentum range up to 700 MeV/c. The *DCH* is a compact design, 280 cm-long cylinder with an inner radius of 23.6 cm and an outer radius of 80.9 cm.

The forward and rear aluminum end-plates are 12 mm and 24 mm thick respectively. The readout electronics are mounted on the backward end-plate, minimizing, in this way, the amount of material in the forward direction and thus preventing performances degradation for the outer *BABAR* detector components.

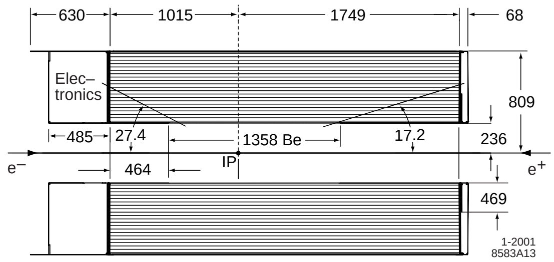

Figure 3.6: Longitudinal section of the *DCH* with principal dimensions; the chamber center is offset by 370 mm from the interaction point. Numbers are in mm

Since momentum resolution is limited by multiple scattering in the inner cylinder, *DCH* is built using light materials, low mass wires and helium-based gas mixture. The mixture of 80% helium and 20% isobutane is chosen to provide good spatial and $\mathrm{d}E/\mathrm{d}x$ resolution, and a reasonably short drift time, while minimizing the material.

A longitudinal section of the *BABAR* *DCH* is shown in Figure 3.6. The *DCH* may be imagined organized into 7104, 1.2 x 1.8 cm, hexagonal cells clustered in 40 concentric layers. Each hexagonal cell consists of one sense wire surrounded by six field-shaping wires; in such a configuration an approximate circular symmetry of the equipotential contours is reached over a large portion of the cell. The field wires are at ground potential, while a positive high voltage is applied on the sense wire.

The 40 layers are grouped by into super-layers. Figure 3.7(b) shows the four innermost superlayers. A complete symmetry along the z-axis does not allow the track position reconstruction along that direction. For this reason two different wire types are used: the wire type A, parallel to the z-axis, provides position measurements in the $x - y$ plane, while longitudinal position information is obtained with wires placed at small angles with respect to the z axis (U or V wire type). Sense and field wires have the same orientation in each super-layer and are alternating following the scheme AUVAUVAUVA.

The design value for the spatial resolution for single hits in *DCH* is 140 μm. The single cell resolution, obtained from all charged tracks in hadronic events, is shown in Figure 3.8(a) for a working voltage around 1960 V; its mean value is $\sim$ 125 μm. The chamber hit timing information is reconstructed using TDCs. Flash-ADCs are used to monitor the shape of pulse signal as a function of time. Both information are fundamental to reconstruct the energy deposit inside the cells. A correction for the gain factor is computed as function of a known injected amount of charge.

Apart from precise measurements of charged particle momenta and directions, the drift chamber also provides particle identification by the determination of the ionization loss $\mathrm{d}E/\mathrm{d}x$. Corrections to $\mathrm{d}E/\mathrm{d}x$ due to saturation, cell internal and single wire path lengths and layer gain are computed during offline reconstruction phase[1]. *Bhabha* events (i.e. $e^+e^- \to e^+e^-$) are used to determine the resolution on the mean of energy loss, which is (Figure 3.8(b)) of about 7.5%.

---

[1] All correction have been proved to be stable as a function of time

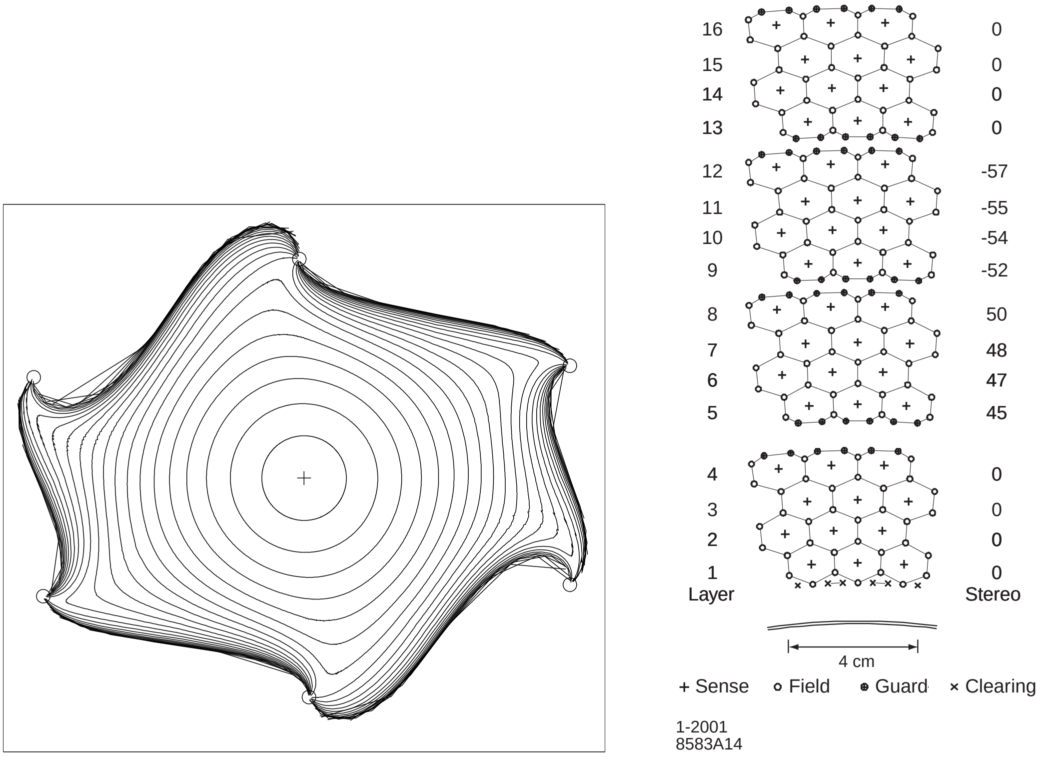

(a) (b)

Figure 3.7: *DCH*: view of a single cell (a) and schematic layout of drift cells for the four innermost superlayers (b). Lines have been added between field wires to aid in visualization of the cell boundaries. The numbers on the right side give the stereo angles (mrad) of sense wires in each layer. The 1 mm-thick beryllium inner wall is shown inside of the first layer.

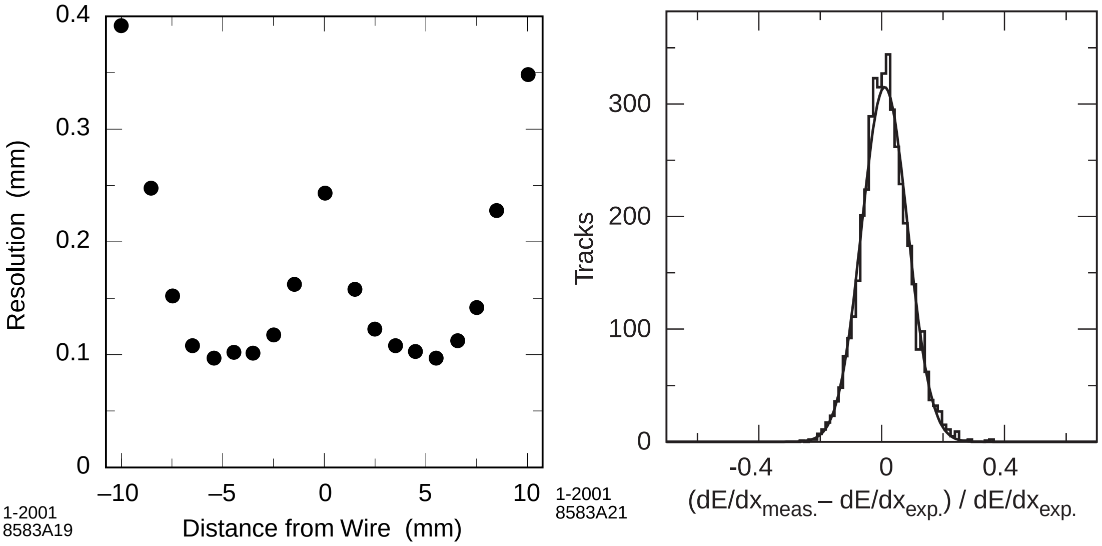

Figure 3.8: (a) *DCH* single hit resolution. (b) dE/dx resolution for *Bhabha* electrons.

3.4 Detector of Internally Reflected Čerenkov Light (*DIRC*)

Above ~ 700 MeV/c the dE/dx information does not allow to separate pions and kaons. *BABAR* has therefore a dedicated PID subdetector. It is a new type of ring-imaging Čerenkov detector called *DIRC* [29]. It was designed to be able to provide π/K separation of $\sim 3\sigma$ or greater for all tracks from B or D meson decays from the pion Čerenkov threshold up to 4.2 GeV/c. The phenomenon of Čerenkov light emission is widely used in particle detectors technology. A charged particle traversing a medium with a velocity of β greater than the speed of light in that medium (that is $\beta > \frac{1}{n}$, where n is the medium refraction index) emits directional electromagnetic radiation (called Čerenkov light). The angle of emission θ_c of the photons with respect to the track direction is called Čerenkov angle and is determined by the velocity of the particle with the relation

$$cos\theta_c = \frac{1}{n\beta}$$

where $\beta = \frac{v}{c}$, v is the particle velocity, and c the light velocity.

Thus, the measurement of θ_c determines β and, given the momentum of the particle (measured in the *DCH*), the mass of the particle can be obtained. The *DIRC* (Figure 3.9) is placed before the electromagnetic calorimeter. In order to minimize the worsening of the energy resolution and volume, and hence cost, of the electromagnetic calorimeter, the *DIRC* has been designed to be thin and uniform in terms of radiation lengths. Moreover, for operation at high luminosity, it needs fast signal response, and should be able to tolerate high background.

Figure 3.10 shows a schematic view of *DIRC* geometry and basic principles of Čerenkov light production, transport and image reconstruction.

Since particles are produced mainly forward in the detector because of the boost, the *DIRC* photon detector is placed at the backward end: the principal components of the *DIRC* are shown in Figure (3.9). The *DIRC* is placed in the barrel region and consists of 144 long, straight bars arranged in a 12-sided polygonal barrel. The bars are 1.7 cm-thick, 3.5 cm-wide and 4.90 m-long: they are placed into 12 hermetically sealed containers, called *bar boxes*, made of very thin aluminum-hexcel panels. Within a single bar box, 12 bars are optically isolated by a ~ 150 μm air gap enforced by custom shims made from aluminum foil.

The radiator material used for the bars is synthetic fused silica: the bars serve both as radiators and as light pipes for the portion of the light trapped in the radiator by total internal reflection. Synthetic silica has been chosen because of its resistance to ionizing radiation, its long attenuation length, its large index of refraction, its low chromatic dispersion within its wavelength acceptance.

The Čerenkov radiation is produced within these bars and is brought, through successive total internal reflections, in the backward direction outside the tracking and magnetic volumes: only the backward end of the bars is instrumented. A mirror placed at the other

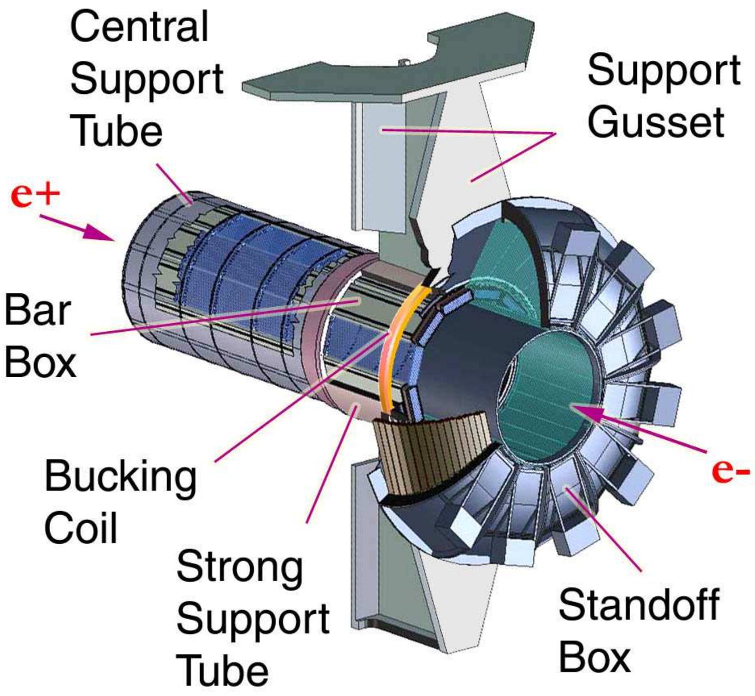

Figure 3.9: Exploded view of the *DIRC* mechanical support structure without the iron magnetic shield.

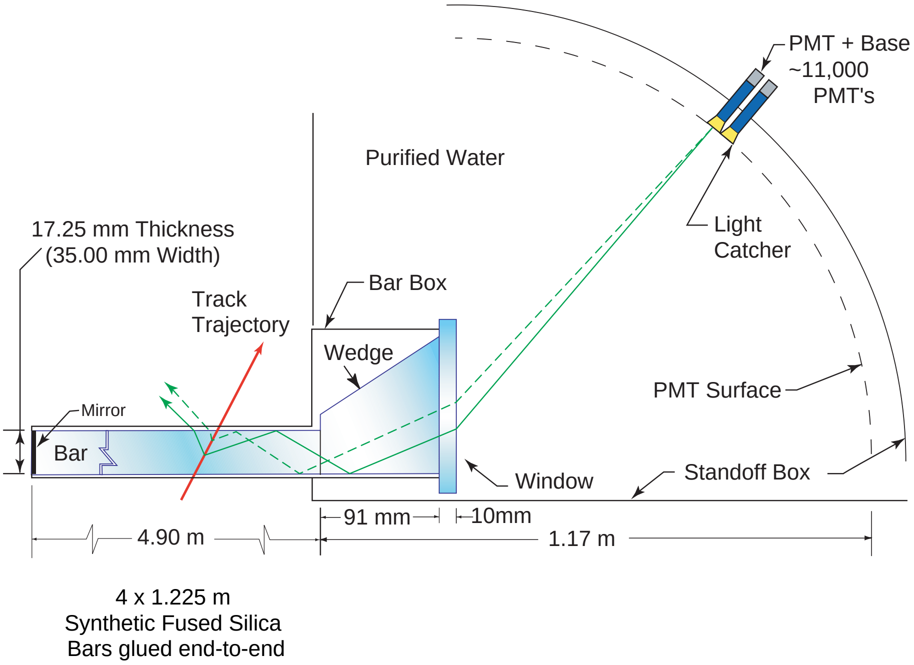

Figure 3.10: Schematics of the *DIRC* fused silica radiator bar and imaging region.

end on each bar reflects forward-going photons to the instrumented end. The Čerenkov angle at which a photon was produced is preserved in the propagation, with some discrete ambiguities (the forward-backward ambiguity can be resolved by the photon arrival-time measurement, for example). The *DIRC* efficiency grows together with the particle incidence angle because more light is produced and a larger fraction of this light is totally reflected. To maximize the total reflection, the material must have a refractive index (fused silica index is $n = 1.473$) higher than the surrounding environment (the *DIRC* is surrounded by air with index $n = 1.0002$).

Once photons arrive at the instrumented end, most of them emerge into a water-filled expansion region, called the *Standoff Box*: the purified water, whose refractive index matches reasonably well that of the bars ($n_{H_2O} = 1.346$), is used to minimize the total internal reflection at the bar-water interface.

The standoff box is made of stainless steel and consists of a cone, cylinder and 12 sectors of PMTs: it contains about 6000 liters of purified water. Each of the 12 PMTs sectors contains 896 PMTs in a close-packed array inside the water volume: the PMTs are linear focused $2.9\,cm$ diameter photo-multiplier tubes, lying on an approximately toroidal surface.

The *DIRC* is intrinsically a three-dimensional imaging device, giving the position and arrival time of the PMT signals. The three-dimensional vector pointing from the center of the bar end to the center of the PMT is computed, and then is extrapolated (using Snell's law) into the radiator bar in order to extract, given the direction of the charged particle, the Čerenkov angle. Timing information is used to suppress background hits and to correctly identify the track emitting the photons.

3.4.1 *DIRC* performance

The *DIRC* detector offers a powerful mean to discriminate kaons and pions. In Figure 3.11 the Čerenkov angle distribution for several particles is shown. As can be noted, kaons and pions present a large discrepancy for low momenta. The discrimination between pions and leptons is guaranteed by the associated information of the *EMC* and *IFR* detectors. Performance plots for kaons and pions identification and fake rates as a function of momenta are shown in Section 4.1.2.

3.5 The Electromagnetic Calorimeter *EMC*

The electromagnetic calorimeter (*EMC*) is designed to measure electromagnetic showers with excellent efficiency, energy and angular resolution over the energy range from 20 MeV to 9 GeV. The understanding of *CP* violation in the B meson system requires the reconstruction of final state containing a direct π^0, or that can be reconstructed through a decay chain containing one or more π^0. Moreover, by identifying electrons the *EMC* contributes to the flavor tagging of neutral B-mesons via semi-leptonic decays, to the

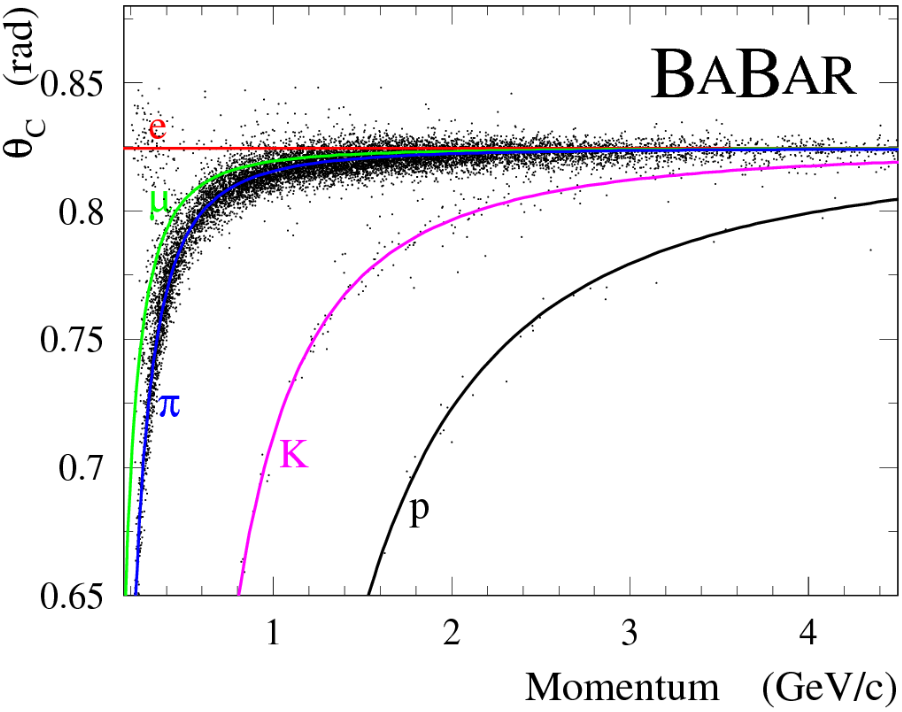

Figure 3.11: Čerenkov angle distribution in the *DIRC* for different particles.

reconstruction of vector mesons like J/ψ and to the study of semi-leptonic and rare decays of B and D mesons, and τ leptons.

The upper bound of the energy range is set by the need to measure QED processes, like $e^+e^- \to e^+e^-(\gamma)$ and $e^+e^- \to \gamma\gamma$ for calibration and luminosity determination. The lower bound is set by the need for highly efficient reconstruction of B-mesons decays containing multiple π^0 s and η^0s. The measurement of very rare decays containing π^0 s in the final state (for example, $B^0 \to \pi^0\pi^0$) puts the most stringent requirements on energy resolution, expected to be of the order of $1-2\%$. Below 2 GeV energy, the π^0 mass resolution is dominated by the energy resolution, while at higher energies, the angular resolution becomes dominant and it is required to be of the order of few mrad. The *EMC* is also used for electron identification and for completing the *IFR* output on μ and K_L^0 identification. It also has to operate in a $1.5\,T$ magnetic field.

The *EMC* has been chosen to be composed of a finely segmented array of thallium-doped cesium iodide (CsI(Tl)) crystals. The crystals are read out with silicon photodiodes that are matched to the spectrum of scintillation light. The energy resolution of a homogeneous crystal calorimeter can be described empirically in terms of a sum of two terms added in quadrature:

$$\frac{\sigma_E}{E} = \frac{a}{\sqrt[4]{E(\,\mathrm{GeV})}} \oplus b$$

where E and σ_E (measured in GeV) refer to the energy of a photon and its r.m.s.

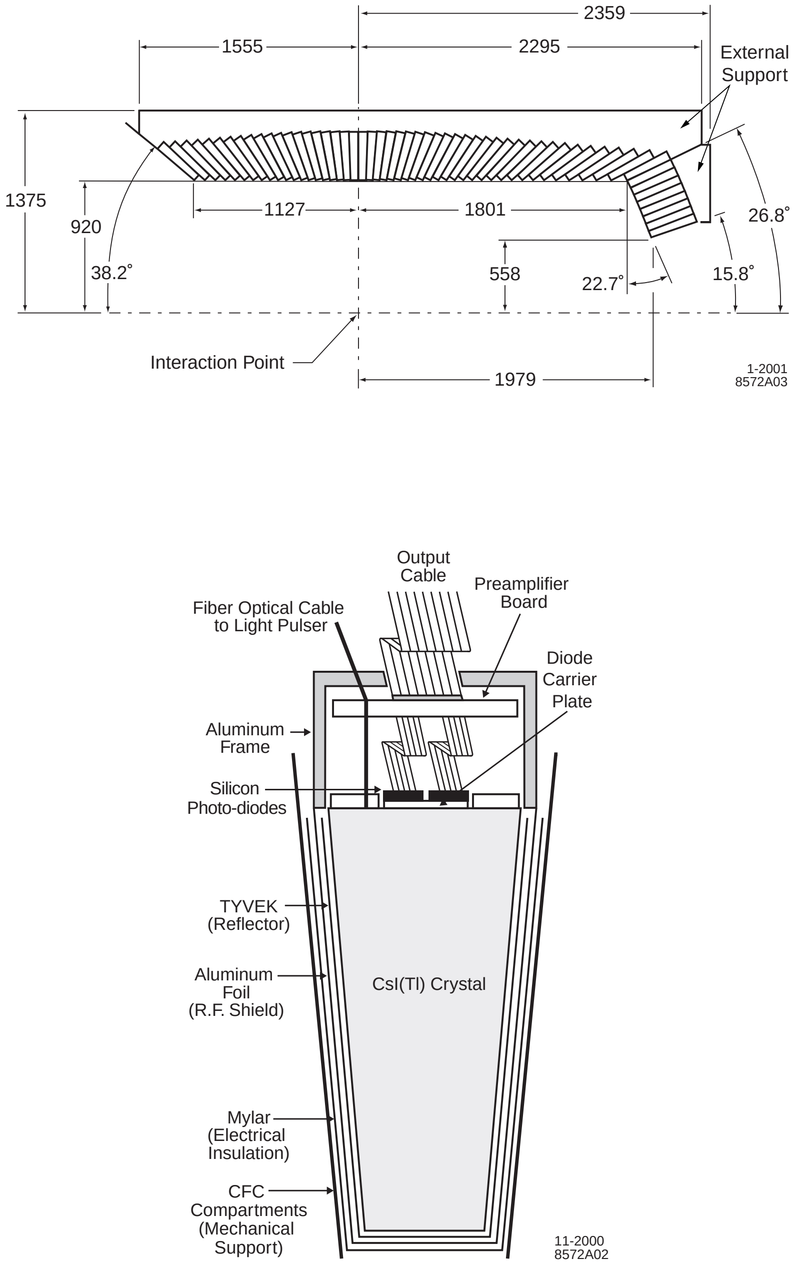

Figure 3.12: The electromagnetic calorimeter layout in a longitudinal cross section and a schematic view of the wrapped CsI(Tl) crystal with the front-end readout package mounted on the rear face (not to scale).

error. The energy dependent term a arises from the fluctuations in photon statistics. Other sources are the electronic noise of the photon detector and electronics and from the beam-generated background that leads to large numbers of additional photons. This first term dominates at low energy, while the constant term b is dominant at higher energies ($>$ 1 GeV). The latter derives from non-uniformity in light collection, leakage or absorption in the material in front of the crystals and uncertainties in the calibration.

The angular resolution is determined by the transverse crystal size and the distance from the interaction point: it can be empirically parameterized as a sum of an energy-dependent and a constant term

$$\sigma_\theta = \sigma_\phi = \frac{c}{\sqrt{E(\,\mathrm{GeV})}} + d \tag{3.1}$$

where E is measured in GeV. In CsI(Tl), the intrinsic efficiency for photon detection is close to 100% down to a few MeV, but the minimum measurable energy in colliding beam data is about 20 MeV for the *EMC*: this limit is determined by beam and event-related background and the amount of material in front of the calorimeter. Thallium-doped CsI meets the needs of *BABAR* in several ways. Its properties are listed in Table 3.3. The high light yield and small Molière radius allow for excellent energy and angular resolution, while the short radiation length allows for shower containment at *BABAR* energies with a relatively compact design.

Parameter	Values
Radiation length	1.85 cm
Moliére radius	3.8 cm
Density	4.53 g/ cm^3
Light yield	50.000 γ/ MeV
Light yield tem. coeff.	0.28% /C
Peak emission λ_{max}	565 nm
Refractive index (λ_{max})	1.80
Signal decay time	680 ns (64%)
	3.34 μs(36%)

Table 3.3: Properties of CsI(Tl)

The *BABAR EMC* consists of a cylindrical barrel and a conical forward end-cap: it has a full angle coverage in azimuth, while in polar angle it extends from 15.8° to 141.8° corresponding to a solid angle coverage of 90% in the CM frame. Radially the barrel is located outside the particle ID system and within the magnet cryostat; the barrel has an inner radius of 92 and an outer radius of 137.5 cm and it's located asymmetrically with respect to the interaction point, extending 112.7 cm in the backward direction and 180.1 cm in the forward direction. The barrel contains 5760 crystals arranged in 48 rings with 120 identical crystals each: the end-cap holds 820 crystals arranged in eight rings, adding up to a total of 6580 crystals. They are truncated-pyramid CsI(Tl) crystals: they are tapered along their length with trapezoidal cross-sections with typical transverse dimensions of 4.7×4.7 cm ^{2} at the front face, flaring out towards the back to about 6.1×6.0 cm ^{2}. All crystals in the backward half of the barrel have a length of 29.6 cm: towards the forward end of the barrel, crystal lengths increase up to 32.4 cm in order to limit the effects of shower leakage from increasingly higher energy particles. All end-cap crystals are of 32.4 cm length. The barrel and end-cap have total crystal volumes of 5.2 m^3 and 0.7 m^3, respectively. The CsI(Tl) scintillation light spectrum has a peak emission at 560 nm: two independent photodiodes view this scintillation light from each crystal. The readout package consists of two silicon PIN diodes, closely coupled to the crystal and to two low-noise, charge-sensitive preamplifiers, all enclosed in a metallic housing.

A typical electromagnetic shower spreads over many adjacent crystals, forming a *cluster* of energy deposit: pattern recognition algorithms have been developed to identify these clusters and to differentiate single clusters with one energy maximum from merged clusters (*bumps*) with more than one local energy maximum. Clusters are required to contain at least one seed crystal with an energy above 10 MeV: surrounding crystals are considered as part of the cluster if their energy exceeds a threshold of 1 MeV or if they are contiguous neighbors of a crystal with at least 3 MeV signal. The level of these thresholds depends on the current level of electronic noise and beam-generated background.

A bump is associated with a charged particle by projecting a track to the inner face of the calorimeter: the distance between the track impact point and the bump centroid is calculated and if it is consistent with the angle and momentum of the track, the bump is associated with this charged particle. Otherwise it is assumed to originate from a neutral particle.

On average, 15.8 clusters per hadronic event are detected: 10.2 are not associated to any charged particle. Currently, the beam-induced background contributes on average with 1.4 neutral clusters with energy above 20 MeV.

At low energy, the energy resolution of the *EMC* is measured directly with the radiative calibration source yielding $\sigma_E/E = 5.0 \pm 0.8\%$ at 6.13 MeV. At high energy, the resolution is derived from Bhabha scattering where the energy of the detected shower can be predicted from the polar angle of the electrons and positrons. The measured resolution is $\sigma_E/E = 1.9 \pm 0.1\%$ at 7.5 GeV.

The angular resolution measurement is based on the analysis of π^0 and η decays to two photons of approximately equal energy: the resolution varies between about 12 mrad at low energy and 3 mrad at high energies.

Left plot in Fig. 3.13 shows the two-photon invariant mass in $B\bar{B}$ events: the reconstructed π^0 mass is measured to be 135.1 MeV/c^2 and is stable to better than 1% over the full photon energy range. The width of 6.9 MeV/c^2 agrees well with the prediction obtained from detailed Monte Carlo simulation.

The *EMC* electron identification is based on the shower energy, lateral shower moments and track momentum to separate electrons from charged hadrons. In addition, the $\mathrm{d}E/\mathrm{d}x$ energy loss in the *DCH* and the *DIRC* Čerenkov angle are required to be consistent with an electron. The most important variable for hadron discrimination is the ratio of shower energy to track momentum (E/p). Right plot in Fig. 3.13 shows the efficiency for electron

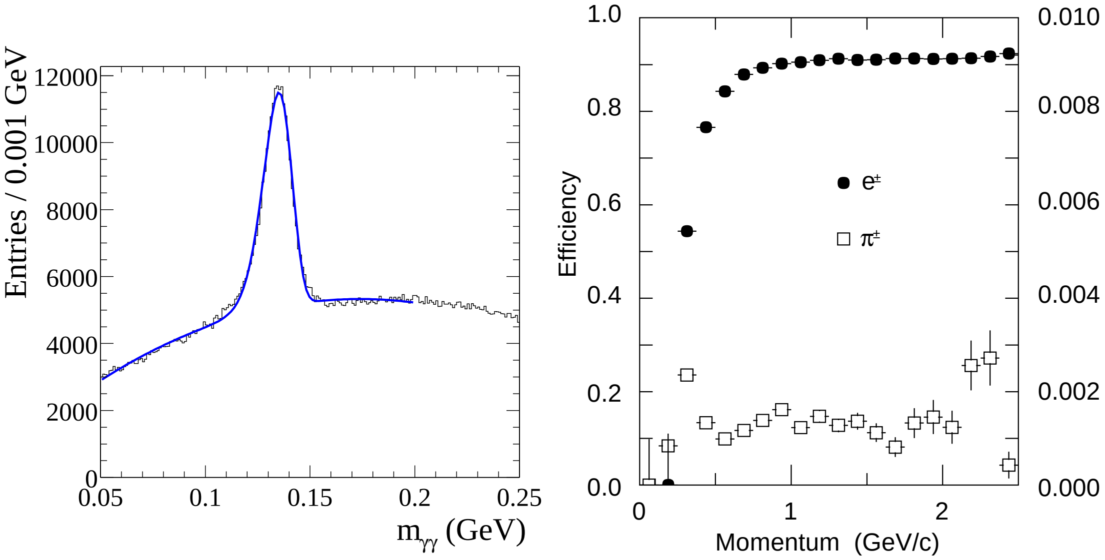

Figure 3.13: The invariant mass of two photons from π^0 decays (left) and efficiency for electron identification and pion mis-identification probability (right) in $B\overline{B}$ events. The solid curve on the left is a fit to the π^0 mass. In the right plot the energies of the photons and the π^0 s are required to exceed 30 MeV and 300 MeV respectively.

identification and the pion mis-identification probability as functions of momentum. The electron efficiency is measured using radiative Bhabha and $e^+e^- \rightarrow e^+e^-e^+e^-$ events, while the pion mis-identification uses selected charged pions from K^0_S decays and three-prong τ decays: a tight selector results in an efficiency plateau at 94.8% above 1 GeV/c and a pion mis-identification probability of the order of 0.2%.

3.6 The Instrumented Flux Return *IFR*

The Instrumented Flux Return (*IFR*) is designed to identify muons and neutral hadrons (primarily K^0_L and neutrons). Muons are important for tagging the flavor of neutral B mesons via semi-leptonic decays, for the reconstruction of vector mesons, like the J/ψ, and the study of semi-leptonic and rare decays involving leptons from B and D mesons and τ leptons. K^0_L detection allows for the study of exclusive B decays, in particular CP eigenstates; it could also help in vetoing charm decays and improve the reconstruction of neutrinos. The principal requirements for *IFR* are large solid angle coverage, good efficiency and high background rejection for muons down to momenta below 1 GeV/c. For neutral hadrons, high efficiency and good angular resolution are most important.

The *IFR* uses the steel flux return of the magnet as muon filter and hadron absorber. Single gap resistive plate chambers (RPC) with two-coordinate readout, operated in limited streamer mode constitute the active part of the detector [30]. RPCs detect streamers from ionizing particles via capacitive readout strips. They offer the advantage of simple and low cost construction. Further benefits are large signals and fast response allowing for simple and robust front end electronics and good time resolution, typically 1-2 ns. The position resolution depends on the segmentation of the readout; few millimeters are achievable. A cross section of an RPC is shown schematically in Figure 3.14. The planar RPCs consist of two bakelite sheets, 2 mm thick and separated by a gap of 2 mm. The bulk resistivity of the bakelite sheets has been especially tuned to $10^{11} - 10^{12} \Omega\,\mathrm{cm}$. The external surfaces are coated with graphite to achieve a surface resistivity of approximately 100 $k\Omega/\,\mathrm{cm}^2$. These two graphite surfaces are connected to high voltage (approximately 8 kV) and ground, and protected by an insulating mylar film. The bakelite surfaces facing the gap are treated with linseed oil to improve performance. The modules are operated in limited streamer mode and the signals are read out capacitively, on both sides of the gap, by external electrodes made of aluminum strips on a mylar substrate.

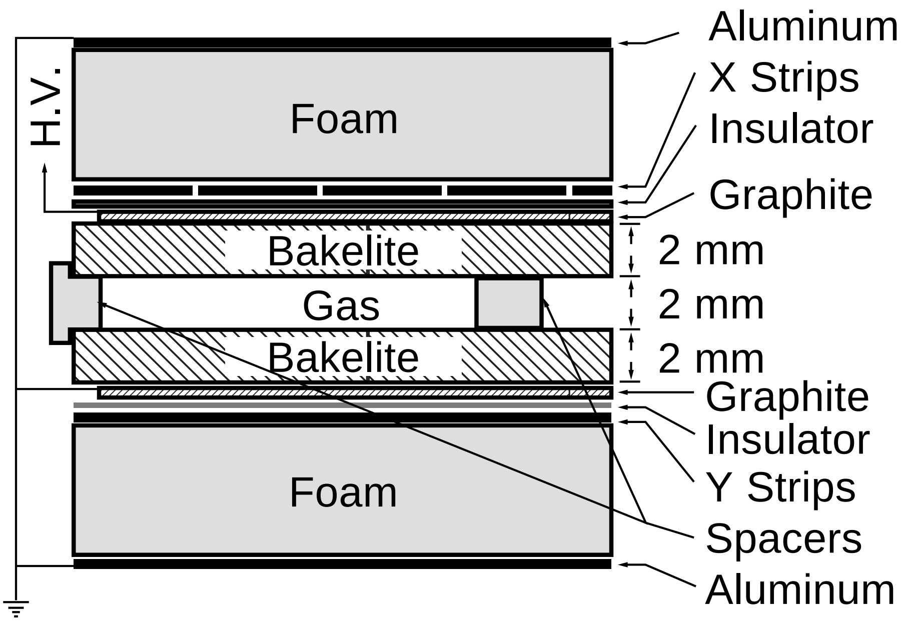

Figure 3.14: Cross section of a planar RPC with the schematics of the HV connection.

The RPC are installed in the gaps of the finely segmented steel of the six barrel sectors and the two end-doors of the flux return, as illustrated in Figure 3.15. The steel segmentation has been optimized on the basis of Monte Carlo studies of muon penetration and charged and neutral hadron interactions. The steel is segmented into 18 plates, increasing in thickness from 2 cm of the inner 9 plates to 10 cm of outermost plates for a total 65 cm. In addition, two layers of cylindrical RPCs are installed between the *EMC* and the magnet cryostat to detect particles exiting the *EMC*.

Soon after the installation (which took place in Summer 1999), the efficiency of a significant fraction of the chambers (initially greater then 90%) started to deteriorate at a rate of 0.5-1%/month. In order to solve some of the inefficiency problems an extensive improvement program was developed and made relevant advances. The RPCs in the forward end-cap region were replaced in Summer 2002 with new ones based on the same

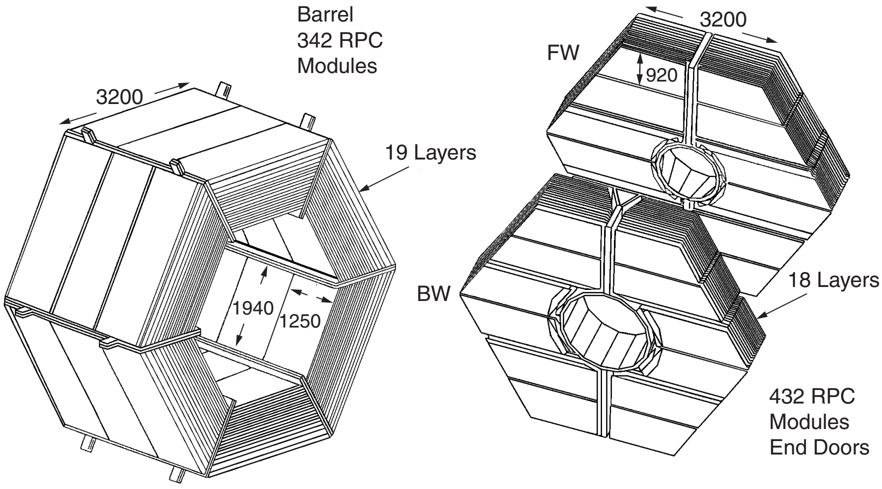

Figure 3.15: Overview of the *IFR* Barrel sectors and forward and backward end-doors; the shape of the RPC modules and the way they are stratified is shown.

base concept but with improved fabrication technique and quality controls. The RPCs in the barrel region were replace with limited streamer tube (LST) detectors.

A “standard” LST configuration [31] consists of a silver plated wire 100 μm in diameter, located at the center of a cell of 9x9 μm^2 section. A plastic (PVC) extruded structure, or profile, contains 8 such cells, open on one side (see Figure 3.16). The profile is coated with a resistive layer of graphite, having a typical surface resistivity between 0.1 and 1 MΩ/square. The profiles, coated with graphite and strung with wires, are inserted in plastic tubes (“sleeves”) of matching dimensions for gas containment. The signals for the measurement of one coordinate can be read directly either from the wires or from external strip planes attached on both side of the sleeve.

More than one year of R&D studies have been done before choosing the final LST design. R&D program has been concentrated on several critical issues like: selection of safe gas mixture, rate capability, wire surface quality and uniformity, aging test and performance of the prototypes. Final results led us to a 15x17 μm^2 cell design (which is more reliable and efficient) where each tube is composed by 7 or 8 cells and assembled in modules. We use wire readout for the azimuthal coordinate, ϕ, and strips plans for the z coordinate (along the beam direction). In order to obtain high performances and to respect the safety requirements it has been chosen a ternary gas mixture of $Ar/C_4H_{10}/CO_2$ (3/8/89)%.

Two of the six sextants of the barrel have been replaced in Summer 2004 (affecting data of Run5 and later) while the remaining four sextants have been replaced in Summer 2006 (affecting data of Run6 and later). Extensive quality control studies have been performed before the installation to check the reliability of these detectors, which are expected to operate until the end of the experiment with $\approx 90\%$ efficiency, as measured in cosmic ray runs.

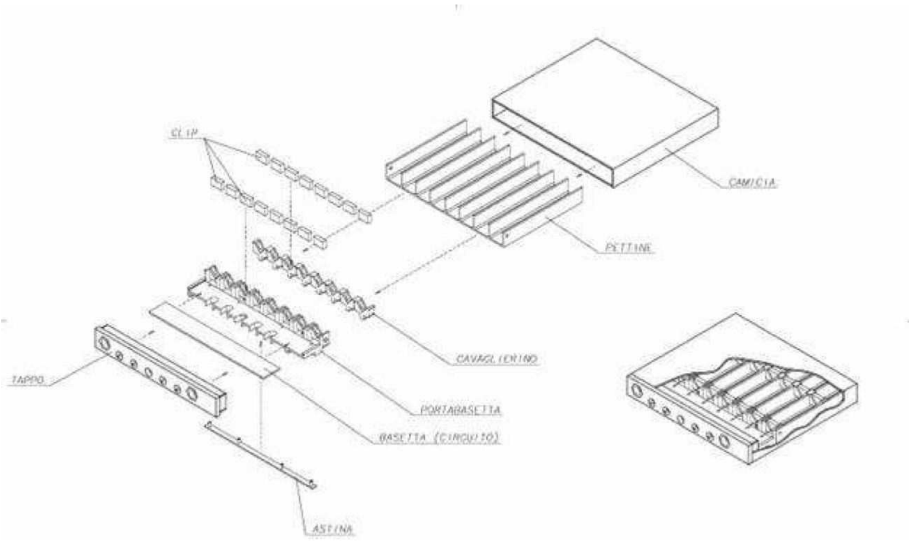

Figure 3.16: Schematic of the “standard” Limited Streamer Tube configuration.

3.6.1 Detector performance

The efficiency of the RPCs and LSTs is evaluated from samples of high momentum muons collected both in normal collision data (from the process $e^+e^- \to \mu^+\mu^-$) and monthly dedicated cosmic ray runs. The efficiency is found by counting the number of times a hit found in a certain chamber when a charged track is expected, based on information from the other chambers and from the tracking system, to traverse it. The absolute efficiency at the nominal working voltage (typically 7.6 kV for RPC, 5.5 kV for LST) is stored in the *BABAR*condition database for use in the event reconstruction software.

Following the installation and commissioning of the *IFR* system all the RPC modules were tested with cosmic rays and their average efficiency was measured to be approximately 92%.

As previously said, soon after installation, a progressive, steady efficiency deterioration has been observed in a significant fraction of the chambers. Detailed efficiency studies revealed large regions of very low efficiencies in the modules, but no clear pattern was identified. The overall effects are shown into Figure 3.17. Tests to understand the efficiency decrease excluded several possible causes as the primary source of the problem, such as a change in the bakelite bulk resistivity, gas flow or composition. On the other hand, it was found that a number of prototype RPCs developed similar efficiency problems after being operated above a temperature 36°C[2] for a period of two weeks: in some of these modules evidence was found that the linseed oil had accumulated at various spots under the influence of the electric field.

The LST performance has proved itself quite constant with time. The tubes performances have proved insensitive to most of the external conditions. The system efficiency

---

[2] Similar temperatures had been reached inside the iron during the first summer of operations due to the temperature in the experimental hall and the absence of a water cooling system

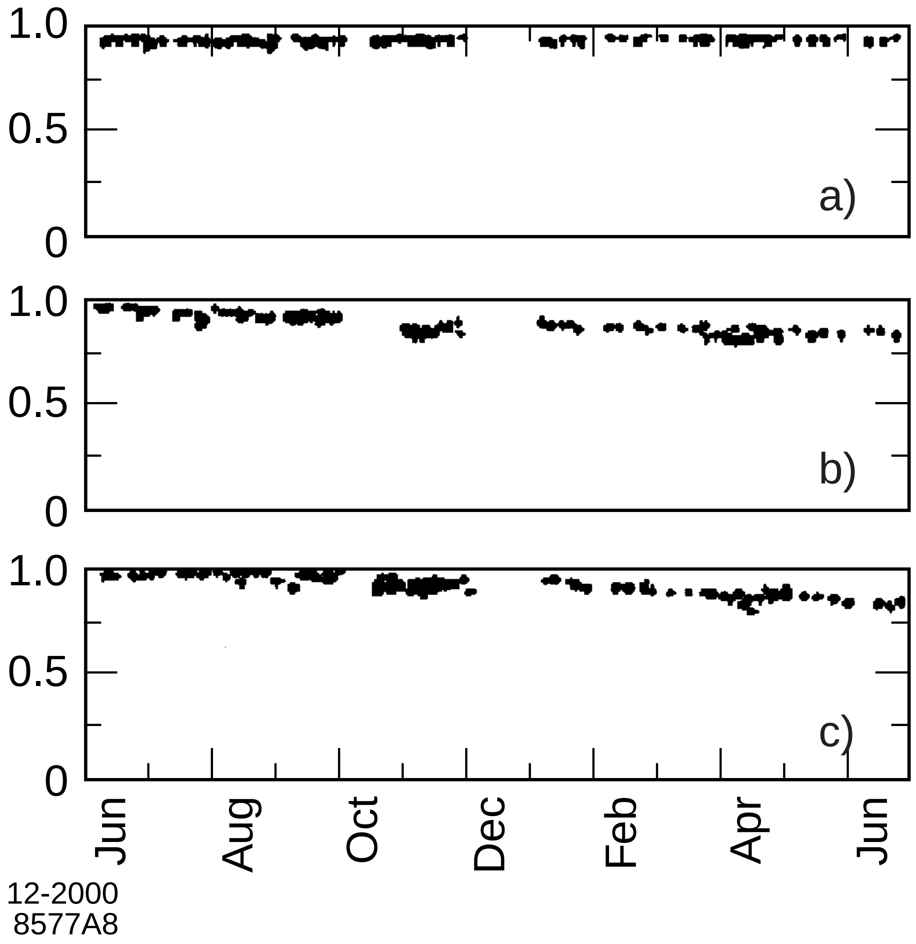

Figure 3.17: Efficiency history for 12 months starting in June 1999 for RPC modules showing different performance. Top: highly efficient and stable. Middle: slow continuous decrease in efficiency. Bottom: faster decrease in efficiency.

has been constant over time, but for small periods of time in which depletions in efficiency have been observed. These were mainly due to impurities in the gas mixture that affected the streamer features inside the detector. Figure 3.18 shows the efficiency in a four months period.

3.7 The trigger

The PEP-II high luminosity is also due to the $1.2\,m$ bunch spacing: the bunch time spacing is $4.2\,ns$ corresponding to a cross frequency of $238\,MHz$. At design luminosity, beam-induced background rates are typically about $20\,kHz$ each for one or more tracks in the drift chamber with $p_t > 120$ MeV/c or at least one *EMC* cluster with $E > 100$ MeV. This rate is to be contrasted with the desired logging rate of less than $120\,Hz$. The trigger and data acquisition subsystems are designed to record data at no more than the latter

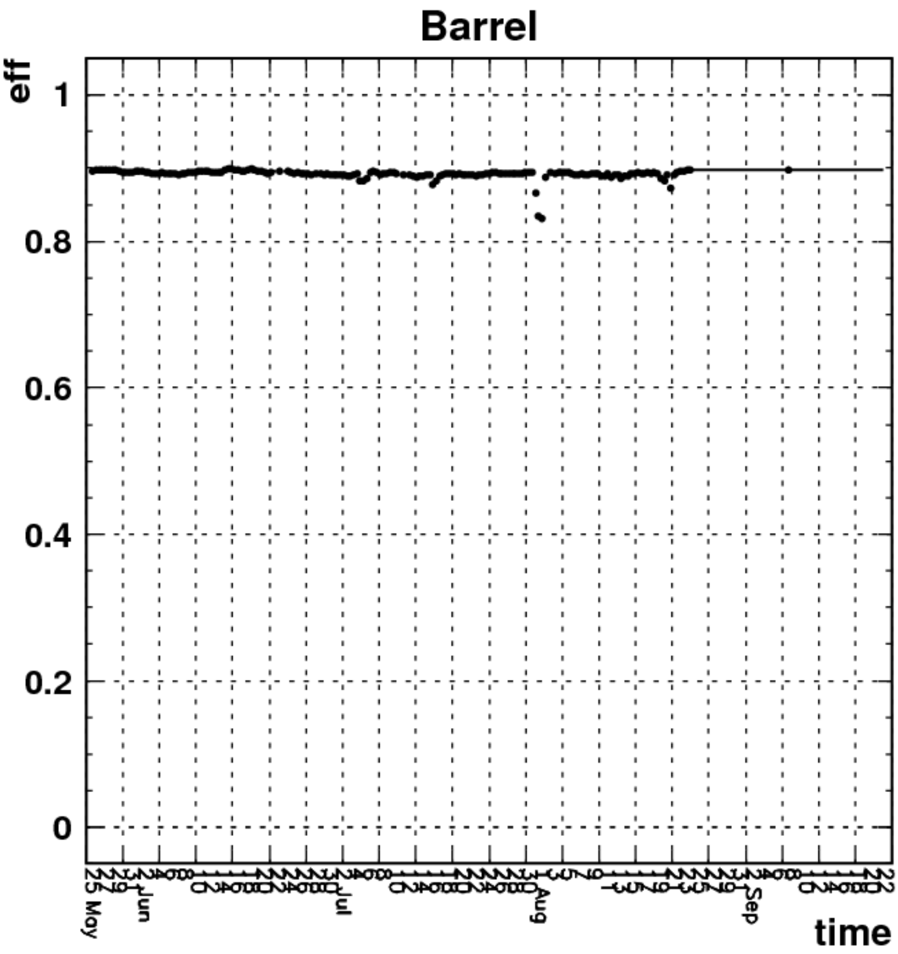

Figure 3.18: Efficiency history for 4 months starting in May 2007 for LST modules. The dip at the beginning of August was due to a flawed valve in the gas mixing system.

rate: the purpose of the trigger is to reject backgrounds while selecting a wide variety of physics processes. The total trigger efficiency is required to exceed 99% for all $B\overline{B}$ events and at least 95% for continuum events. The trigger should also contribute no more than 1% to dead time.

The *BABAR*trigger has two levels: Level 1 which executes in hardware and Level 3 which executes in software after the event assembly. The Level 1 trigger system is designed to achieve very high efficiency and good understanding of the efficiency. During normal operation, the L1 trigger is configured to have an output rate of typically $1\,kHz$, while the L3 filter acceptance for physics is $\sim 90\,Hz$.

Event signatures are used to separate signal from background. Combinations of the following global event properties are used in the L1 trigger as general event selection criteria: charged track multiplicity, calorimeter cluster multiplicity and event topology. These selection criteria have associated thresholds for the following parameters: charged-track transverse momentum (p_t), energy of the calorimeter clusters (E_{clus}), solid angle separation (ϕ) and track-cluster match quality. The trigger definition can contain selection criteria that differ only by the values of thresholds. A small fraction of random beam crossings and events that failed to trigger are also selected for diagnostic purposes.

For a given trigger level, the global selection is a logical OR of a number of specific trigger selection lines, where each line is the result of a boolean operation on any combination of *trigger objects*: Table 3.4 shows some examples of trigger objects.

It is important to notice that the trigger configuration doesn't influence our analysis because it doesn't rely on any cut on the vertex impact parameter. This is not true at hadronic machines.

	object description	threshold
B	Short track reaching *DCH* super-layer 5	120 MeV/c
A	Long track reaching *DCH* super-layer 10	180 MeV/c
A'	High p_t track	800 MeV/c
M	All-θ MIP energy	100 MeV/c
G	All-θ intermediate energy	250 MeV/c
E	All-θ high energy	700 MeV/c

Table 3.4: Trigger objects for the Level 1 trigger.

Level 1 Trigger	$\epsilon_{B\bar{B}}(\%)$	$\epsilon_{c\bar{c}}(\%)$	$\epsilon_{uds}(\%)$	$\epsilon_{ee}(\%)$	Rate (Hz)
$A \geq 3\&B^* \geq 1$	97.1	88.9	81.1	–	180
$A \geq 1\&B^* \geq 1\&A' \geq 1$	95.0	89.2	85.2	98.6	410
$M \geq 3\&M^* \geq 1$	99.7	98.5	94.7	–	160
$E - M \geq 1$	71.4	77.1	79.5	97.8	150
$B \geq 3\&A \geq 2\&M \geq 2$	99.4	94.8	87.8	–	170
$M^* \geq 1\&A \geq 1\&A' \geq 1$	95.1	90.1	87.0	97.8	250
$E \geq 1\&B \geq 2\&A \geq 1$	72.1	77.7	79.2	99.3	140
Combined Level 1 Triggers	> 99.9	99.9	98.2	> 99.9	970

Table 3.5: Trigger efficiencies and rates at a luminosity of 2.2 $10^{33}\,\mathrm{cm}^{-2}\mathrm{s}^{-1}$ for selected triggers applied to various physics samples. Symbols refer to the counts for each object in Table 3.4.

Table 3.7 shows some trigger lines together with their L1 trigger rates and their efficiencies for various physics processes: the star (*) symbol next to a trigger object indicates that a minimum angular separation was required in order to count more than one object (typically 90°). Back-to-back topologies among clusters are written like $E - M$ meaning an E cluster back to back to an M cluster, while the & symbol denotes requiring clusters and tracks in coincidence, a non-orthogonal selection criterion.

Level 3 trigger is part of the online farm and consists of a network of commercial processors: input are the L1 trigger data and the full event data for events that passed the L1 trigger. Output to mass storage is the full event and trigger data of events accepted by L3. L3 trigger algorithms have all event information available and they operate by refining and improving the selection methods used by L1: better *DCH* tracking (vertex resolution) and *EMC* clustering filters allow for greater rejection of beam backgrounds and Bhabha events. A cut on the vertex position can be made to reject events that did not originate at the interaction point. L3 trigger also includes a variety of filters to perform event classification and background reduction: the logging decision is based on two orthogonal filters, one relying exclusively on *DCH* data and the other relying only on *EMC* data.

The drift chamber filters select events with one *tight* ($p_t > 600$ MeV/c) track or two *loose* ($p_t > 250$ MeV/c) tracks originating from the IP: track selection is based on the $x - y$ closest approach distance (d_0) to the IP and the corresponding z coordinate for that closest approach point (z_0). The IP is a fixed location close to the average beam position over many months. Tight (loose) tracks have to satisfy a vertex condition defined as $|d_0| < 1.0\,cm$ ($|d_0| < 1.5\,cm$) and $|z_0 - z_{IP}| < 7.0\,cm$ ($|z_0 - z_{IP}| < 10.0\,cm$).

The calorimeter filters select events with either high energy deposits ($E_{CM} > 350$ MeV) or high cluster multiplicity (at least 4 clusters): they also require a high effective mass (> 1.5 GeV/c^2) calculated from the cluster energy sums and the energy weighted centroid positions of all clusters in the event assuming mass-less particles. A Bhabha veto filter is also used: it selects one-prong (only a positron in the back part of the detector) and two-prong events (with both e^+ and e^- detected) and it applies stringent criteria on *EMC* energy deposits relying on the track momenta and E/p values.

During a typical run on the $\Upsilon(4S)$ peak with an average luminosity of 2.6 10^{33} cm^{-2}s^{-1}, the physics events represent the 13% of the total L3 output (with a rate of 16 Hz), while the calibration and diagnostic samples comprise 40% (with a rate 49 Hz): the total output rate is 122 Hz. The remaining fraction of events comprises two-photon events, Bhabha backgrounds and beam-induced backgrounds.

Chapter 4

Event selection

In this chapter, we describe the main event selection criteria we consider in order to isolate our signal in the *BABAR* dataset. The sample we use consists of both *on-peak* and *off-peak* events, for a total luminosity of 384 fb^{-1}.

To allow for background studies and cut optimization, we also consider Monte Carlo (MC) events in which the full detector reconstruction has been simulated. The MC sample consists of $\sim$ 400 fb^{-1} events, reproducing the following production mechanisms: $e^+e^- \rightarrow [c\bar{c}, B^0\overline{B}^0, B^+B^-, uds$ and $\tau^+\tau^-$].

The optimization of the selection criteria is done, unless otherwise reported, maximizing in the MC sample the statistical significance, defined as:

$$\text{statistical significance } = \frac{S}{\sqrt{S+B}} \tag{4.1}$$

where S is the number of signal events and B is the number of background events in the MC sample.

4.1 Selection criteria

4.1.1 The π^0 selection

π^0 s are reconstructed in the decay $\pi^0 \rightarrow \gamma\gamma$. Photons are taken from a list of candidates which present a cluster in the electromagnetic calorimeter not associated with a reconstructed track. Since the acceptance of the tracking system is slightly smaller than the acceptance of the *EMC*, a cut on the azimuthal angle rejects as a neutral particle a bump in the calorimeter outside the *BABAR* tracking system. In order to consider only candidates with a good energy information, we select photons which have $E_\gamma > 100$ MeV. This cut also reduces the combinatoric background.

Besides photons, there are other neutral particles that can leave a signal into the calorimeter. These are mainly K_L^0 s. These particles can produce an hadronic shower in the detector. Photons typically interact while crossing the CsI(Tl) crystals of *EMC*, through the formation of electromagnetic showers. These showers have a transverse spatial distributions which are at 99% contained in $3R_{Moli\grave{e}re}$, where $R_{Moli\grave{e}re}$ is the Molière radius, whose value is 3.8 cm for the *BABAR* calorimeter. A K_L^0 typically interacts in the *EMC* through a hadronic shower, which is at 99% transversally contained inside an absorption length ($\sim$ 34 cm for the *EMC*). For this reason it is natural, for a reliable K_L^0/γ discrimination, to parameterize the calorimeter cluster shapes using a variable sensitive to the different particle interactions inside the detector. We define the Lateral moment (LAT) to be:

$$\frac{\sum_{i=2,n} E_i \cdot r_i^2}{(\sum_{i=2,n} E_i \cdot r_i^2) + 25(E_0 + E_1)} \tag{4.2}$$

with the i-th crystal in descending energy order. LAT is very sensitive to cluster shapes. In the case of a signal due to a photon shower LAT is expected to be small, since the two most energetic crystals are not considered in the numerator. By the other hand, a hadronic shower is characterized by a more spread energy distribution; in this case, numerator and denominator are not supposed to be very different. We only select photons which have $0.01 < LAT < 0.8$. In Figure 4.1, the typical distribution of the LAT for a photon is shown. As can be noted, a discrepancy between data and MC is present. We correct our MC sample for this efficiency discrepancy, as explained in Section 6.1.

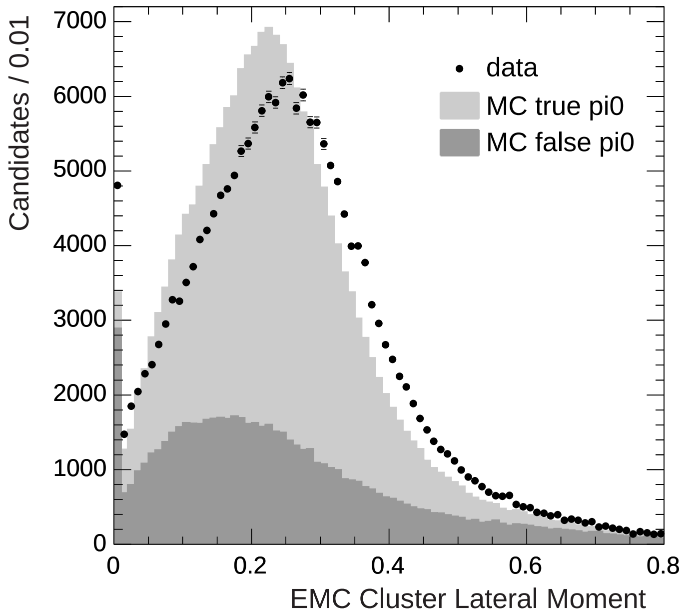

Figure 4.1: LAT distribution for photons in the RS sample. Data (dots) and MC (solid histograms) are shown. The MC sample is divided for photons coming from a true π^0 and those coming from a fake π^0.

Once the two photons are selected, we perform a fit to the π^0 candidate constraining the total invariant mass to the PDG value of 134.9766 MeV/c^2 [37]. The probability of the fit χ^2 is required to be higher than 1%. The momentum of the fitted π^0 is required to be higher than 350 MeV/c. In Figure 4.2 we show the distribution of the unconstrained π^0 mass for both data and MC. As can be observed, a discrepancy arises. This does not influence our result, as we constraint the π^0 mass to the PDG value. One could argue that constraining the mass to a fixed value might move this discrepancy to the π^0 momentum distribution. In Figure 4.3 the π^0 momentum shows a good agreement between data and MC for the selected region.

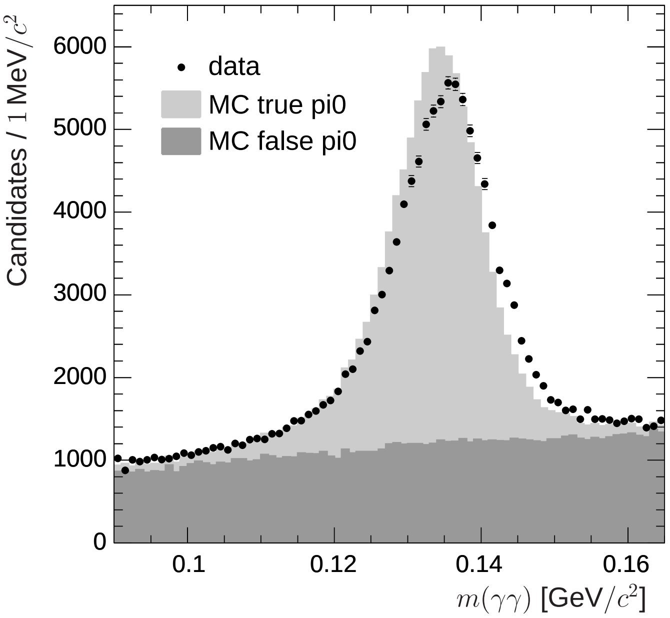

Figure 4.2: Mass distribution for the π^0 s of the RS sample before the mass constrained fit. Dots show the data, while the solid histograms show the MC.

4.1.2 Pions and kaons selection

Both the $\pi^\pm$ and the $K^\pm$ candidates are taken from lists of particles produced at the Event Processing stage. These lists provide a Particle Identification (PID) for the different candidates given by a selector. For each track, the selector calculates likelihoods $\mathcal{L}$ for several particle hypotheses. The particle types checked are π, K, e, p and μ. The likelihood calculations use information from the *SVT* and *DCH*, such as dE/dx and number of hits; information from the *EMC* such as E/p; information from the *DIRC*, such as the Čerenkov angle and the number of photons. The selector combines the likelihoods into ratios, and makes cuts to select tracks with a given efficiency and fake rate. The most powerful information in the $K-\pi$ discrimination is the Čerenkov angle.

In Figure 4.4, the efficiency of pion reconstruction for this selector is shown. As kaons are the main source of background for this selector, in Figure 4.5 we report the kaon fake

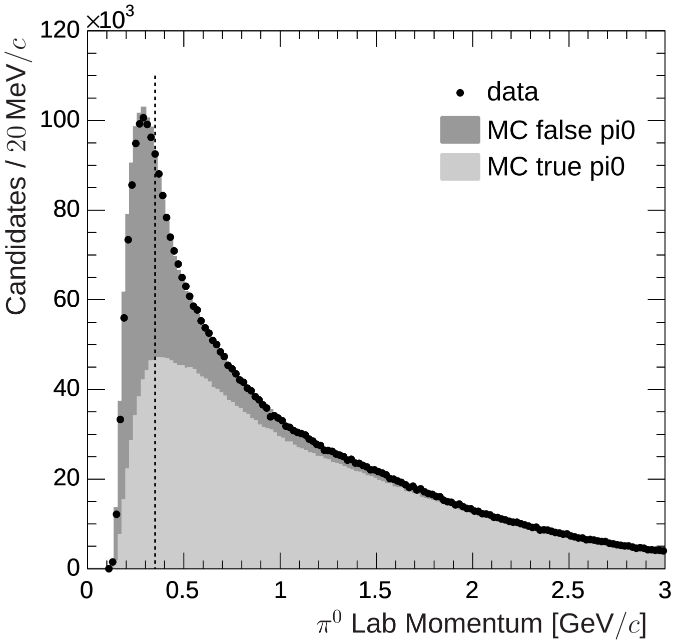

Figure 4.3: Momentum distribution for the π^0 s of the RS sample after the mass constrained fit. Dots show the data, while the solid histograms show the MC.

rate. In order to understand our efficiency and fake rate, we present in Figure 4.6 the typical momentum distribution of pions from RS data. It is important to note that most of the reconstructed pions have a momentum in the region where efficiency is the highest and fake rate is the lowest.

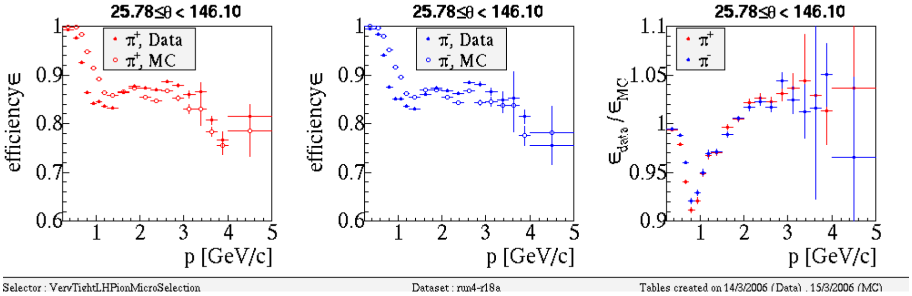

Figure 4.4: Efficiency for selecting $\pi^{\pm}$s in MC and data. The histograms show the efficiency as a function of momentum for the entire detector acceptance range. The left shows the efficiency for selecting π^+ s, the center shows the efficiency for selecting π^- s, and the right shows the ratio of efficiency in data to that in MC.

In Figure 4.7, the efficiency of kaon reconstruction for this selector is shown. As pions are the main source of background for this selector, in Figure 4.8 we report the pion fake rate. Again, in Figure 4.9 we show the typical momentum distribution of the reconstructed kaons from RS data. Kaons too have typical momenta that lie in the region where efficiency is the highest and fake rate is the lowest.

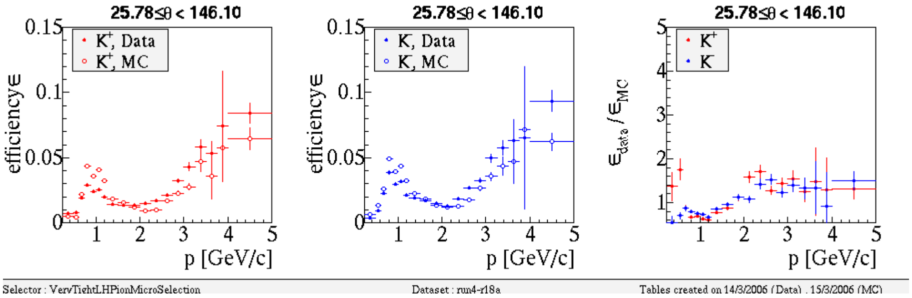

Figure 4.5: Efficiencies for selecting $K^{\pm}$ using the pion selection in MC and data. The histograms show the efficiency as a function of momentum for the entire detector acceptance range. The left shows the efficiency for selecting K^{+} s, the center shows the efficiency for selecting K^{-} s, and the right shows the ratio of efficiency in data to that in MC.

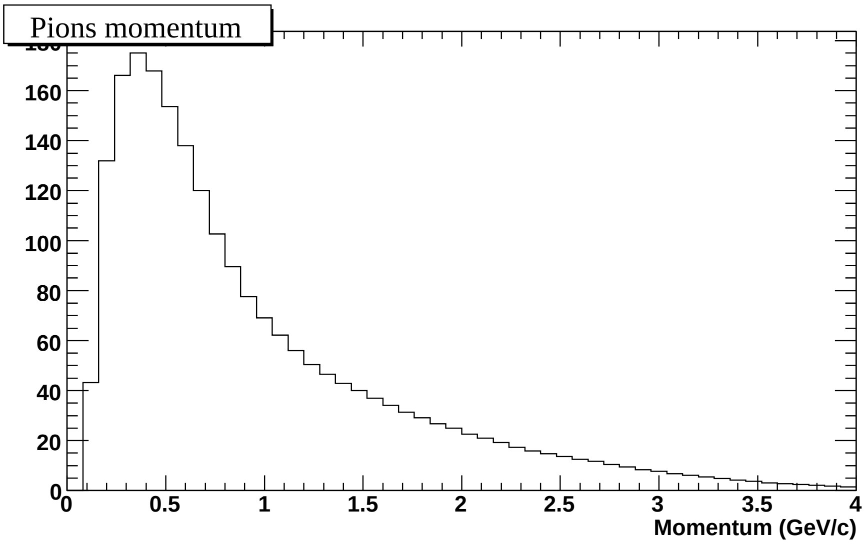

Figure 4.6: Distribution of pion momentum for the RS data.

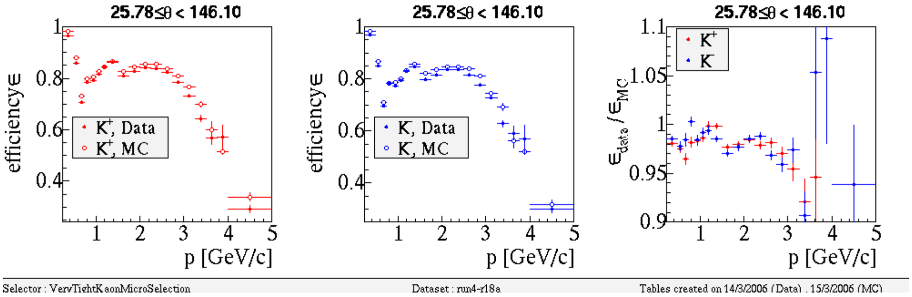

Figure 4.7: Efficiency for selecting $K^{\pm}$s in MC and data. The histograms show the efficiency as a function of momentum for the entire detector acceptance range. The left shows the efficiency for selecting K^{+} s, the center shows the efficiency for selecting K^{-} s, and the right shows the ratio of efficiency in data to that in MC.

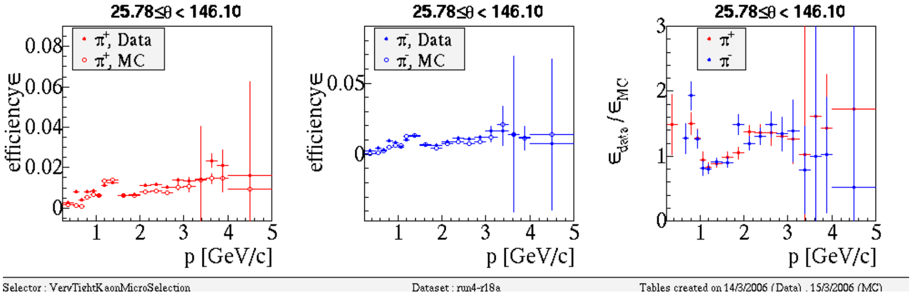

Figure 4.8: Efficiencies for selecting $\pi^{\pm}$ using the kaon selection in MC and data. The histograms show the efficiency as a function of momentum for the entire detector acceptance range. The left shows the efficiency for selecting π^+ s, the center shows the efficiency for selecting π^- s, and the right shows the ratio of efficiency in data to that in MC.

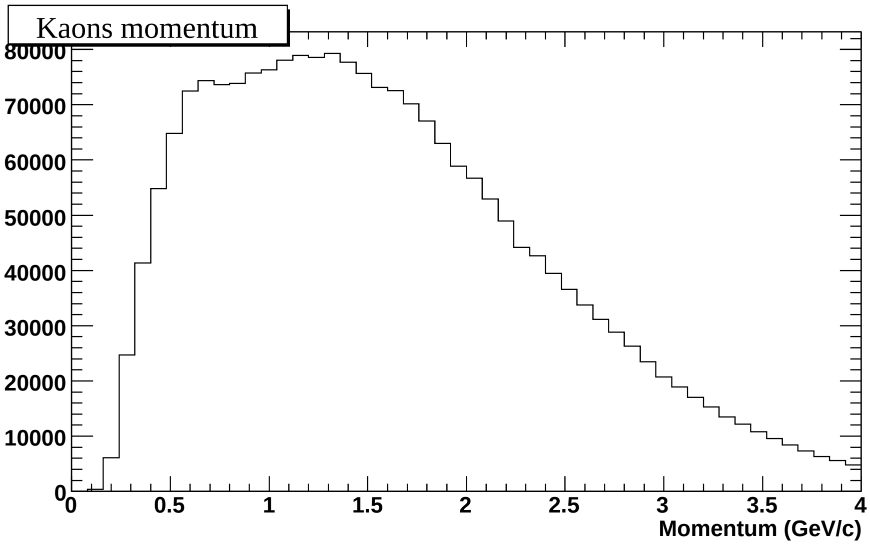

Figure 4.9: Distribution of kaon momentum for the RS data.

4.1.3 Slow pion reconstruction

As the pion from the D^* decay is characterized by a very slow momentum, some additional care is needed for its reconstruction. Firstly, the PID criteria described in Section 4.1.2 cannot be applied here: most of the $\pi_s^\pm$ s do not reach the *DIRC* detector. As all the charged particle selectors use the *DIRC* information in their likelihood, this makes them not effective for low momentum pions.

The $\pi_s^\pm$ reconstruction can suffer a large background contribution due to slow electrons misidentified as slow pions. This background can be removed without compromising the signal efficiency. A first selection looks for gamma conversions and Dalitz π^0 decays in the event. Two charged tracks are combined to form a photon, constraining the mass of the photon candidate to be lower than 150 MeV/c^2. To fit this decay chain, a particular fitting algorithm for γ conversions is used. These photon candidates are also combined with other photons to create a π^0 candidate. The overlap of the electrons used for these photon lists is used to veto $\pi_s^\pm$ candidates.

Another selection criterion that can dramatically reduce the contamination of slow electrons and muons is a cut on the dE/dx information for the $\pi_s^\pm$ candidate. Using the dE/dx information calculated in the Event Processing a pull is built for the distribution of the measured dE/dx with respect to the theoretical estimation. Both the *SVT* and *DCH* information is used to construct the pull. We request the absolute value of the pull to be lower than 2.58, which brings to a signal efficiency of $\sim 98\%$. Most of the electrons and muons are removed with this selection.

For completeness, in Figure 4.10 we report the distribution of $\pi_s^\pm$ momentum from RS data.

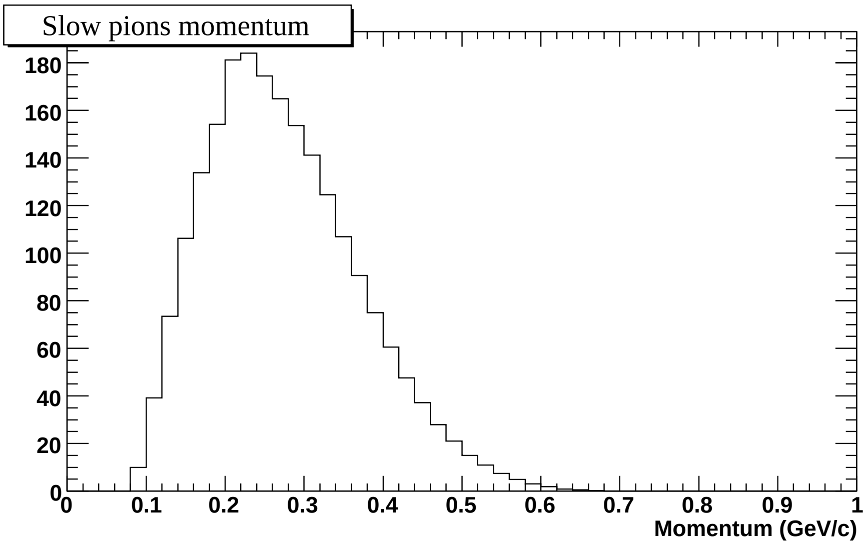

Figure 4.10: Distribution of $\pi_s^\pm$ momentum for the RS data.

4.1.4 Final selection

Once all the particles have been selected, we construct the decay chain $D^* \to D^0\ \pi_s^\pm$, $D^0 \to K^\pm\ \pi^\mp\ \pi^0$. The entire decay tree is refitted, with the following constraints:

- A constraint on the π^0 mass to be the nominal value from the PDG;
- A constraint to the D^0 mass to be the value of the PDG, i.e. 1864.84 MeV/c^2. This constraint ensures that the Dalitz plot of the D^0 will have sharp, well defined limits, avoiding the smearing effect on the kinematical borders due to detector resolution. The D^0 mass prior to the constrained fit is saved to be used later for signal and background characterization;
- The D^0 mass prior to the fit must satisfy: $1.74 < m_{K\pi\pi^0} < 1.98$ GeV/c^2;
- For the entire decay chain, the probability of the fit χ^2 must be higher than 1%;
- $p^*_{D^0} > 2.4$ GeV/c, where $p^*_{D^0}$ is the D^0 momentum in the center of mass frame. This cut ensures that no D^0 candidates from B decays are retained. Charmed neutral mesons coming from B decays will have a momentum lower than the momentum of D^0 s coming from the continuum and therefore a worse vertex resolution requiring a dedicated effort to analyze them;
- From the full decay chain fit: $0.139 < \Delta m < 0.155$ GeV/c^2, where $\Delta m = m^*_D - m_{D^0}$;
- $\sigma_t < 0.5$ (ps) where σ_t is the the D^0 lifetime error. This requirement discards all the events with poorly reconstructed D^0 vertexes. Further details on this cut are provided in Section 8.1.

4.1.5 Best candidate selection

Based on the selection described above, we expect to have a multiplicity of ~ 1.2 D^* candidates per event. In most cases, simple criteria to select the best candidate of the event can allow to retain the composite which is more likely to be a signal event. The algorithm we use for the best candidate determination is proceeds with the following steps:

1. If two π^0 candidates share a γ, the π^0 in the decay with the higher $p(\chi^2)$ value is selected. Approximately 5% of events exhibit this;
2. If two D^0 candidates share a π^0, the D^0 in the decay with the higher $p(\chi^2)$ value is selected. Approximately 2% of events exhibit this;
3. Consider two D^{*+} candidates reconstructed as follows:

$$D^{*+} \to D^0\pi_1^+, \quad D^0 \to K^-\pi_2^+\pi^0$$
$$D^{*+} \to D^0\pi_2^+, \quad D^0 \to K^-\pi_1^+\pi^0$$

It is found that the ambiguity can be resolved correctly in 90% of these cases by choosing the candidate that has mass values $m_{K\pi\pi^0}$ and Δm closer to the expected signal values. This ambiguity occurs in cases where the D^0 decays through the channel $D^0 \to K^-\rho^+$. If the ρ^+ is emitted in the direction of the D^0 momentum, its consequent longitudinal decay will often produce a π^+ that is traveling with almost the same momentum magnitude and direction as the π^+ from the D^{*+} decay. Approximately 6% of events exhibit this;

4. If two D^{*+} candidates share either a D^0 or a π_s^+ candidate, the D^{*+} with the higher $p(\chi^2)$ value is selected. Approximately 0.6% of events exhibit this;

5. If two D^0 candidates share one track and one π^0, the D^0 with the higher $p(\chi^2)$ value is selected. Fewer than 0.1% of events exhibit this;

6. If two D^0 candidates share both tracks, the D^0 with the higher $p(\chi^2)$ value is selected. Fewer than 0.05% of events exhibit this;

7. If a D^0 can be associated with either a π^+ ($D^0 \to K^-\pi^+\pi^0$) or π^- ($D^0 \to K^+\pi^-\pi^0$), the $D^0 \to K^-\pi^+\pi^0$ combination is selected, as its prior probability is two orders of magnitude higher. Approximately 7% of $D^0 \to K^+\pi^-\pi^0$ events exhibit this. This selection eliminates 10% of the WS mistag background, while it has a very large signal efficiency (∼99.5%). Since the WS mistag background has the RS Dalitz-plot structure, the presence of which reduces the precision with which the WS Dalitz structure can be determined, this selection is well motivated.

Approximately 0.15% of events have two reconstructed D^{*+} candidates with no shared tracks or clusters. In these cases, both of the candidates are kept. This fraction agrees generally with expectations, based on charm fragmentation and the branching fractions involved.

4.2 Background composition

Using the selection criteria described in the previous sections, we apply them on the MC sample.

We consider the reconstructed WS sample in the signal region of the $m_{K\pi\pi^0}$ and Δm distributions, defined as

$$\begin{aligned} 1.8495 < m_{K\pi\pi^0} < 1.8795\,\mathrm{GeV}/c^2 \\ 0.1449 < \Delta m < 0.1459\,\mathrm{GeV}/c^2 \end{aligned} \tag{4.3}$$

We identify different sources of background that will need particular care. Since we will use the $m_{K\pi\pi^0}$ and Δm shapes to discriminate the remaining background from the signal, it is important to know what the behavior of the background sources in those two variables is. The background sources we isolated are:

- *Mistag*: events where an uncorrelated $\pi_s^\pm$ candidate has been chosen. Since the D^0 has been correctly reconstructed, this background presents a peak in the D^0 mass distribution similar to signal. In the Δm distribution we expect it not to show any significant peak (see Figure 4.11). For the RS sample, this background consists of RS events with an uncorrelated $\pi_s^\pm$. For the WS sample, this background is composed of RS events with an uncorrelated $\pi_s^\pm$ having an opposite charge. This statement is based on the observation that in the mistag sample, the D^0 has been correctly reconstructed, and its probability of belonging to a RS decay is much larger that that of belonging to a WS decay;

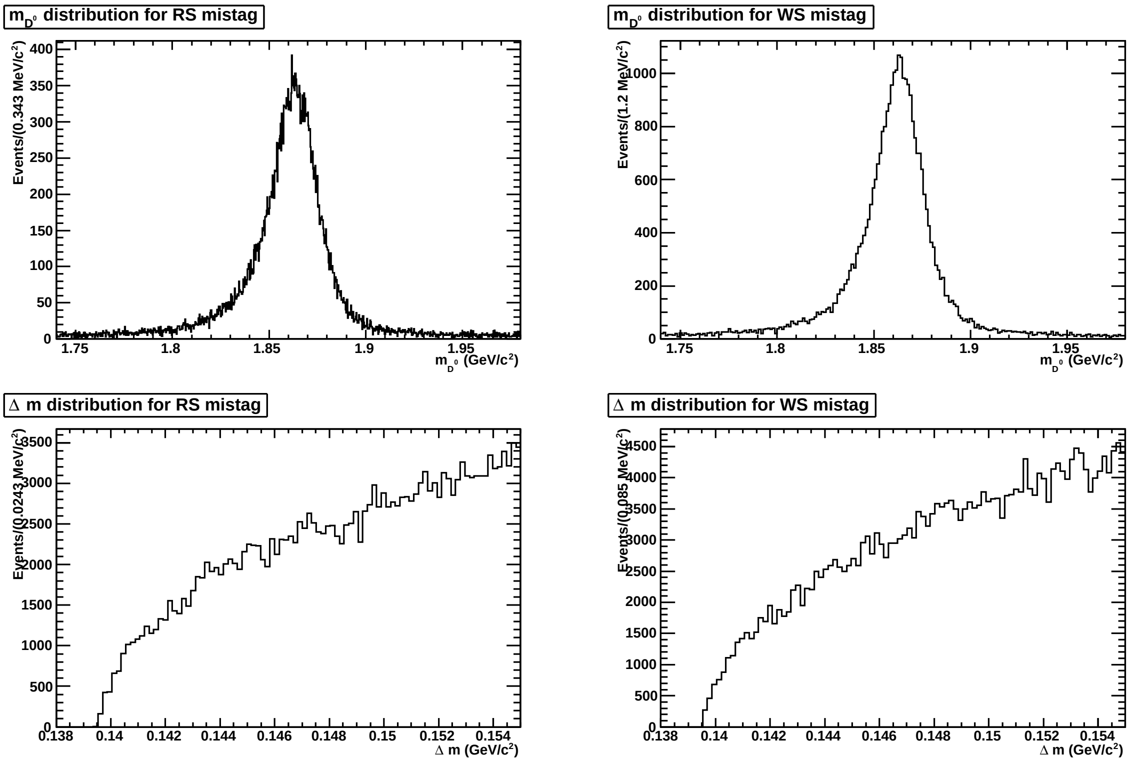

Figure 4.11: Distribution of the MC events corresponding to the mistag background.

- D^+ *candidates*: events where the $K^\pm$ and the $\pi^\mp$ belong to a D^+ decay. These events are expected not to show any significant peak in both of the variables;
- *Swapped K-π (bad-D^0)*: events where the kaon has been misidentified as a pion, and the pion as a kaon. Since the masses of the $K^\pm$ and of the $\pi^\mp$ have been wrongly assigned, the D^0 mass distribution is expected to have no particular peak. The Δm distribution, instead, may present a peak due to the fact that the mis-ID contributes at a higher order in the Δm calculation (see Figure 4.12);
- *Signal bad-D^0* : events where a signal D^0 was present, but was not correctly reconstructed. These events are supposed not to show any significant peak in both the discriminating variables;

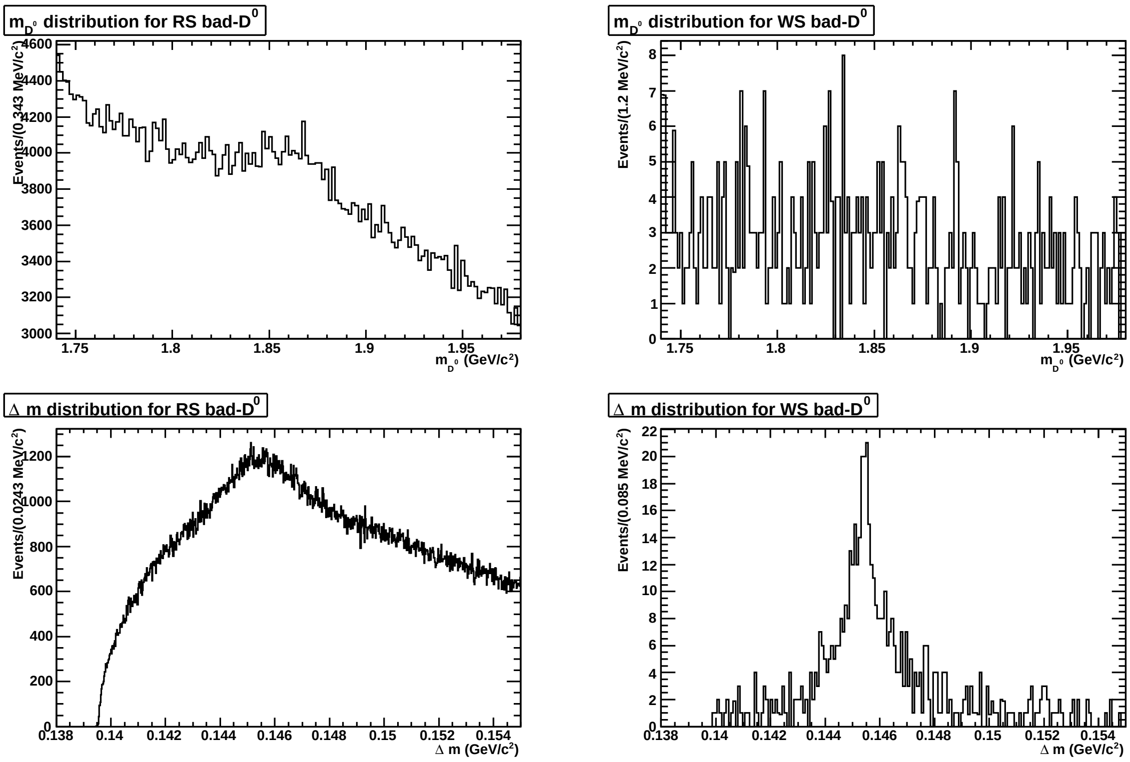

Figure 4.12: Distribution of the MC events corresponding to the *bad-*D^0 background.

- *Background bad-*D^0 : events where a D^0 was present, but decayed through a different channel. Again, no significant peak is expected:
- *Fake* π *- Fake K*: events where the kaon or the pion have been wrongly identified. No significant peak is expected here too.

The contribution of the different categories to the total background are shown in Table 4.1. They have been isolated using the MC information. We also select the signal region of $m_{K\pi\pi^0}$,Δm distribution defined in Equation 5.8. It must be noted that some events are present in more than one category, so the sum of the fractions doesn't return 100%. The category "Other" covers all the background that does not apply for the categories described above. They are mainly combinatorial background. They are expected to produce no peaking distribution in $m_{K\pi\pi^0}$ and Δm (see Figure 5.3). We notice that the main contributions come from the mistag and the combinatorial events.

The total number of $B\overline{B}$, B^+B^-, *uds* and $\tau^+\tau^-$ events that pass all the selection criteria and are found in the signal region is reported in Table 4.2.

4.2.1 Signal events in $b - \bar{b}$ events

Since the B^0 and B^+ can decay in many modes with a D^{*+} resonance, we must test that we do not reconstruct D^{*+} candidates from those channels. This would be very dangerous:

Category	Fraction of background
Mistag	43%
D^+ candidates	3%
Swapped Kπ	1%
Signal *bad*-D^0	2%
Background *bad*-D^0	8%
Fake π	1%
Fake K	4%
Other	39%

Table 4.1: Contribution of different background categories to the total WS background. Some events overlap between the categories.

Background event category	Number of events in $400\,\mathrm{fb}^{-1}$
$B\overline{B}$	319
B^+B^-	233
uds	438
$\tau^+\tau^-$	0

Table 4.2: Number of MC events of $B\overline{B}$, B^+B^-, uds and $\tau^+\tau^-$ that pass all the selection cuts and are found in the $m_{K\pi\pi^0}$,Δm signal region.

firstly, these candidates would produce a D^0 daughter that would have a distorted lifetime. Moreover, since the D^0 decay would happen after the B decay only, its lifetime would mimic the D-mixing features.

Considering the $b-\bar{b}$ MC, we find 552 signal events in $\sim 400\,\mathrm{fb}^{-1}$ before the kinematic cuts described in Section 4.1.4 and the signal region of $m_{K\pi\pi^0}$,Δm distribution. Only 2 events, though, survive the cuts in the signal region.

Chapter 5

Fit to the $m_{K\pi\pi^0}$ and Δm distributions

In order to discriminate signal and background events, a binned χ^2 fit is performed to the reconstructed D^0 mass and to $\Delta m = m_{D^*} - m_{D^0}$ variables. The 2D scatter plots for both RS and WS are in Figure 5.1. During the fit procedure, we allow to float both the Probability Density Functions (PDF) shape parameters and the number of events in each signal and background categories. Since the PDF describing the signal is expected to be the same for both the RS and WS samples, a simultaneous fit is performed to reduce the systematic errors due to the shapes chosen. Since the shape of the signal distribution on the WS category will mainly be driven by the RS sample, where the statistics is higher, and the WS presents a lot of background events, the results of the binned fit are identical to those obtained from an unbinned fit within the numerical precision of the minimization program. The number of bins chosen for the fit procedure is 65x65 in the two variables. Several choices of binning were made to examine the fit dependency with number of bins. We found that any choice of binning between 50 to 80 for both variables gives the same number of events of signal and of the different background categories within the statistical error. For choices of number of bins larger than 80, the statistical error for the WS sample starts to be too large, and the fluctuations in the bins too severe, hence compromising the fit quality. For number of bins lower than 50, the binning starts to be comparable with the typical resolution of the D^0 mass; this worsens our knowledge of the signal PDF.

Some of the background categories described in Section 4.2 present significant peaks in the signal region of the two discriminating variables. Therefore it is necessary to perform a two-dimensional fit. The different categories showed in Table 4.1 can then be summarized in three categories: non-peaking (also called combinatorial) background, $m_{K\pi\pi^0}$ peaking (also called mistag) background and Δm peaking (also called *bad*-D^0) background.

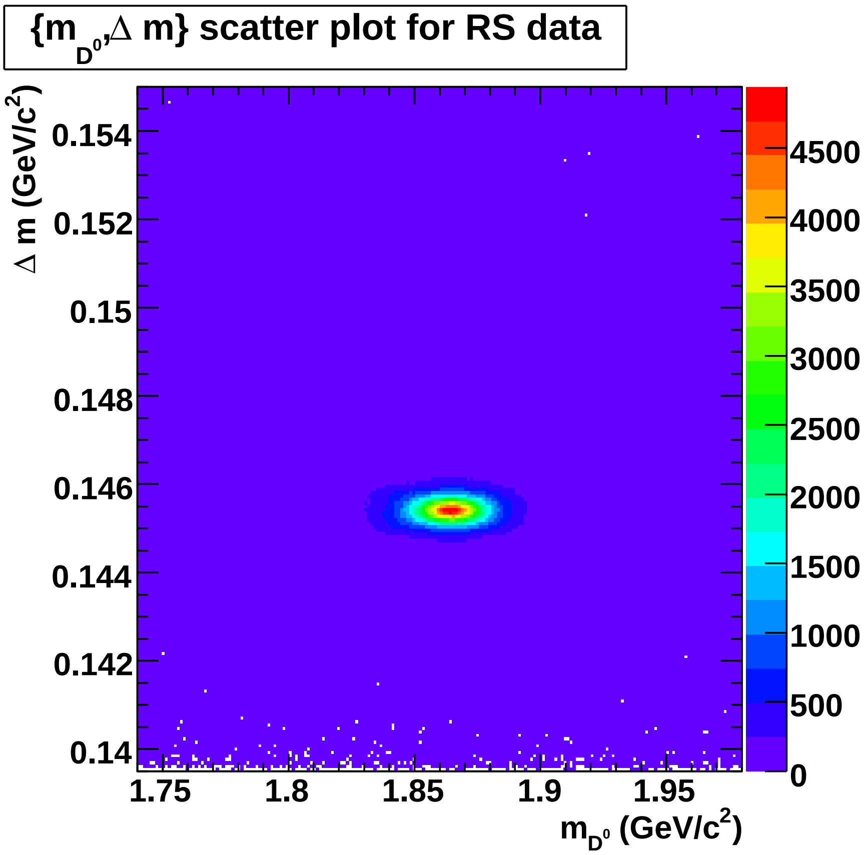

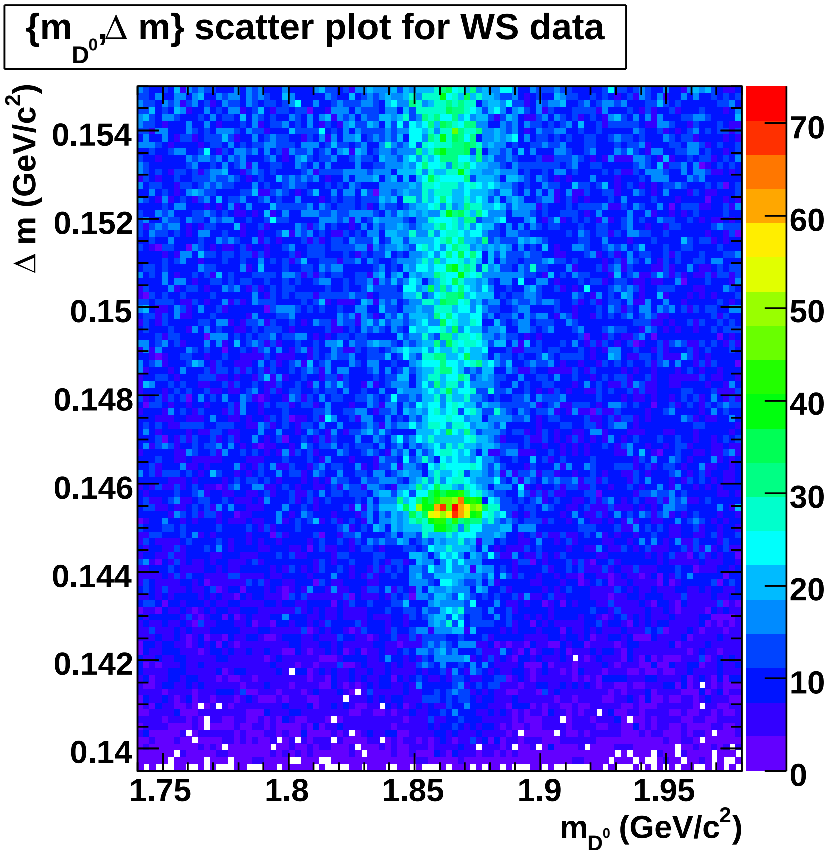

Figure 5.1: Reconstructed D^0 mass versus Δm for the RS and WS samples.

5.1 Signal and background parametrization

5.1.1 Signal PDF

The signal category has significant peaks in both $m_{K\pi\pi^0}$ and Δm distributions. Figure 5.2 shows the distribution of the two variables in the MC sample for signal. As can be noted, the $m_{K\pi\pi^0}$ distribution is asymmetric with respect to the peak. This is due to the presence of radiative losses in the left tail of the distribution, and must be accounted for in the signal description. The peak in $m_{K\pi\pi^0}$ is expected to be wider than the one obtained from the reconstruction of the $D^0 \to K^- \pi^+$ channel, because of the uncertainty in the determination of the π^0 momentum. This feature is not present in the Δm distribution, where the π^0 uncertainty contributes at higher orders.

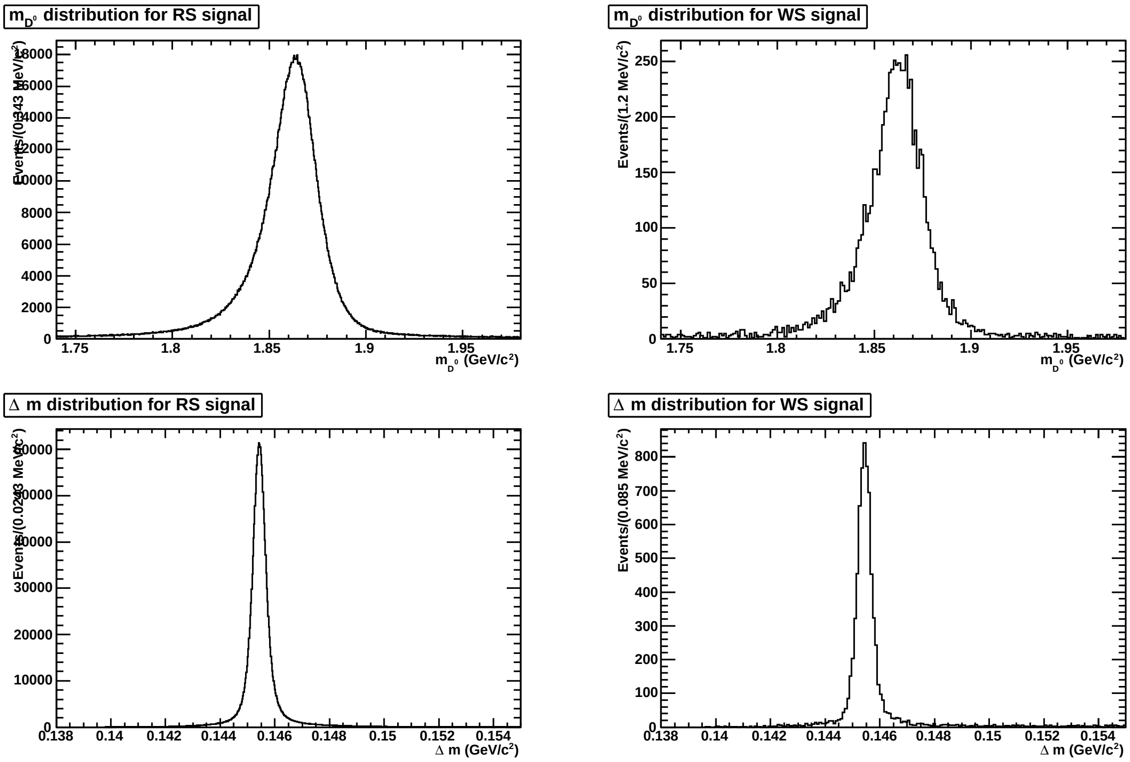

Figure 5.2: Distribution of the MC events corresponding to signal.

As observed in a previous analysis of this channel [24], a correlation between the two discriminating variables is expected. The signal PDF takes into account this correlation. The shapes used to compose the PDF are:

$$g(x;\overline{x},\sigma) = \exp\left(-\frac{(x-\overline{x})^2}{2\sigma^2}\right) \tag{5.1}$$

$$cb_s(x;\overline{x},\sigma,\alpha) = \begin{cases} \exp\left(-\frac{(x-\overline{x})^2}{2\sigma^2}\right) & \text{if } \frac{(x-\overline{x})}{\sigma} < \alpha \\ \\ a\left(b+\frac{(x-\overline{x})}{\sigma}\right)^{-2} & \text{if } \frac{(x-\overline{x})}{\sigma} \geq \alpha \end{cases} \tag{5.2}$$

$$a = (2/\alpha)^2 \exp(-\alpha^2/2), \quad b = (2/\alpha) - \alpha$$

$$s(x,y;\overline{x},\sigma_x,\overline{y},\sigma_y,c) = \exp\left(-\frac{(x-\overline{x})^2}{2\sigma_x^2}\right)\exp\left(-\frac{(y-\overline{y})^2}{2\left(\sigma_y + c((x-\overline{x})/\sigma_x)^2\right)^2}\right). \tag{5.3}$$

Given these components, the complete signal PDF is:

$$\mathcal{S}(m,\Delta m) = f_{s1}\cdot s_1 + (1-f_{s1})\cdot\{f_{s2}\cdot s_2 + (1-f_{s2})\cdot[f_{s3}\cdot s_3 + (1-f_{s3})\cdot s_4]\} \tag{5.4}$$

with

$$\begin{aligned} s_1 &= s(m,\Delta m;\overline{m}_1,\sigma_{m1},\overline{\Delta m}_1,\sigma_{\Delta m1},c_1) \\ s_2 &= s(m,\Delta m;\overline{m}_2,\sigma_{m2},\overline{\Delta m}_2,\sigma_{\Delta m2},c_2) \\ s_3 &= s(m,\Delta m;\overline{m}_3,\sigma_{m3},\overline{\Delta m}_3,\sigma_{\Delta m3},c_3) \\ s_4 &= g(m;\overline{m}_4,\sigma_{m4}) \times cb_s(\Delta m;\overline{\Delta m}_4,\sigma_{\Delta m4},\alpha_4). \end{aligned}$$

There are several interesting features of this parametrization that are worth to be pointed out:

- As can be noted, the PDF takes into account the correlation between the measured value of the D^0 mass and the Δm error in an event. The reason for this is that the closer the reconstructed D^0 mass value is to the nominal value of the PDG, the better Δm is determined;
- What was defined as cb_s is also known as *Crystal Ball* function, named after the omonimous Collaboration; it consists of a Gaussian core portion and a power-law low-end tail. This parametrization is useful to take into account the asymmetric tail in the D^0 mass distribution due to the radiative losses;
- the sum of the single components of signal in Equation 5.4 seems peculiar: it has been proved that when summing more than two components, this recursive approach gives a more stable fit [1].

---

[1] If one adds two components with a single fraction, one can impose the fraction parameter between 0

5.1.2 Combinatoric background

The combinatoric background is composed by candidates which have been reconstructed using uncorrelated tracks or clusters. This background is expected to have no significant peaks in the two discriminating variables. The distribution of this background can be estimated considering the MC sample, and is shown in Figure 5.3.

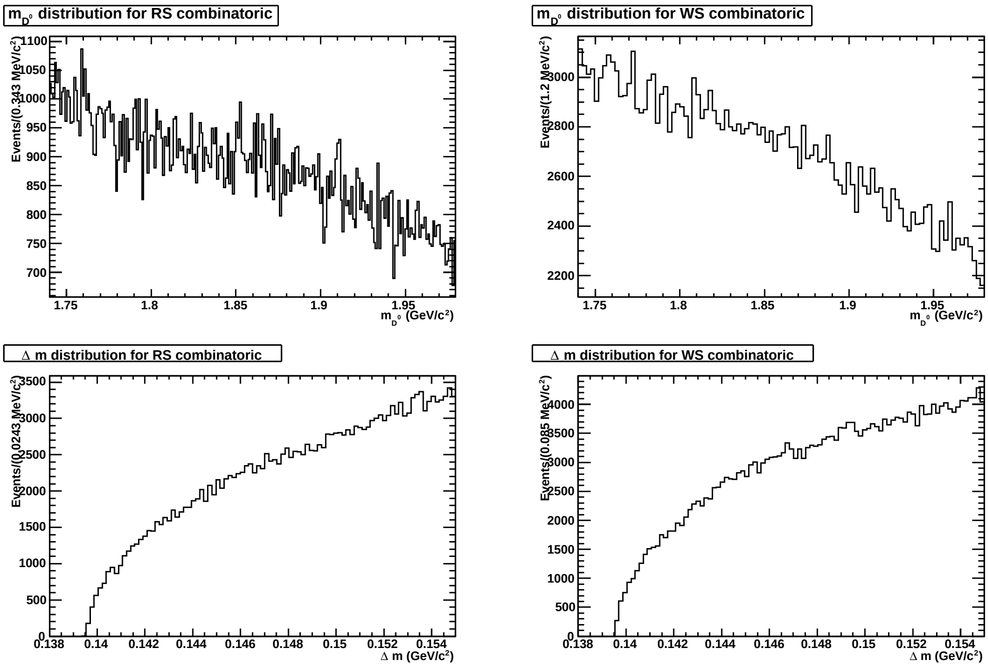

Figure 5.3: Distribution of the MC events corresponding to the combinatoric background.

The $m_{K\pi\pi^0}$ dependence can be represented using a straight line, with different slopes for the RS and the WS samples. The Δm distribution chosen is:

$$a(x;c) = x\sqrt{(x/x_0)^2-1}\,\exp\left(-\xi\left((x/x_0)^2-1\right)\right)\cdot\theta(x>x_0), \tag{5.5}$$

where $x_0 = 0.13957\,\mathrm{GeV}/c^2$ is the kinematic endpoint (i.e. the $\pi^\pm$ mass). Since there are different contributions in the RS and WS samples to the non-peaking background, ξ is expected to be different in the two cases. The complete PDF is:

$$\mathcal{C}(m,\Delta m) = (1 + b_1(m - 1.865\,\mathrm{GeV}/c^2)) \times a(\Delta m;\xi). \tag{5.6}$$

---

and 1. If one has three components and two fractions, the physical region is that where the sum of the fraction parameters is less than one. One can only require each fraction to be between 0 and 1, and may end up with a solution where the sum if greater than one and consequently one of the coefficients becomes negative. By defining the fractions recursively, all solutions are well defined as long as the fractions are inside the {0,1} range.

5.1.3 $m_{K\pi\pi^0}$ peaking Background (mistag)

This category is composed by D^* candidates made by a signal D^0 and an uncorrelated $\pi_s^\pm$. The distribution of this background category for the MC sample is shown in Figure 4.11.

On the $m_{K\pi\pi^0}$ projection, this background is expected to have the same distribution as signal. Therefore, a one-dimensional version of 5.4 is used. As far as Δm is concerned, this background is expected to have a shape similar to the non-peaking background. To prove this assumption we plot the Δm MC distributions for the combinatoric and mistag background on the same plot (see Figure 5.4).

$$\begin{aligned}\mathcal{F}(m,\Delta m) = f_{s1}\cdot s_{1D,1} + (1-f_{s1})\cdot\{f_{s2}\cdot s_{1D,2}\\ + (1-f_{s2})\cdot[f_{s3}\cdot s_{1D,3} + (1-f_{s3})\cdot s_{1D,4}]\}\times a(\Delta m; c)\end{aligned} \tag{5.7}$$

with

$$s_{1D,1} = g(m;\overline{m}_1,\sigma_{m1})$$

$$s_{1D,2} = g(m;\overline{m}_2,\sigma_{m2})$$

$$s_{1D,3} = g(m;\overline{m}_3,\sigma_{m3})$$

$$s_{1D,4} = g(m;\overline{m}_4,\sigma_{m4}).$$

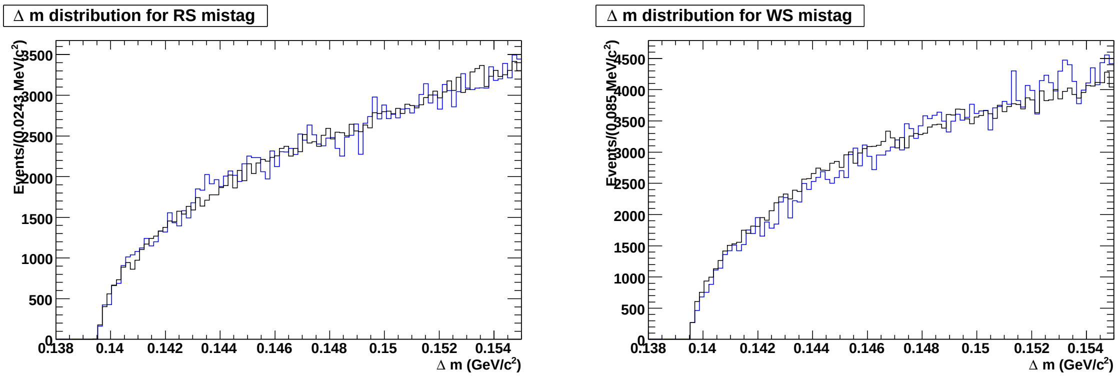

Figure 5.4: Comparison between the mistag and combinatoric Δm lineshape for both RS(left) and WS (right) MC samples. In both plots, the black line is the combinatoric background, the blue line is the mistag background.

5.1.4 Δm peaking background (*bad*-D^0)

This background category is composed by different reconstruction scenarios for the RS and the WS samples. For the RS sample, it comprises candidates with both a real D^0

and a real $\pi_s^{\pm}$, but where the D^0 has been wrongly reconstructed. An example of this would be $D^0 \to K^- \ \pi^+ \ \pi^0 \ \pi^0$ where one of the π^0 candidates is missing. The WS *bad-*D^0 sample contains events with doubly misidentified tracks, where the K^- has been called a π^- and the π^+ has been called a K^+. This background for the MC sample is shown in Figure 4.12. This background category has a clear peak in the signal region for both the RS and WS Δm distributions.

Given the small amount of events for this background category, fitting their $\{m_{K\pi\pi^0}$,Δm $\}$distribution from the data is difficult. We determine this background shape from the MC, and construct a two dimensional empirical PDF from it. We extract the number of events of this category from the data fit.

5.2 Fit results

The fit results for the simultaneous fit of the RS and WS samples are shown in Table 5.1. The plots of the corresponding data are in Figures 5.5 and 5.7. Since the RS sample has a very little background contribution, it is convenient to show it on a logarithmic scale, in Figure 5.6. Looking at the ratio $\frac{N_{sig,WS}}{N_{sig,RS}}$, it is noticeable to observe that it agrees very well with the PDG value ($(2.20 \pm 0.10) \cdot 10^{-3}$) [37].

Since the WS sample is affected by an high amount of background, we define a signal region in the $\{m_{K\pi\pi^0}$,Δm $\}$ plane where we will perform the fit of the WS time dependent Dalitz plot. To determine the number of events for signal and for the different background categories in the signal region, we perform a Monte-Carlo integration of the PDFs. We generate 10^6 events in each category using the PDF obtained from the fit. We generate separately the WS and the RS samples. Then we determine the fraction of events of each of the two samples in the region where

$$\begin{aligned} 1.8495 < m_{K\pi\pi^0} < 1.8795\,\mathrm{GeV}/c^2 \\ 0.1449 < \Delta m < 0.1459\,\mathrm{GeV}/c^2. \end{aligned} \tag{5.8}$$

Note that this selection of the signal region is symmetric with respect to the $m_{K\pi\pi^0}$ and Δm expected values.

The number of events in the signal region is then the fraction of generated events for each category multiplied by the corresponding number of events extracted from the fit of the whole data sample. The number of events generated is chosen so that the error on the fraction of events is negligible with respect to the error on the number of events from the fit. In order to propagate correctly the error on the number of events in the signal region, we add in square to the rescaled statistical error we have from the fit result the binomial error we obtain from the fluctuations of the total number of events in the sample. To better show our choice of the signal region, we report the 2D scatter plot of $\{m_{K\pi\pi^0}$,Δm $\}$ in a restricted region and indicate Equation 5.8 in Figure 5.8. The results are reported

Variable	Value
$\bar{m}_1$	1.85780 ± 0.00013
$\bar{m}_2$	1.864000 ± 0.000046
$\bar{m}_3$	1.84580 ± 0.00058
$\bar{m}_4$	1.864800 ± 0.000039
$\sigma_{m,1}$	0.02332 ± 0.00016
$\sigma_{m,2}$	0.012348 ± 0.000080
$\sigma_{m,3}$	0.0742 ± 0.0013
$\sigma_{m,4}$	0.008130 ± 0.000073
$\bar{\Delta m}_1$	0.1453900 ± 0.0000029
$\bar{\Delta m}_2$	0.1454300 ± 0.0000019
$\bar{\Delta m}_3$	0.145650 ± 0.000010
$\bar{\Delta m}_4$	0.1453800 ± 0.0000025
$\sigma_{\Delta m,1}$	0.0005199 ± 0.0000046
$\sigma_{\Delta m,2}$	0.0002142 ± 0.0000013
$\sigma_{\Delta m,3}$	0.001693 ± 0.000022
$\sigma_{\Delta m,4}$	0.0002657 ± 0.0000028
c_1	0.0000175 ± 0.0000014
c_2	$0.00003138 \pm 0.00000076$
c_3	0.000141 ± 0.000014
α_4	-1.4546 ± 0.015
$f_{s,1}$	0.2209 ± 0.0031
$f_{s,2}$	0.5168 ± 0.0096
$f_{s,3}$	0.3458 ± 0.0080
ξ_{WS}	1.518 ± 0.060
ξ_{RS}	4.574 ± 0.058
$b_{1,RS}$	0.624 ± 0.072
$b_{1,WS}$	-0.2236 ± 0.056
$N_{sig,RS}$	1198329 ± 2575
$N_{comb,RS}$	254222 ± 9515
$N_{mistag,RS}$	46676 ± 685
$N_{bad-D^0,RS}$	46683 ± 11397
$N_{sig,WS}$	2760 ± 96
$N_{comb,WS}$	85261 ± 444
$N_{mistag,WS}$	18946 ± 263
$N_{bad-D^0,WS}$	1011 ± 214

Table 5.1: Fit results for the $\{m_{K\pi\pi^0}, \Delta m\}$ fit.

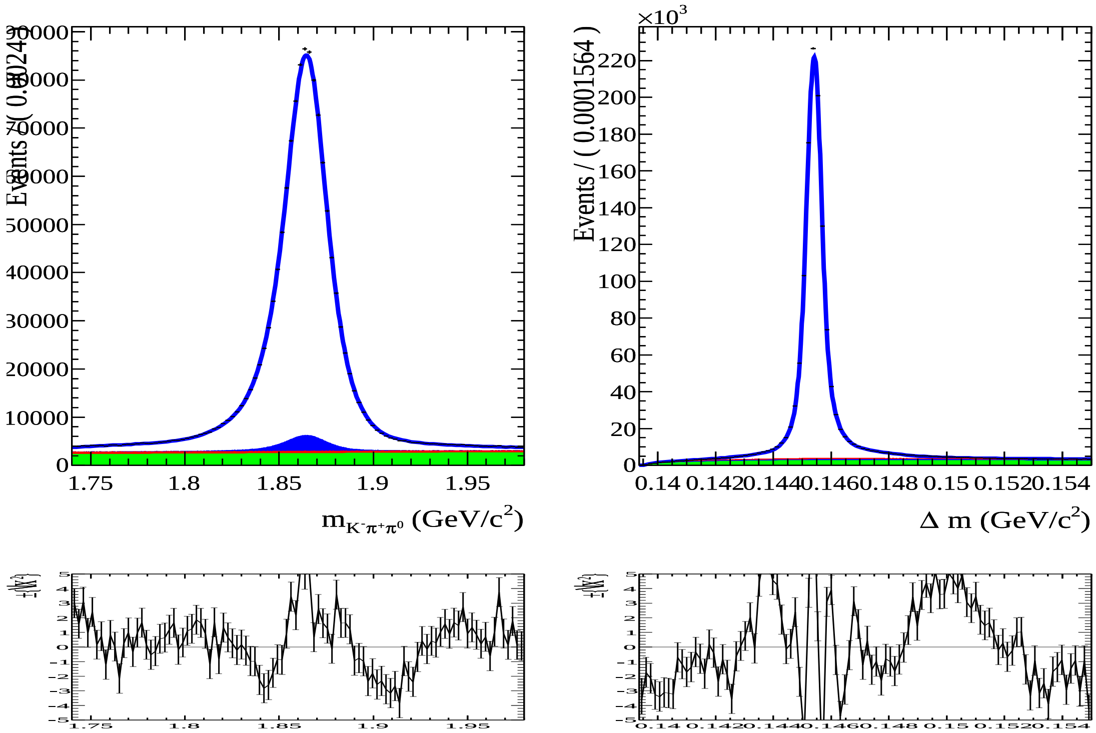

Figure 5.5: Projections of the χ^2 fit to the RS data into $m_{K\pi\pi^0}$ (left) and Δm (right). On bottom the pull distributions are shown. Dots are data and the blue line is the fit result. The green area is the combinatorial component of the fit, the red is the misreconstructed D^0 component and the blue is the mistag background.

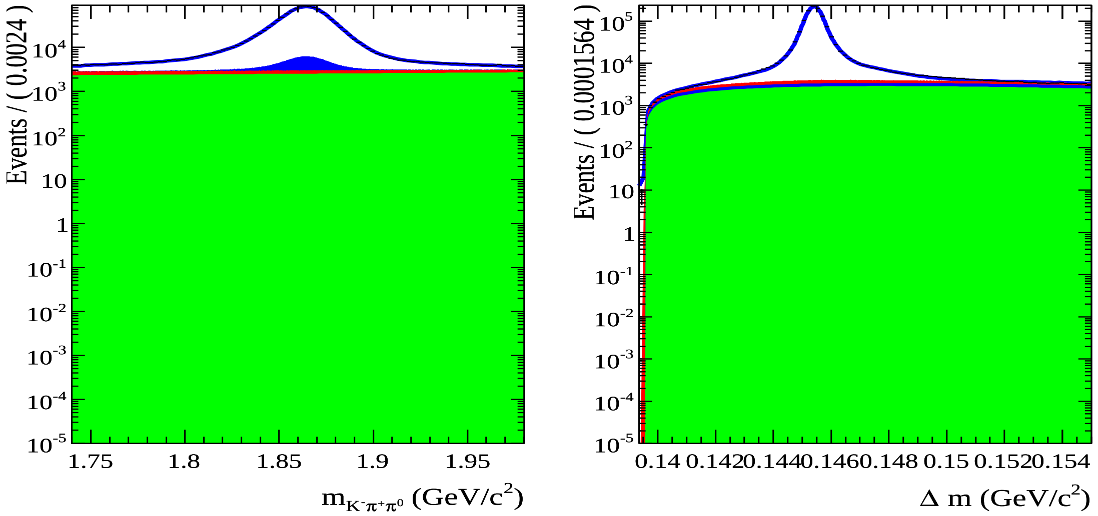

Figure 5.6: Projections of the χ^2 fit to the RS data into $m_{K\pi\pi^0}$ (left) and Δm (right), on a logarithmic scale. Dots are data and the blue line is the fit result. The green area is the combinatorial component of the fit, the red is the misreconstructed D^0 component and the blue is the mistag background.

in Tables 5.2 and 5.3. The plots for the RS and WS data samples and fit in the signal region are shown in Figures 5.9-5.10.

In the signal region, the RS sample is $\sim$ 99% pure, while the WS sample is $\sim$ 50% pure.

Category	Number of events	Cut efficiency
Signal	653962 ± 1581	54.6%
Combinatoric	2255 ± 51	0.9 %
Mistag	2218 ± 52	4.7%
bad-D^0	551 ± 23	1.2%

Table 5.2: Number of RS events of signal and background in the $m_{K\pi\pi^0}$ and Δm signal region

5.2.1 Study of the fit results in the sideband regions

Another interesting information comes from the study of the fitted PDF behavior in the sidebands of $m_{K\pi\pi^0}$ and Δm distributions, where signal is largely suppressed. This gives a good information on the ability of the PDF in interpreting the different background components of the data sample. We firstly consider the left sideband on the $m_{K\pi\pi^0}$ distribution, defined as $1.74 < m_{K\pi\pi^0} < 1.81$ GeV/c^2. In this region, both signal and mistag background should be depleted, since they both significantly peak in the D^0 mass

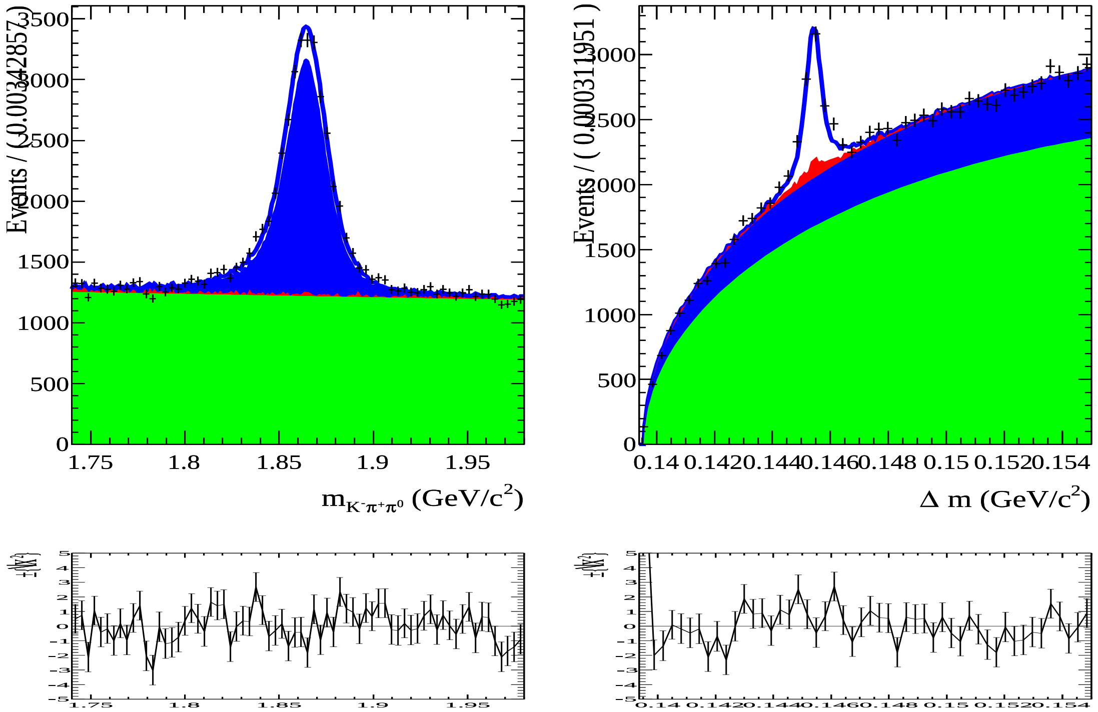

Figure 5.7: Projections of the χ^2 fit to the WS data into $m_{K\pi\pi^0}$ (left) and Δm (right). On bottom the pull distributions are shown. Dots are data and the blue line is the fit result. The green area is the combinatorial component of the fit, the red is the misreconstructed D^0 component and the blue is the mistag background.

Category	Number of events	Cut efficiency
Signal	1508 ± 49	54.6%
Combinatoric	663 ± 61	0.8 %
Mistag	791 ± 39	4.2%
bad-D^0	47 ± 12	4.7%

Table 5.3: Number of WS events of signal and background in the $m_{K\pi\pi^0}$ and Δm signal region

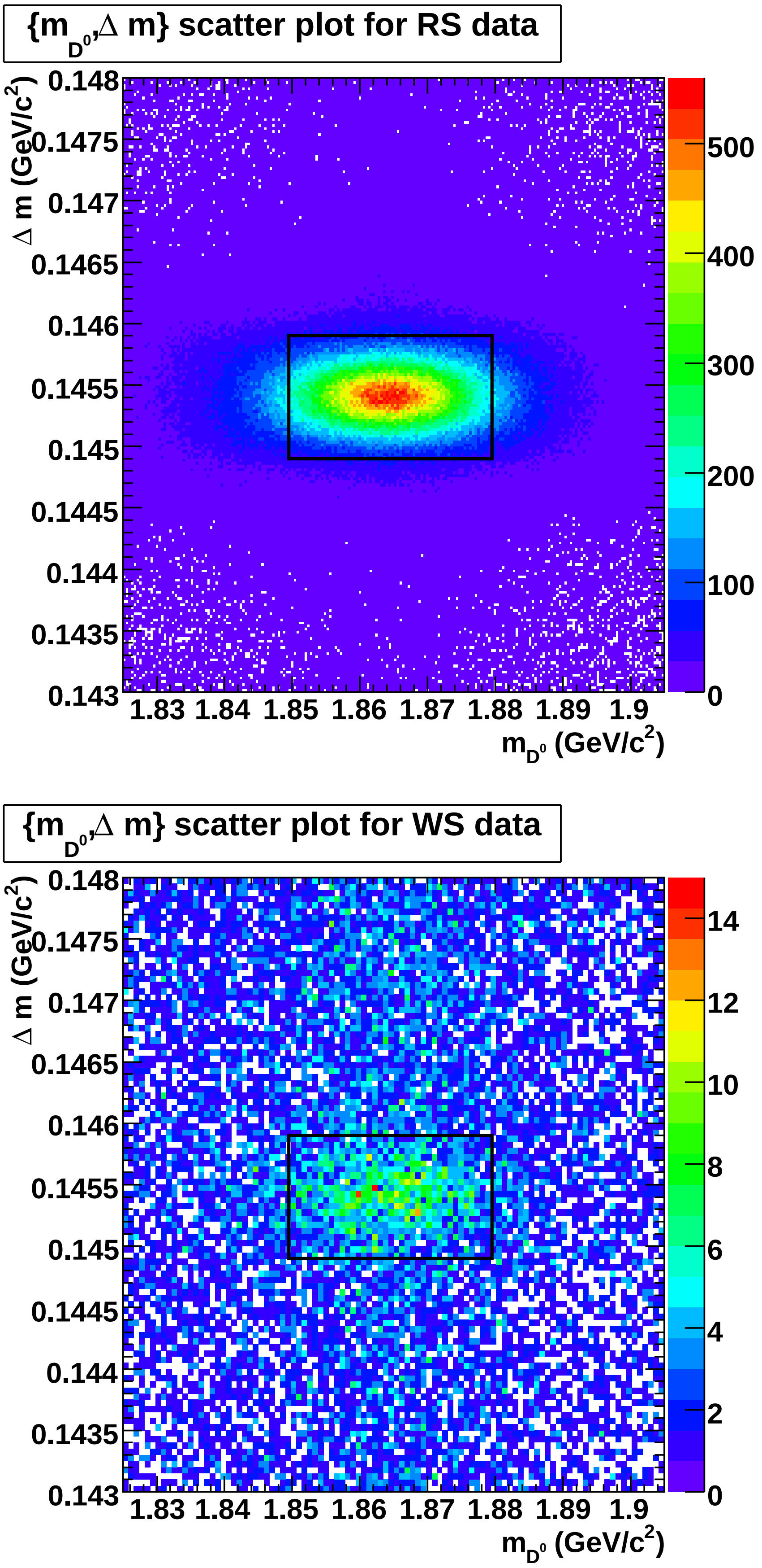

Figure 5.8: Reconstructed D^0 mass versus Δm for the RS and WS samples, in the region of $1.825 < m_{K\pi\pi^0} < 1.905$ GeV/c^2 and $0.143 < \Delta m < 0.148$ GeV/c^2. The box in the plot indicates the signal region defined in Equation 5.8.

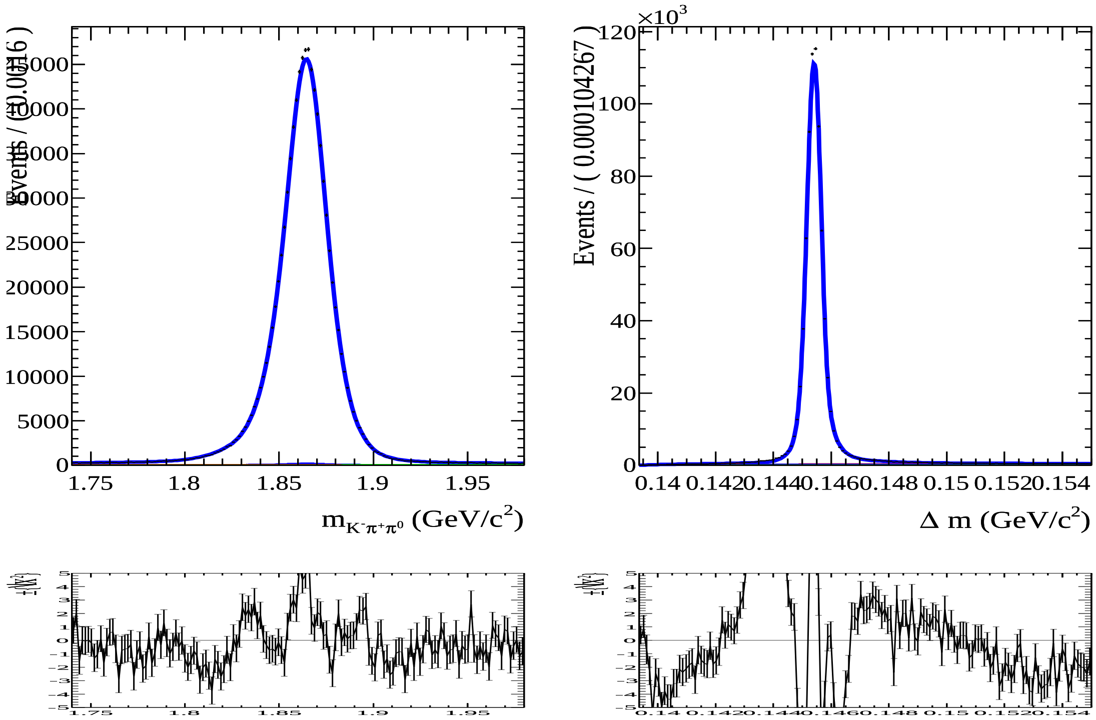

Figure 5.9: Projections of the χ^2 fit to the RS data into $m_{K\pi\pi^0}$ (left) and Δm (right) in the signal region. Dots are data and the blue line is the fit result. The green area is the combinatorial component of the fit, the red is the misreconstructed D^0 component and the blue is the mistag background. The left plot requires $0.1449 < \Delta m < 0.1459$ GeV/c^2, while the right plot requires $1.8495 < m_{K\pi\pi^0} < 1.8795$ GeV/c^2. On bottom the pull distributions are shown.

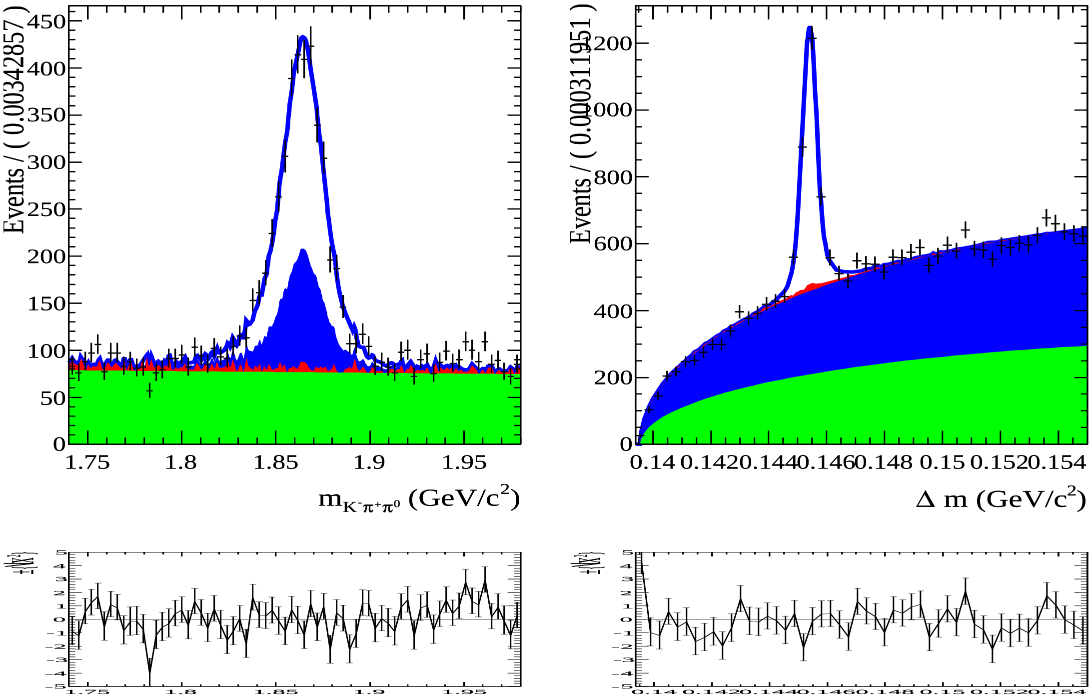

Figure 5.10: Projections of the χ^2 fit to the WS data into $m_{K\pi\pi^0}$ (left) and Δm (right) in the signal region. Dots are data and the blue line is the fit result. The green area is the combinatorial component of the fit, the red is the misreconstructed D^0 component and the blue is the mistag background. The left plot requires $0.1449 < \Delta m < 0.1459$ GeV/c^2, while the right plot requires $1.8495 < m_{K\pi\pi^0} < 1.8795$ GeV/c^2. On bottom the pull distributions are shown.

region. We can consider the Δm distribution in that range, by reducing the dataset to the left $m_{K\pi\pi^0}$ sideband and projecting the total PDF (previously fitted to the whole sample) integrated in the D^0 mass range considered. Figure 5.11 shows, for RS and WS cases, the data in that region, along with the projected PDF. Using the same procedure, we define the right sideband of the D^0 mass distribution to be $1.91 < m_{K\pi\pi^0} 1.98$ GeV/c^2.

The corresponding plots for the Δm distribution are in Figure 5.12. One can notice that in both sidebands, the fit results agree reasonably well with the data. As far as the RS sample is concerned, the small discrepancies that one may observe are very small if compared with the size of the number of signal events in the data sample. For the WS sidebands, one can notice a tiny underestimation of the number of background events in the right sideband. This effect is mitigated in the left sideband. Assuming that this behavior is linear with the D^0 mass, one can expect that in the signal region, the discrepancy will be an intermediate case between the two sidebands. This will be treated as a systematic uncertainty in our final fit, as described in Section 12.5.

On the other side, one may want to look at the sidebands regions of the Δm distribution. We define the left sideband as $0.138 < \Delta m < 0.143$ GeV/c^2. The corresponding plots of $m_{K\pi\pi^0}$ are shown in Figure 5.13 for both RS and WS. The right sideband of Δm is defined to be $0.149 < \Delta m < 0.155$ GeV/c^2. The corresponding plot for the D^0 mass is in Figure 5.14. Also in this case, the small discrepancies observed in the RS sidebands are tiny if compared with the size of the number of events of signal in the sample. The WS fit, instead, reasonably matches the data.

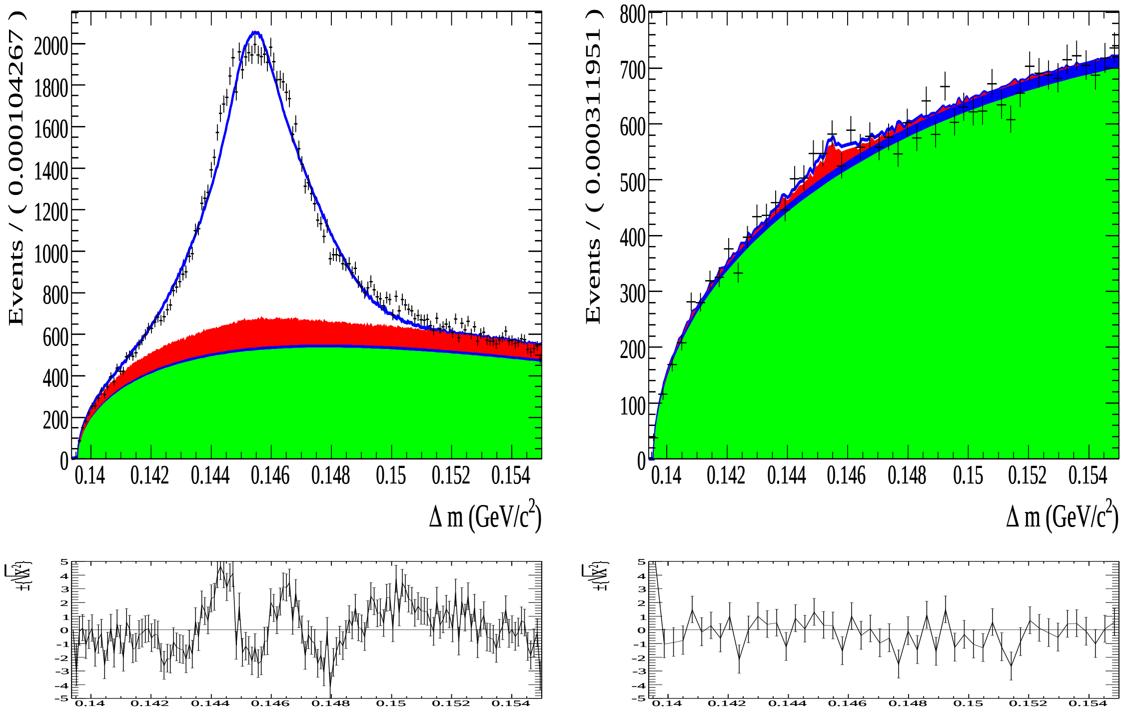

Figure 5.11: Projections of the χ^2 fit to the RS (left) and WS (right) data in the far left sideband of $m_{K\pi\pi^0}$ into the Δm distribution. Dots are data and the blue line is the fit result. The green area is the combinatorial component of the fit, the red is the misreconstructed D^0 component and the blue is the mistag background. The left sideband of $m_{K\pi\pi^0}$ is defined as $1.74 < m_{K\pi\pi^0} < 1.81$ GeV/c^2.

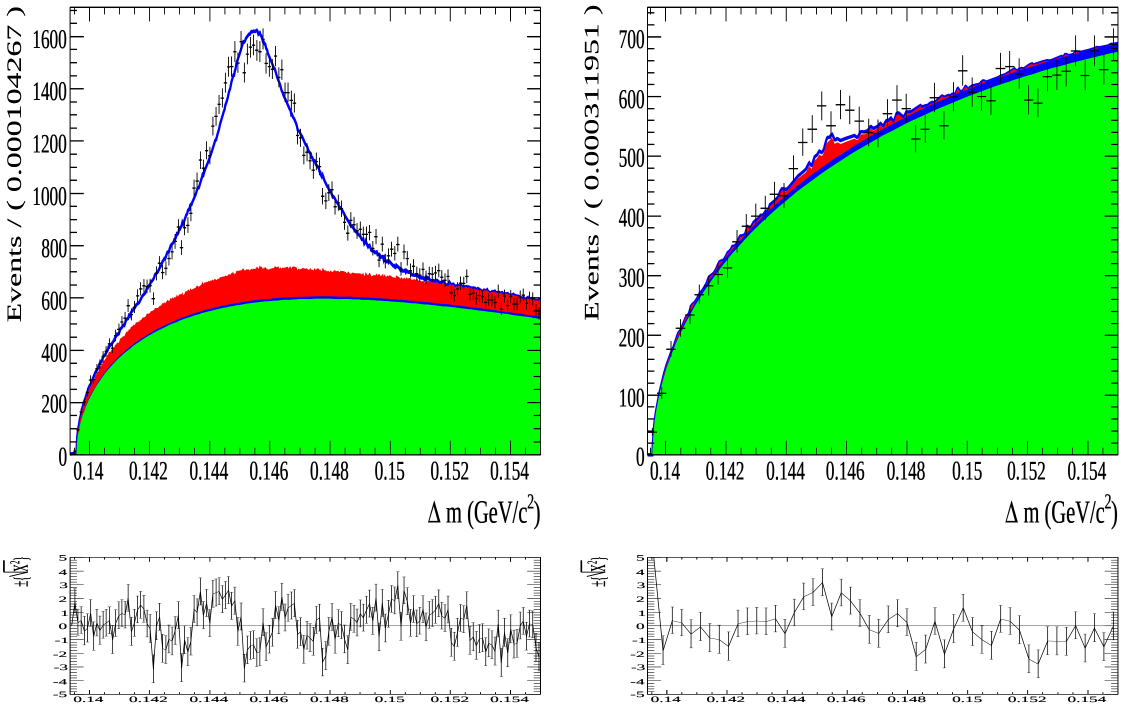

Figure 5.12: Projections of the χ^2 fit to the RS (left) and WS (right) data in the far right sideband of $m_{K\pi\pi^0}$ into the Δm distribution. Dots are data and the blue line is the fit result. The green area is the combinatorial component of the fit, the red is the misreconstructed D^0 component and the blue is the mistag background. The right sideband of $m_{K\pi\pi^0}$ is defined as $1.91 < m_{K\pi\pi^0} < 1.98$ GeV/c^2.

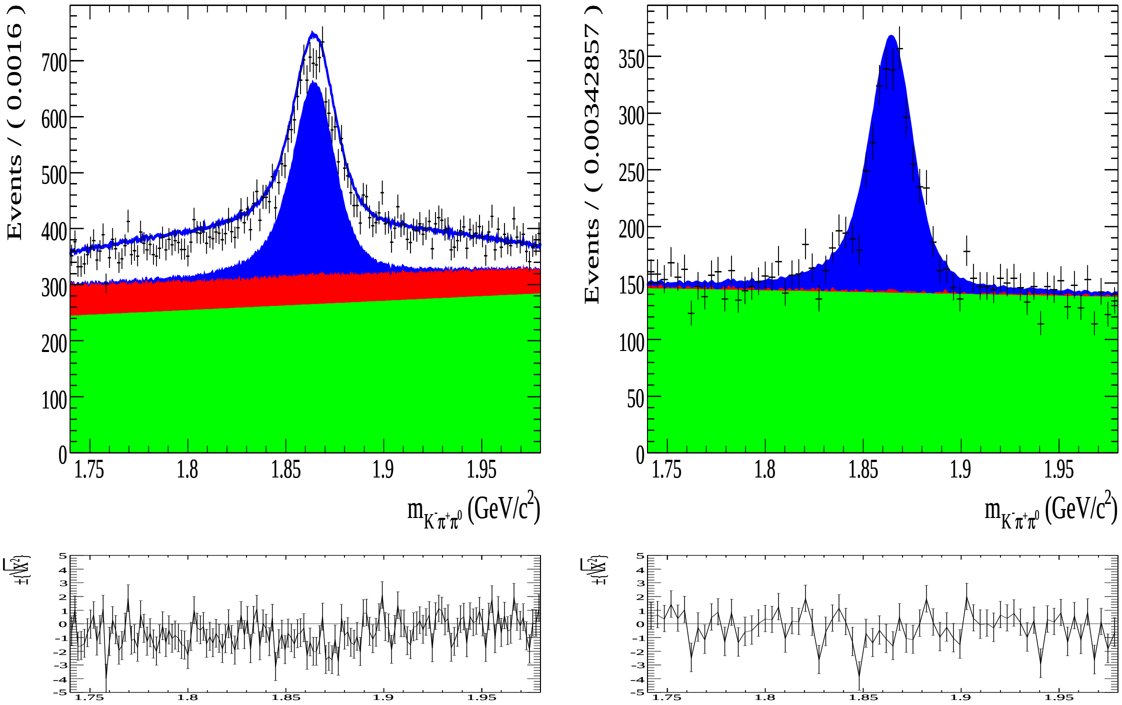

Figure 5.13: Projections of the χ^2 fit to the RS (left) and WS (right) data in the far left sideband of Δm into the $m_{K\pi\pi^0}$ distribution. Dots are data and the blue line is the fit result. The green area is the combinatorial component of the fit, the red is the misreconstructed D^0 component and the blue is the mistag background. The left sideband of Δm is defined as $0.138 < \Delta m < 0.143$ GeV/c^2.

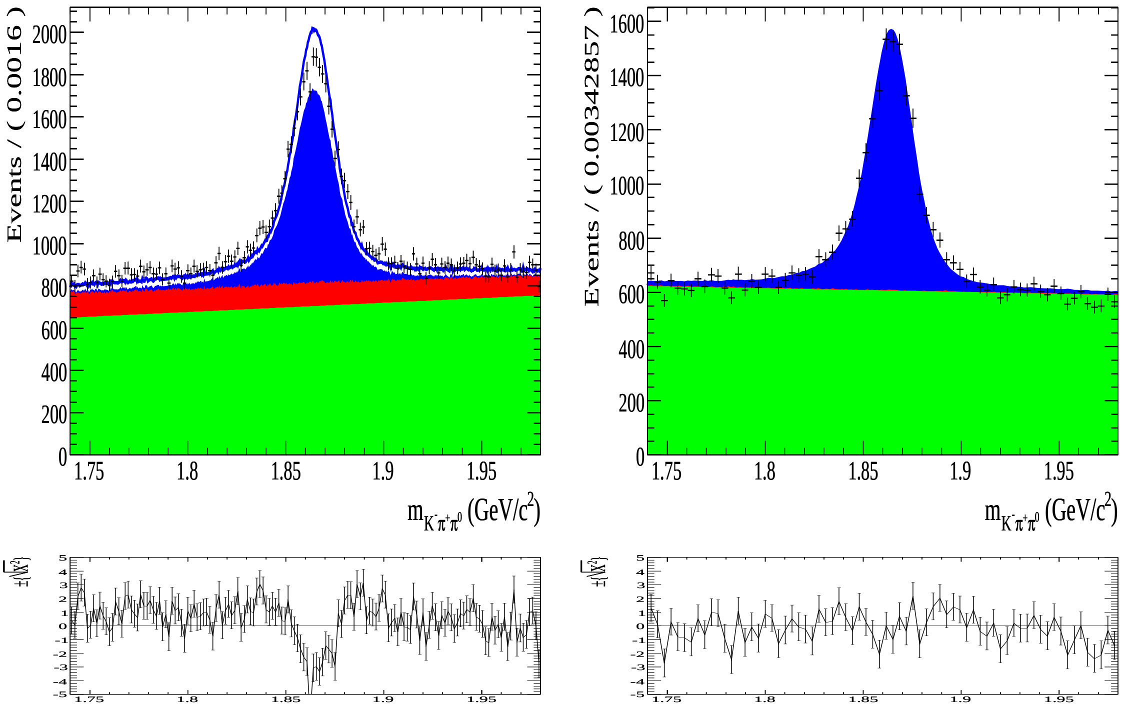

Figure 5.14: Projections of the χ^2 fit to the RS (left) and WS (right) data in the far right sideband of Δm into the $m_{K\pi\pi^0}$ distribution. Dots are data and the blue line is the fit result. The green area is the combinatorial component of the fit, the red is the misreconstructed D^0 component and the blue is the mistag background. The right sideband of Δm is defined as $0.149 < \Delta m < 0.155$ GeV/c^2.

Chapter 6

Dalitz plot efficiency

In order to fit both the RS time-independent and the WS time-dependent Dalitz plots, a parametrization of the reconstruction efficiency over the Dalitz plot is needed. For this estimation we used 15 million signal MC events, where the D^0 is allowed to decay isotropically, constrained only by the kinematics of the phase space (PHSP MC). This sample comprises both D^{*+} and D^{*-} particles in the generation. The efficiency is determined ignoring any charge asymmetry in reconstruction.

Using the MC information, we isolated a reconstructed signal sample which passed all the selection criteria described in Section 4. The efficiency is estimated with a parametrization dependent on the helicity angle of a pair of the D^0 decay products. This technique has proved before to be convenient to avoid fit uncertainties on the borders of the non-rectangular kinematical region of the Dalitz plot [36], where rectilinear efficiency bins have reduced statistics.

The $m^2_{K\pi}$ invariant mass and the cosine of the $K^{\pm}\pi^{\mp}$ helicity angle $cos\theta$ (i.e. the angle between the K and the π directions in the D^0 rest frame) are considered in the fit [1]. Notice that the efficiency determination is independent on the particular pair chosen to calculate the helicity angle. The efficiency of the Dalitz plot can be parametrized as:

$$\epsilon(cos\theta) = \frac{dN^j_{reco}}{dcos\theta} / \frac{dN^j_0}{dcos\theta} = \frac{N^j_{reco} \sum_i c^j_i P_i(cos\theta)}{N^j_0 P_0(cos\theta)} \tag{6.1}$$

where j indicates the j-th bin of $m^2_{K\pi}$, N^j_{reco} is the number of reconstructed D^0's in the j-th bin, N^j_0 is the number of generated D^0's in that bin and P_i is the i-th Legendre polynomial. We divide $m^2_{K\pi}$ in 40 bins, and for each bin we do a binned χ^2 fit to $\epsilon(m, cos\theta)$ to determine the c^j_i coefficients. The fit is a binned χ^2 fit, where $cos\theta$ was binned in 30 divisions. The fit is performed extracting the coefficients of the Legendre polynomials up to the 5^{th} order. The bins with a reasonably flat distribution could be fitted with a lower order polynomial. However, the fit in $m^2_{K\pi}$ bins with high statistics show a c^j_5 non

---

[1] On the side, one could describe the Dalitz plot structure by using the invariant mass and the helicity angle. This description would be equivalent to the use of two invariant masses.

compatible with zero within the error. For this reason we decide to use the Legendre polynomials up to the 5^{th} order.

6.1 π^0 efficiency correction

Since the π^0 reconstruction efficiency is generally underestimated in the *BABAR* simulation, we apply a correction to the efficiency calculated in each bin of $m^2_{K\pi}$. This correction depends on the π^0 momentum, so it is not constant along the Dalitz plot. We reweight each MC event using the relation:

$$\mathcal{W}(p_{\pi^0}) = 0.976776 + 0.00591363 p_{\pi^0} \tag{6.2}$$

where p_{π^0} is the π^0 momentum in the laboratory frame.

This π^0 efficiency correction is determined using a control sample of τ decays, simulating and reconstructing the process $e^+e^- \to \tau^+\tau^-$. The channels $\tau \to \rho\nu$ $(\rho \to \pi^+\pi^0)$ and $\tau \to \pi\nu$ are considered, and the double ratio

$$\varepsilon_{\pi^0} = \frac{N_{\tau\to\rho\nu,DATA}}{N_{\tau\to\rho\nu,MC}} \cdot \frac{N_{\tau\to\pi\nu,MC}}{N_{\tau\to\pi\nu,DATA}} \tag{6.3}$$

is considered in bins of the π^0 momentum. Using this double ratio technique, the π^0 efficiency is independent on the particular control sample used for the calculation [2].

6.2 Dalitz plot efficiency determination

In Figures 6.1 and 6.2 we show the MC events and fits of $\cos\theta$ in bins of $m^2_{K\pi}$. We observe that the helicity angle distributions are generally flat. In Figure 6.3 we report the Dalitz plot efficiency both from the PHSP MC events and from the fit result. In the PHSP MC Dalitz plot the efficiency in the j^{th} bin is defined as $N_{reco,j}/N_{0,j}$. To easily evaluate the compatibility between the two distributions we also plot the pull (Figure 6.4 top). In each bin the pull is calculated by considering the difference between the fit result and the PHSP MC efficiency, divided by the error on the fit result. Bins with less than 5 reconstructed events have been excluded from this plot, as the statistical fluctuations become too severe. It can be noted that the values of the pull in each bin are equally distributed among the range considered, and no particular structure is present. Considering the one dimensional projection of the pull distribution (see Figure 6.4 bottom), we find that the mean value of the pull is 0.01 ± 0.06, indicating that no bias is present. The RMS of the distribution

---

[2] This efficiency correction has a systematic uncertainty of $\sim 2\%$. Since this uncertainty does not depend on the π^0 momentum, it does not vary along the Dalitz plot. For this reason, we can ignore this effect: we are only interested in the shape of the efficiency, not in the absolute size. Varying the integral of the functional description of the efficiency by any value will not change our result.

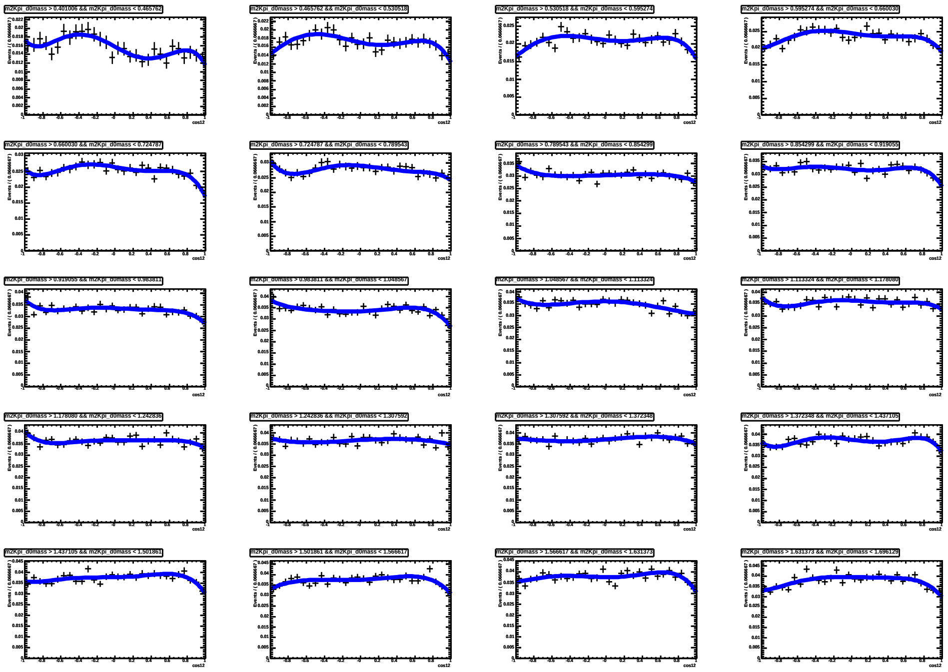

Figure 6.1: Fit of the helicity angle cosine in bins of $m^2_{K\pi}$. The dots are the MC events, the blue line is the fit result. These plots refer to the 15 bins of $m^2_{K\pi}$ in the range $0.40 < m^2_{K\pi} < 1.29$ GeV/c^2. The first bin corresponds to the top left plot, the second to the top middle plot, the last to the bottom right plot.

is 1.37 ± 0.05; this indicates that the errors on the efficiency in each bin of the Dalitz plot may be underestimated. This is not a problem, as we do not use these errors to evaluate the efficiency parametrization systematic uncertainty.

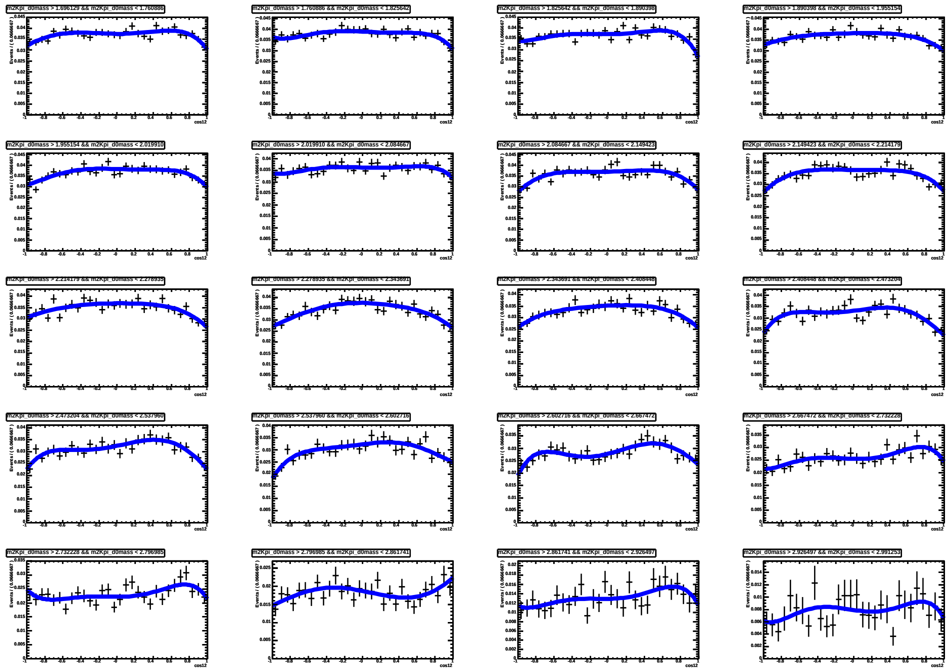

Figure 6.2: Fit of the helicity angle cosine in bins of $m^2_{K\pi}$. The dots are the MC events, the blue line is the fit result. These plots refer to 15 bins of $m^2_{K\pi}$, in the range to $1.29 < m^2_{K\pi} < 2.99$ GeV/c^2. The first bin corresponds to the top left plot, the second to the top middle plot, the last to the bottom right plot.

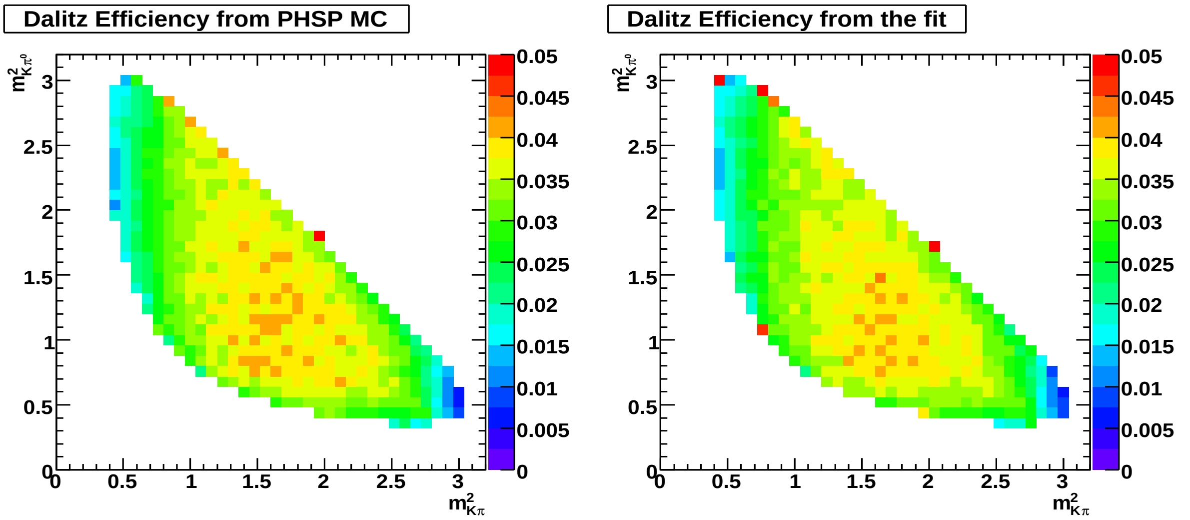

Figure 6.3: Dalitz plot efficiency for PHSP MC (left) and from the fit (right) on the $m^2_{K\pi}$ and $m^2_{K\pi^0}$ plane. The $\chi^2/ndof$ between the two distributions is 0.73

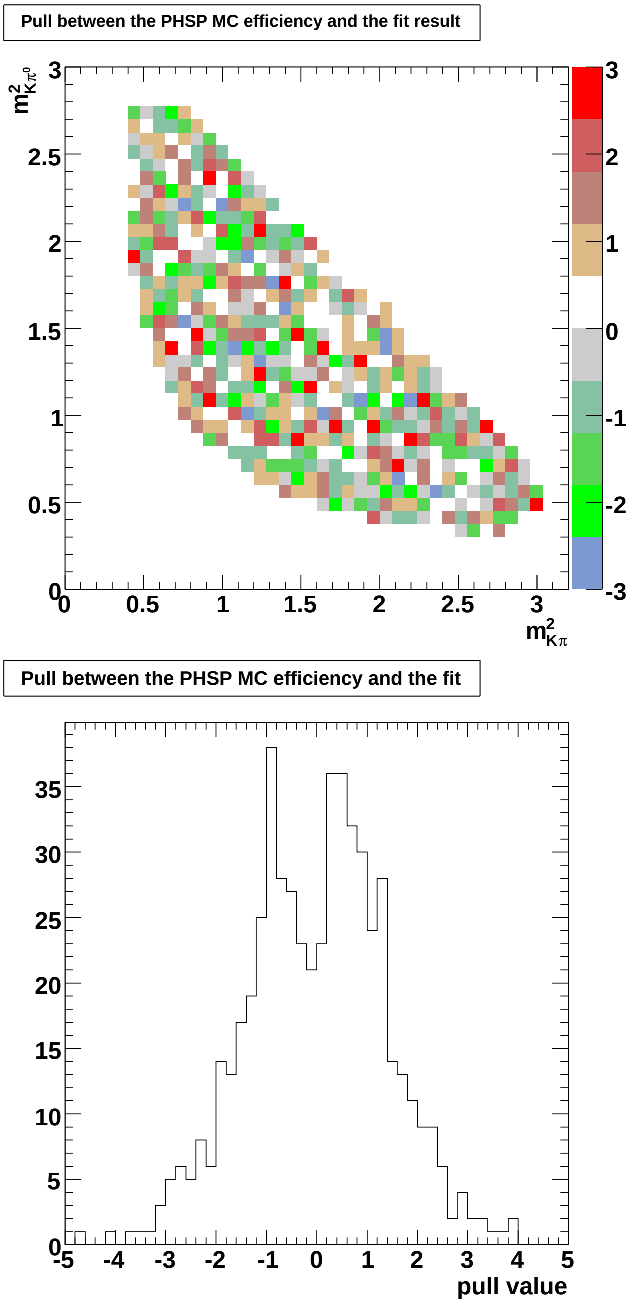

Figure 6.4: Pull distributions between PHSP MC and efficiency fit on the $m^2_{K\pi}$ and $m^2_{K\pi^0}$ plane (top) and on a one-dimensional histogram (bottom). The value in each bin of the Dalitz plot is in units of the statistical error.

Chapter 7

Fit of the time-independent RS Dalitz plot

In Equation 2.22 it appears that a reliable Dalitz fit of the RS sample is necessary in order to perform this mixing analysis. The RS Dalitz can be fitted separately with respect to the WS sample, and its results can be used to fix the Cabibbo-favored amplitude in the decay rate formula for the WS sample. The Dalitz plot of the RS sample is shown in Figure 7.1. Many structures emerge from this plot. Firstly, it is clear from the accumulation of events on the diagonal of the Dalitz plot that the main contribution comes from the $\rho^+(770)$ resonance. Next to this, the second largest contribution comes from the K^{*-} (892) resonance and the third from the K^{*0} (892). Clear destructive interference patterns emerge when the ρ^+ and K^* s distributions cross each other.

Since the D mixing is a small effect, we expect that only the main components (in terms of fit fractions) of the CF amplitude will contribute; the A_{CF} contributes to the $D^0 \to K^+\pi^-\pi^0$ total amplitude with terms proportional to the mixing parameters x and y, so the smaller resonant components of this amplitude will not add much to our sensitivity. Therefore, a high precision fit of the RS sample is not needed. Nevertheless, the high statistics available allows a rather precise determination of the various contributions.

7.1 Signal parametrization

The total signal amplitude as a function of $m^2_{K\pi}$ and $m^2_{K\pi^0}$ is parametrized as a sum of isobar components, as described in Section 2.4. The list of resonances considered in the fit and their main properties are reported in Table 7.1.

The reader should be reminded that for the scalar contribution to the amplitude, we use the LASS effective range parametrization described in Section 2.5. For consistency, we extract from our data sample the mass M and the width Γ along with a and r that play the role of a scattering length and effective interaction length respectively. The LASS parameters are differentiated for the $K_0^{*-}(1430)$ and $K_0^{*0}(1430)$ contributions. The δ_R

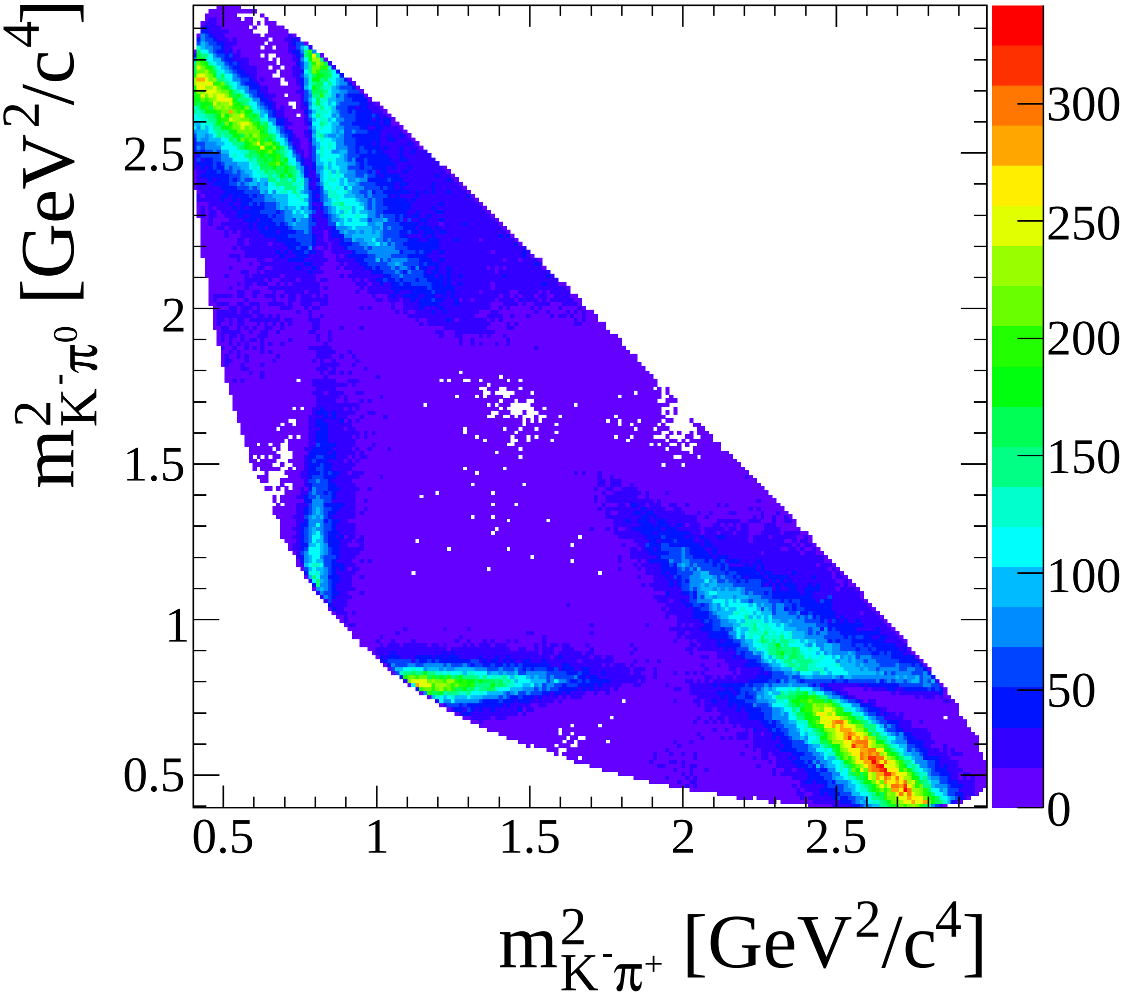

Figure 7.1: Dalitz Plot of the RS data sample. The two squared invariant masses $m^2_{K\pi}$ and $m^2_{K\pi^0}$ are used to represent the Dalitz plot. The data sample considered is in the signal region defined in Section 5.8. As described in the event selection section. a D^0 mass constrain is applied to the decay tree fit. Therefore the data has a sharp edge on the borders of the Dalitz plot.

Resonance	J^{PC}	Mass (GeV/c^2)	Width (GeV/c^2)
$\rho^+(770)$	1^{--}	0.7755 ± 0.0004	0.1494 ± 0.001
$\rho^+(1700)$	1^{--}	1.720 ± 0.020	0.250 ± 0.100
$K^{*-}(892)$	1^-	0.89166 ± 0.000026	0.0508 ± 0.009
$K^{*-}(1410)$	1^-	1.414 ± 0.015	0.232 ± 0.021
$K_0^{*-}(1430)$	0^+	1.414 ± 0.006	0.290 ± 0.021
$K_2^{*-}(1430)$	2^+	1.4256 ± 0.0015	0.0985 ± 0.0027
$K^{*-}(1680)$	1^-	1.717 ± 0.027	0.322 ± 0.110
$K^{*0}(892)$	1^-	0.89600 ± 0.00025	0.0503 ± 0.006
$K^{*0}(1410)$	1^-	1.414 ± 0.015	0.232 ± 0.021
$K_0^{*0}(1430)$	0^+	1.414 ± 0.006	0.290 ± 0.021
$K_2^{*0}(1430)$	2^+	1.4324 ± 0.0013	0.109 ± 0.005

Table 7.1: Summary of the Dalitz plot contributions considered in the RS time-independent fit. The masses and widths considered are taken from the 2006 PDG values [37].

mass dependence is described by a Breit-Wigner parametrization.

7.2 Background characterization

The background categories that enter this Dalitz Plot are the combinatoric and the *bad*-D^0 . Since the mistag background is composed by correctly reconstructed RS D^0 candidates, the Dalitz structure is the same as signal, and is effectively treated as such. As the fit on the D^* candidate had a constraint on the D^0 mass (see Section 4.1.4), we expect that the background shape will change along the $m_{K\pi\pi^0}$ distribution. This is because the combinatoric background is composed by tracks whose kinematic responds only to the PHSP constraints. Imposing the D^0 mass means that when the fitter encounters a background event, it will distort the momenta of the particles in order to match the constraint. It is therefore necessary to include this dependence with $m_{K\pi\pi^0}$ in the description.

In order to parametrize the background, we consider two different sidebands of $m_{K\pi\pi^0}$. We choose those sidebands to be:

$$\begin{aligned} \textit{left}\text{ region: } & 1.75 < m_{K\pi\pi^0} < 1.77\,\mathrm{GeV}/c^2 \\ \textit{right}\text{ region: } & 1.95 < m_{K\pi\pi^0} < 1.97\,\mathrm{GeV}/c^2 \end{aligned} \tag{7.1}$$

In this way we have two samples which are a mixture of combinatoric and $bad - D^0$ events. The samples are considered in the signal region of the Δm distribution. Since the fraction of combinatoric and *bad*-D^0 events depends also on the cut on Δm, this selection is necessary to avoid underestimating the *bad*-D^0 contribution in the sidebands. The distribution in the sidebands of the three invariant masses for both data and MC are shown in Figures 7.2-7.4 .It can be noted that data and MC show similar distributions within the statistical error. From these plots, we conclude that the data and the MC have similar behaviors. Nevertheless, the MC cannot be trusted to perfectly mimic the background in data, as many rare charm decays are missing in the simulation.

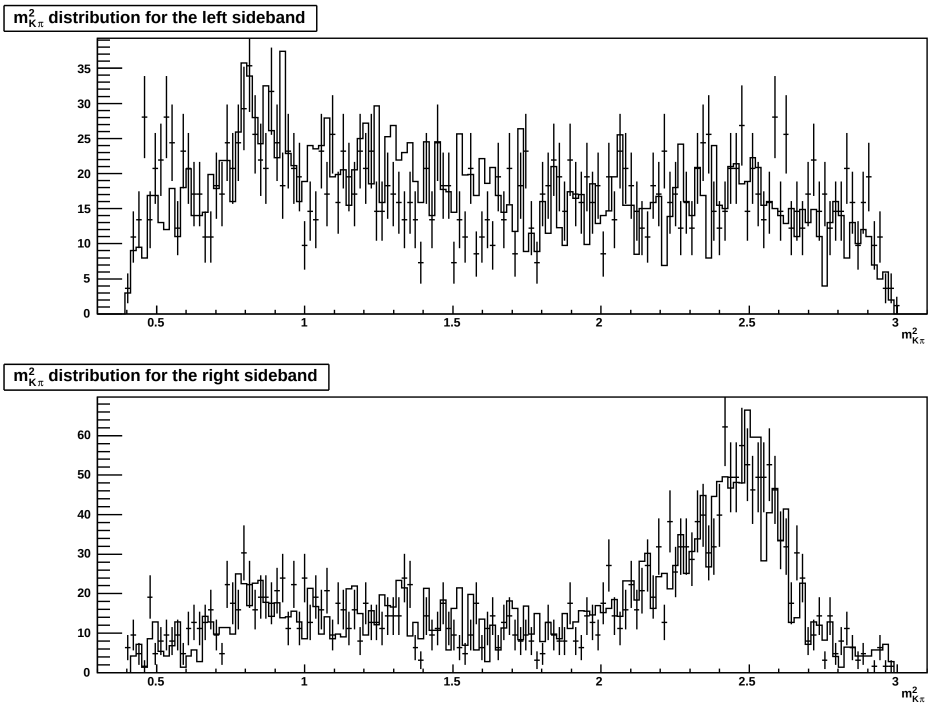

Figure 7.2: Distribution of $m^2_{K\pi}$ for the left and right $m_{K\pi\pi^0}$ sidebands of the RS data (dots) and MC (line). The MC distribution is normalized to the data.

In order to estimate the Dalitz plot structure of the background in the signal region, we prefer to use the information from the data, but use the MC to know the fractional contribution of each sideband to the signal region description. We perform the following procedure:

- We select the sidebands of the MC sample, and construct an interpolation of the distributions. The right distribution is normalized to the left one;
- We construct the PDF of the background in the signal region as the sum of the interpolations of the two sidebands, i.e.

$$bkg(m^2_{K\pi}, m^2_{K\pi^0}) = f_B bkg_{left}(m^2_{K\pi}, m^2_{K\pi^0}) + (1 - f_B) bkg_{right}(m^2_{K\pi}, m^2_{K\pi^0})$$

- We consider the Dalitz plot distribution of the MC background in the signal region;
- We fit the MC background in the signal region using the PDF and extract f_B;
- We consider the sidebands in the data sample, construct their interpolation, and consider the background parametrization in the signal region as the sum of the two interpolations, using the fraction f_B.;

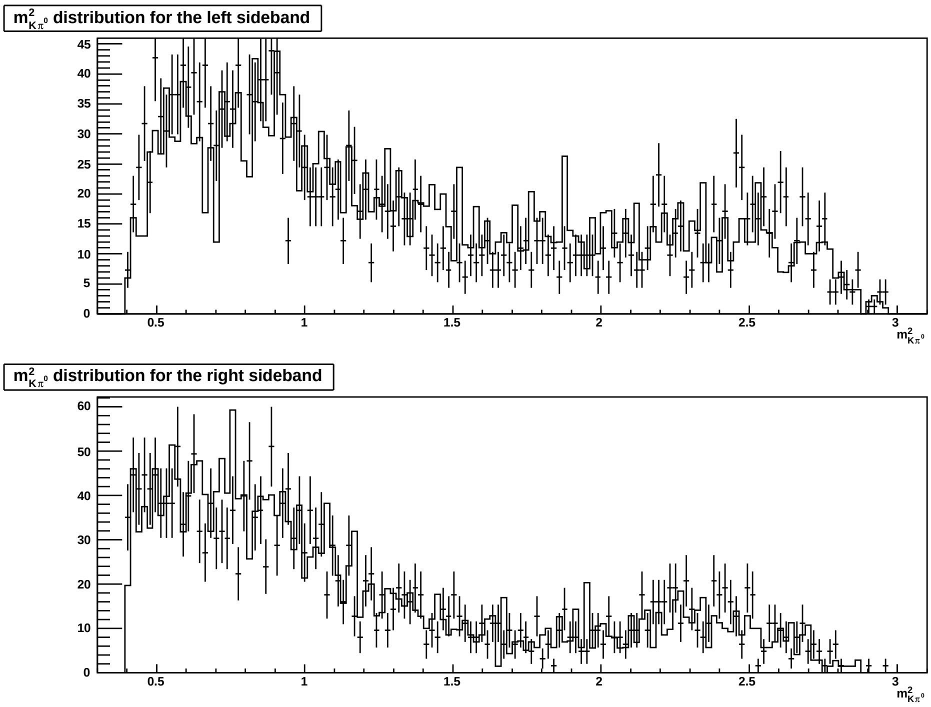

Figure 7.3: Distribution of $m^2_{K\pi^0}$ for the left and right $m_{K\pi\pi^0}$ sidebands of the RS data (dots) and MC (line). The MC distribution is normalized to the data.

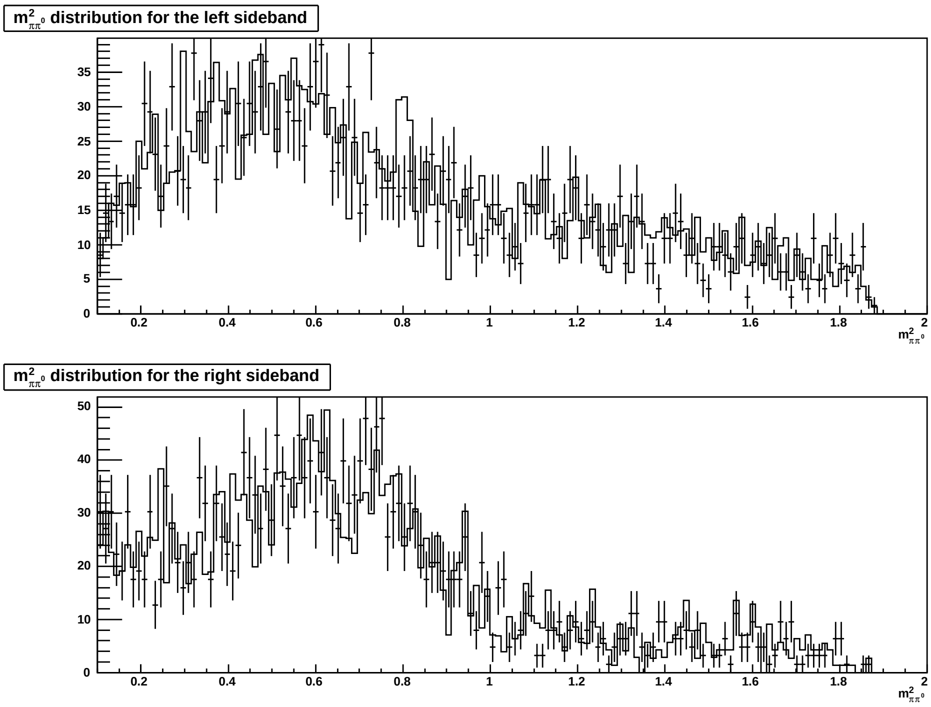

Figure 7.4: Distribution of $m^2_{\pi\pi^0}$ for the left and right $m_{K\pi\pi^0}$ sidebands of the RS data (dots) and MC (line). The MC distribution is normalized to the data.

This procedure takes into account that the behavior of the background in the signal region is a weighted sum of the behavior in the two sidebands. Since the distribution of $m^2_{K\pi}$ and $m^2_{K\pi^0}$ in the two sidebands is not very different in data and MC, we expect that the value of f_B is similar in the two cases. The fit result is

$$f_B = 0.738 \pm 0.026$$

The plot of the MC background in the signal region and of the weighted sum of the sidebands can be found in Figure 7.5.

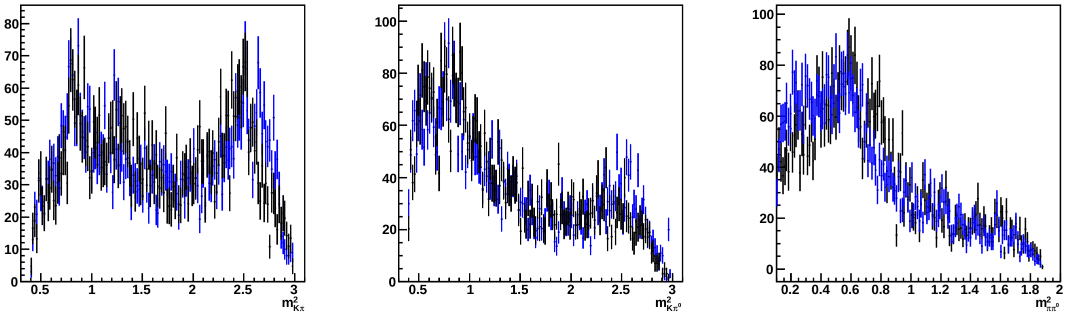

Figure 7.5: Comparison between the truth matched RS MC background in the signal region (black) and the weighted sum of the sidebands used to characterize it (blue). The $\chi^2/ndof$ for the three distributions is 1.12, 1.32 and 0.98 for $m^2_{K\pi}$,$m^2_{K\pi^0}$ and $m^2_{\pi\pi^0}$ respectively.

Since the RS sample is very pure, one may consider to cut tightly in the signal region of $m_{K\pi\pi^0}$ and Δm and fit neglecting the background contributions. This strategy would then need an estimation of the systematic error arising from this assumption. This test has been performed and can be found in Appendix A. As can be observed comparing the results in the Appendix with the nominal fit, the resonances which contribute the most to the RS Dalitz plot (i.e. the $\rho^+(770)$, the K^{*0} and the K^{*-}) are compatible with each other within the statistical error. This is a good hint that we don't need a very accurate characterization of the RS background in order to have a valid CF amplitude estimation.

7.3 Fit strategy

Using the parametrization described above, we perform a binned χ^2 fit of the RS sample. The fit is performed in 500 bins in the two invariant masses chosen to represent the Dalitz Plot, $m^2_{K\pi}$ and $m^2_{K\pi^0}$. We notice from Equation 2.31 that all the resonance amplitudes and phases can be determined up to an overall complex number. Therefore during the fit procedure we must fix the parameters of one resonance. To reduce the systematic errors, we choose to fix the resonance which contributes most, that is the $\rho^+(770)$. This also allows to easily compare the fit results with the ones obtained by other experiments, which used the same convention [34]. The $\rho^+(770)$ amplitude and phase are fixed to 1 and 0 respectively.

We select the RS data sample in the signal region of $m_{K\pi\pi^0}$ and Δm, that is in the intervals $1.8495 < m_{K\pi\pi^0} < 1.8795$ GeV/c^2 and $0.1449 < \Delta m < 0.1459$ GeV/c^2. The purity of the sample in this region is $\sim 99\%$.

Since the determination of LASS parameters from the fit leads to a non accurate error matrix (the parameters are too correlated), we let them float together with the resonance amplitudes and phases. Then we fix them and refit the other parameters.

For the Dalitz plot model, we consider all the possible spin 0, 1 and 2 resonances that may contribute to the amplitude. Among them, we consider a possible contribution from the $\rho^+(1770)$. Note that this resonance has a mass higher than the kinematical limits in the process. Nevertheless, its width is enough large to contribute to the $D^0 \to K^-\pi^+\pi^0$ Dalitz plot with its lower tail. One may also consider that the same is valid for the $\rho^+(1450)$. Since both the $\rho^+(1450)$ and $\rho^+(1770)$ are outside the kinematically allowed region, the fit is unable to distinguish between their tails. We decide to adopt the same choice as CLEO by choosing to include the $\rho^+(1770)$ only.

A parameter we can extract from the resonance amplitudes and phases is the fit fraction of a given resonance. It allows to better compare results with other experiments, as the conventions on amplitudes and phases may not always be the same. It is defined as:

$$\text{Fit fraction} = \frac{\int |a_r e^{i\delta_r} BW_r(DP)|^2 dDP}{\int |\sum_r a_r e^{i\delta_r} BW_r(DP)|^2 dDP} \tag{7.2}$$

so it is the integral of one component divided by the coherent sum of all components. Note that the sum of the fit fractions of all resonances does not generally give 100% because of interference. It is a general rule, though, that the closer the fit fraction is to 100%, the more likely is that the orbital components of the amplitude are properly described. In the general case, a fit fraction much larger than 100% may be an indication of problems in the model.

One must also consider the error on the fit fractions. In order to do so, we use the final parameters value and the covariance matrix to generate 300 sets of parameter values. For each of these sets we calculate the fit fractions and record them in histograms. The mean value of the final histogram is taken as the central value of the fit fraction, the RMS is its error. In this way, all the correlations between the fit parameters are taken into account.

7.4 Fit results

In Figure 7.6 the plot of data and fit result for the three invariant masses is shown. The corresponding results for the amplitudes and phases, the fit fractions and the LASS parameters are shown in Tables 7.2 and 7.3. We notice that the fit fraction is close to

100% , indicating that the model used to fit the Dalitz is appropriate.

Resonance	Amplitude	Phase (degrees)	Fit Fraction (%)
$\rho(770)$	1 (fixed)	0 (fixed)	63.6 ± 5.2
$K^{*-}(1680)$	4.46 ± 0.04	141.4 ± 0.7	4.0 ± 0.3
$K_2^{*-}(1430)$	0.023 ± 0.001	-147.9 ± 2.6	0.12 ± 0.01
$K_2^{*0}(1430)$	0.0408 ± 0.0008	-8.4 ± 1.1	0.51 ± 0.04
$K^{*-}(1410)$	0.16 ± 0.01	43.1 ± 4.4	0.09 ± 0.01
$K_0^{*-}(1430)$	2.28 ± 0.04	170.9 ± 0.9	2.2 ± 0.2
$K^{*-}(892)$	0.380 ± 0.001	162.1 ± 0.2	9.2 ± 0.7
$K^{*0}(1410)$	0.19 ± 0.01	-281.5 ± 2.6	0.15 ± 0.02
$K_0^{*0}(1430)$	2.67 ± 0.01	82.8 ± 0.4	7.8 ± 0.6
$K^{*0}(1680)$	5.07 ± 0.04	-40.4 ± 0.6	6.0 ± 0.5
$K^{*0}(892)$	0.399 ± 0.001	0.5 ± 0.3	9.5 ± 0.8
$\rho(1700)$	4.06 ± 0.07	152.9 ± 0.9	1.9 ± 0.2
Total fit fraction = 105%			

Table 7.2: Fit results for the RS data sample. Amplitudes, phases and fit fractions are reported.

Parameter	Value
$F_{K^{*-}}$	1.064 ± 0.031
$F_{K^{*0}}$	-1.469 ± 0.017
$R_{K^{*-}}$	0.471 ± 0.006
$R_{K^{*0}}$	0.257 ± 0.008
$a_{K^{*-}}$	15.9 ± 1.1
$a_{K^{*0}}$	0.943 ± 0.022
$\phi_{F,K^{*-}}$	-93.3 ± 2.1
$\phi_{F,K^{*0}}$	-67.6 ± 0.6
$\phi_{R,K^{*-}}$	186.8 ± 2.8
$\phi_{R,K^{*0}}$	155.3 ± 1.4
$r_{K^{*-}}$	-1.78 ± 0.17
$r_{K^{*0}}$	-3.81 ± 0.08

Table 7.3: Fit results for the LASS parameters.

As a cross-check, one may consider the previous Dalitz plot fit results obtained by the CLEO experiment [34]. Since we adopted the same phase conventions, a comparison of the amplitudes and phases should straightforward. Nevertheless, in our model the non-resonant contribution is treated inside the LASS parametrization of the $K-\pi$ S-wave. Moreover, they use a simple Breit-Wigner description for the $K-\pi$ S-wave, which is expected to be less accurate in describing scalar contributions. The results are reported in Table 7.4. If one considers only the two resonances that contribute the most (besides the ρ^+, which has fixed parameters), i.e. the K^{*-} (892) and K^{*0} (892), the results for the amplitudes and phases seem reasonably similar. It must be noted that they excluded the

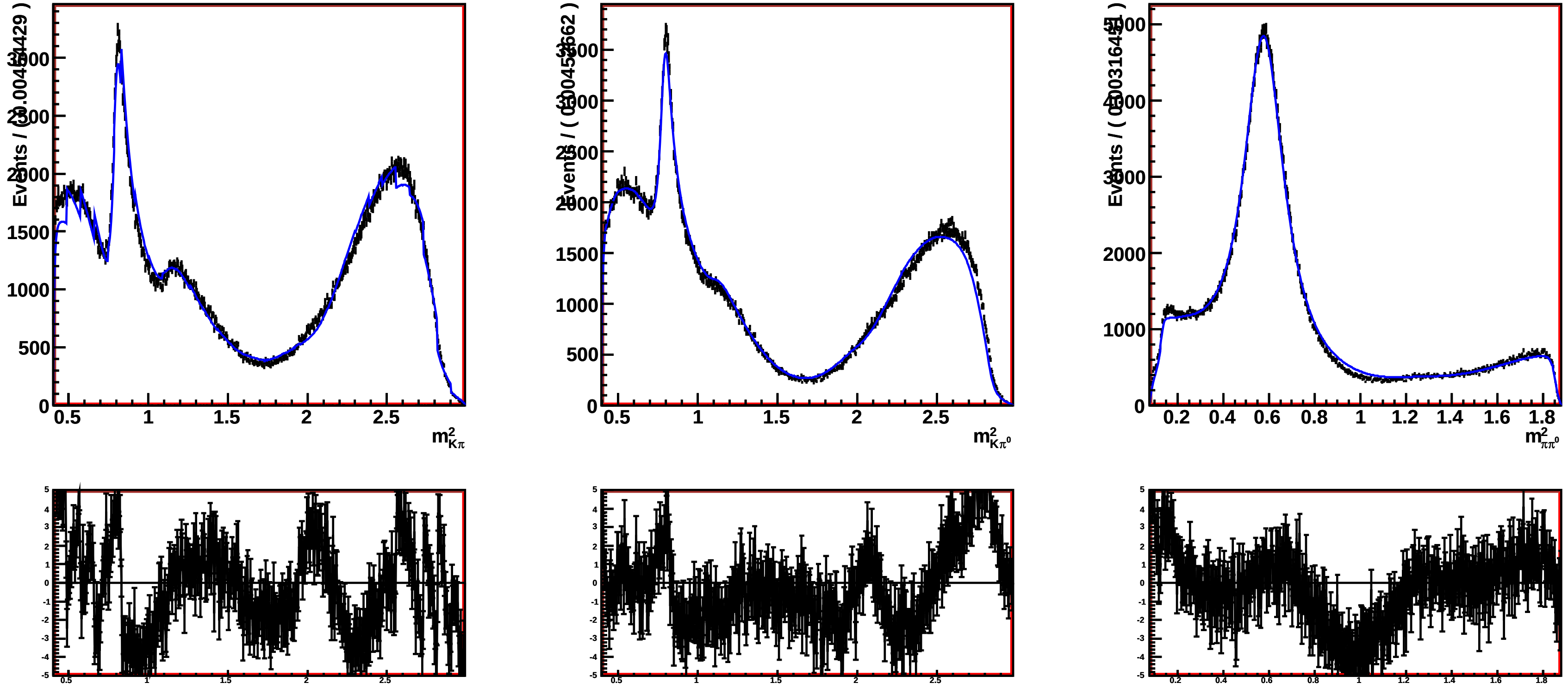

Figure 7.6: RS Dalitz plot data and fit results (top) along with the residuals of the fit (bottom). The dots are the RS data sample, the blue line is the fit result.

contributions from some resonances, whose amplitude was compatible with zero within the error.

Resonance	Amplitude	Phase (degrees)
$\rho(770)$	1 (fixed)	0 (fixed)
$K^{*-}(1680)$	2.50 ± 0.3	103 ± 8
$K_0^{*-}(1430)$	0.77 ± 0.08	55.5 ± 5.8
$K^{*-}(892)$	0.44 ± 0.01	163 ± 2.3
$K_0^{*0}(1430)$	0.85 ± 0.06	166 ± 5
$K^{*0}(892)$	0.39 ± 0.01	-0.2 ± 3.3
$\rho(1700)$	2.5 ± 0.3	171 ± 6
$NonRes$	1.75 ± 0.12	31.2 ± 4.3

Table 7.4: Fit results for the RS Dalitz plot fit of the CLEO analysis [34].

As a crosscheck of the ability of our Dalitz fit to reproduce the CLEO results we have fit the signal MC events. They were produced with this CLEO result (see Table 7.4). We have configured the fit to use the same model components with the same parameters and we obtain the results given in Table 7.5. Most of the discrepancies are related to the resonances that sit on the boundary of the Dalitz region ($K^{*-}(1680)$ and $\rho(1700)$). This may be due to an inability of the efficiency mapping to perfectly describe the boundaries of the Dalitz. In order to take this systematic into account, we consider the difference between the MC generated value of the amplitude of these two resonances, and the value extracted from the fit. We apply this discrepancy as a systematic in the WS fit.

Resonance	Amplitude	Phase (degrees)
$\rho(770)$	1 (fixed)	0 (fixed)
$K^{*-}(1680)$	2.953 ± 0.029	101.39 ± 0.61
$K_0^{*-}(1430)$	0.7801 ± 0.0074	53.98 ± 0.82
$K^{*-}(892)$	0.4494 ± 0.0010	162.41 ± 0.39
$K_0^{*0}(1430)$	0.8652 ± 0.0081	166.51 ± 0.42
$K^{*0}(892)$	0.3908 ± 0.0011	-1.41 ± 0.72
$\rho(1700)$	2.731 ± 0.063	174.12 ± 0.64
$NonRes$	1.742 ± 0.015	30.34 ± 0.41

Table 7.5: Fit results for the RS signal MC sample generated with the CLEO model.

Chapter 8

Signal resolution function

In this chapter we describe the study of the D^0 lifetime resolution properties. Due to experimental effects (detector misalignments, granularity, inefficiency among them), the lifetime of the D meson will be smeared with respect to its natural distribution.

In order to characterize the resolution function of the decay time distribution of the signal, we considered the RS sample. The RS decay $D^0 \to K^-\pi^+\pi^0$ has the same topology as our signal, so it is proper to assume that the resolution function will be the same as the $D^0 \to K^+\pi^-\pi^0$ one. Being pure and with high statistics, the RS sample allows to easily study the resolution function of a D^0 decay through a simple exponential law.

8.1 D^0 lifetime error from the reconstruction fit

In order to reject events with a poorly measured D^0 decay time, a cut on the time error σ_t is imposed for both the RS and WS samples. This error is calculated from the fit to the decay chain described in Section 4.1.4. Its magnitude is determined considering the whole covariance matrix from the fit. As explained in Section 4.1.4, we require $\sigma_t < 0.5$ ps, and this cut is taken into account in the Dalitz plot efficiency determined in Chapter 6. A plot of the RS and WS decay time error distributions is shown in Figure 8.1. As can be observed, data and MC present a substantial disagreement in the lifetime error distribution. This is mainly due to the fact that in the *BABAR* MC sample, the beamspot position simulated in any event is fixed, while in real data it is normally oscillating around the center of the beam pipe. Since the D^* candidate is constrained to be produced in the beamspot region, this difference affects the lifetime of the D^0. One can also easilier appreciate this discrepancy by looking to the ratio between data and MC; this is shown in Figure 8.2.

The mean lifetime error for data is ~ 0.43 ps, higher to the correspondent variable in a two-body decay (like $D^0 \to K^+\ \pi^-$). The D^0 vertex information is given by the charged tracks that belong to its decay. It can be demonstrated that when a vertex is determined using two tracks, the larger is the angle between the directions of the two particles the better can the vertex be determined. In $D^0 \to K^+\pi^-\pi^0$, the K^+ and π^- have a lower momentum with respect to their equivalents in $D^0 \to K^+ \pi^-$. This is due to the π^0 presence. Since the momentum of the two tracks is lower, the angle between their two directions is smaller.

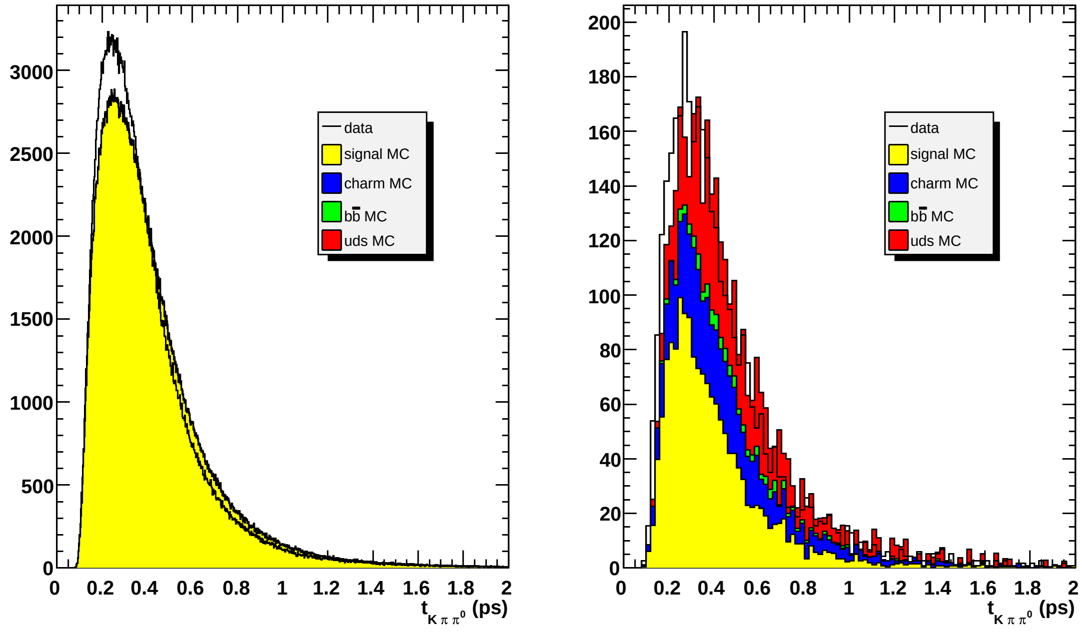

Figure 8.1: Decay time error distributions for the RS (left) and WS (right) samples. Data and the different MC contributions are shown. The samples are required to have $0.1449 < \Delta m < 0.1459$ GeV/c^2 and $1.8495 < m_{K\pi\pi^0} < 1.8795$ GeV/c^2.

A cut in σ_t can dramatically change the Dalitz plot structure, as the σ_t distribution and the $m^2_{K\pi}$ distribution are highly correlated. As said above, higher momentum tracks lead to a better vertex determination, which means lower σ_t. This is not by itself a problem, as long as the Dalitz efficiency parametrization takes this effect into account. Nevertheless problems may arise if the region which is most affected by the cut had a difficult efficiency estimation in the MC. An example of that is the region where the low-momentum π^0 s lie. In Figure 8.3 the distribution of the average σ_t along the Dalitz can be seen. One can note that the region most affected by the σ_t cut is the high-momentum π^0 s, which is expected to be well simulated. The region where low momentum π^0's lie is not affected by this cut.

Another important property to study is the dependence of the mean value of the D^0 lifetime on the Dalitz Plot. Is is also necessary to see if the lifetime has any evident offset in a particular region of the Dalitz plot. For this reason we consider the average distribution of the pull of D^0 lifetime over the Dalitz plot, i.e.

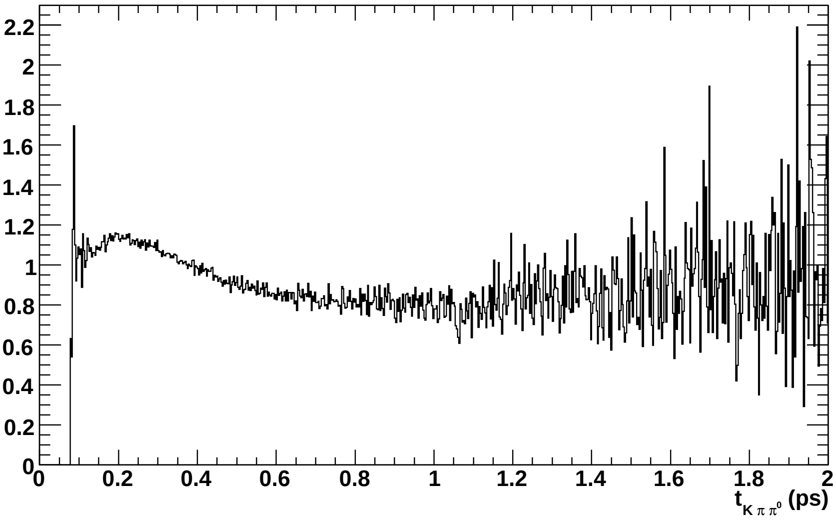

Figure 8.2: Data/MC ratio for the decay time error distribution of the RS sample. The samples are required to have $0.1449 < \Delta m < 0.1459$ GeV/c^2 and $1.8495 < m_{K\pi\pi^0} < 1.8795$ GeV/c^2.

$$pull = \frac{t_{D^0} - \tau_{PDG}}{\sigma_{t_{D^0}}} \tag{8.1}$$

where $\tau_{PDG} = 410.1 \pm 1.5$ (ps) [37].

The plot for this quantity is shown in Figure 8.4. It can be observed that no particular structure is evident on the Dalitz plot. Hence, no variation of the pull distribution is expected along the Dalitz plot. It is interesting also to look at the plot of the mean pull distribution in bins of $m^2_{K\pi}$. Since the resolution is strongly connected to the $K - \pi$ vertex, it is important to check that the pull does not depend on the $K - \pi$ momentum. This is shown in Figure 8.5.

We also consider the plot of $t_{D^0} - \tau_{PDG}$, shown in Figure 8.6. It can be noted that there is no evident dependence on the Dalitz plot position, but a general offset for negative values of the D^0 lifetime is observed. This suggests that it may be appropriate to consider an offset in the resolution function.

8.2 Signal resolution function parametrization

To parametrize the signal PDF of the RS decay time, we consider an exponential function convolved with a Gaussian resolution function.

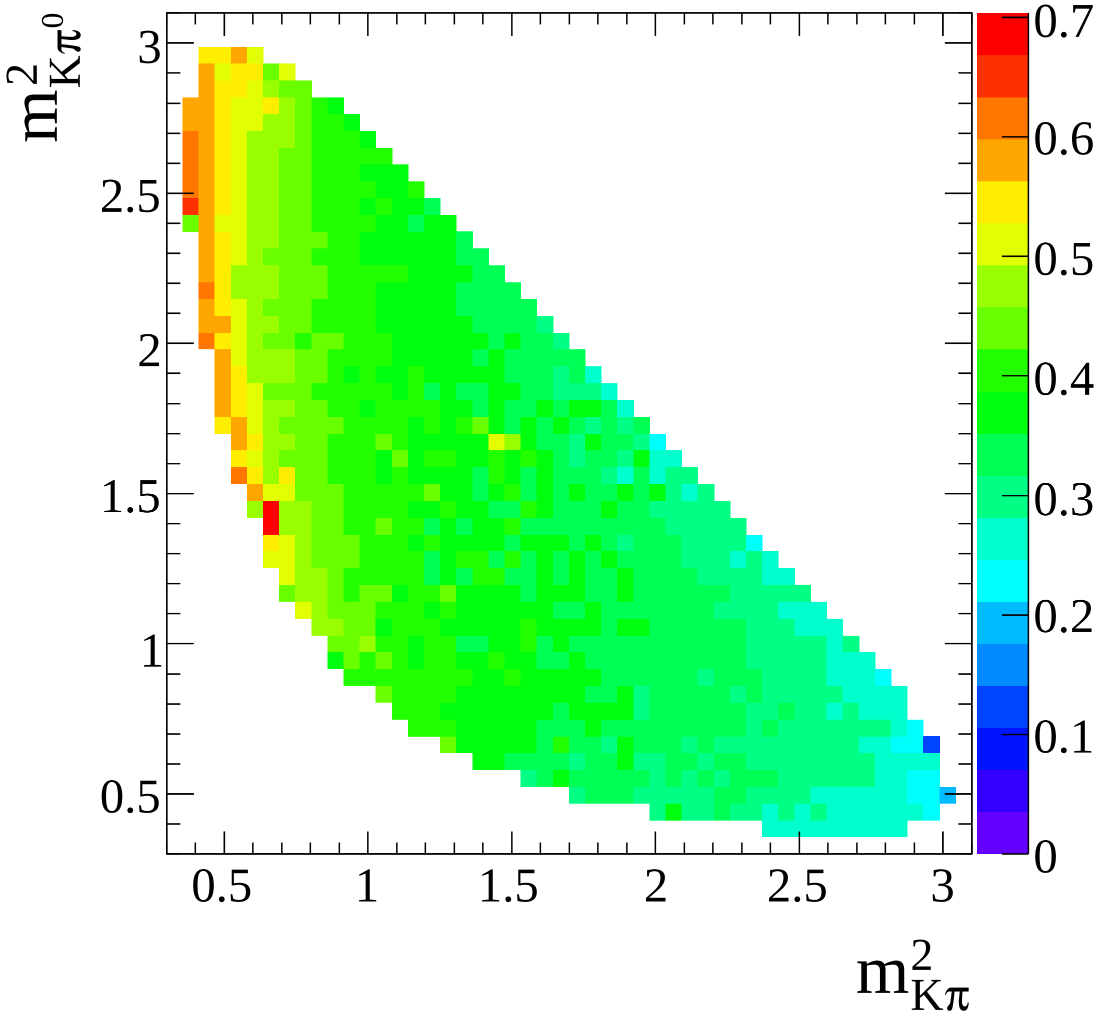

Figure 8.3: Average σ_t on the Dalitz plot of $m^2_{K\pi}$ and $m^2_{K\pi^0}$ for the RS sample. The scale is in ps. The samples are required to have $0.1449 < \Delta m < 0.1459$ GeV/c^2 and $1.8495 < m_{K\pi\pi^0} < 1.8795$ GeV/c^2.

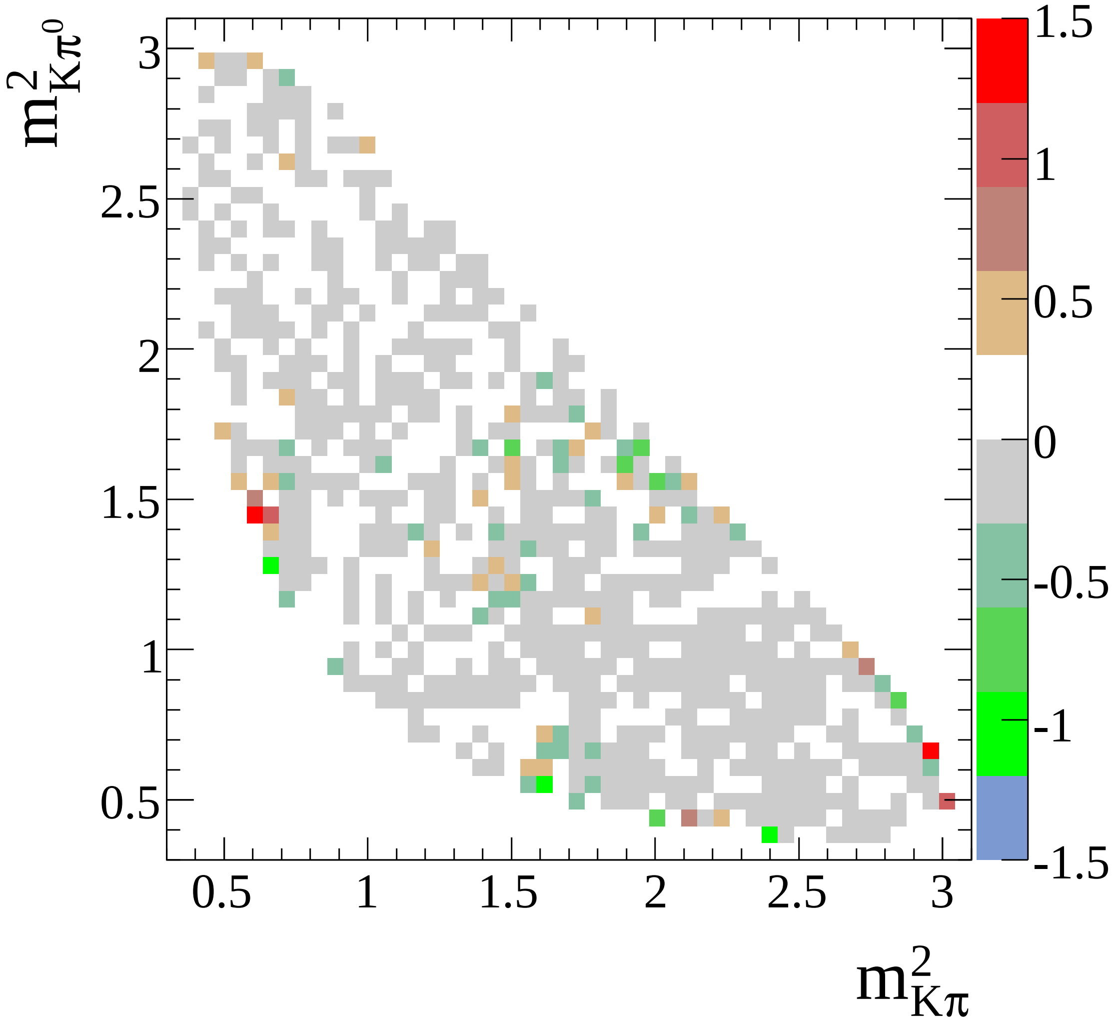

Figure 8.4: Average pull of the D^0 lifetime on the Dalitz plot of $m^2_{K\pi}$ and $m^2_{K\pi^0}$ for the RS sample. The samples are required to have $0.1449 < \Delta m < 0.1459$ GeV/c^2, $1.8495 < m_{K\pi\pi^0} < 1.8795$ GeV/c^2 and $\sigma_t < 0.5$ (ps).

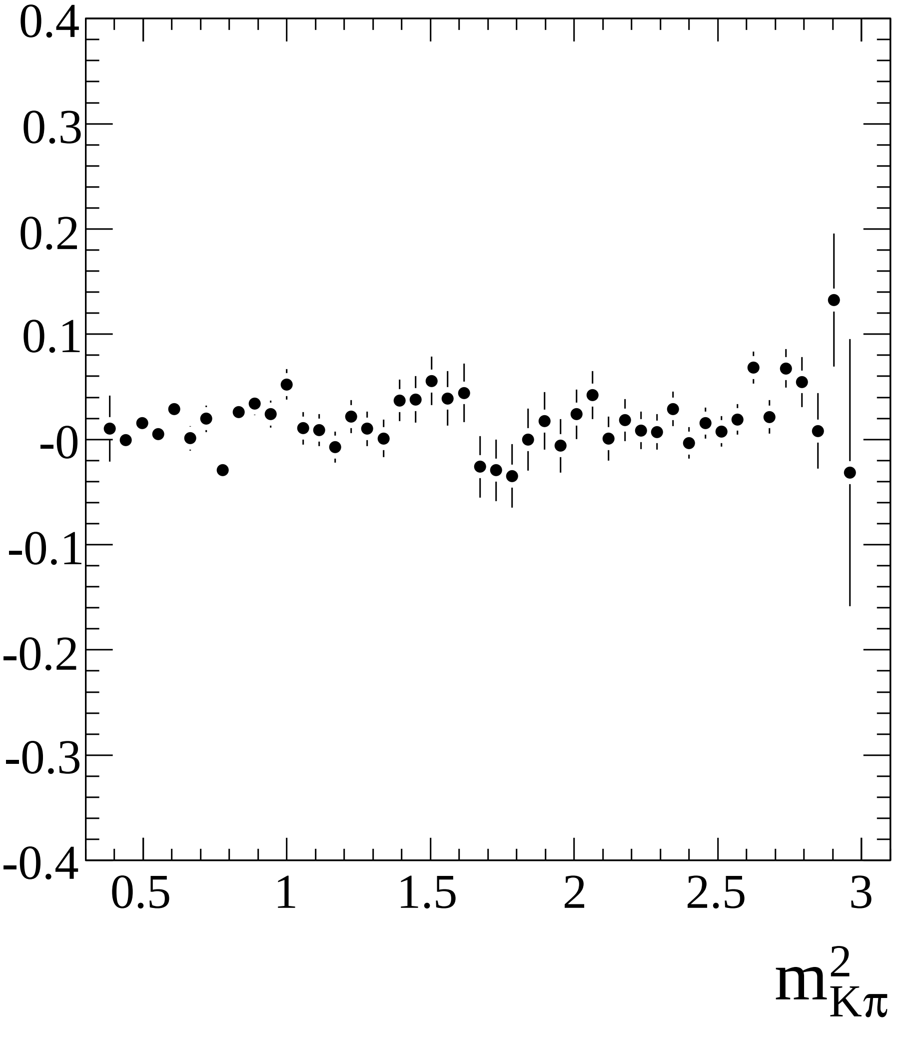

Figure 8.5: Average pull of the D^0 lifetime in bins of $m^2_{K\pi}$ for the RS sample. The scale is in ps. The samples are required to have $0.1449 < \Delta m < 0.1459$ GeV/c^2,$1.8495 < m_{K\pi\pi^0} < 1.8795$ GeV/c^2 and $\sigma_t < 0.5$ (ps).

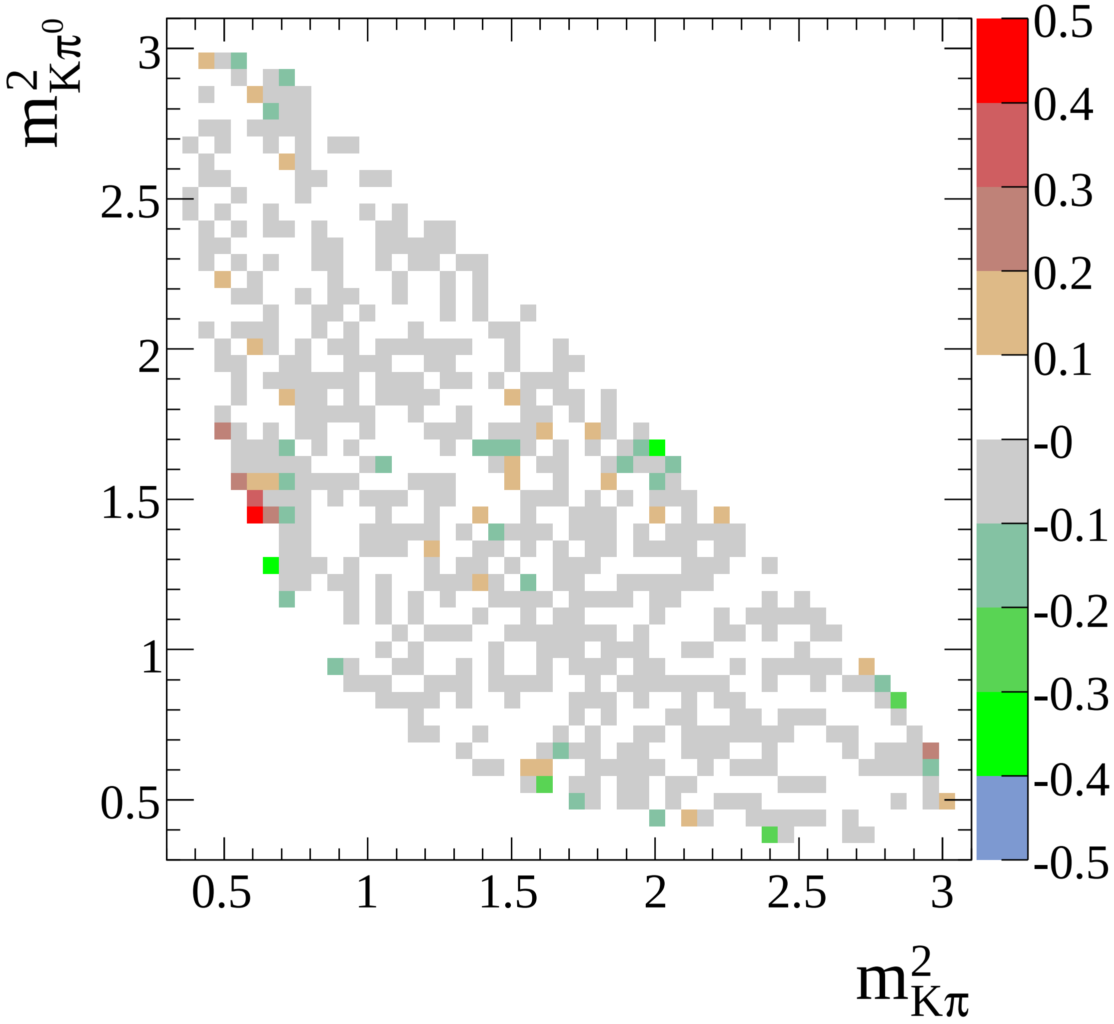

Figure 8.6: Average $t_{D^0} - \tau_{PDG}$ on the Dalitz plot of $m^2_{K\pi}$ and $m^2_{K\pi^0}$ for the RS sample. The scale is in ps. The samples are required to have $0.1449 < \Delta m < 0.1459$ GeV/c^2, $1.8495 < m_{K\pi\pi^0} < 1.8795$ GeV/c^2 and $\sigma_t < 0.5$ (ps).

$$\rho_{RS,i}(t;\tau,k) = e^{-\frac{t}{\tau}} \otimes e^{-\frac{(t-t_0)^2}{2(k\sigma_i)^2}} \tag{8.2}$$

This PDF explicitly depends on the event measured errors on the D^0 decay time σ_i. The parameter k specifies the resolution model. This is a scale factor of order $\approx O(1)$. It takes into account that, even though the event uncertainties are relatively accurate, they may be under or overestimated by a global scale factor. t_0 is the offset introduced in the resolution function, justified by Figure 8.6. We allow the contribution of three different resolution models. This is the same parametrization of the resolution function chosen in all the *BABAR* charm mixing analyses. The complete signal PDF is:

$$P_{RS,i}(t) = f_1 \cdot \rho_{1,i} + (1-f_1) \cdot [f_2 \cdot \rho_{2,i} + (1-f_2)\rho_{3,i}] \tag{8.3}$$

with

$$\begin{aligned} \rho_{1,i} &= \rho_{RS,i}(t;\tau,k_1) \\ \rho_{2,i} &= \rho_{RS,i}(t;\tau,k_2) \\ \rho_{3,i} &= \rho_{RS,i}(t;\tau,k_3) \end{aligned} \tag{8.4}$$

As explained for Equation 5.4, this recursive parametrization of the fractions of each component in the total PDF is numerically more stable.

Note that the fractions $f_{1,2}$ and the scale factors $k_{1,2,3}$ are very correlated. A change in the scale factor can be balanced by an appropriate change in the normalization of the Gaussian, which affects the fraction, obtaining the same PDF.

8.3 RS background parametrization

We select the signal region of the RS sample by requiring $0.1449 < \Delta m < 0.1459$ GeV/c^2 and $1.8495 < m_{K\pi\pi^0} < 1.8795$ GeV/c^2 . The mistag background is fitted with the same PDF as signal, since its temporal distribution is expected to be the same. The combinatoric and *bad-*D^0 backgrounds are treated as a whole. The method used for their estimation is similar to the one used in Section 7.2. We consider the left and right sidebands of the $m_{K\pi\pi^0}$ distribution, defined in 7.1 in the signal region of Δm. We merge the two distributions of the D^0 lifetime according to the different fractions of background in the $m_{K\pi\pi^0}$ and Δm fit. We consider this as a representation of the background in the signal region. To test this method we applied it to the MC sample, and compared it with the background in the signal region obtained using the MC information. The plot of the background and of its estimation from the sidebands can be found in Figure 8.7. We notice a discrepancy, that will be taken into account in the systematics determination (see Section 12.2.4).

In Appendix C, we perform the same fit described in this chapter, ignoring any background contribution. We find values of the resolution function compatible with the values found in the nominal fit described here. This is a good hint of the fact that the background is so tiny that an extremely precise description of it is not necessary.

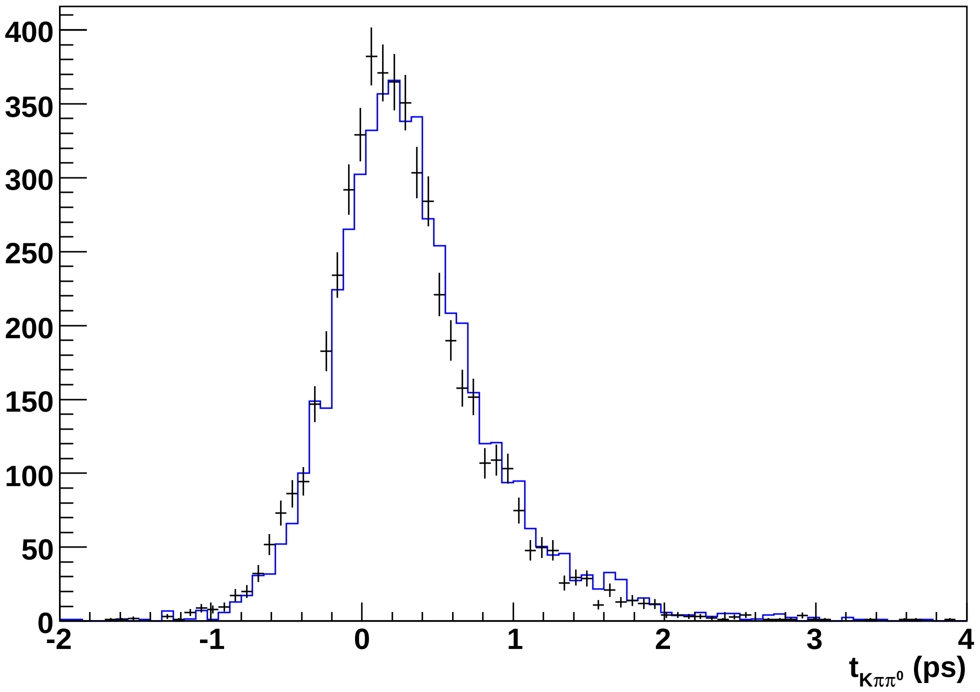

Figure 8.7: RS sample: comparison between the MC background sample (dots), selected using the MC truth, and the background estimation from the sidebands (blue histogram) for the D^0 lifetime. The $\chi^2/ndof$ of the two histograms is 0.98.

The number of events in each background category is determined from the $m_{K\pi\pi^0}$ and Δm fit.

8.4 Fit results

Since the scale factors k and the Gaussian fractions f are very correlated, after the fit has converged we fix the scale factors and refit. This is done to allow an accurate error matrix. The fit results are reported in Table 8.1. The corresponding plot is in Figure 8.8. The D^0 mean lifetime is compatible with the PDG value within the error.

We observe than even though the offset is very small, it is not negligible. It has several different origins: tracking system misalignments and selection criteria are the two main components. The detector performance may differ in different regions of the acceptance. For this reason, we split the RS sample in bins of the polar angle θ and the azimuthal

Parameter	Value
f_1	0.0052 ± 0.0005
f_2	0.179 ± 0.049
t_0	0.0042 ± 0.0007 (ps)
τ	0.4099 ± 0.0009 (ps)
k_1	3.20 ± 0.48
k_2	1.42 ± 0.08
k_3	0.94 ± 0.01

Table 8.1: Fit results for the RS time distribution

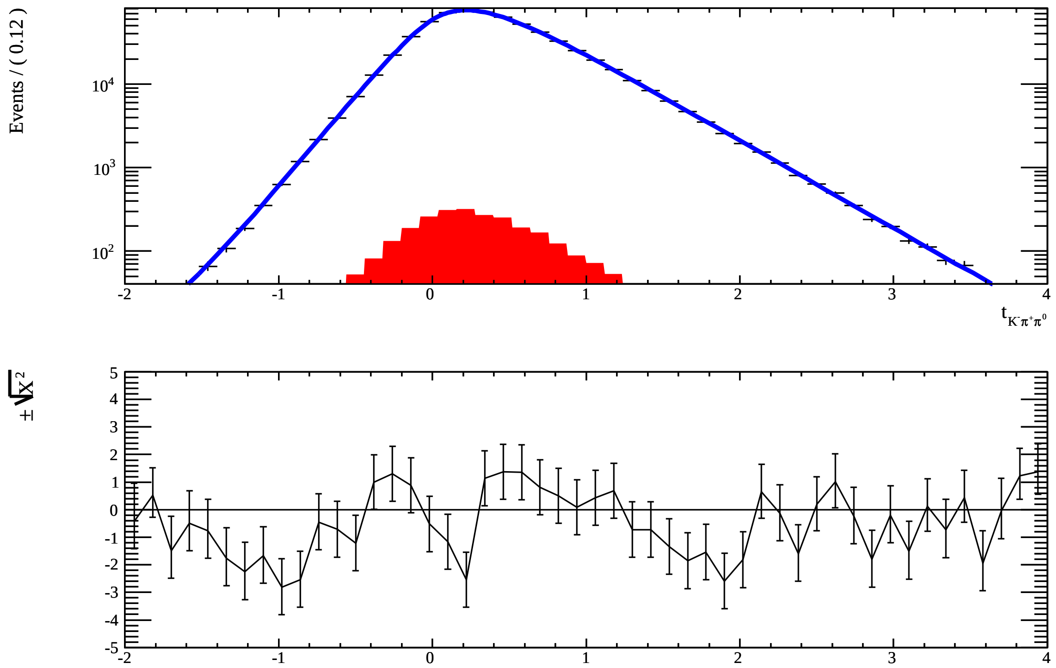

Figure 8.8: Plot of the RS decay time distribution (dots) and its fit (blue line) in a logarithmic scale. The red plot represents the combinatoric and *bad-*D^0 background contributions. On bottom, the $\pm\sqrt{\chi^2}$ of the fit is shown.

angle ϕ of the D^0 momentum in the CM frame. We fit the same resolution function in those bins. We consider 12 divisions in ϕ and 4 divisions in θ. In Tables 8.2 and 8.3 we report the value of t_0 as extracted from the fits in bins of ϕ and θ respectively. A plot of t_0 as a function of the azimuthal angle is shown in Figure 8.9. The lifetime resolution function parameters are reasonably compatible within the different bins of θ and ϕ, for this reason we do not differentiate the resolution function in bins of the two angles.

Bin in ϕ(deg)	t_0 value (ps)
$-180 < \phi < -150$	0.0034 ± 0.0029
$-150 < \phi < -120$	0.0018 ± 0.0026
$-120 < \phi < -90$	0.0134 ± 0.0027
$-90 < \phi < -60$	0.0043 ± 0.0026
$-60 < \phi < -30$	0.0030 ± 0.0028
$-30 < \phi < 0$	0.0027 ± 0.0028
$0 < \phi < 30$	0.0001 ± 0.0027
$30 < \phi < 60$	-0.0016 ± 0.0023
$60 < \phi < 90$	0.0074 ± 0.0023
$90 < \phi < 120$	0.0104 ± 0.0023
$120 < \phi < 150$	-0.0010 ± 0.0025
$150 < \phi < 180$	0.0022 ± 0.0028

Table 8.2: Values of the offset t_0 in different ϕ bins.

Bin in θ(rad)	t_0 value (ps)
$0.3 < \theta < 0.8$	0.0062 ± 0.0016
$0.8 < \theta < 1.3$	0.0042 ± 0.0011
$1.3 < \theta < 1.8$	-0.0007 ± 0.0015
$1.8 < \theta < 2.5$	0.0094 ± 0.0034

Table 8.3: Values of the offset t_0 in different θ bins.

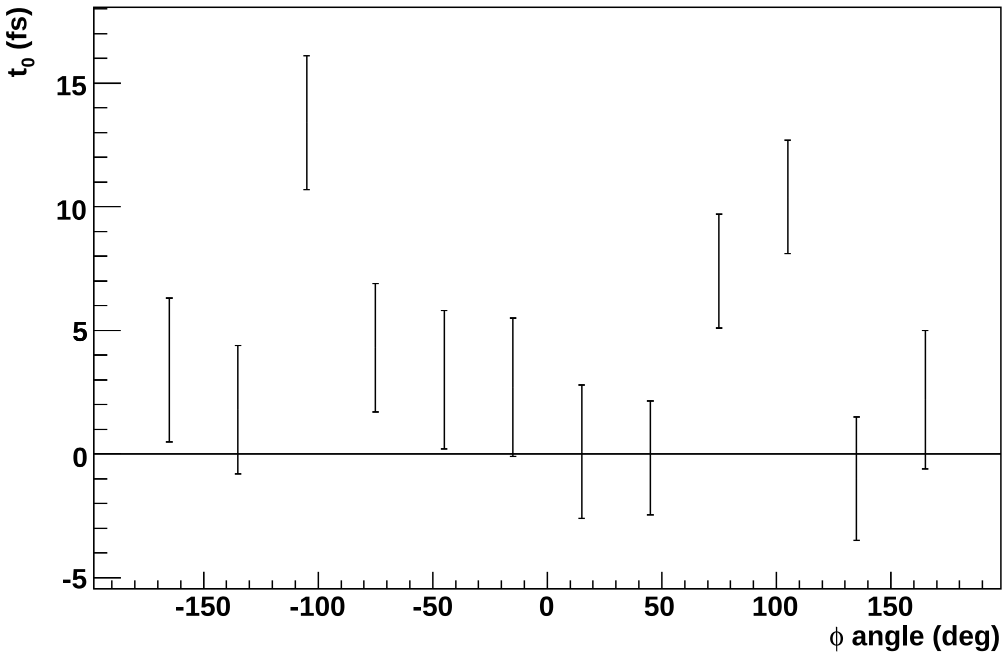

Figure 8.9: Plot of t_0 as a function of the azimuthal angle ϕ.

Chapter 9

Description of the WS time-dependent Dalitz plot fit

In this chapter, we describe the main features of the parametrization of signal and background in the time-dependent Dalitz plot fit of the WS sample. One of the main innovations of this work, besides the amplitude analysis, is the identification of a different base of the mixing parameters in which mixing effects are more visible. This both eases up the fit procedure and gives larger sensitivity.

9.1 Signal parametrization

Equation 2.30 shows that we can extract both x' and y' performing a time-dependent Dalitz fit of the WS sample. In general, one could fit the data and determine x', y', r_0 and the $2n-2$ amplitudes and phases simultaneously. However, one can factorize a r_0^2 term our of Equation 2.30, and absorb it into the normalization of the PDF.

The differential decay rate will be described by the following PDF

$$\begin{aligned} PDF_{sig}(m_{12}^2, m_{13}^2, t) &= \\ &= \frac{1}{N} \cdot e^{-\Gamma t} \Big[|A_{\bar{f}}^{DCS}(m_{12}^2, m_{13}^2)|^2 + \Big(c_1 \Re(A^{*DCS}_{\bar{f}}(m_{12}^2, m_{13}^2) \bar{A}_{\bar{f}}^{CF}(m_{12}^2, m_{13}^2)) \\ &\quad -c_2 \Im(A^{*DCS}_{\bar{f}}(m_{12}^2, m_{13}^2) \bar{A}_{\bar{f}}^{CF}(m_{12}^2, m_{13}^2)) \Big) (\Gamma t) \\ &\quad + \frac{c_1^2 + c_2^2}{4} |\bar{A}_{\bar{f}}^{CF}(m_{12}^2, m_{13}^2)|^2 (\Gamma t)^2 \Big] \end{aligned} \tag{9.1}$$

where

$$c_1 = \frac{y'}{r_0} \text{ and } c_2 = \frac{x'}{r_0}$$

.

N is a normalization coefficient such that:

$$\iiint PDF_{sig}(m_{12}^2, m_{13}^2, t) dt dm_{12}^2 dm_{13}^2 = 1 \tag{9.2}$$

One can notice that in presence of mixing c_1 and c_2 must be different from zero. The parametrization in Equation 9.1 has two main advantages with respect to the *standard* mixing rate parametrization shown in Equation 2.30:

1. This PDF leads to a much more stabler fit, as there is one less parameter to be determine. This lowers the errors and the correlation among the remaining parameters;
2. c_1 and c_2 are more sensitive to mixing with respect to x' and y', because the uncertainty on r_0 is left out.

Since the parameters of interest for combining the results on mixing are x' and y', our final goal remains to extract them. Knowing c_1 and c_2 from the fit result, we will then extract x' and y' using the correlation matrix from the fit (see Section 11.2.2).

The amplitude for the DCS transition $A_{\bar{f}}^{DCS}$ can in general be expressed as a superposition of n_{DCS} isobar component as for the CF transition (see Section 2.31):

$$A_{\bar{f}}^{DCS} = \frac{\sum_{i=1}^{n_{DCS}} a_i e^{i\delta_i} A_i(m_{12}^2, m_{13}^2)}{\sqrt{\int dm_{12}^2 dm_{13}^2 |\sum_{i=1}^{n_{DCS}} a_i e^{i\delta_i} A_i(m_{12}^2, m_{13}^2)|^2}} \tag{9.3}$$

where a_i and δ_i [1] are the isobar coefficients and phases that are extracted from the data along with c_1 and c_2. In general, they are different for the DCS transition with respect to the CF. The a_i and δ_i for the $\bar{A}_{\bar{f}}^{CF}$ are taken from the previous fit to the RS sample and are held fixed in the fit to the WS sample. Table 9.1 shows the main properties of the resonances chosen to describe the DCS amplitude. To parametrize the $K_0^{*+}(1430)$ and $K_0^{*0}(1430)$ lineshapes, we use again the LASS parametrization described in Section 2.5. The values of the parameters F, R, r, a and ϕ are fixed to the values obtained from the RS fit.

We must notice that the normalization N in Equation 9.1 can be evaluated partly analytically and partly numerically. The integral in the D^0 lifetime variable can be done analytically. The integral over the Dalitz plot can be done numerically with simple numerical observations.

It can be demonstrated that N depends on the integral of bilinear products of the isobar components

---

[1] In general a_i and δ_i can be different for f and $\bar{f}$ if direct *CP* violation is allowed. We completely neglect direct CPV in this analysis.

Resonance	J^{PC}	Mass (GeV/c^2)	Width (GeV/c^2)
$\rho^-(770)$	1^{--}	0.7755 ± 0.0004	0.1494 ± 0.001
$\rho^-(1700)$	1^{--}	1.720 ± 0.020	0.250 ± 0.100
$K^{*+}(892)$	1^-	0.89166 ± 0.000026	0.0508 ± 0.009
$K_0^{*+}(1430)$	0^+	1.414 ± 0.006	0.290 ± 0.021
$K^{*0}(892)$	1^-	0.89600 ± 0.00025	0.0503 ± 0.006
$K_0^{*0}(1430)$	0^+	1.414 ± 0.006	0.290 ± 0.021
$K_2^{*0}(1430)$	2^+	1.4324 ± 0.0013	0.109 ± 0.005

Table 9.1: Summary of the Dalitz plot contributions considered in the DCS amplitude.

$$I_{ij} = \int\int A_i(m_{12}^2, m_{13}^2) A_j^*(m_{12}^2, m_{13}^2) dm_{12}^2 dm_{13}^2 \qquad (9.4)$$

The I_{ij} integrals can be evaluated using a numerical integration on a grid of points over the Dalitz plot. In the case when the parameters describing the shapes of the functions (mass and width of the resonances) are constant, these values can be cached, as they do not vary during the fit.

Consider the integrals:

$$\begin{aligned}
I_1 &= \iint |A_{\bar{f}}^{DCS}(m_{12}^2, m_{13}^2)|^2 dm_{12}^2 dm_{13}^2 & (9.5)\\
I_2 &= \iint \Big(c_1 \Re(A^*{}_{\bar{f}}^{DCS}(m_{12}^2, m_{13}^2) \bar{A}_{\bar{f}}^{CF}(m_{12}^2, m_{13}^2)) \\
&\quad - c_2 \Im(A^*{}_{\bar{f}}^{DCS}(m_{12}^2, m_{13}^2) \bar{A}_{\bar{f}}^{CF}(m_{12}^2, m_{13}^2)) \Big) dm_{12}^2 dm_{13}^2 & (9.6)\\
I_3 &= \iint |\bar{A}_{\bar{f}}^{CF}(m_{12}^2, m_{13}^2)|^2 dm_{12}^2 dm_{13}^2 & (9.7)
\end{aligned}$$

In terms of these integrals, we find:

$$\iiint PDF_{sig}(m_{12}^2, m_{13}^2, t) dt dm_{12}^2 dm_{13}^2 = \frac{1}{N} \cdot e^{-\Gamma t} \left[I_1 + I_2 r_0 \Gamma t + I_3 \frac{c_1^2 + c_2^2}{4} (\Gamma t)^2 \right] \qquad (9.8)$$

Using Equation 9.4, I_2 can be written in terms of the I_{ij} integrals:

$$\begin{aligned}
I_2 &= \frac{c_1}{2} \Re(\sum_{ij}^{n_{DCS} n_{CF}} a_i^{DCS} a_j^{CF} e^{i\delta_i^{DCS}} e^{i\delta_j^{CF}} I_{ij}) \\
&\quad + \frac{c_2}{2} \Im(\sum_{ij}^{n_{DCS} n_{CF}} a_i^{DCS} a_j^{CF} e^{i\delta_i^{DCS}} e^{i\delta_j^{CF}} I_{ij}) & (9.9)
\end{aligned}$$

Only events on the signal region of the $\{m_{K\pi\pi^0}, \Delta m\ \}$ distribution (as defined by Equation 5.8) enter the dataset that is fit to extract the signal parameters.

The number of signal and background events is fixed in the fit to the number in Tab.5.3. The statistical error on these event yields are accounted for in the systematics uncertainty evaluation. Having less background events in the final sample simplifies in fact the extraction of the Dalitz model parameters.

9.2 WS background parametrization

Since the WS sample is affected by a high level of background, it is necessary to parametrize it both on the Dalitz plot and in the D^0 lifetime component. The mistag background is very easy to parametrize: since it is composed of RS D^0 decays associated to an uncorrelated $\pi_s^\pm$ with an opposite charge, we can use the RS data sample to parametrize both the Dalitz plot and the lifetime distribution. We then construct a three dimensional histogram from the RS data. This allows our parametrization to take into account any possible correlation between the RS Dalitz plot and the RS D^0 decay time. Since the RS sample has very high statistics, the three dimensions histogram retains enough events in each bin. Alternatively, one could use the RS Dalitz plot fit result obtained in Section 7.4, along with a simple exponential parametrization as the one used in Section 8.4 for the temporal dependence. Though this would be correct, it would also introduce a systematic error due to the parametrization chosen.

The combinatorial and *bad-*D^0 backgrounds require more study. We consider the contribution of the two categories to this background together. In order to estimate it we consider the left and right sidebands of $m_{K\pi\pi^0}$ distribution, defined in Section 7.1. The two samples are taken in the signal region of the Δm distribution. This avoids to underestimate the *bad-*D^0 contribution. The distribution of this background in the three invariant masses and of the lifetime is shown in Figures 9.1-9.4 for both data and MC. Though the MC describes the data in many regions reasonably well, some discrepancies emerge. For this reason, we do not use the MC information for the background parametrization.

In order to estimate this background we consider the left and right sideband distributions of data and construct a three dimensional histogram-based PDF in $m^2_{K\pi}$, $m^2_{K\pi^0}$ and the D^0 lifetime. In this way, any correlation between the Dalitz plot and the lifetime is preserved. The distribution of the right sideband is normalized to that of the left one. This normalized three dimensional histogram-based PDF is used as a parametrization for the background in the signal region. An alternative way to describe the WS background is presented in Appendix B.

It is also interesting to look at the background time dependence. In order to do this, we plot the two invariant masses $m^2_{K\pi}$ and $m^2_{K\pi^0}$ for the background histogram description in five bin of time (Figure 9.5). No difference in the Dalitz plot projections emerges in the five bins.

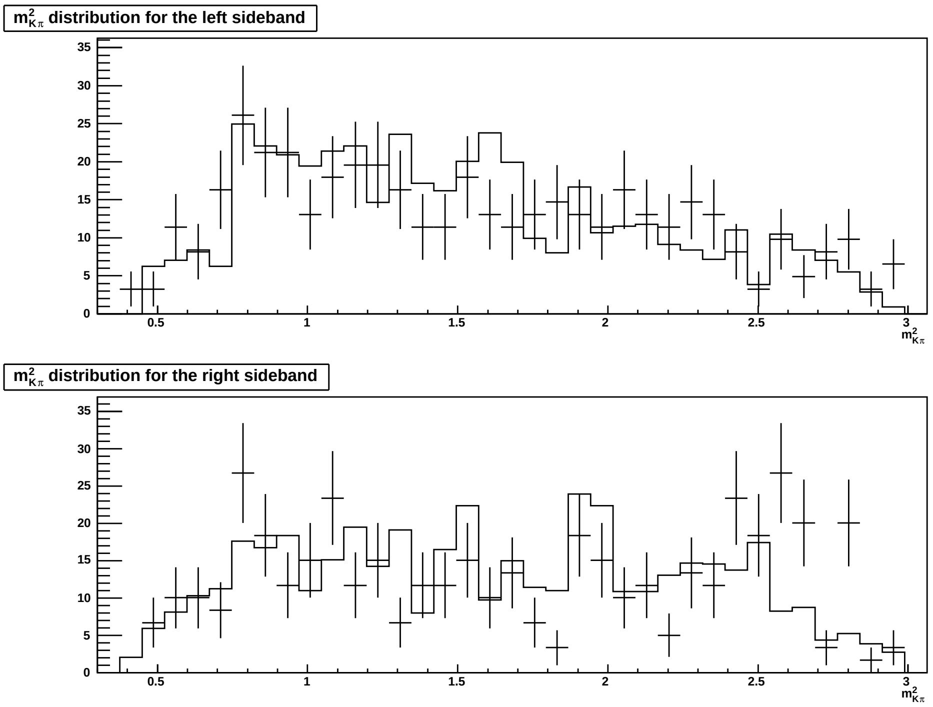

Figure 9.1: Distribution of $m^2_{K\pi}$ for the left and right $m_{K\pi\pi^0}$ sidebands of the WS data (dots) and MC (line).

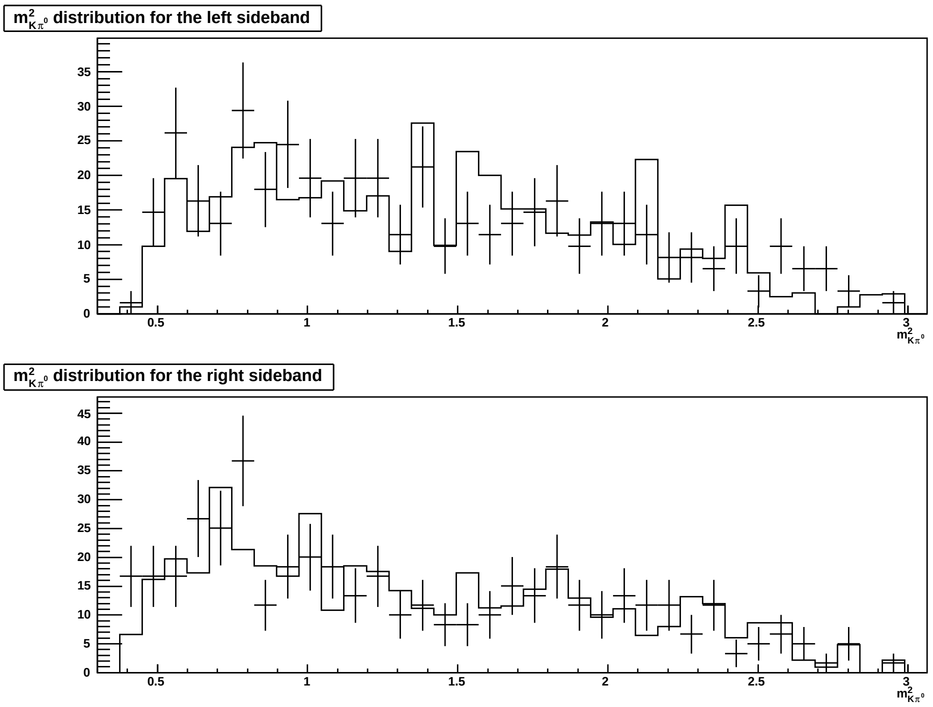

Figure 9.2: Distribution of $m^2_{K\pi^0}$ for the left and right $m_{K\pi\pi^0}$ sidebands of the WS data (dots) and MC (line).

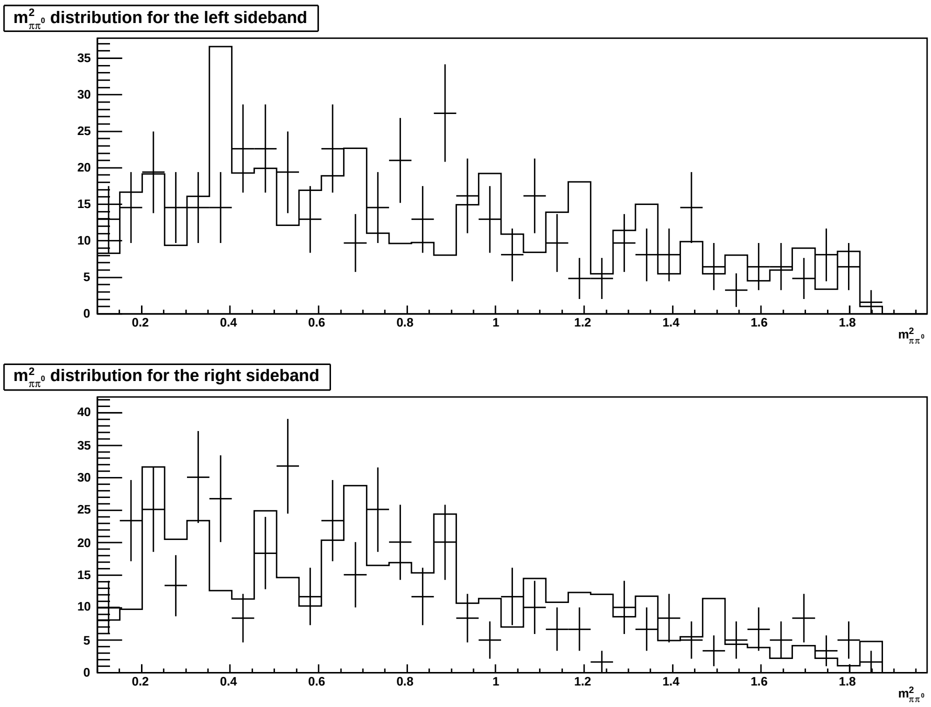

Figure 9.3: Distribution of $m^2_{\pi\pi^0}$ for the left and right $m_{K\pi\pi^0}$ sidebands of the WS data (dots) and MC (line).

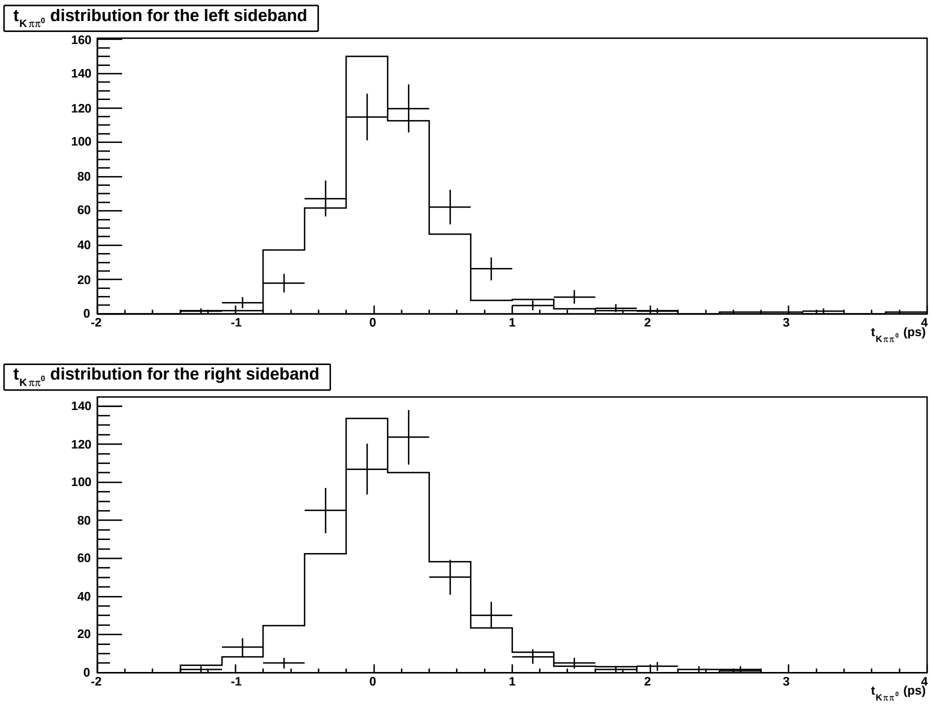

Figure 9.4: Distribution of the D^0 lifetime for the left and right $m_{K\pi\pi^0}$ sidebands of the WS data (dots) and MC (line).

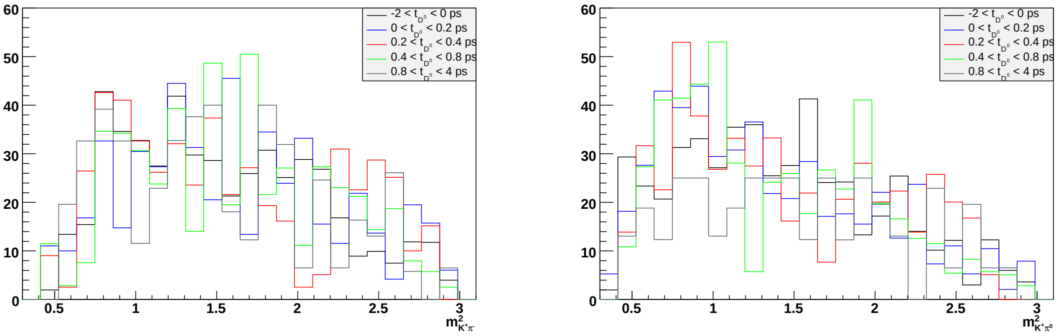

Figure 9.5: Comparison of WS Dalitz plot background description in five different bins of D^0 lifetime for $m^2_{K\pi}$ (left) and $m^2_{K\pi^0}$ (right). All the histograms are normalized to the first bin of time ($-2 < t_{D^0} < 0$ ps).

9.2.1 Test the absence of $D^+ \to K^+\ \pi^+\ \pi^-$

One possible source of background in the *bad-*D^0 category is the decay channel

$$\begin{aligned} D^{*+} \to \quad & D^+ \quad \pi^0 \\ & \to \quad K^+\pi^+\pi^- \end{aligned} \tag{9.10}$$

This channel may be easily mistaken for signal if the π^0 is swapped with a charged pion of the D^+ decay. This process would represent a problematic structure in the WS background, having a peculiar Dalitz plot structure. Moreover, since the D^+ has a long lifetime it would be present in the far regions of the D^0 lifetime background, where the mixing signal should be more evident. To test the contribution of this decay mode, we generated $3.5 \cdot 10^5$ MC events reproducing this decay, corresponding to ~ 400 fb^{-1}. The MC is produced with a phase-space amplitude. Looking at the previous analyses of this Dalitz plot [38] this approximation is enough accurate to estimate the efficiency of our reconstruction against this particular background. We applied the selection described in Section 4.1. Zero events are observed for the WS sample, and 2 for the RS. We make the request that if both a RS and a WS D^0 are found in event, and they share the $\pi^\pm_s$, the WS D^0 is discarded. Since both the π^+ and the π^- from the D^+ decay have the same probability to be assigned the $\pi^\pm_s$ hypothesis, the selection on the best candidate only retains the RS candidate.

9.2.2 Validation of the mistag background description

To test if the RS data appropriately describe the WS mistag, we analyze the MC sample. We compare the RS MC sample with the MC WS mistag. The plots are shown in Figures 9.6-9.9. We observe that the behavior of the two samples is reasonably similar.

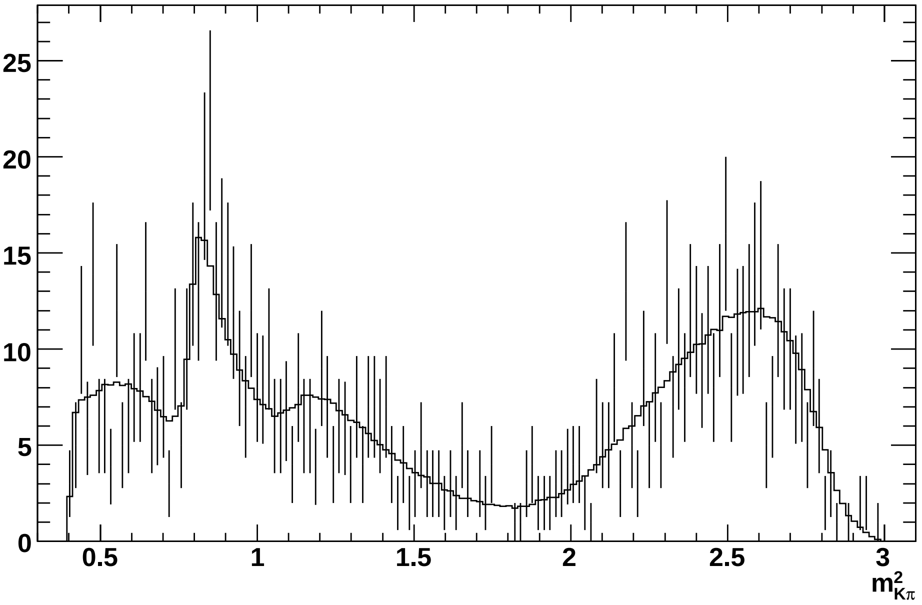

Figure 9.6: Comparison between the MC WS mistag sample (dots), selected using the MC, and the RS MC sample (solid histogram) for the $m^2_{K\pi}$ invariant mass. Both samples are considered in the signal region of $\{m_{K\pi\pi^0}$,Δm $\}$. We observe a $\chi^2/ndof = 0.99$.

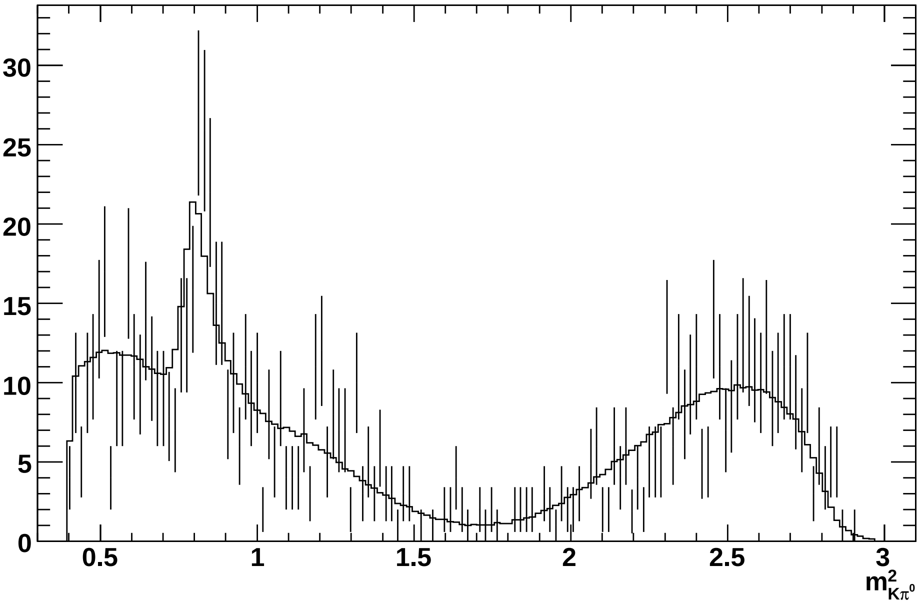

Figure 9.7: Comparison between the MC WS mistag sample (dots), selected using the MC, and the RS MC sample (solid histogram) for the $m^2_{K\pi^0}$ invariant mass. Both samples are considered in the signal region of $\{m_{K\pi\pi^0}$,Δm $\}$. We observe a $\chi^2/ndof = 1.01$.

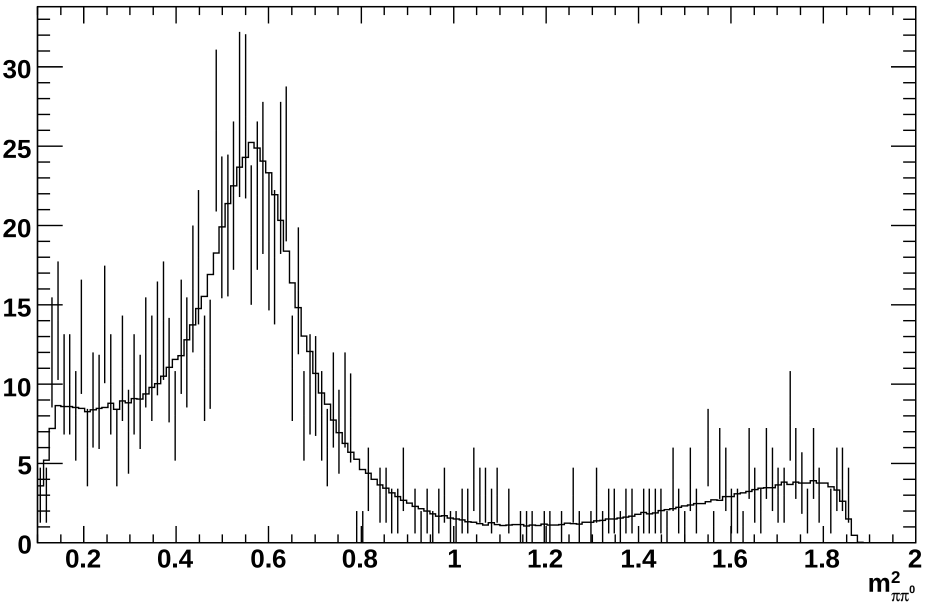

Figure 9.8: Comparison between the MC WS mistag sample (dots), selected using the MC, and the RS MC sample (solid histogram) for the $m^2_{\pi\pi^0}$ invariant mass. Both samples are considered in the signal region of $\{m_{K\pi\pi^0}$,Δm $\}$. We observe a $\chi^2/ndof = 0.85$.

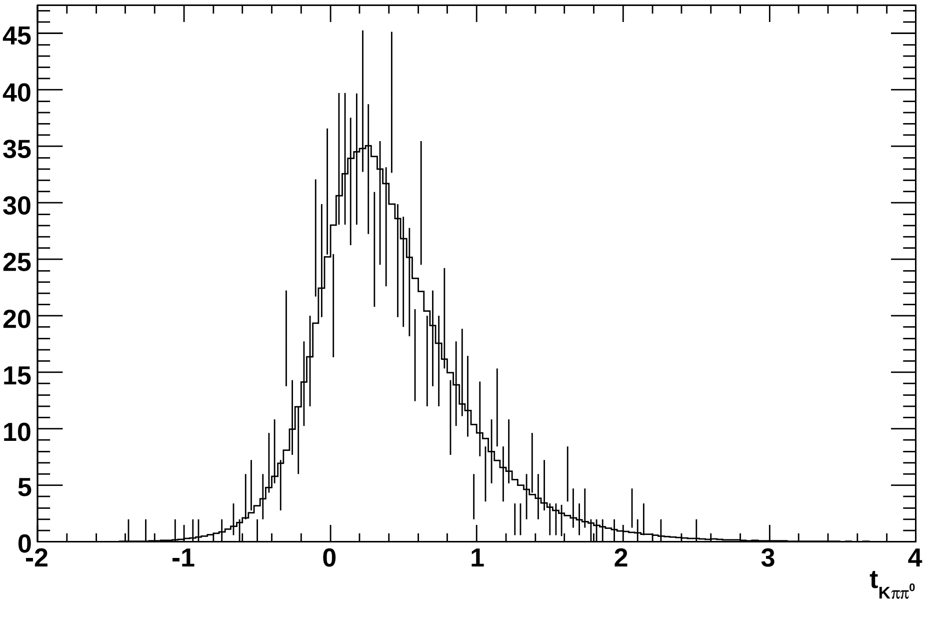

Figure 9.9: Comparison between the MC WS mistag sample (dots), selected using the MC, and the RS MC sample (solid histogram) for the D^0 lifetime distribution. Both samples are considered in the signal region of $\{m_{K\pi\pi^0}$,Δm $\}$. We observe a $\chi^2/ndof = 0.88$.

9.2.3 Validation of the combinatoric and *bad*-D^0 background description

To verify this background description, we consider the MC sample and apply the method described in the previous section. Then, we compare the Dalitz plot background distribution obtained using this technique with the MC sample in the signal region where the MC is applied to reject signal and mistag events. The plots for the three invariant masses projections and for the D^0 lifetime are shown in Figures 9.10-9.13. The projections are made with 30 bins for the invariant masses and 15 for the D^0 lifetime. The χ^2 is calculated for each plot, and reported in Table 9.2. We conclude that the method leads to a reasonable representation of the background distribution in the signal region.

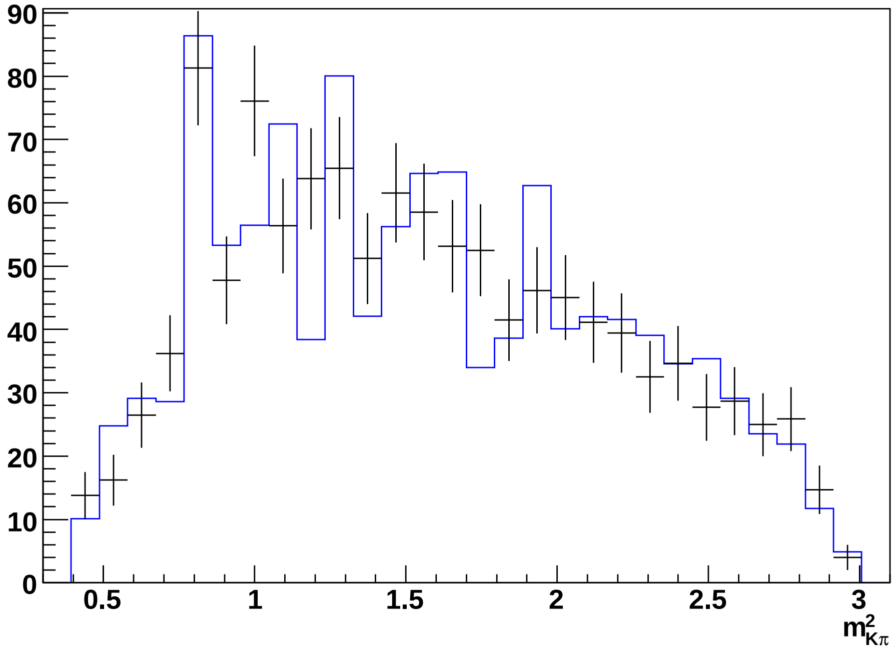

Figure 9.10: Comparison between the MC background sample (dots), selected using the MC, and the background estimation from the sidebands (blue histogram) for the $m^2_{K\pi}$ invariant mass of the WS sample.

Variable	$\chi^2/ndof$ value
$m^2_{K\pi}$	0.908
$m^2_{K\pi^0}$	0.331
$m^2_{\pi\pi^0}$	0.439
D^0 lifetime	0.508

Table 9.2: χ^2 values for the comparison between the MC background sample and the background estimation from the sidebands for the WS sample.

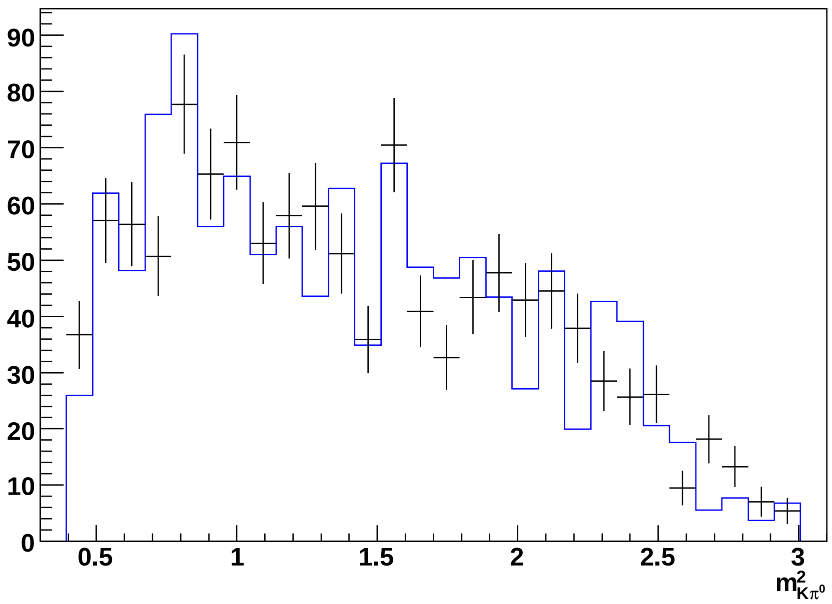

Figure 9.11: Comparison between the MC background sample (dots), selected using the MC, and the background estimation from the sidebands (blue histogram) for the $m^2_{K\pi^0}$ invariant mass of the WS sample.

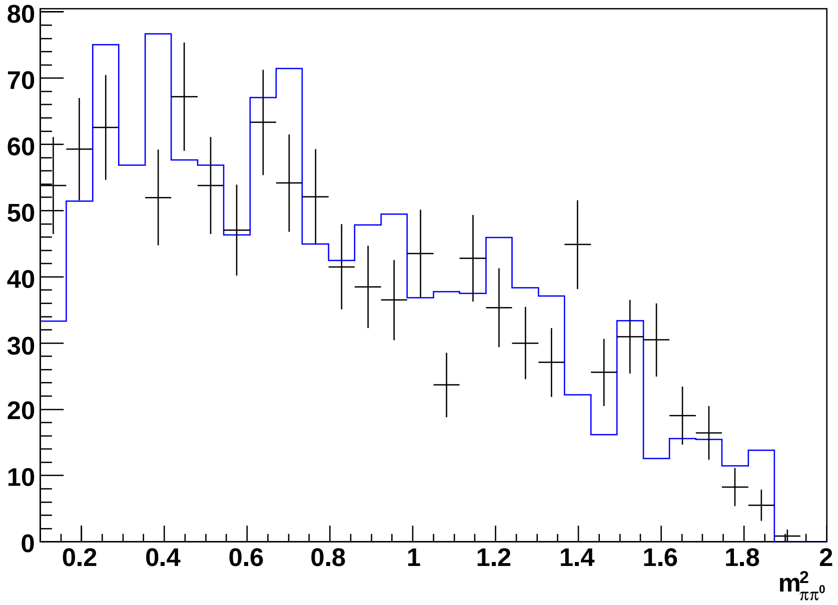

Figure 9.12: Comparison between the MC background sample (dots), selected using the MC, and the background estimation from the sidebands (blue histogram) for the $m^2_{\pi\pi^0}$ invariant mass of the WS sample.

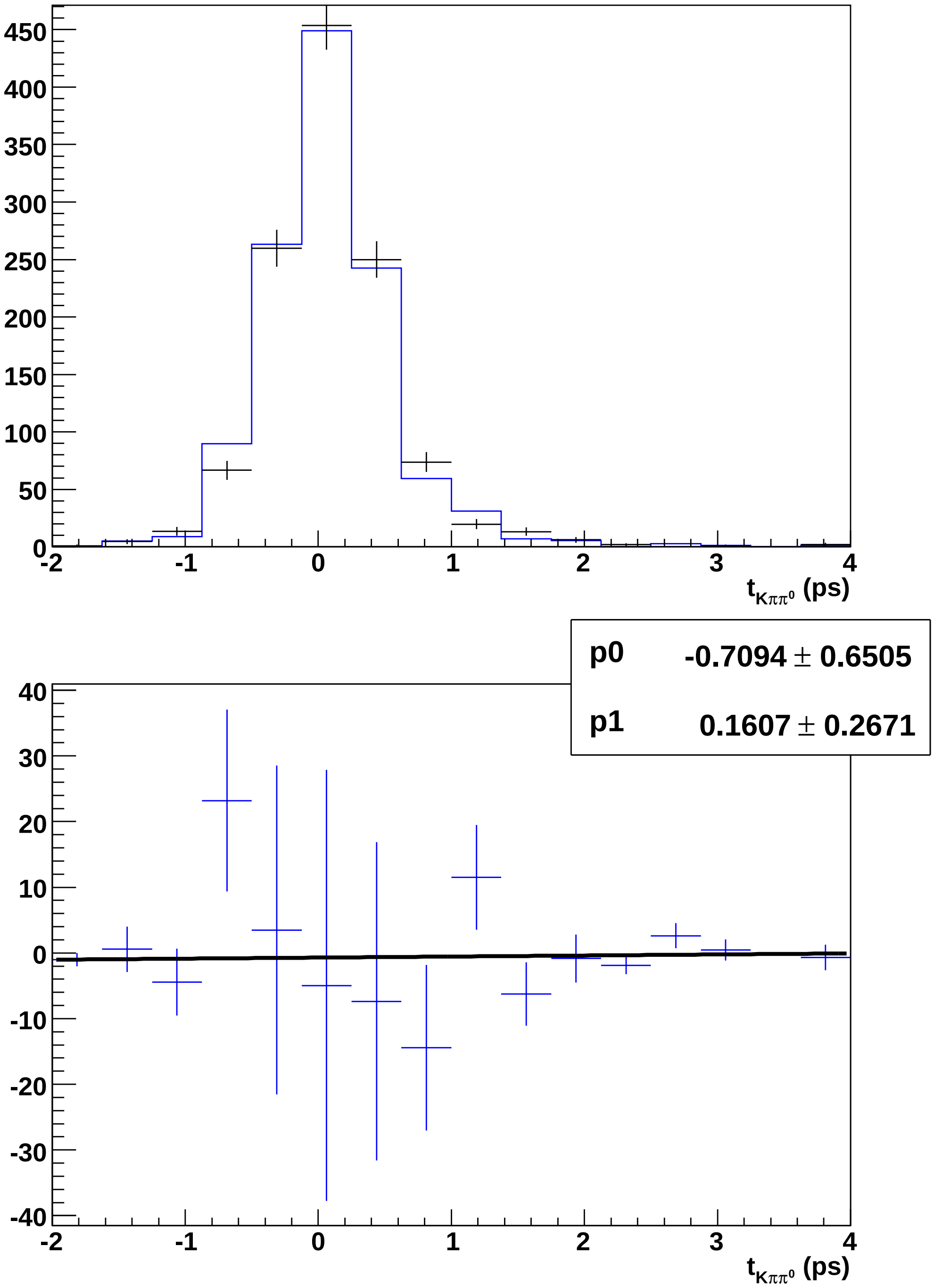

Figure 9.13: On top, comparison between the MC background sample (dots), selected using the MC, and the background estimation from the sidebands (blue histogram) for the D^0 lifetime of the WS sample. On the bottom, difference between the sideband-interpolated D^0 lifetime distribution and the background in the signal region selected using the MC (dots). The black line is the fit result for a linear distribution $y = p_0 + p_1 x$. The fit results are also shown. The χ^2 between the histogram and the linear fit is 0.969

The D^0 lifetime comparison shows a possible offset between the interpolation of the sidebands and the background in signal region from the MC. In order to test this observation, we subtract the two histograms and fit the resulting fit with a linear parametrization. The plot and fit result are also in Figure 9.13. We will apply a systematic error to take this discrepancy into account (see Section 12.2.4).

One can also compare the MC background in the signal region with the interpolation from the sidebands in bins of time, for the Dalitz plot variables. This is shown in Figures 9.14-9.15.

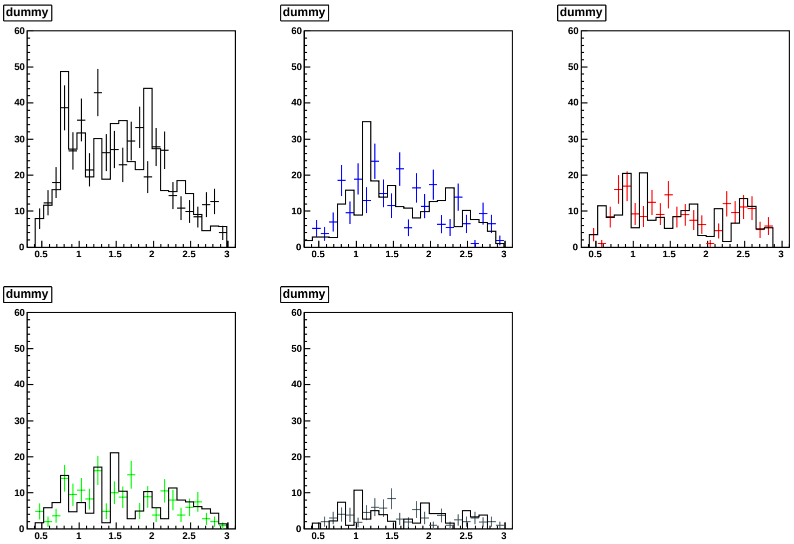

Figure 9.14: Comparison of the $m^2_{K\pi}$ distribution, in different bins of time, for the MC background (dots) and the sidebands interpolation (solid line). The time bins chosen are the same as those considered in Figure 9.10, in increasing values of time from left to right, from top to bottom

9.3 Distribution of σ_t for signal and background

One must also consider the difference in the distributions of σ_t for the signal and background categories to properly fit the tails of the lifetime distribution. This difference can lead to a significant bias if ignored, even if the background information on σ_t is not used; this is called *Punzi* bias [39]. To parametrize these distribution, we use the signal region of the RS and the two sidebands of the WS sample. The distribution are then interpolated and multiplied with the respective PDFs. The RS signal interpolation of σ_t is used for both signal and mistag background, as their events present the same topology. The plots of the two distributions are shown in Figures 9.16 and 9.17. We also tested that the MC distributions of background interpolated from the sidebands regions and from MC in signal region are compatible. The plot of the comparison between the two distributions is in Figure 9.18.

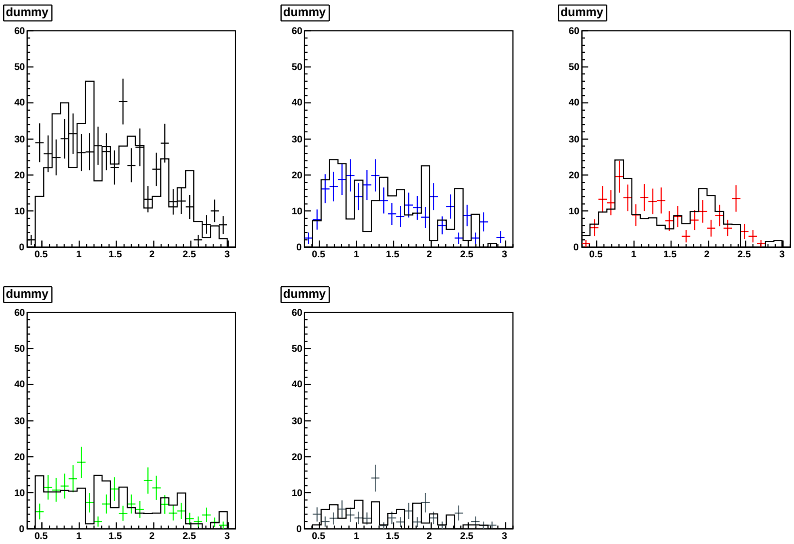

Figure 9.15: Comparison of the $m^2_{K\pi^0}$ distribution in different bins of time, for the MC background (dots) and the sidebands interpolation (solid line). The time bins chosen are the same as those considered in Figure 9.11, in increasing values of time from left to right, from top to bottom

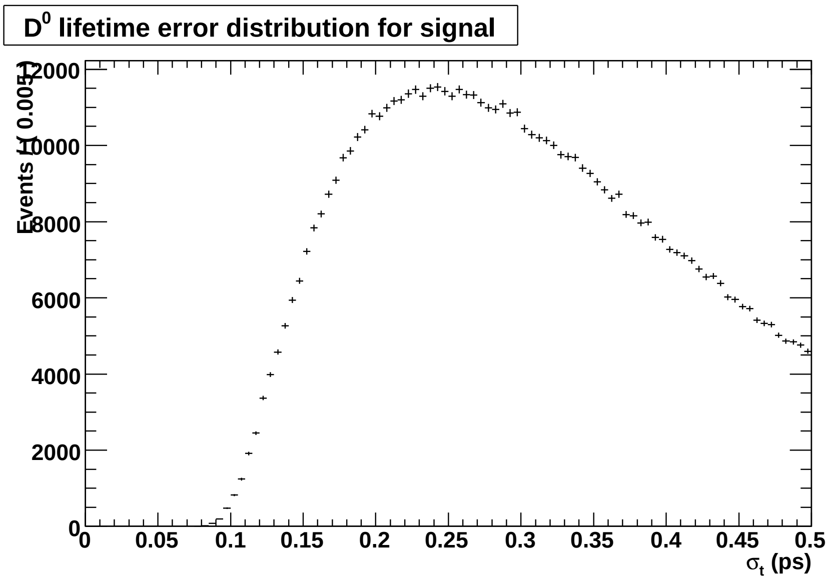

Figure 9.16: D^0 lifetime error distribution for signal and mistag background

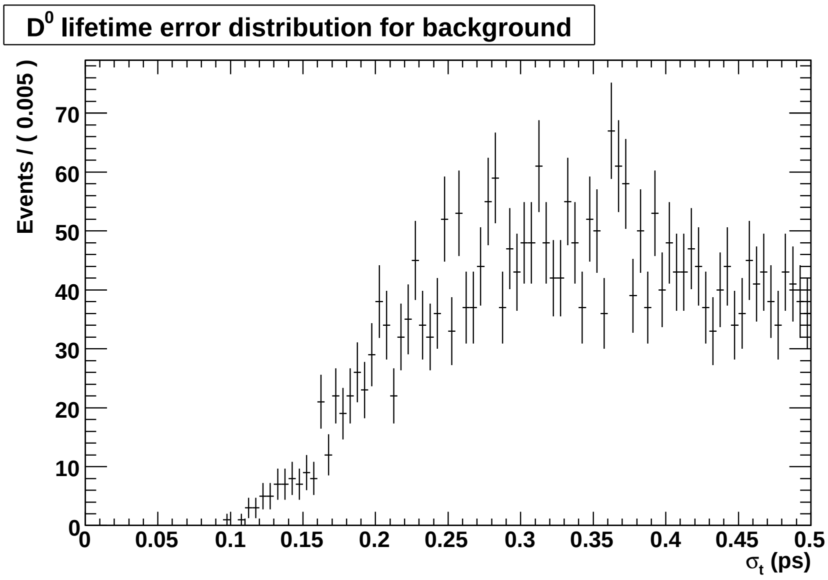

Figure 9.17: D^0 lifetime error distribution for the combinatoric and *bad*-D^0 background

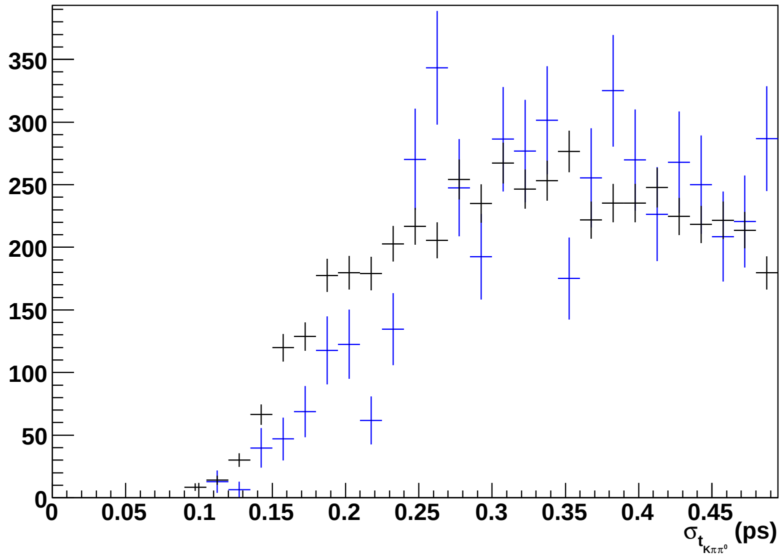

Figure 9.18: D^0 lifetime error distribution for the interpolation of the sidebands (black dots) and for the background events in the signal region selected using the MC (blue dots). The χ^2 between the two distributions is 0.341 .

Chapter 10

Validation of the WS fit

The functional form for signal and background described in Chapter 9 is used in the nominal fit of the WS data sample. Before fitting the data, it is necessary to validate this parametrization and the fitting code. In this chapter, several procedures are adopted for this purpose. Firstly, we fit the data sample blinding the fit code to the final result on the parameters c_1 and c_2, and obtain a parametrization for the DCS Dalitz plot. Secondly, we fit the MC sample and extract the mixing parameters. Finally, we perform toy-MC studies to test the robustness of our fit.

10.1 Partial blind fit of the WS sample

In order to have a reasonable model for the DCS amplitude, we perform a fit to the data, with c_1 and c_2 blinded. Because of the minor statistics, we expect to have a sensitivity to few resonances compared to the CF amplitude in the RS sample. The model used to parametrize the DCS resonances structure in the WS Dalitz plot is similar to the one used for the fit of the RS sample, described in Chapter 7.

The signal model used for this fit is described in detail in Section 9.1. The CF amplitude parametrization is chosen to be the one extracted from the fit of the RS sample. The background parametrization is described in Section 9.2.

We firstly allow to vary all the resonances contributions (all the charge conjugate resonances of those in Table 7.1), then exclude those with an amplitude compatible with zero, and refit for the remaining contributions. We use an unbinned maximum likelihood fit. Since one phase of the DCS model can be absorbed in the c_1 and c_2 parameters and one module can be absorbed in the r_0 calculation, we are allowed to fix the amplitude and phase of one resonance. For consistency with the RS results, we choose to fix the $\rho(770)$ contribution. Note that, besides the mixing results which are the main purpose of this thesis, this is the first fit of the DCS amplitude in the $D^0 \to K^+ \, \pi^- \, \pi^0$ decay.

The final model and the fit results are summarized in Table 10.1, along with the fit fractions for the resonances. The method used to extract the fit fractions is the same used for the Dalitz plot fit of the RS sample (see Section 7.3. The projection of the fitted PDF along with the data are in Figure 10.1 for the Dalitz, and in Figure 10.2 for the D^0 lifetime. It is interesting to notice that the total fit fraction is very close to 100% , suggesting that the Dalitz plot model chosen is appropriate. The errors on the blind values of c_1 and c_2 are also reported. The χ^2 is calculated for the 2D projection of the PDF on the Dalitz plot. We use an adaptive binning for the calculation. The Dalitz plot is initially divided in 40x40 bins in $m^2_{K\pi}$ and $m^2_{K\pi^0}$. The bins with less than 9 events are merged with the next bins until the total bin has at least 9 events.

Notice that in the DCS amplitude the K^{*+} (892) contribution to the Dalitz plot (in terms of fit fractions) is of the same order of the $\rho(770)$ contribution. This differs from the CF case; if one look in Table 7.2, the $\rho(770)$ contribution is by far the largest.

We also report the covariance matrix obtained from the fit. It is shown in Tables 10.2-10.3.

Resonance	Amplitude	Phase (degrees)	Fit Fraction (%)
$\rho(770)$	1 (fixed)	0 (fixed)	39.8 ± 6.5
$K_2^{*0}(1430)$	0.088 ± 0.017	-17.2 ± 12.9	2.0 ± 0.7
$K_0^{*+}(1430)$	6.78 ± 1.00	69.1 ± 10.9	13.1 ± 3.3
$K^{*+}(892)$	0.899 ± 0.005	-171.0 ± 5.9	35.6 ± 5.5
$K_0^{*0}(1430)$	1.65 ± 0.59	-44.4 ± 18.5	2.8 ± 1.5
$K^{*0}(892)$	0.398 ± 0.038	24.1 ± 9.8	6.5 ± 1.4
$\rho(1700)$	5.4 ± 1.6	157.4 ± 20.3	2.0 ± 1.1
$\chi^2/ndof = 188/215 = 0.876$			
Total fit fraction = 102%			
$c_1 = xxxx \pm 0.091$ $c_2 = xxxx \pm 0.090$			

Table 10.1: Fit results for the WS data sample.

10.2 Fit of the MC sample (no mixing)

Another important test to perform is to fit the WS MC sample to extract the mixing parameters. The BABAR MC has been generated without mixing, so this test is can exclude that the background may produce a fake signal structure. It also gives an upper limit at the total systematic error we can determine for this analysis.

In the BABAR simulation, the DCS amplitude is generated phase space like. No analysis before the one presented in this thesis had ever attempted a Dalitz plot fit of the WS sample, so no results were available as an input for the simulation. We fit the MC sample with a non-resonant component only for the DCS Dalitz. In our MC, the CF model, and hence the mistag Dalitz plot model, is the one obtained by the CLEO analysis of $D^0 \to K^-\pi^+\pi^0$ [34] . Since there is a no mixing assumption for D^0 s in the BaBar MC, one can use any CF model to perform this test. We use the same parametrization

	$a_{K_2^{*0}(1430)}$	$\phi_{K_2^{*0}(1430)}$	$a_{K_0^{*-}(1430)}$	$\phi_{K_0^{*-}(1430)}$	$a_{K^{*-}}$	$\phi_{K^{*-}}$	$a_{K_0^{*0}(1430)}$
$a_{K_2^{*0}(1430)}$	0.00028	-0.0091	0.0021	-0.023	0.0001	-0.026	-0.0011
$\phi_{K_2^{*0}(1430)}$	-0.0091	1.6e+02	-0.19	59	0.044	3.3	0.18
$a_{K_0^{*-}(1430)}$	0.0021	-0.19	0.67	-2.9	0.023	-0.78	0.11
$\phi_{K_0^{*-}(1430)}$	-0.023	59	-2.9	1.2e+02	-0.14	16	-0.92
$a_{K^{*-}}$	0.0001	0.044	0.023	-0.14	0.003	-0.13	0.0078
$\phi_{K^{*-}}$	-0.026	3.3	-0.78	16	-0.13	31	0.22
$a_{K_0^{*0}(1430)}$	-0.0011	0.18	0.11	-0.92	0.0078	0.22	0.19
$\phi_{K_0^{*0}(1430)}$	0.0013	21	-3.3	1.3e+02	-0.45	25	-3.3
$a_{K^{*0}}$	6.7e-05	-0.0019	0.0016	-0.077	0.00083	-0.048	-0.00093
$\phi_{K^{*0}}$	-0.015	26	-1.7	41	-0.078	9.3	-0.049
$a_{\rho(1700)}$	0.0045	12	-0.17	18	0.01	-0.84	-0.4
$\phi_{\rho(1700)}$	-0.19	1.3e+02	-13	70	-0.12	38	1.6
c_1	0.00014	-0.34	0.028	-0.72	0.0027	-0.16	0.012
c_2	-1.6e-06	0.3	-0.018	0.7	-0.0021	0.17	-0.0062

Table 10.2: Covariance matrix from the fit result for the WS data sample (I).

	$\phi_{K_0^{*0}(1430)}$	$a_{K^{*0}}$	$\phi_{K^{*0}}$	$a_{\rho(1700)}$	$\phi_{\rho(1700)}$	c_1	c_2
$a_{K_2^{*0}(1430)}$	0.0013	6.7e-05	-0.015	0.0045	-0.19	0.00014	-1.6e-06
$\phi_{K_2^{*0}(1430)}$	21	-0.0019	26	12	1.3e+02	-0.34	0.3
$a_{K_0^{*-}(1430)}$	-3.3	0.0016	-1.7	-0.17	-13	0.028	-0.018
$\phi_{K_0^{*-}(1430)}$	1.3e+02	-0.077	41	18	70	-0.72	0.7
$a_{K^{*-}}$	-0.45	0.00083	-0.078	0.01	-0.12	0.0027	-0.0021
$\phi_{K^{*-}}$	25	-0.048	9.3	-0.84	38	-0.16	0.17
$a_{K_0^{*0}(1430)}$	-3.3	-0.00093	-0.049	-0.4	1.6	0.012	-0.0062
$\phi_{K_0^{*0}(1430)}$	3.4e+02	-0.15	46	17	-62	-1.2	1.1
$a_{K^{*0}}$	-0.15	0.0013	-0.1	0.0033	0.075	0.00068	-0.00071
$\phi_{K^{*0}}$	46	-0.1	70	5.2	69	-0.26	0.27
$a_{\rho(1700)}$	17	0.0033	5.2	5	-2.6	-0.095	0.081
$\phi_{\rho(1700)}$	-62	0.075	69	-2.6	7.7e+02	-0.18	-0.0015
c_1	-1.2	0.00068	-0.26	-0.095	-0.18	0.0082	-0.0066
c_2	1.1	-0.00071	0.27	0.081	-0.0015	-0.0066	0.0084

Table 10.3: Covariance matrix from the fit results for the WS data sample (II).

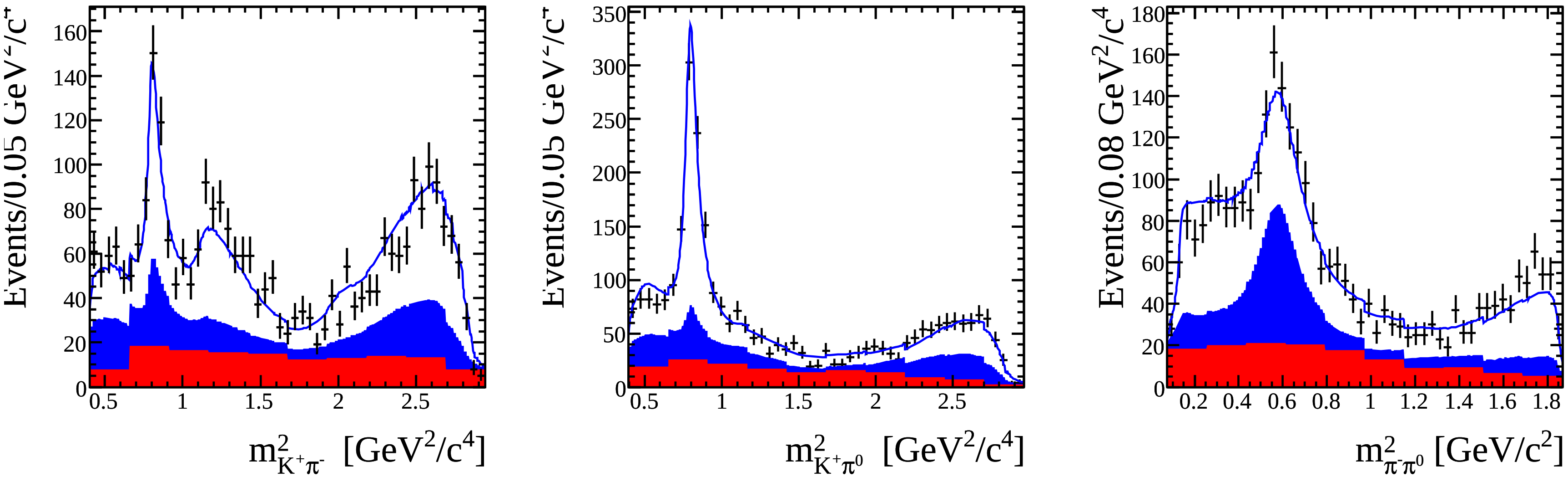

Figure 10.1: WS Dalitz plot data and fit results. The dots are the WS data, the blue line is the fit result.

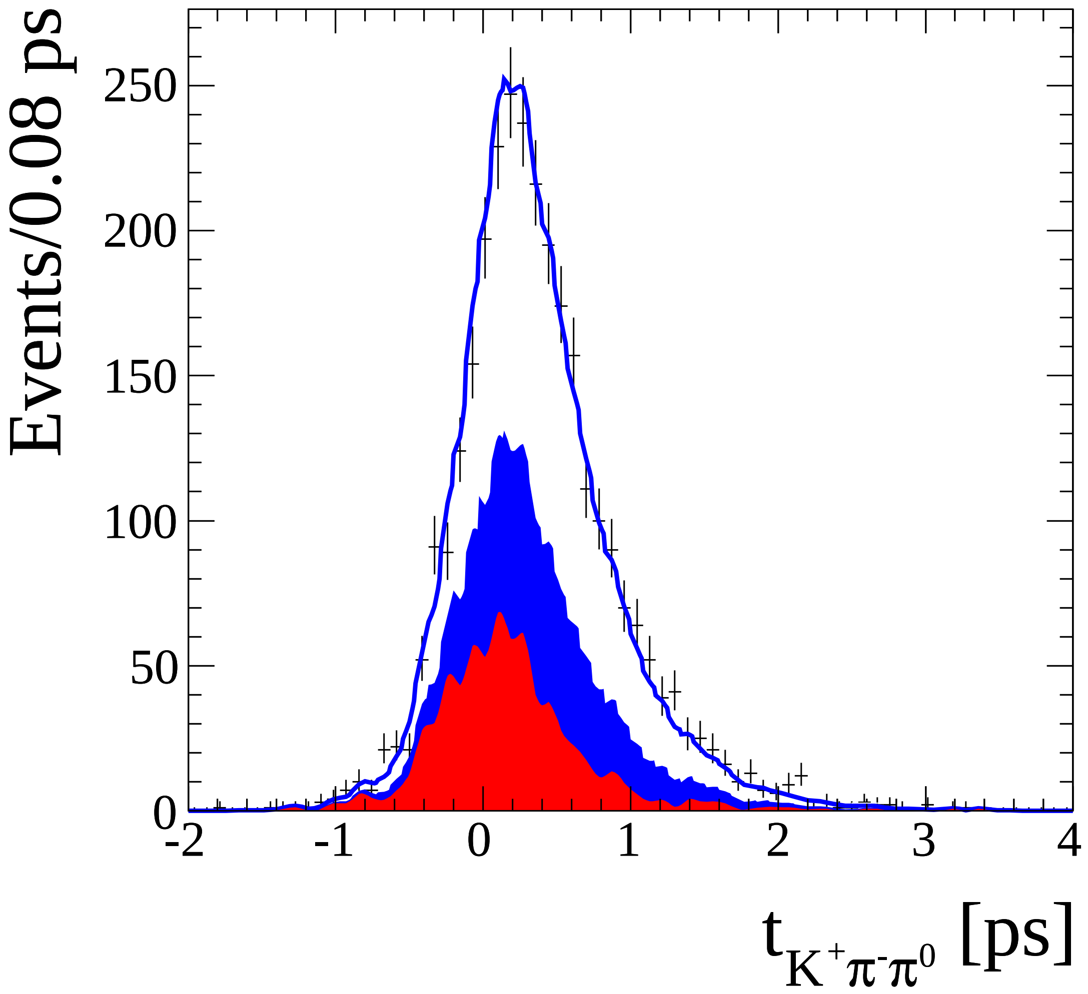

Figure 10.2: WS D^0 lifetime data and fit results. The dots are the WS data sample, the blue line is the fit result. The red histogram represents the interpolation of the WS combinatoric and *bad*-D^0 background, while the blue histogram is the mistag background contribution.

described in Chapter 8 for the resolution function of the MC. The background description uses the method described in Section 10.1.

In Table 10.4 we report the values of c_1 and c_2 extracted from the fit. They are both compatible with zero within the error. It must be noticed that the error on c_1 and c_2 depends on the Dalitz model itself. In this fit of the *BABAR* MC sample we do not extract any amplitude or phase for the DCS Dalitz model (since none is generated) and therefore the errors on the mixing parameters are smaller. This is different with respect to the case of no-mixing (but not trivial DCS Dalitz model) discussed in the toy-MC Section 10.3.

Another important test is to use the RS Dalitz fit result as a model for the mistag background and CF amplitude. One must notice that using this parametrization is wrong, since the BaBar MC is produced using the CLEO model and the CLEO fit results (a comparison can be found in Section 7.4). Anyway, this test is very useful to have an hint on how the result is sensitive to the RS parametrization. The result for c_1 and c_2 is reported in Table 10.5. One can notice that also in the second case the mixing parameters are compatible with zero, and are very close to the values in the case where the correct CF parametrization is used.

Parameter	Fit value (%)
c_1	-1.32 ± 2.27
c_2	2.13 ± 2.64

Table 10.4: Values of c_1 and c_2 from the fit of the WS MC sample

Parameter	Fit value (%)
c_1	-1.98 ± 2.27
c_2	2.02 ± 2.72

Table 10.5: Values of c_1 and c_2 from the fit of the WS MC sample, using the RS fit as the mistag parametrization

10.3 Toy-MC studies

Another important test is to verify that the fitting procedure gives a correct estimation of the errors on the mixing parameters, and that c_1 and c_2 are not affected by any bias. For this reason, we perform toy-MC studies. We generate MC samples using our signal and background PDFs with a particular choice for the mixing parameters, and then fit each sample. With the fitted values and errors on c_1 and c_2 we construct pull distributions to study the statistical features of the parameters.

The model chosen for the generation and for the fit of the DCS amplitude is the one obtained from the blind fit described in Section 10.1. We initially consider two different mixing scenarios:

1. The *no-mixing* case → $c_1 = 0$ and $c_2 = 0$

   This scenario is useful to have a good hint of the sensitivity of the analysis.

2. $c_1 = 0.25$ and $c_2 = 0.18$

   With an estimate of $r_0 \sim 10^{-3}$, this scenario represents the values of c_1 and c_2 more likely from the world average [1] of x and y (see Section 1.6).

We generated and fitted 2000 samples for each D^0 mixing scenario. Once the fit has converged the distribution of the pulls is considered for several fit parameters. The pulls are defined as:

$$\text{pull} = \frac{x_{fit} - x_{true}}{\sigma_X} \tag{10.1}$$

where x_{fit} is value of the parameter x obtained from the fit, x_{true} is the value of x used for the generation, and σ_x is the error of x from the fit. The pulls are fitted with a Gaussian distribution to check the absence of bias and to determine the spread of the error for the parameter. We report the results for c_1, c_2. We also present the results of the fit of the pulls for amplitude and phase of one resonance of the DCS Dalitz plot, the K^{*0} (892). The behavior of the other resonances is similar.

Since the presence of a small bias is found for c_1, we test its statistical dependence by generating a set of 1000 toy-MC, each one having 10 times the statistics we have for this analysis. The bias disappears with the increase of statistics. It is due to the non-Gaussian features of our likelihood at the statistic regime we are in our data sample. We will correct the final result for the offset found in the toy-MC studies for c_1.

The toy-MC study also shows that the pulls in each set of experiments have a standard deviation compatible with 1 within the error. This demonstrates that the error from the fit describes accurately the statistical fluctuation of the parameters.

For each scenario, the plot of the fitted values for the parameters, the errors and the pulls are shown in Appendix D.

10.3.1 The *no-mixing* scenario

The fit results for the pull distributions are in Table 10.6. As can be observed, the pull show a Gaussian behavior within the statistical error. A small bias is observed for c_1 and the amplitude of the resonance.

10.3.2 The $c_1 = 0.25$ and $c_2 = 0.18$ scenario

This case takes into account the possibility of having both c_1 and c_2 with large values. With a rough estimation of $r_0 \sim 10^{-3}$ this leads to values of x' and y' of the order of 10^{-2},

---

[1] This preliminary estimation assumes $\delta_0 = 0$

Parameter	Value
c_1 pull mean value	-0.22 ± 0.02
c_1 pull σ	0.94 ± 0.03
c_2 pull mean value	-0.05 ± 0.02
c_2 pull σ	1.05 ± 0.02
$a_{K^{*0}}(892)$ pull mean value	0.07 ± 0.02
$a_{K^{*0}}(892)$ pull σ	0.98 ± 0.02
$\delta_{K^{*0}}(892)$ pull mean value	-0.05 ± 0.02
$\delta_{K^{*0}}(892)$ pull σ	1.02 ± 0.02

Table 10.6: Mean value and σ for the pull distributions of c_1, c_2 and the K^{*0} (892) amplitude and phase for the *no-mixing* scenario.

in good accord with the current estimation on x and y. c_1 and c_2 are assigned a value of 0.25 and 0.18 The fit results for the pull distributions are in Table 10.7.

As in the previous scenario, a small bias is observed for the c_1 value and the $K^{*0}(892)$ parameters.

Parameter	Value
c_1 pull mean value	-0.13 ± 0.02
c_1 pull σ	0.90 ± 0.01
c_2 pull mean value	0.04 ± 0.02
c_2 pull σ	1.06 ± 0.02
$a_{K^{*0}}(892)$ pull mean value	0.13 ± 0.02
$a_{K^{*0}}(892)$ pull σ	0.97 ± 0.02
$\delta_{K^{*0}}(892)$ pull mean value	-0.11 ± 0.03
$\delta_{K^{*0}}(892)$ pull σ	1.01 ± 0.01

Table 10.7: Mean value and σ for the pull distributions of c_1, c_2 and the $K^{*0}(892)$ Dalitz plot parameters for the $c_1 = 0.25$ and $c_2 = 0.18$ mixing scenario.

10.3.3 Toy MC linearity test

From the previous sections it is clear that c_1 is affected by a bias, though small compared with the statistical error. The value of the bias seems to depend on the true value of c_1 used in the generation. For this reason, we extend the study of the previous subsection to a full set of (c_1, c_2) generated values. We produce a set of 500 toy experiment for each (c_1, c_2) value in the range ([-0.2,0.2]; [-0.2,0.2]). The fitted values averaged over each set and the RMS of the fitted values are plotted versus the generated values. Each toy experiment has the same statistics of our data sample. The results are show in Figure 10.3 and Fig.10.4 for c_1 and c_2 respectively. They are compared with a line (45^o degree). The error bars represent the RMS of the fitted value in each toy-MC set.

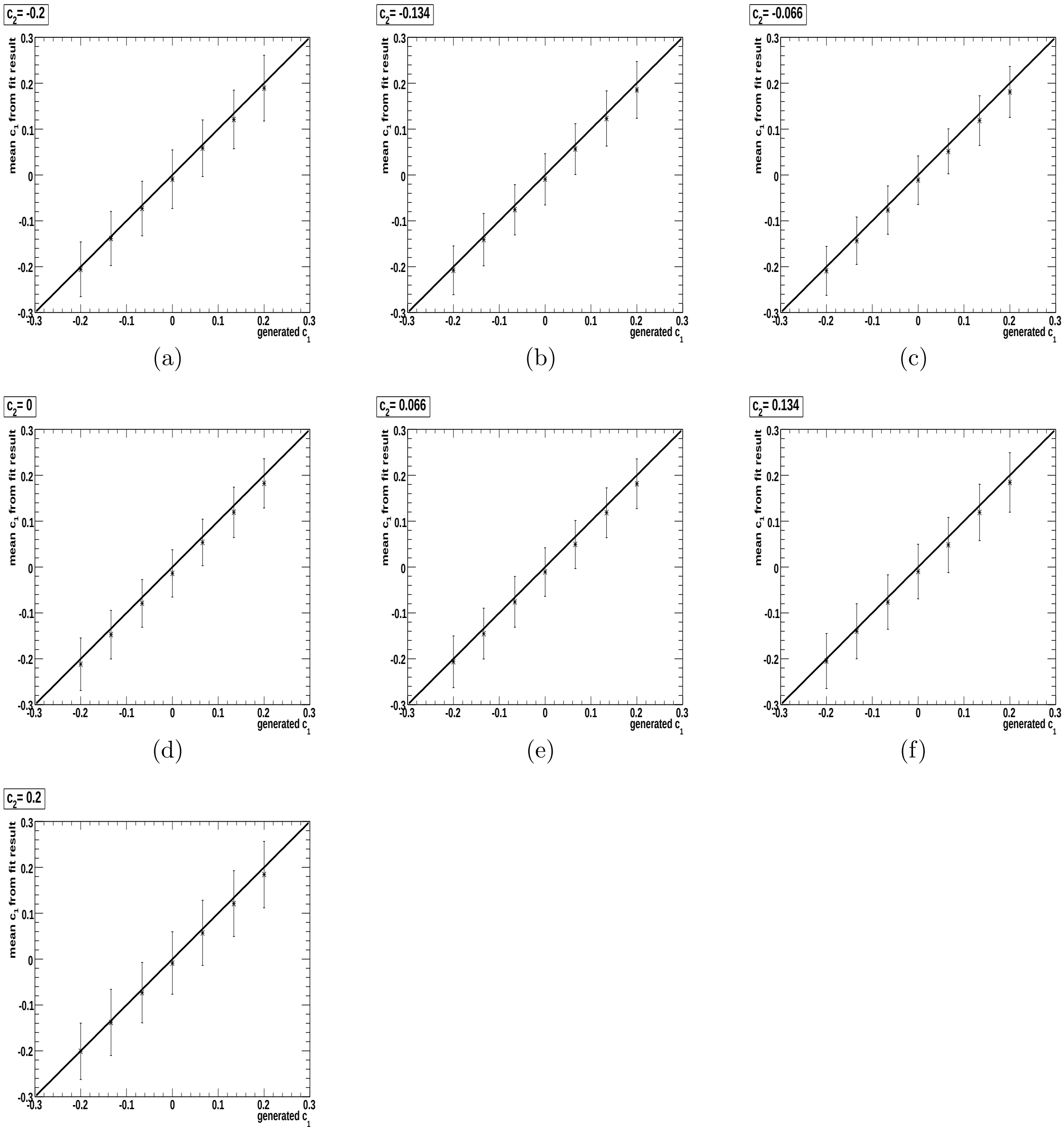

(a) (b) (c)

(d) (e) (f)

(g)

Figure 10.3: Mean value of fitted c_1 versus generated c_1 in various set of toy-MC experiments. Each plot corresponds to a different generated value of c_2, which varies from -0.2 (top left) to 0.2 (bottom). The error bars represent the RMS of the distribution of the fitted c_1 values.

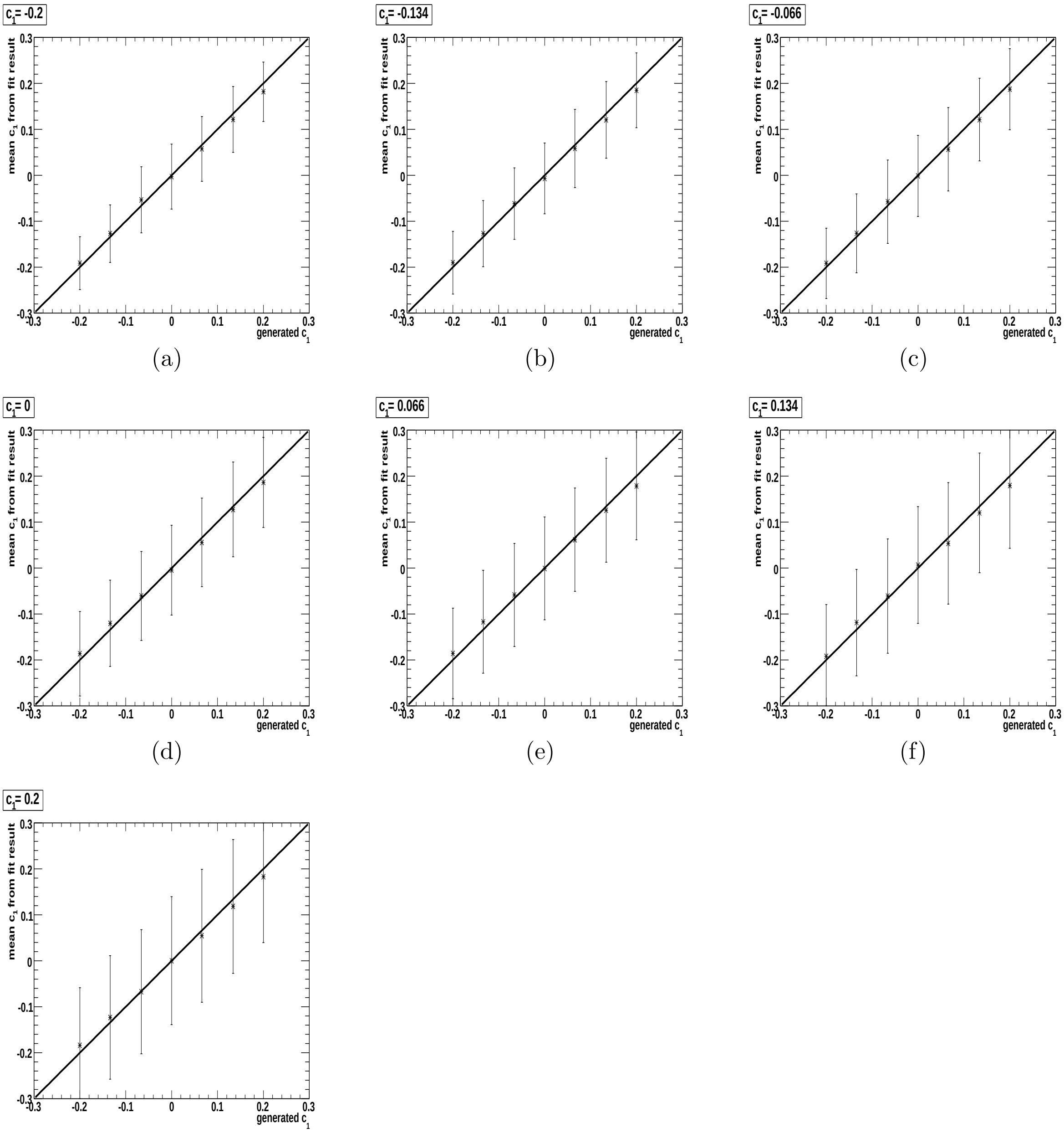

(a) (b) (c)

(d) (e) (f)

(g)

Figure 10.4: Mean value of fitted c_2 versus generated c_2 in various set of toy-MC experiments. Each plot corresponds to a different generated value of c_1, which varies from -0.2 (top left) to 0.2 (bottom). The error bars represent the RMS of the distribution of the fitted c_2 values.

It can be observed that no particular trend for the fitted vs generated values is observed for the two parameters. This linearity test shows that there is no trend biasing our extraction of c_1 and c_2. Nevertheless, a small offset with respect to the 45 line is observed. Though small, this offset cannot be ignored. We will correct our final result for c_1 and c_2 for the offset.

10.4 Time independent Dalitz plot fit in bins of D^0 lifetime

A simplified version of the fit to the WS signal sample can be used as a sanity check of a positive result of mixing. We have considered one toy-MC experiment with $y' = 0.012$ and $x' = 0.008$ and the statistics equivalent to 10 times the data statistics. It has been divided into 5 time bins of unequal size. The binning has been chosen so that for each bin resides the same number of events. In each bin a time independent Dalitz plot fit has been performed. The Dalitz model is based on the blind fit result to the WS sample described in Section 10.1. In each bin the fit fractions have been computed for all the components. In Table 10.8 we show the fit fraction evolution for the main components, the $\rho(770)$ and K^{*+} (892). If mixing occurs, it is expected to see an increase of the ρ fit fraction (main contribution of the CF amplitude) over time. We observe this behavior in the toy-MC.

time bin (ps)	$\rho(770)$	$K^{*+}(892)$
-2.0 - 0.0	7.4 ± 1.5	49.3 ± 5.8
0.0 - 0.2	12.2 ± 1.8	53.6 ± 5.0
0.2 - 0.4	14.3 ± 2.0	43.9 ± 5.2
0.4 -0.8	18.5 ± 2.3	47.9 ± 5.3
0.8 - 4.0	24.9 ± 3.5	44.6 ± 6.0

Table 10.8: Fit fraction in time bins for $\rho^- K^+$ and $\pi^- K^{*+}$ in a toy-MC experiment.

Chapter 11

Interpretation of the results and extraction of x' and y'

In this chapter, we present the final results in terms of c_1 and c_2. After a brief discussion on the method to convert the result in terms of x' and y', we present the values on the mixing parameters too. Particular care is required in order to take into account all the correlations between the fit parameters when the transformation $(c_1, c_2) \rightarrow (x', y')$ is made. We will also extract the mixing parameters separately for the D^0 and $\overline{D}^0$, to have some information on the *CP* violation in this channel in mixing.

11.1 Fit results on c_1 and c_2

We obtain from the fit to data:

$$\begin{aligned} c_1 &= -0.002 \pm 0.090 \text{ (stat.) } \pm 0.059 \text{ (syst.)} \qquad (11.1) \\ c_2 &= 0.346 \pm 0.091 \text{ (stat.) } \pm 0.052 \text{ (syst.)} \qquad (11.2) \end{aligned}$$

The determination of the systematic errors is presented in Chapter 12. We find that $c_1 = \frac{y'}{r_0}$ is compatible with zero, while $c_2 = \frac{x'}{r_0}$ is not compatible with zero within 3σ.

11.1.1 Correction of the results for the offset on c_1 and c_2

In order to estimate the size of the expected offset on c_1 and c_2, we run 2000 toy-MC, using our fit results in the generation. The fit results to the pull distributions are shown in Table 11.1. As can be seen, a bias is present in the c_2 distribution. This offset will be corrected in the final result.

Given these results for the pull distributions, we can correct the final results on c_1 and

Parameter	Value
c_1 pull mean value	-0.01 ± 0.02
c_1 pull σ	1.02 ± 0.02
c_2 pull mean value	-0.08 ± 0.02
c_2 pull σ	1.03 ± 0.02

Table 11.1: Mean value and σ for the pull distributions of c_1 and c_2 in the fit result scenario (2000 toy-MC experiments).

c_2 for the offset. We shift the c_2 distribution of $+0.08\sigma_{c_2}$, with σ_{c_2} being the statistical error on c_2. In this way, the final result on the parameters is

$$c_1 = -0.002 \pm 0.090 \text{ (stat.) } \pm 0.059 \text{ (syst.)} \tag{11.3}$$

$$c_2 = 0.353 \pm 0.091 \text{ (stat.) } \pm 0.052 \text{ (syst.)} \tag{11.4}$$

11.1.2 Significance of the result

We want to test the compatibility of the no-mixing hypothesis with our results in a frequentistic approach. In other words, we want to know how likely it is that, in case mixing doesn't exist, our data fluctuated to the result we find[1]. This is called the coverage probability, which we indicate with α. In order to test this hypothesis, we measure

$$-2\Delta Log(\mathcal{L}) = -2[Log(\mathcal{L}(c_{1,fit}, c_{2,fit})) - Log(\mathcal{L}(0,0))] \tag{11.5}$$

We take twice the difference in log likelihood between the fit with mixing and another fit where $x' = y' = 0$. All the other parameters are allowed to float in both fits. It can be demonstrated that in a Gaussian regime, $-2\Delta \log \mathcal{L}$ is distributed as a χ^2 distribution with n degrees of freedom. The probability of α for exceeding χ^2 with n degrees of freedom is given by

$$\alpha(\chi^2, n) = \left[2^{\frac{n}{2}}\Gamma(\frac{n}{2})\right]^{-1} \int_{\chi^2}^{\infty} t^{\frac{n}{2}-1} e^{-\frac{t}{2}} dt \tag{11.6}$$

For two degrees of freedom, Equation 11.6 becomes

$$\alpha(\chi^2, 2) = \frac{1}{2}\int_{\chi^2}^{\infty} e^{-\frac{t}{2}} dt = e^{-\frac{\chi^2}{2}} \tag{11.7}$$

---

[1] It is much better to determine the statistical significance of the result in the $\{c_1, c_2\}$ base instead of the $\{x', y'\}$ base. This is because in order to extract the values of the mixing parameters we need to use an information on r_0, which will suffer on of own uncertainty. One can think this uncertainty as an additional smearing to the likelihood that will dilute our significance.

Systematic errors (described in Chapter 12) were included in the statistical significance calculation by smearing the likelihood function before taking the $-2\Delta \log \mathcal{L}$ value. The smearing function is a two dimensional Gaussian in the mixing parameters, whose error is the systematic uncertainty on each parameter. The correlation between the parameters was included in the Gaussian function.

We find $-2\Delta \log \mathcal{L} = 13.5$. With two degrees of freedom, the confidence level that the result is due to no-mixing is 0.1%. Hence, this is an evidence of mixing. The significance of the result corresponds to 3.2 standard deviations.

In Appendix F we discuss the test of the statistical coverage of this method.

11.1.3 Contour plots on the c_1 and c_2 plane

It is also interesting to look at the probability contour plot for c_1 and c_2. In other words, we want to identify on the $\{c_1, c_2\}$ plane regions were the points belong to the same likelihood probability interval. In order to do so, we generate a sample of $\{c_1, c_2\}$ values. At each generation step, we take the covariance matrix and generate a set of parameters using the matrix elements. In this way, all correlations between the fit parameters are taken into account in the $\{c_1, c_2\}$ generation. This is done with a square root method [40]. With these generated values, we construct the two dimensional histogram on $\{c_1, c_2\}$ and integrate it to find the probability contour regions. The contour plot for the statistical error only is shown in Figure 11.1. As can be noted, the contours differ from an elliptical distribution. This tells us that the Gaussian assumption doesn't hold in this statistical regime.

We also want to produce the contour plots with the systematic error included. For this reason, we sum the systematic covariance matrix described in Section 12.6.3 to the statistical covariance matrix from the fit before generating the parameters. This can be thought as an equivalent of summing the square of the errors. The contour plot with the systematic errors included is shown in Figure 11.2.

11.2 Extraction of x' and y' from the fit result

11.2.1 Determination of r_0^2

From Equation 9.1 it is clear that in order to do the transformation $(c_1, c_2) \rightarrow (x', y')$ we need to know the value of r_0^2. As stated in Section 2.2 we explained that r_0 is the module of the relative complex number between the CF and DCS amplitudes. If there was no mixing, r_0^2 would simply be the ratio of the DCS and CF widths, and could be determined, for example, measuring the ratio between the measured WS and RS signal events. In order to have the signal PDF in Equation 9.1 normalized, we must have that $N = N_{WS}/(N_{RS} r_0)$. Hence, we can measure r_0^2 by computing

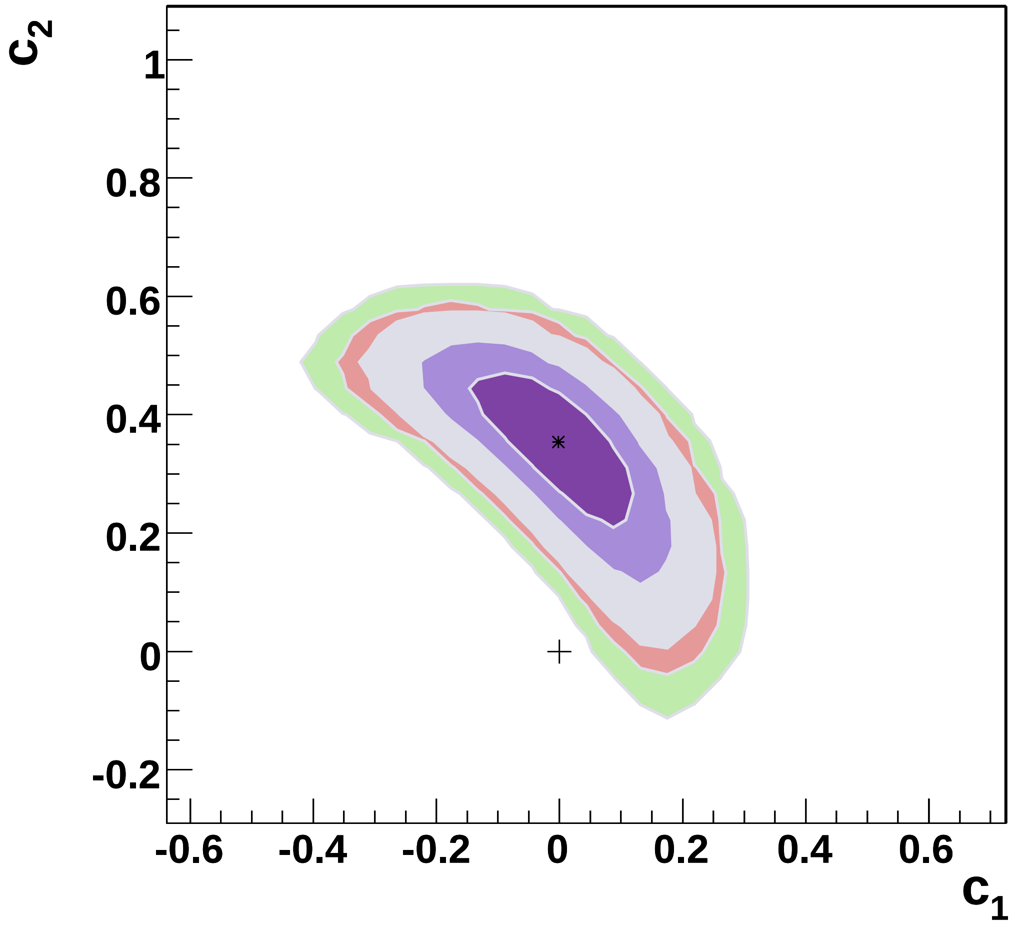

Figure 11.1: Probability contour plot for c_1 and c_2 (statistical error only). The 68.3%, 95.5%, 99.7%, 99.9% and 99.99% probability contour lines are shown.

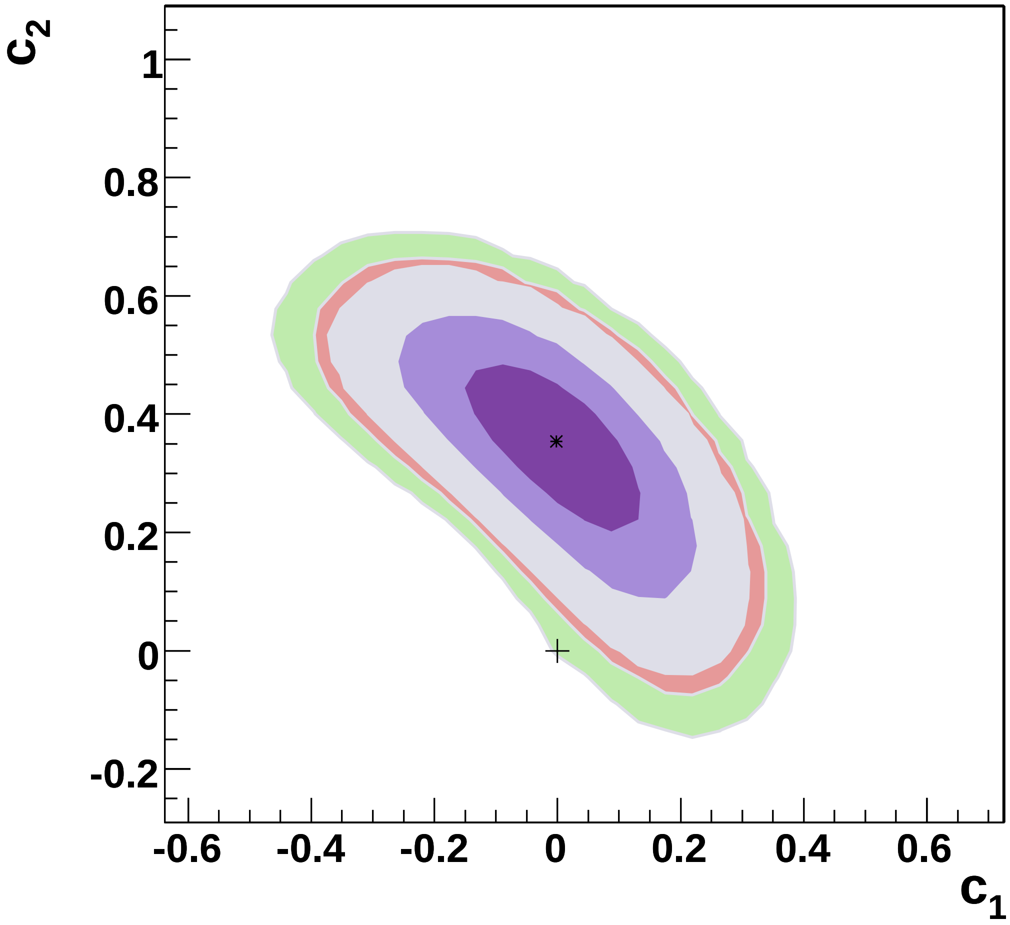

Figure 11.2: Probability contour plot for c_1 and c_2 (statistical and systematic errors included). The 68.3%, 95.5%, 99.7%, 99.9% and 99.99% probability contour lines are shown.

$$r_0^2 = \frac{N_{WS}}{N_{RS}\int PDF_{sig}(m_{12}^2, m_{13}^2, t)dm_{12}^2dm_{13}^2dt} \tag{11.8}$$

N_{WS} and N_{RS} are known from the fit to the data sample described in Chapter 5.

11.2.2 Extraction of the mixing parameters

Given the method to extract r_0^2 described in the previous section, we can now determine the values for the mixing parameters. This is done by generating all the useful parameters for the calculation of x' and y' simultaneously, in order to take all the correlations into account. With the distributions of the generated values we will estimate the best value for x' and y'.

Since Figure 11.1 shows a non-Gaussian behavior for c_1 and c_2 at higher probability intervals, we must take this effect into account for the determination of the mixing parameters. For this reason, we use the probability contour plot distribution described in Section 11.1.3 for the generation.

We generate 2000 sets of parameters; for each step

- we generate c_1 and c_2 using the probability distribution of Figure 11.1;
- we generate all the Dalitz plot amplitudes and phases, using a Gaussian generation, taking into account the correlations from the fit covariance matrix;
- we generate N_{WS} and N_{RS} with a one dimensional Gaussian distribution for each parameter, using as a mean and error the values contained in Table 5.1;
- given the values of c_1, c_2 and the amplitudes and phases, we can calculate

  $$\int PDF_{sig}(m_{12}^2, m_{13}^2, t)dm_{12}^2dm_{13}^2dt.$$

  Knowing the integral value and knowing N_{WS} and N_{RS} we calculate r_0^2;
- knowing c_1, c_2 and r_0^2, we can finally compute x' and y'.

Note that this procedure decouples the generation of c_1 and c_2 from the generation of the Dalitz plot amplitudes and phases. This procedure is correct as long as c_1 and c_2 and the Dalitz plot model are poorly correlated.

The central values and errors on the mixing parameters are extracted using a Bayesian approach, integrating the likelihood transformed in the $\{x', y'\}$ base using a flat prior distribution. We determine:

$$\begin{aligned} x' &= (2.61^{+0.57}_{-0.68})\% \\ y' &= (-0.06^{+0.55}_{-0.64})\% \end{aligned} \tag{11.9}$$

where the error is statistical only.

We can also produce the probability contour plot for x' and y'. It is shown in Figure 11.3. Note that our procedure perfectly reproduces the non-Gaussian behavior.

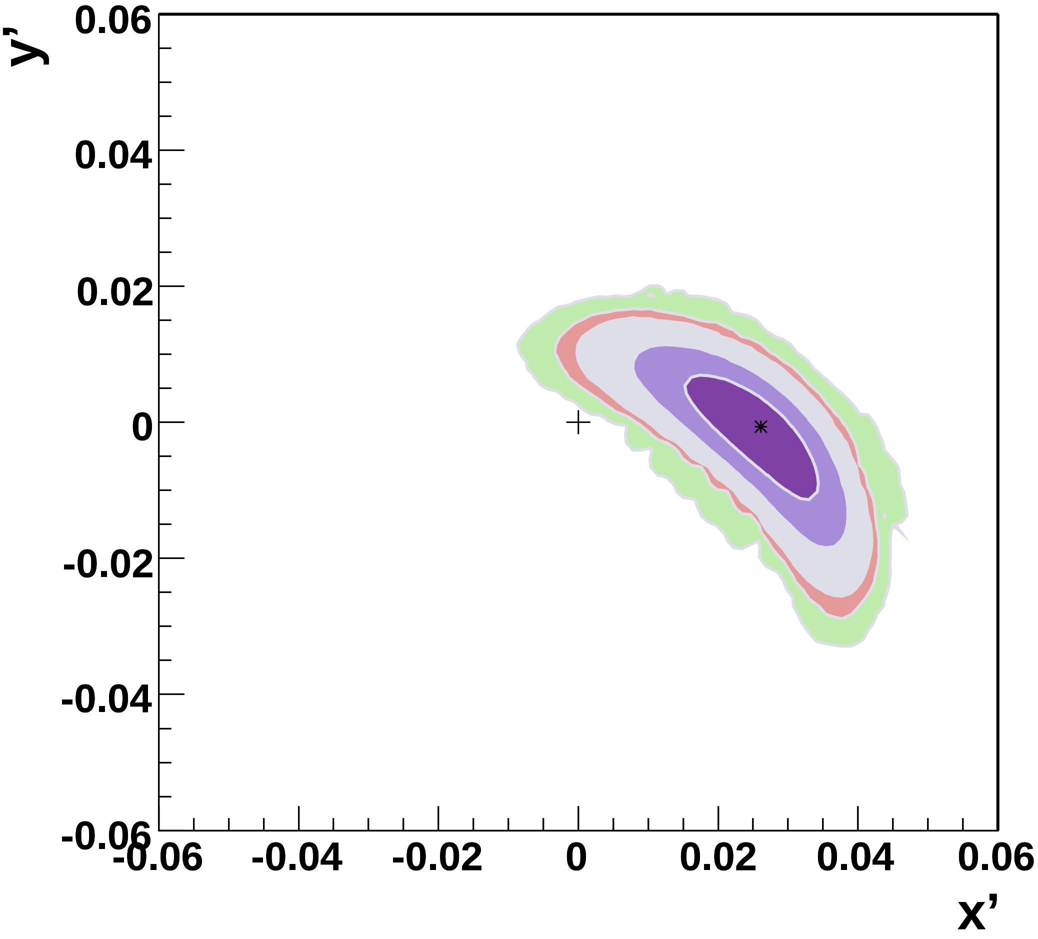

Figure 11.3: Probability contour plot for x' and y' (statistical error only). The 68.3%, 95.5%, 99.7%, 99.9% and 99.99% probability contour lines are shown. The fuzzy behavior of the 99.99% region is due to the low toy-MC statistic in the region far from the central value.

11.2.3 Final results on x' and y' with systematic errors included

In Section 12.6.3, we describe a method to determine a systematic errors covariance matrix. In order to propagate the systematic errors to x' and y', we sum the systematic errors covariance matrix to the statistical one before performing the method described in Section 11.2.2. This is equivalent to sum in square all the errors accounting for the correlations.

The final result on the mixing parameters is:

$$\begin{aligned} x' &= (2.61^{+0.57}_{-0.68}\ (\text{stat.})\ \pm 0.39\ (\text{syst.})\ )\% \\ y' &= (-0.06^{+0.55}_{-0.64}\ (\text{stat.})\ \pm 0.34\ (\text{syst.})\ )\% \end{aligned} \tag{11.10}$$

with a linear correlation of -0.75. We can also produce the probability contour plot for x' and y' with the systematic error. It is shown in Figure 11.4.

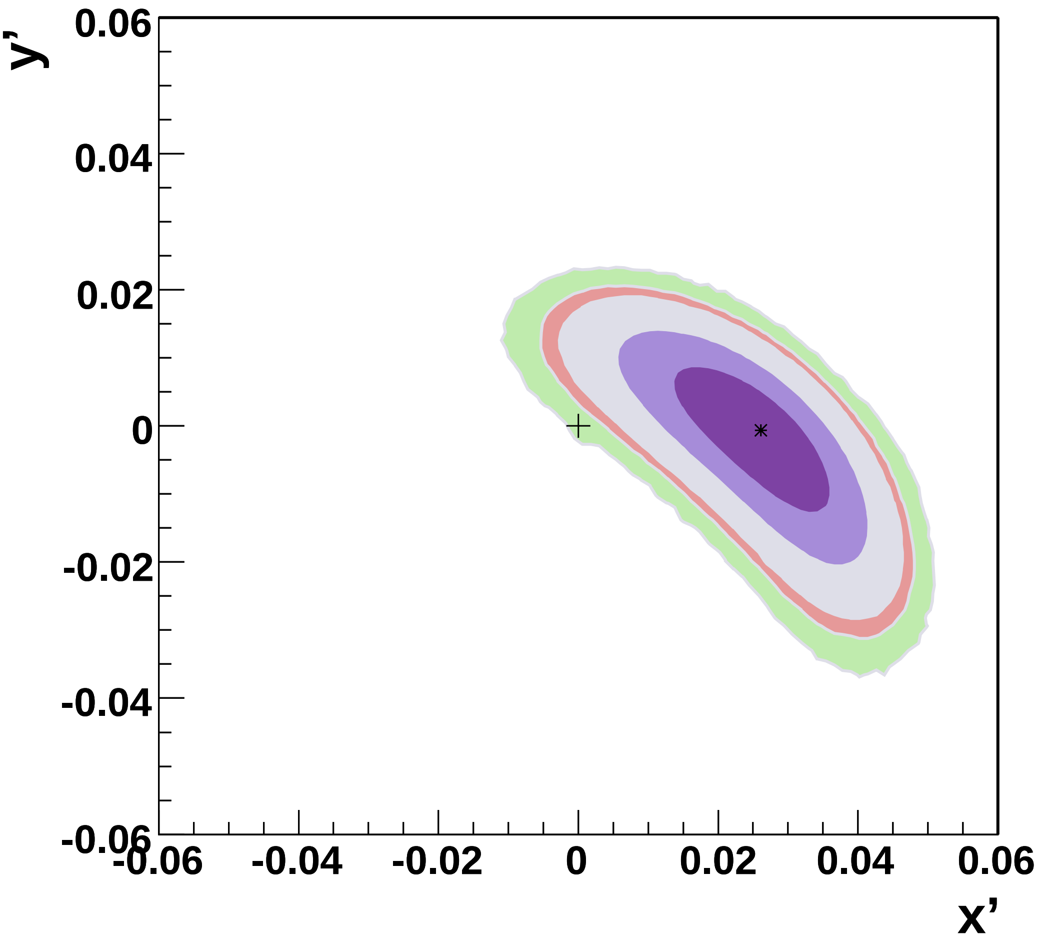

Figure 11.4: Probability contour plot for x' and y' (statistical and systematic errors included). The 68.3%, 95.5%, 99.7%, 99.9% and 99.99% probability contour lines are shown.

11.2.4 Measurement of r_0^2

Another parameter determined during the extraction of x' and y' is the ratio

$$r_0^2 = \frac{N_{WS}}{N_{RS} \int PDF_{sig}(m_{12}^2, m_{13}^2, t) dm_{12}^2 dm_{13}^2 dt} \tag{11.11}$$

From the distribution obtained in the generation (with the systematic covariance matrix included), we obtain

$$r_0^2 = 0.00525^{+0.00025}_{-0.00031} \text{ (stat.)} \ \pm 0.00012 \text{ (syst.)} \tag{11.12}$$

The probability plot for r_0^2 with the systematic error included is shown in Figure 11.5. Notice that this is the first measurement of this quantity.

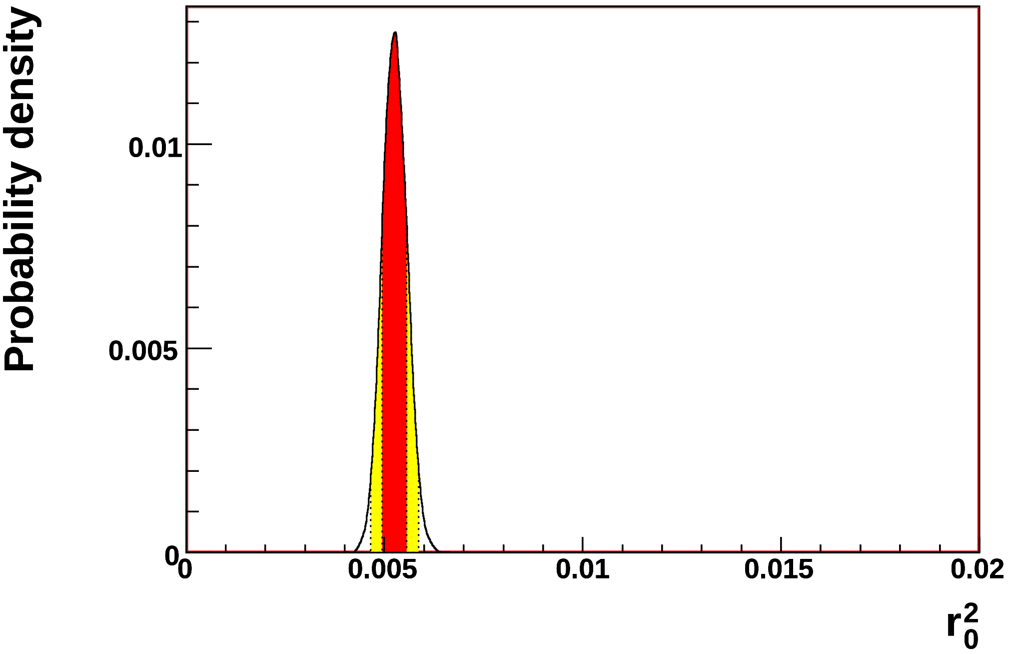

Figure 11.5: Probability contour plot for r_0^2 with the systematic error included. The 68.3% and 95.5% probability intervals are shown.

11.3 D^0-$\overline{D}^0$ mixing result for separate flavors

It is also very interesting to measure x' and y' separately for the D^0 and $\overline{D}^0$ samples. This can give an important information to constraint new physic models using the limits on *CP* violation obtained by this result.

We perform a separate fit to the WS sample for the D^0 and $\overline{D}^0$ categories. We call x'^+ and y'^+ the mixing parameters of the D^0 and x'^- and y'^- those of the $\overline{D}^0$. The fit procedure and the x' and y' parameter extraction are performed with the same method described for the flavor integrated case in the previous sections of this chapter.

Performing the x' and y' extraction and systematic error propagation described for the flavor integrated case in Section 11.2.3 we obtain the following values of the mixing parameters:

$$\begin{aligned} x'^+ &= (2.53^{+0.54}_{-0.63}\ \text{(stat.)}\ \pm 0.39\ \text{(syst.)}\ )\% \\ y'^+ &= (-0.05^{+0.63}_{-0.67}\ \text{(stat.)}\ \pm 0.50\ \text{(syst.)}\ )\% \end{aligned} \tag{11.13}$$

$$\begin{aligned} x'^- &= (3.55^{+0.73}_{-0.83}\ \text{(stat.)}\ \pm 0.65\ \text{(syst.)}\ )\% \\ y'^- &= (-0.54^{+0.40}_{-1.16}\ \text{(stat.)}\ \pm 0.41\ \text{(syst.)}\ )\% \end{aligned} \tag{11.14}$$

We observe that the parameters $x'^{\pm}(y'^{\pm})$ are compatible within one standard deviation. Therefore, no signal for *CP* violation is present within the error. The no-mixing point is compatible at the 2.9% level for the D^0 case and 2.8% level for the $\overline{D}^0$ case (including systematic uncertainties). The correlation between $x^{\pm'}$ and $y^{\pm'}$ is -0.69 for the D^0 case and -0.66 for the $\overline{D}^0$ case. The contour plots for $x^{\pm'}$ and $y^{\pm'}$ for the D^0 and $\overline{D}^0$ cases are in Figures 11.6 and 11.7 respectively.

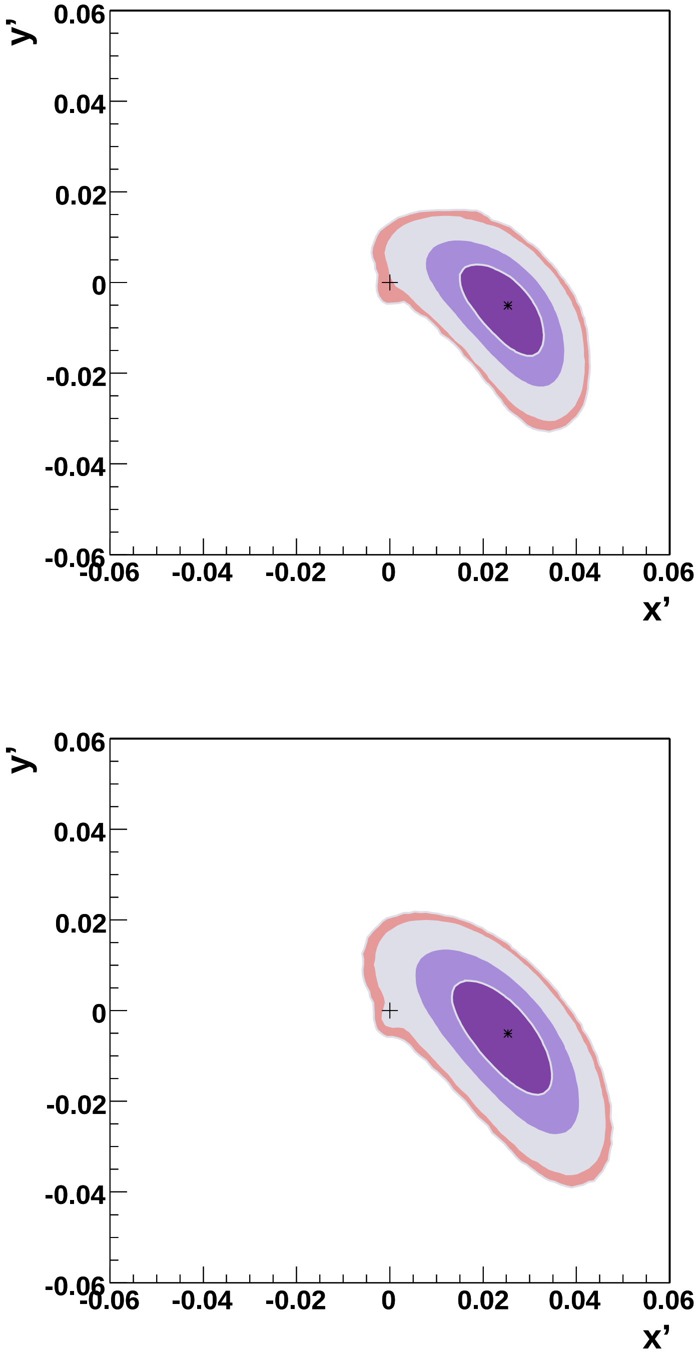

Figure 11.6: Probability contour plot for $x^{+'}$ and $y^{+'}$ with statistical error only (top) and with statistical and systematic error (bottom). The 68.3%, 95.5%, 99.7% and 99.9% probability contour lines are shown.

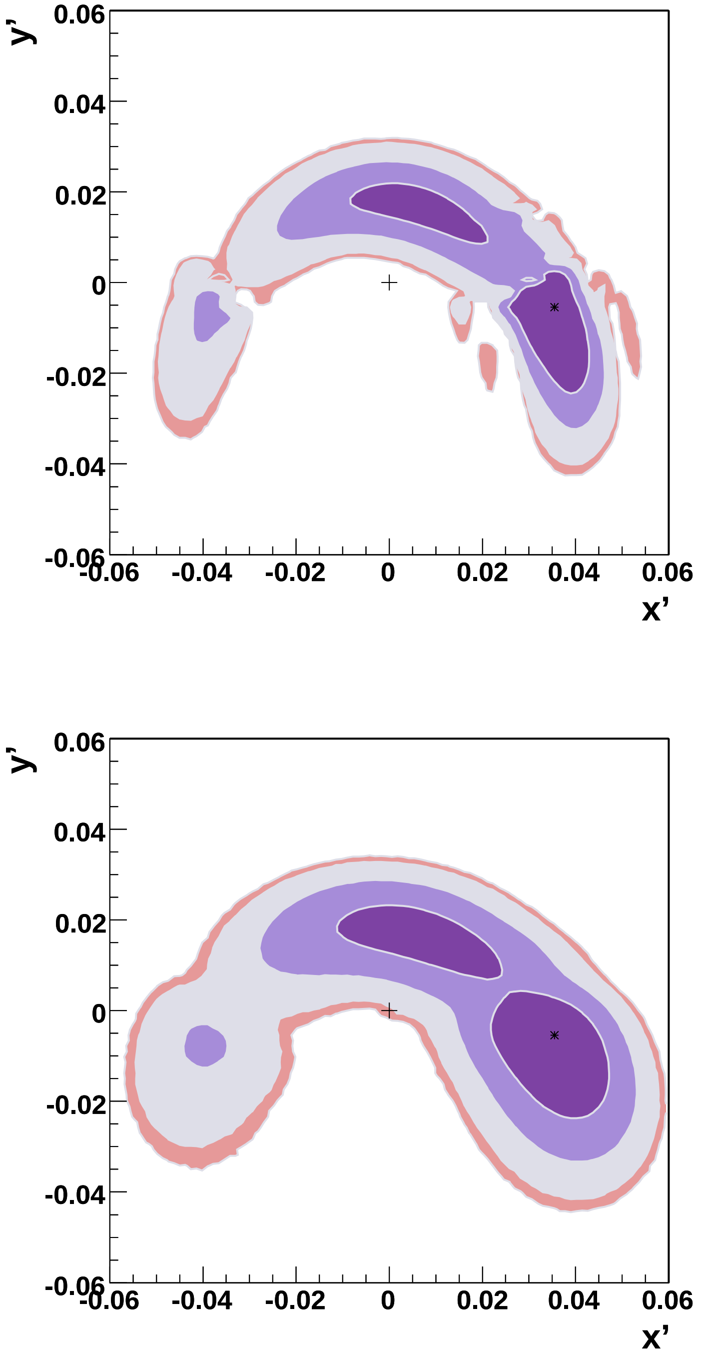

Figure 11.7: Probability contour plot for $x^{-\prime}$ and $y^{-\prime}$ with statistical error only (top) and with statistical and systematic error (bottom). The 68.3%, 95.5%, 99.7% and 99.9% probability contour lines are shown.

Chapter 12

Studies on systematic uncertainties

In this chapter, we discuss the study on systematic uncertainties for the c_1 and $c_2$parameters. We mainly considered as a source of systematic error the signal and background parametrizations, the event selection criteria and the Dalitz plot efficiency evaluation. After this, we describe a method to propagate the error from the $\{c_1, c_2\}$ base to the $\{x', y'\}$ base.

In all the systematic error evaluations, the technique used was to vary the analysis for a particular systematic, refit the data sample, and determine the variation of the parameters with respect to the standard fit. In order to avoid accidental systematics, we performed the systematic error estimation using the blind fit described in Section 10.1. The blinding has been performed by adding to c_1 and c_2 from the fit an unknown constant offset. In this way the blinded fit can be a useful tool for the study in this chapter.

12.1 Signal Dalitz plot model

12.1.1 CF amplitude systematics

Since the mixing is a small effect, we expect that the CF contributions in the WS sample will be dominated by the resonances with the highest fit fraction in the RS Dalitz plot fit. We can estimate the systematics due to the model assumptions using the CLEO model [34] of the Dalitz plot fit of $D^0 \to K^-\pi^+\pi^0$. We refit this model to our RS data, and use the result as the parametrization of the CF amplitude in the WS fit.

12.1.2 DCS amplitude systematics

The systematic contributions coming from the DCS amplitude description are due to the parameters which are fixed in the standard fit and the Dalitz plot model chosen. The first are essentially the mass and width of the resonances and the LASS parametrization coefficients taken from the RS fit. They are estimated by varying the parameters of $\pm 1\sigma$.

The systematic associated to the LASS parametrization can be tested by using a Breit-Wigner function to describe the K^* (1430) s-wave and a flat non-resonant contribution. This systematic is reported as "LASS WS" in Tables 12.1-12.2.

In Section 9.1 we explained that for the nominal fit, only the resonances with an amplitude different from zero within 3σ were retained for the DCS amplitude parametrization. We can test the choice of the model for the Dalitz plot by considering in the fit also those resonances which are not compatible with zero at a 2σ level. These resonances are the K^{*0} (1680) and K^{*+} (1680). This systematic is reported together with the CF Dalitz model systematic as "Dalitz Model" in Tables 12.1-12.2.

12.1.3 Systematic uncertainties for $K^{*\pm}$ (1680) and $\rho(1700)$

As shown in 7.4, the resonances that lie outside our Dalitz plot, and contribute to our amplitudes with their tails, are determined with a shift in their amplitude value. This is mainly due to the inability of our efficiency map to perfectly describe the boundaries of our Dalitz plot. In order to take this effect into account, we determine the difference between the MC generated amplitude value and our fit result of the MC sample, and apply this shift as a systematic to the $K^{*\pm}$ (1680) and $\rho(1700)$ amplitudes.

12.1.4 Resolution effects along the Dalitz plot

Resolution effects along the Dalitz plot may influence our mixing result. This is particularly true for those resonances whose strong phase is rapidly shifted of 180 degrees close to the peak position. One considers this to be rapid if the invariant mass interval in which this shift occurs is compatible with the resolution. To test this effect, we produced a toy-MC of 10^4 signal events. For the generation we considered the Dalitz plot model described for the nominal fit in Section 10.1. For the mixing parameters used in the generation we chose the values obtained from the unblinded fit. We then smeared the Dalitz plot distribution with a Gaussian function having a width of 10 MeV/c^2 in both $m^2_{K\pi}$ and $m^2_{K\pi^0}$. No correlation between the two Dalitz plot variables is considered in the resolution function. We then refitted the smeared sample and compared the mixing results with the values used in generation. No significant change in the parameters is observed within 0.1σ, with σ being the statistical error. Hence we neglect this systematic error.

12.2 Signal resolution function

12.2.1 Resolution offset

We test the source of systematic error due to the presence of a resolution offset by both fixing it to zero and by allowing a different offset for each of the three Gaussian of the resolution model. Floating the offset of the three Gaussian gets the parameters $t_{0,1} = 1.2$,

$t_{0,2} = 2.4$ and $t_{0,3} = 6.1$ fs.

12.2.2 D^0 mean lifetime

In the standard fit the value of the D^0 mean lifetime is taken from the 2006 PDG world average [37]. In order to test this assumption, we use the value extracted from the fit of the RS sample.

12.2.3 Gaussian fractions and scale factors

The Gaussian fractions and scale factors of the resolution function are fixed to the RS D^0 lifetime fit in the standard fit. In order to test the contribution of this assumption to the systematic error, we fit varying them of $\pm 1\sigma$. They are indicated as "Res. factor k" and "Res. fract. f" in Tables 12.1-12.2.

12.2.4 Background parametrization of the RS sample

As shown in 8.3, our estimation in MC of the D^0 lifetime for the RS shows a discrepancy with respect to the MC truth matched background. Assuming that the same behavior is present in the WS data, we must take into account this effect in the resolution function parametrization systematics. To do this, we refit the RS D^0 lifetime data, using the MC truth matched background. We determine the systematic variation for the Gaussian fractions, the scale factors and the resolution offset. We sum in quadrature this errors with the statistical ones, and use them to vary the values of the resolution parameters, as described in the previous subsections.

12.3 Dalitz plot efficiency parametrization

The efficiency parametrization described in Chapter 6 uses one of the invariant masses used to describe the Dalitz plot ($m^2_{K\pi}$) and the helicity angle between the $K-\pi$ directions. One way to test this possible source of systematic is using another couple of particles of the final state to extract the parametrization. We choose to perform it with the $K-\pi^0$ couple. This is reported as "Dalitz plot eff." in Tables 12.1-12.2. Additional plots for the $K-\pi^0$ efficiency calculation and comparison with the nominal choice are reported in Appendix E.

12.4 Combinatoric background parametrization

For the combinatoric and *bad*-D^0 parametrization, one can estimate the systematic using the truth-matched background from the MC sample in the fit. Since Figure 9.13 shows a possible shift between the true D^0 lifetime background distribution and our estimation from the sidebands, this effect is taken into account in this approach. This estimation is reported as "Comb. backgr." in Tables 12.1-12.2.

12.5 Parameters from the $\{m_{K\pi\pi^0}$,Δm $\}$ fit

To determine the contribution of the choice of these parameters to the systematic error, we vary them of $\pm\sigma$ of the statistical error. This systematics effects are indicated as N_{sig}, N_{mis} and $N_{comb} + N_{bad-D^0}$ in Tables 12.1-12.2. Since in Figure 5.12 it appears that the number of *bad-*D^0 events can be underestimated, we conservatively inflate the systematic error on the number of signal events by varying this parameter of $\pm 1.5\sigma$ of the statistical error.

Another potential source of systematic error is the choice of the signal region of $m_{K\pi\pi^0}$,Δm $\}$ distribution. In order to estimate this systematic, we vary the signal region definition. We firstly redefine the cut in the D^0 mass, by moving it from $1.8495 < m_{K\pi\pi^0} < 1.8795$ to $1.846 < m_{K\pi\pi^0} < 1.882$ GeV/c^2. This cut is still symmetric with respect to the PDG value of the D^0 mass. The systematic effect is reported as "$m_{K\pi\pi^0}$ region" in Tables 12.1-12.2.

To estimate the systematic effect due to the choice of the Δm signal region, we move the cut from $0.1449 < \Delta m < 0.1459$ to $0.14485 < \Delta m < 0.14595$ GeV/c^2. Also this cut is symmetric with respect to the PDG value of Δm. This effect is reported as "Δm region" in Tables 12.1-12.2.

12.6 Selection criteria

12.6.1 Proper time and proper time error selection

In the standard fit, we require the D^0 lifetime to be $-2 < t < 4$ (ps). We test the sensitivity of c_1 and c_2 to this cut by both restricting the interval to $-1 < t < 3.5$ (ps) and by widening it to $-5 < t < 10$ (ps). We cannot select a lifetime range with positive values only because in that region we cannot disentangle the RS lifetime and the resolution function distributions.

The standard cut on the D^0 lifetime error is $\sigma_t < 0.5$ (ps). We test the sensitivity of c_1 and c_2 to this cut by both restricting the cut to $\sigma_t < 0.4$ (ps) and by widening it to $\sigma_t < 0.6$ (ps).

12.6.2 Best candidate selection systematic

We determine this contribution to the systematic by either varying and removing the selection of the best candidate of the event. Only the one which has the highest variation is taken as a systematic estimation.

12.6.3 Systematic errors propagation to x' and y'

In order to propagate the systematic errors to the x' and y' determination, we construct a systematics covariance matrix, for a given variation of the fit, based on the variation of the signal parameters from the nominal values. The (i, j) matrix element is given as

$$s_{ij} = \delta_i \delta_j \tag{12.1}$$

where δ_i is the difference between the two fits for the variable i. The total systematics covariance matrix is obtained by adding together the covariance matrices from the different systematics sources linearly, which is equivalent to sum the square of the errors with correlations included. We then sum the total systematics covariance matrix to the statistical covariance matrix and use this sum to generate x' and y' as described in 11.2.2.

12.7 Summary of systematic errors

The contributions to the systematic error on the signal parameters in the fit are summarized in Tables 12.1-12.2, in units of the statistical error of the standard blind fit. For completeness we also report the total systematics covariance matrix, obtained summing all the systematics matrices from each contribution, in Tables 12.3-12.4.

	$a_{K_2^{*0}(1430)}$	$\phi_{K_2^{*0}(1430)}$	$a_{K_0^{*-}(1430)}$	$\phi_{K_0^{*-}(1430)}$	$a_{K^{*-}}$	ϕ_{Kstarm}	$a_{K_0^{*0}(1430)}$
K^{*-} mass	0.00233	0.0421	0.0221	0.0614	0.0372	0.00269	0.018
K^{*-} width	0.000536	0.00713	0.00276	0.000738	0.0357	0.0123	0.00395
ρ mass	0.0176	0.0551	0.0779	0.151	0.112	0.0925	0.0428
ρ width	0.00392	0.0226	0.00927	0.0488	0.0178	0.0206	0.0167
K^{*0} mass	0.00182	0.0116	0.0144	0.0338	0.0196	0.0115	0.0114
K^{*0} width	0.00147	0.000857	0.000183	0.00591	0.0076	0.0041	0.00325
$K^{*-}(1430)$ mass	0.00386	0.0167	0.0112	0.0329	0.000842	0.00787	0.00404
$K^{*-}(1430)$ width	0.00211	0.00618	0.0212	0.00821	0.000539	0.00576	0.0296
$K^{*0}(1430)$ mass	0.00614	0.001	0.00342	0.00414	0.00583	0.00037	0.00561
$K^{*0}(1430)$ width	0.000588	0.00239	0.00199	0.00593	0.00176	0.00192	0.00797
$K_2^{*0}(1430)$ mass	0.0349	0.0344	0.00217	0.00759	0.00691	0.014	0.00782
$K_2^{*0}(1430)$ width	0.2	0.0518	0.0174	0.0443	0.00585	0.0513	0.03
Res. factor k_1	0.000492	0.00511	0.00675	0.00913	0.00452	0.00425	0.00138
Res. factor k_2	0.0015	0.0189	0.00756	0.0418	0.00204	0.02	0.00596
Res. factor k_3	0.00121	0.00858	0.0011	0.0138	0.00116	0.00919	0.00362
Res. fract. f_1	0.000157	0.00205	0.00238	0.00443	0.00116	0.00191	0.00049
Res. fract. f_2	0.000413	0.0274	0.00179	0.0508	0.00238	0.0291	0.0118
N_{sig}	0.0882	0.00343	0.0372	0.0547	0.176	0.0351	0.0153
N_{mis}	0.083	0.05	0.22	0.101	0.161	0.0739	0.158
$N_{comb} + N_{bad-D^0}$	0.0173	0.077	0.314	0.271	0.0389	0.0749	0.304
Lifetime error	0.327	0.28	0.348	0.536	0.539	0.34	0.844
Lifetime range	0.0894	0.0453	0.193	0.132	0.242	0.11	0.0787
Mean D^0 lifet.	0.000842	0.00143	0.000538	0.00427	0.000369	0.00408	0.00228
Res. offset	0.024	0.0215	0.0624	0.0415	0.0561	0.023	0.0713
Dalitz Plot eff.	0.0836	0.0047	0.0654	0.137	0.0389	0.123	0.0567
Dalitz model	0.2	0.0556	0.138	0.0281	0.0418	0.0484	0.0883
$\rho(1700)$ param.	0.0283	0.545	0.182	0.494	0.0655	0.0863	0.213
LASS WS	2.11	4.83	0	0	0.0671	0.407	0
Comb. backgr.	0.0889	0.0744	0.202	0.086	0.0274	0.124	0.0497
m_{D^0} region	0.246	0.0555	0.198	0.05	0.0258	0.0457	0.0609
Δm region	0.0909	0.103	0.323	0.217	0.0669	0.0905	0.321
Total	2.18	4.878	0.7483	0.8658	0.6664	0.6089	1.006

Table 12.1: Systematic error contributions summary (I), the contributions are in units of σ of the parameters.

	$\phi_{K_0^{*0}(1430)}$	$a_{K^{*0}}$	$\phi_{K^{*0}}$	$a_{\rho(1700)}$	$\phi_{\rho(1700)}$	c_1	c_2
K^{*-} mass	0.0429	0.0195	0.0264	0.0417	0.0082	0.0746	0.0757
K^{*-} width	0.00893	0.00438	0.000508	0.00339	0.00994	0.012	0.000222
ρ mass	0.148	0.0456	0.078	0.0763	0.0302	0.192	0.193
ρ width	0.0452	0.00274	0.0228	0.034	0.00221	0.0657	0.0499
K^{*0} mass	0.0303	0.00343	0.00356	0.0215	0.000479	0.0373	0.0394
K^{*0} width	0.00904	0.0186	0.00698	0.0026	0.00479	0.0127	0.00812
$K^{*-}(1430)$ mass	0.0223	0.00646	0.00016	0.0262	0.00904	0.0188	0.016
$K^{*-}(1430)$ width	0.00688	0.00278	0.00359	0.00139	0.00595	0.00712	0.00482
$K^{*0}(1430)$ mass	0.00665	0.00198	0.00134	0.00402	0.00279	0.00683	0.00462
$K^{*0}(1430)$ width	0.00478	0.000305	0.00237	0.00618	0.00102	0.0062	0.00678
$K_2^{*0}(1430)$ mass	0.00409	0.0056	0.00393	0.0109	0.00548	0.0118	0.00389
$K_2^{*0}(1430)$ width	0.0296	0.00896	0.0275	0.00868	0.0393	0.0436	0.0504
Res. factor k_1	0.00587	0.00211	0.00798	0.00469	0.00582	0.00659	0.0117
Res. factor k_2	0.022	0.0144	0.0314	0.0263	0.00696	0.00433	0.0539
Res. factor k_3	0.00711	0.00659	0.0113	0.00833	0.00216	0.00132	0.0184
Res. fract. f_1	0.00258	0.00103	0.00351	0.00272	0.00186	0.00191	0.00521
Res. fract. f_2	0.0266	0.0212	0.0397	0.0313	0.00673	0.00322	0.0683
N_{sig}	0.0204	0.0827	0.0779	0.0424	0.0252	0.00351	0.0954
N_{mis}	0.0579	0.00417	0.0039	0.109	0.0546	0.0768	0.0243
$N_{comb} + N_{bad-D^0}$	0.135	0.143	0.13	0.267	0.135	0.125	0.203
Lifetime error	0.578	1.12	0.652	0.39	0.785	0.421	0.271
Lifetime range	0.306	0.123	0.0806	0.0461	0.0786	0.231	0.155
Mean D^0 lifet.	0.00273	0.00224	0.00382	0.000949	0.000359	0.00073	0.00933
Res. offset	0.0501	0.00987	0.0105	0.0553	0.00575	0.11	0.0114
Dalitz Plot eff.	0.106	0.0627	0.0706	0.106	0.0525	0.0947	0.102
Dalitz model	0.169	0.135	0.0188	0.00948	0.134	0.0225	0.0579
$\rho(1700)$ param.	0.0678	0.0761	0.245	0	0	0.213	0.116
$LASSWS$	0	0.819	0.163	1.99	0.688	0.221	0.234
Comb. backgr.	0.212	0.0198	0.186	0.123	0.261	0.0241	0.000666
m_{D^0} region	0.177	0.0429	0.054	0.0494	0.292	0.0215	0.188
Δm region	0.272	0.0721	0.00769	0.354	0.000507	0.147	0.0374
Total	0.8221	1.418	0.7714	2.091	1.137	0.6656	0.5712

Table 12.2: Systematic error contributions summary (II), the contributions are in units of σ of the parameters.

	$a_{K_2^{*0}(1430)}$	$\phi_{K_2^{*0}(1430)}$	$a_{K_0^{*-}(1430)}$	$\phi_{K_0^{*-}(1430)}$	$a_{K^{*-}}$	$\phi_{K^{*-}}$	$a_{K_0^{*0}(1430)}$
$a_{K_2^{*0}(1430)}$	0.0013	2.1	0.0017	0.018	-0.00025	0.086	-0.0019
$\phi_{K_2^{*0}(1430)}$	2.1	3.7e+03	-1.3	25	-0.17	1.3e+02	0.61
$a_{K_0^{*-}(1430)}$	0.0017	-1.3	0.37	-1.6	0.0031	-0.15	0.094
$\phi_{K_0^{*-}(1430)}$	0.018	25	-1.6	87	-0.21	6.9	-3.3
$a_{K^{*-}}$	-0.00025	-0.17	0.0031	-0.21	0.0013	-0.06	0.013
$\phi_{K^{*-}}$	0.086	1.3e+02	-0.15	6.9	-0.06	11	-0.5
$a_{K_0^{*0}(1430)}$	-0.0019	0.61	0.094	-3.3	0.013	-0.5	0.2
$\phi_{K_0^{*0}(1430)}$	0.032	-28	-3	1e+02	-0.42	15	-5.7
$a_{K^{*0}}$	-0.0012	-1.7	-0.011	-0.23	0.0011	-0.092	0.009
$\phi_{K^{*0}}$	-0.029	-80	-0.21	48	-0.16	5.6	-2.2
$a_{\rho(1700)}$	-0.15	-2.7e+02	-0.33	9.9	-0.015	-9.4	-0.55
$\phi_{\rho(1700)}$	-0.81	-1.1e+03	-8.2	-1.1e+02	0.57	-55	6
c_1	-0.00085	-1.3	0.011	-0.47	0.0018	-0.12	0.021
c_2	0.00089	1.3	-0.013	0.21	-0.00078	0.12	-0.011

Table 12.3: Global systematics covariance matrix (I).

	$\phi_{K_0^{*0}(1430)}$	$a_{K^{*0}}$	$\phi_{K^{*0}}$	$a_{\rho(1700)}$	$\phi_{\rho(1700)}$	c_1	c_2
$a_{K_2^{*0}(1430)}$	0.032	-0.0012	-0.029	-0.15	-0.81	-0.00085	0.00089
$\phi_{K_2^{*0}(1430)}$	-28	-1.7	-80	-2.7e+02	-1.1e+03	-1.3	1.3
$a_{K_0^{*-}(1430)}$	-3	-0.011	-0.21	-0.33	-8.2	0.011	-0.013
$\phi_{K_0^{*-}(1430)}$	1e+02	-0.23	48	9.9	-1.1e+02	-0.47	0.21
$a_{K^{*-}}$	-0.42	0.0011	-0.16	-0.015	0.57	0.0018	-0.00078
$\phi_{K^{*-}}$	15	-0.092	5.6	-9.4	-55	-0.12	0.12
$a_{K_0^{*0}(1430)}$	-5.7	0.009	-2.2	-0.55	6	0.021	-0.011
$\phi_{K_0^{*0}(1430)}$	2.3e+02	-0.31	63	18	-1.9e+02	-0.71	0.33
$a_{K^{*0}}$	-0.31	0.0026	-0.17	0.11	1.4	0.002	-0.0006
$\phi_{K^{*0}}$	63	-0.17	42	11	-70	-0.27	0.078
$a_{\rho(1700)}$	18	0.11	11	22	70	0.028	-0.064
$\phi_{\rho(1700)}$	-1.9e+02	1.4	-70	70	1e+03	1	-0.45
c_1	-0.71	0.002	-0.27	0.028	1	0.0036	-0.0021
c_2	0.33	-0.0006	0.078	-0.064	-0.45	-0.0021	0.0027

Table 12.4: Global systematics covariance matrix (II).

Chapter 13

Impact of the result and conclusions

In this chapter, we make an educated evaluation of the impact of this result to the knowledge of the mixing parameters. As explained in Section 2.2, this analysis is not sensitive to x and y directly, but rather to those parameters rotated by an unknown strong phase. Nevertheless, using other constraints on the mixing parameters, one can obtain information on mixing using this result. It is also possible to get a sense of the size of the strong phase.

13.1 Combination of results

13.1.1 Input parameters considered

In most cases, the input values considered for different parameters were taken from the official 2008 averages made by the HFAG group [22]. They are summarized in Table 1.1. Where provided by the authors, correlation coefficients were used during the extraction procedure. When no correlation was provided, we considered a negligible correlation between the mixing parameters. We generate 10^7 events for the extraction of the parameters.

13.1.2 Combination procedure

We perform the combination of all the measurements using a Bayesian approach. We generate the mixing parameters x and y, the strong phases $\delta_{K\pi}$ (present in the $D^0 \to K^+ \pi^-$ mixing analysis) and δ_0 with a flat distribution. We reweight each uniformly generated event with the distribution of the experimental results shown in Table 1.1. All the results are considered to be in a Gaussian regime. We then plot the distribution of the reweighted events and integrate it to get probability intervals.

13.1.3 Combination of the experimental results with and without this analysis

The first exercise, is to plot the distribution of x, y and $\delta_{K\pi}$ using all the results except the one presented in this analysis. The one dimensional probability distributions for the three parameters are in Figures 13.1-13.3 (top). A summary of the combined values for the three parameters are presented in Table 13.1. In any case, the most important plot is the two dimensional probability contour plot in the $x - y$ plane. This plot allows to see with which precision the no-mixing point is excluded. For the combination of all results except the $D^0 \to K^+\pi^-\pi^0$, it is shown in Figure 13.4 (top). One can determine directly from the probability contour plot that the no-mixing point is excluded with a probability of 0.001%.

Parameter	Central value and error	95% interval
x	0.742 ± 0.329 %	[0.11-1.39]%
y	0.694 ± 0.178 %	[0.34-1.05]%
$\delta_{K\pi}$	17.6 ± 26.9	[-66.8-61.1]

Table 13.1: Summary of the combined values of x, y and $\delta_{K\pi}$ without the $D^0 \to K^+\pi^-\pi^0$ result.

The next step is to add the $D^0 \to K^+\pi^-\pi^0$ result presented in this thesis to the combination. Note that in this case, we can also determine the δ_0 phase from the combination. We use the same procedure described above for the previous combination. The probability plots corresponding to the x, y, $\delta_{K\pi}$ and $delta_0$ are shown in Figures 13.1-13.5 (bottom). In this case the no-mixing point is excluded with a probability of 0.0004%, which constitutes an improvement over the previous scenario. It is also very interesting to notice that the central value of the two strong phases seem compatible. One should remember that these phases can be directly determined by performing an analysis of coherently produced D^0-$\overline{D}^0$ couples. This analysis could be performed in the CLEOc or BESIII environments.

Parameter	Central value and error	95% interval
x	0.901 ± 0.325 %	[0.24-1.52]%
y	0.736 ± 0.181 %	[0.38-1.09]%
$\delta_{K\pi}$	21.1 ± 22.8	[-58.0-61.9]
δ_0	10.2 ± 32.8	[-59.1-72.8]

Table 13.2: Summary of the combined values of x, y and $\delta_{K\pi}$ with the $D^0 \to K^+\pi^-\pi^0$ result.

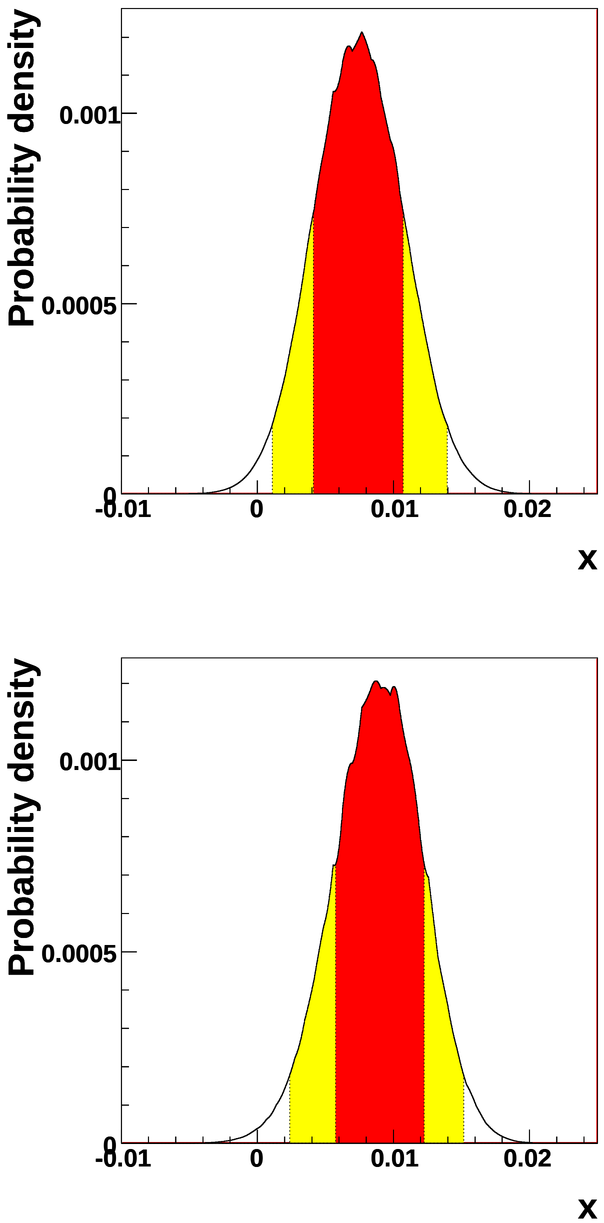

Figure 13.1: Probability distribution for the combined x without the $D^0 \to K^+\pi^-\pi^0$ result (top) and with it (bottom). The red (yellow) area represent the 68% (95%) probability interval.

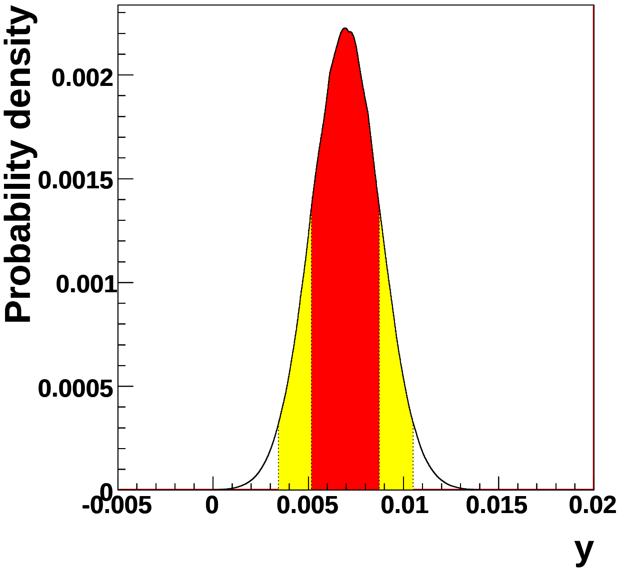

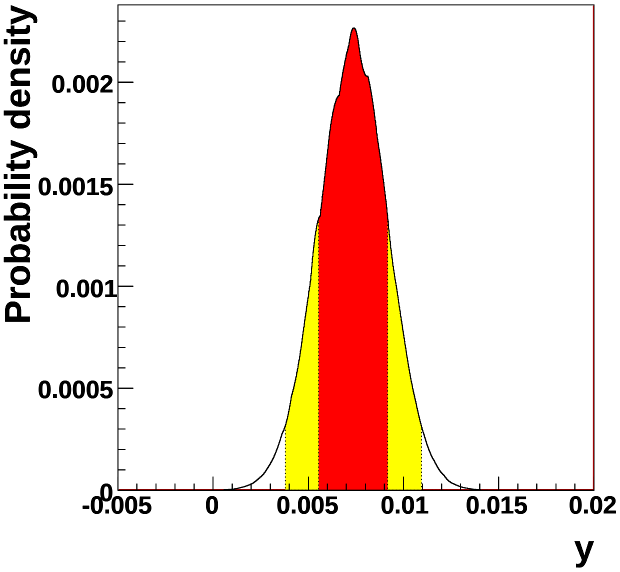

Figure 13.2: Probability distribution for the combined y without the $D^0 \to K^+\pi^-\pi^0$ result (top) and with it (bottom). The red (yellow) area represent the 68% (95%) probability interval.

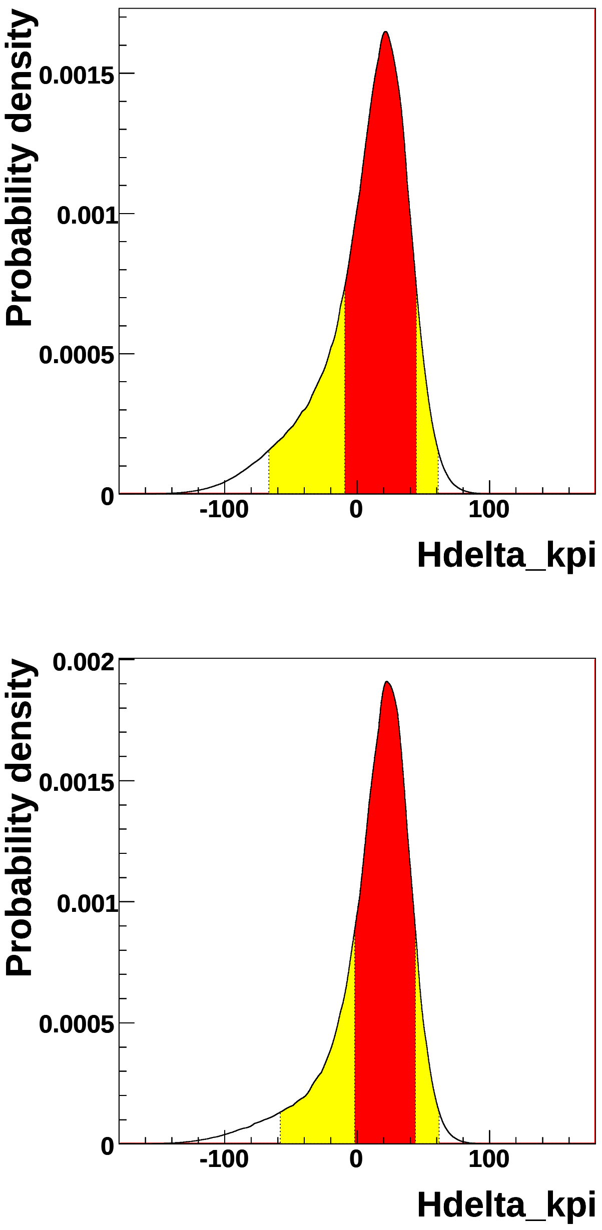

Figure 13.3: Probability distribution for the combined $\delta_{K\pi}$ without the $D^0 \to K^+\pi^-\pi^0$ result (top) and with it (bottom). The red (yellow) area represent the 68% (95%) probability interval.

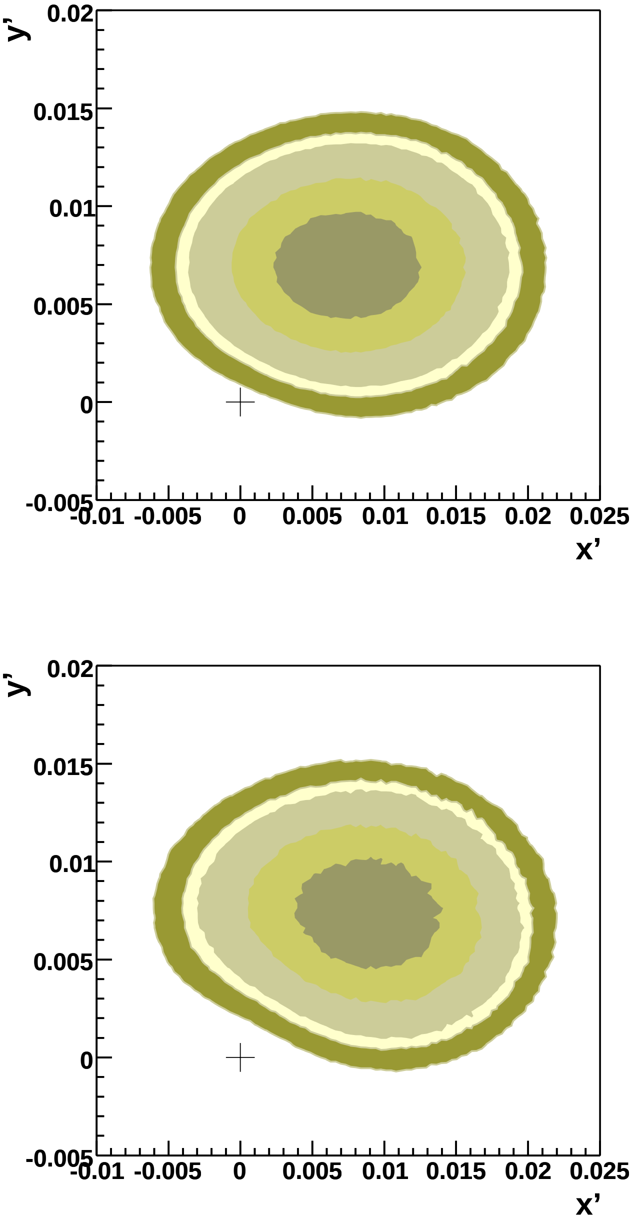

Figure 13.4: Probability contour plot on the $x-y$ plane for the combination of all the mixing results excluding $D^0 \rightarrow K^+\pi^-\pi^0$ (top) and including it (bottom). The contours correspond to the 68%, 95%, 99%, 99.9% and 99.99%.

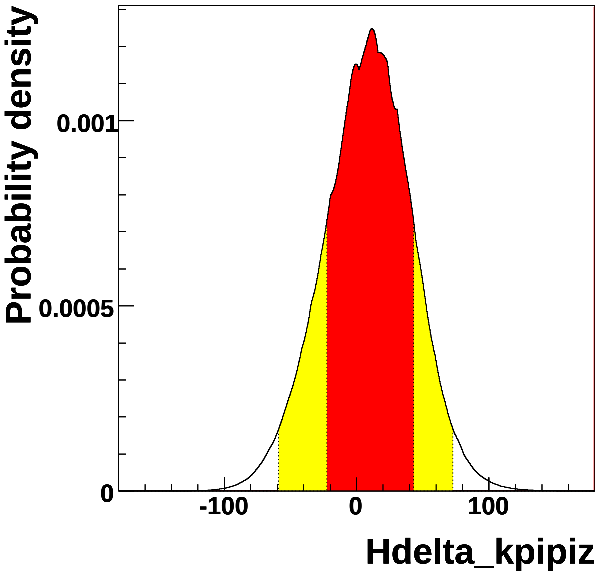

Figure 13.5: Probability distribution for the combined δ_0 adding the $D^0 \rightarrow K^+\pi^-\pi^0$ result. The red (yellow) area represent the 68% (95%) probability interval.

13.2 Conclusions

In the previous section, we show with a very simplified combination technique that this analysis provides a significant constraint on the mixing parameters. The no-mixing point in the $x-y$ plane is excluded with significantly higher precision (from 0.001% to 0.0004%). This proves that the time-dependent Dalitz plot technique used to extract the mixing parameters is competitive with the two-body decays analyses. Moreover, the PDF in our case presents a linear dependence in both the parameters x' and y'. Using the measured value of y_{CP} (in the CP conservation limit) or an external input on the unknown strong phase δ_0, this analysis can put a powerful (indirect) constraint on x.

It has to be pointed out that one of the strengths of this work is the possibility to use the $D^0 \rightarrow K^-\pi^+\pi^0$ decay as a source of information on our signal, as it shares its topological structure. Other decay channels, like $D^0 \rightarrow K_S\pi^+ \pi^-$ can provide a direct measurement of x but do not have a similar control sample. For that reason, the study of self-conjugate final states is much more difficult, and higher systematic errors are expected.

Another observation can be made at this point. D^0-$\overline{D}^0$ mixing is a small effect. It is much more natural to look for it on top of a process that has a small rate too (so a DCS decay like $D^0 \rightarrow K^+\pi^-\pi^0$). The search for mixing in CF decays (like $D^0 \rightarrow K_S\pi^+ \pi^-$) or SCS (like $D^0 \rightarrow \pi^+ \pi^- \pi^0$) is instead an attempt to look for a small effect inside a sample with higher statistics.

This analysis is also the first determination of the DCS component of the $D^0 \rightarrow K^+\pi^-\pi^0$ decay. Previous studies of this decay neglected any mixing contributions, so in fact the superposition of a DCS and a CF amplitude times the mixing parameters was studied.

13.3 Prospectives

As pointed out in Chapter 1, it is very difficult to give a prediction of the mixing parameters within and beyond the SM. Though it is important to have the most precise determination of x and y, it seems unlikely that any NP contribution will be evident solely in mixing. From the combination of the results in Section 13.1 it appears that x and y are of the same order of magnitude. One could have had an hint of the presence of NP contributions if $|x|$ was found to be at least one order of magnitude larger than $|y|$. This is because, as explained in Section 1.2, x is more sensitive to the short-range contributions, where NP would have been more likely to appear.

As this is not the case, the next step one should proceed with is the search of *CP* violation in the charm sector. In this case, a good knowledge of the mixing parameters is crucial, as *CP* could be violated in mixing or in the interference between mixing and the direct decay.

Though much information can still be determined within the B-factories dataset, the statistics at disposal in the present scenario limits any finding. The most optimistic expectation of *CP* violation in the SM limits its size to at best 0.1% [41]. The current uncertainty on the *CP* violation parameters is of the order of 0.4-0.8% (for example in [42]), and the statistical error is still dominant. It is obvious that for one to be able to probe the scale of CPV in the SM and beyond a high luminosity flavor factory will be needed.

Appendix A

RS time independent Dalitz plot fit with no background

As a first estimation of the RS Dalitz plot, we performed a fit to the sample selecting the signal region of $m_{K\pi\pi^0}$ and Δm, neglecting the background contributions. For signal, the model used is the same as the one described in Section 7.1. The plot of the fit results for the three invariant masses projections is shown in Figure A.1, while the summary of the results are in Tables A.1 and A.2.

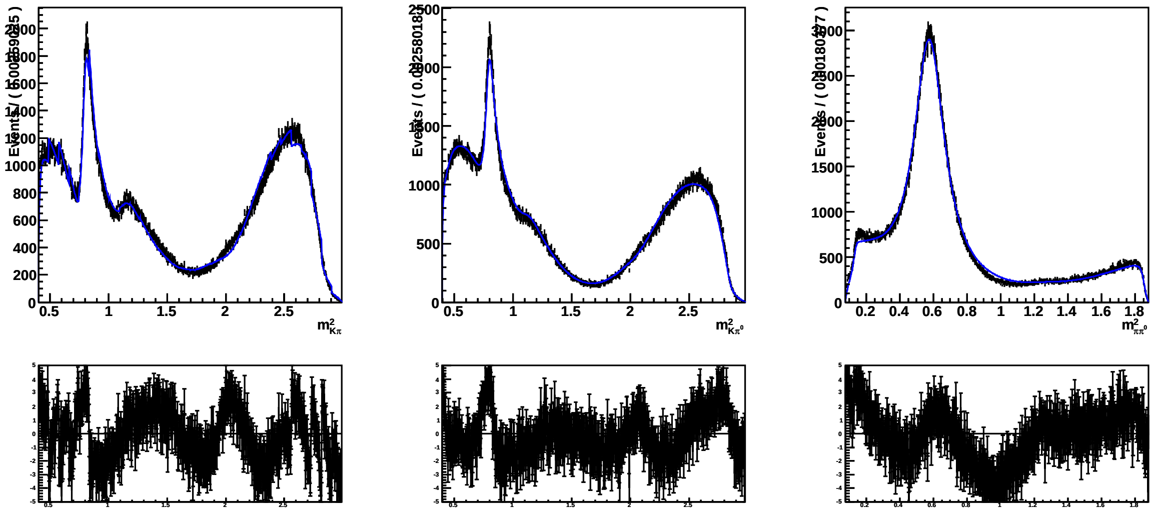

Figure A.1: RS Dalitz plot data and fit results (top) along with the residuals of the fit (bottom). The dots are the RS data sample, the blue line is the fit result. This fit is performed ignoring the background contributions.

Resonance	Amplitude	Phase (degrees)	Fit Fraction (%)
$\rho(770)$	1 (fixed)	0 (fixed)	68.9 ± 7.6
$K^{*-}(1680)$	1.91 ± 0.07	178.0 ± 2.0	0.65 ± 0.09
$K_2^{*-}(1430)$	0.017 ± 0.001	-168.5 ± 3.4	0.13 ± 0.01
$K_2^{*0}(1430)$	0.0374 ± 0.0007	40.6 ± 1.1	0.56 ± 0.05
$K^{*-}(1410)$	0.16 ± 0.01	46.6 ± 5.5	0.09 ± 0.01
$K_0^{*-}(1430)$	3.14 ± 0.04	175.6 ± 0.9	3.5 ± 0.3
$K^{*-}(892)$	0.384 ± 0.001	163.3 ± 0.2	10.6 ± 1.1
$K^{*0}(1410)$	0.07 ± 0.01	-272.9 ± 8.3	0.017 ± 0.006
$K_0^{*0}(1430)$	2.65 ± 0.02	85.4 ± 0.4	4.6 ± 0.5
$K^{*0}(1680)$	3.18 ± 0.06	-12.4 ± 1.2	1.18 ± 0.22
$K^{*0}(892)$	0.396 ± 0.001	5.7 ± 0.3	11.3 ± 1.2
$\rho(1700)$	5.67 ± 0.10	131.5 ± 1.1	3.9 ± 0.4
Total fit fraction = 106%			

Table A.1: Fit results for the RS data sample, ignoring the background contributions. Amplitudes, phases and fit fractions are reported

Parameter	Value
$B_{K^{*-}}$	0.9 ± 0.008
$B_{K^{*0}}$	-1.2 ± 0.009
$R_{K^{*-}}$	0.4 ± 0.005
$R_{K^{*0}}$	0.3 ± 0.007
$a_{K^{*-}}$	4 ± 0.09
$a_{K^{*0}}$	7 ± 0.1
$\phi_{B,K^{*-}}$	-78 ± 1
$\phi_{B,K^{*0}}$	-167 ± 1
$\phi_{R,K^{*-}}$	139 ± 1
$\phi_{R,K^{*0}}$	87 ± 1
$r_{K^{*-}}$	-2.4 ± 0.06
$r_{K^{*0}}$	-6.6 ± 0.2

Table A.2: Fit results for the LASS parameters, with background contributions ignored.

Appendix B

An alternative WS background parametrization

In this appendix we present an alternative method to describe the WS background both on the Dalitz plot and on the D^0 lifetime. This method was not chosen for the nominal fit: this method has the weakness of ignoring any dependence of the background Dalitz plot with respect to the D^0 lifetime distribution. The method described in 9.2, on the contrary, explicitely takes any possible correlation into account.

B.1 Dalitz plot parametrization

As far as the Dalitz plot is concerned, the combinatoric and *bad*-D^0 backgrounds are described using a third order polynomial in the two invariant masses $m^2_{K\pi}$ and $m^2_{K\pi^0}$. Since this sample is composed also by partially reconstructed D^0 s, one can expect to find significant peaks for the mainly contributing resonances of the decay. For this reason, an incoherent sum of Breit-Wigners is added to the polynomial for the ρ, K^{*+} and K^{*0} resonances. The total Dalitz background parametrization is:

$$\begin{aligned} A(m^2_{K\pi}, m^2_{K\pi^0}) &= f_r \sum_{i=1}^{3} |a_i BW_i(m^2_{K\pi}, m^2_{K\pi^0})|^2 + (1-f_r)|1 + a_1 m^2_{K\pi} + a_2 m^2_{K\pi^0} \\ &\quad + a_3 m^4_{K\pi} + a_4 m^2_{K\pi} m^2_{K\pi^0} + a_5 m^4_{K\pi^0} + a_6 m^6_{K\pi} + a_7 m^4_{K\pi} m^2_{K\pi^0} \\ &\quad + a_8 m^2_{K\pi} m^4_{K\pi^0} + a_9 m^6_{K\pi^0}| \end{aligned} \tag{B.1}$$

The interval in which we isolate the two sidebands samples are:

$$\textit{left}\text{ region: } 1.76 < m_{K\pi\pi^0} < 1.78\,\mathrm{GeV}/c^2$$

$$\textit{right}\text{ region: } 1.93 < m_{K\pi\pi^0} < 1.95\,\mathrm{GeV}/c^2$$

Since we used a D^0 mass constraint in the reconstruction procedure, the mass of the resonances in the two sidebands may vary along the $m_{K\pi\pi^0}$ distribution. For this reason the following procedure is adopted to interpolate the background shape of the Dalitz plot in the signal region:

- we consider the interpolated histogram of the left and right sidebands separately. We generate the two samples of background according to the histogram;
- we merge the two samples. The number of events of the merged sample corresponds to the number of events of background in the $m_{K\pi\pi^0}$ signal region:
- the background parametrization is fitted to this sample and the polynomial coefficients are extracted along with the amplitudes associated to the Breit-Wigner's.

In Figure B.1 the distribution of the merged sample and the fit result are presented. The corresponding values of the fit parameters are reported in Table B.1.

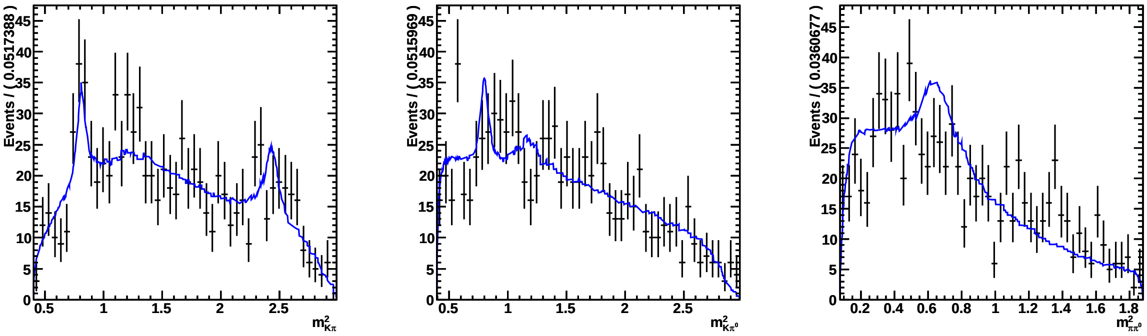

Figure B.1: Plot of the three invariant squared masses of the merged WS background Dalitz plot. Dots are the data, the blue line is the fit result.

B.2 D^0 lifetime parametrization

In order to describe the D^0 lifetime distribution in the sidebands region of $m_{K\pi\pi^0}$, the sum of a Crystal Ball and a Cruijff functions is considered. The total PDF is:

$$\begin{aligned} cb(t,\bar{t},\sigma,\alpha,n) &= \begin{cases} exp(-\frac{(t-\bar{t})^2}{2\sigma^2}) & \text{if } \frac{t-\bar{t}}{\sigma} < \alpha \\ a(b+\frac{t-\bar{t}}{\sigma})^{-n} & \text{if } \frac{t-\bar{t}}{\sigma} > \alpha \end{cases} \qquad \text{(B.2)} \\ \alpha &> 0,\ a = \frac{e^{-\alpha^2/2}}{\alpha},\ b = \frac{1}{\alpha} - \alpha \end{aligned}$$

Parameter	Value
a_ρ	1.33 ± 0.12
m_ρ	0.814 ± 0.214
$a_{K^{*+}}$	0.972 ± 0.169
$m_{K^{*+}}$	0.898 ± 0.004
$a_{K^{*0}}$	0.980 ± 0.199
$m_{K^{*0}}$	0.902 ± 0.004
a_1	11.2 ± 3.0
a_2	-80.7 ± 1.7
a_3	-39.8 ± 1.5
a_4	$44.6 + / - 0.9$
a_5	44.8 ± 3.1
a_6	8.7 ± 0.4
a_7	-8.0 ± 0.3
a_8	-11.1 ± 0.8
a_9	-8.8 ± 1.2
f_r	$0.07 + / - 0.05$

Table B.1: Fit results for the WS background merged sample.

$$Cf(t, t_0, \sigma_{L,R}, \alpha_{L,R}) = \begin{cases} exp(-\frac{(t-t_0)^2}{2\sigma_L^2+\alpha_L(t-t_0)^2}) & \text{if } t < t_0 \\ \\ exp(-\frac{(t-t_0)^2}{2\sigma_R^2+\alpha_R(t-t_0)^2}) & \text{if } t > t_0 \end{cases} \quad (B.3)$$

$$P_{bkg}(t, \bar{t}, \sigma, \alpha, n, t_0, \sigma_{L,R}, \alpha_{L,R}) = f_c \cdot cb(t, \bar{t}, \sigma, \alpha, n) + (1 - f_c) \cdot Cf(t, t_0, \sigma_{L,R}, \alpha_{L,R}) \quad (B.4)$$

The fit results for these parameters are reported in Table B.2. The plot of the data and fit is shown in Figure B.2.

Parameter	Value
$\bar{t}$	0.0757 ± 0.0159
σ	0.210 ± 0.026
α	-0.469 ± 0.073
n	9.9 ± 8.9
t_0	-0.013 ± 0.027
σ_L	0.330 ± 0.016
σ_R	0.407 ± 0.019
α_L	0.110 ± 0.006
α_R	0.091 ± 0.060
f_c	0.273 ± 0.104

Table B.2: Fit results for the WS background time distribution.

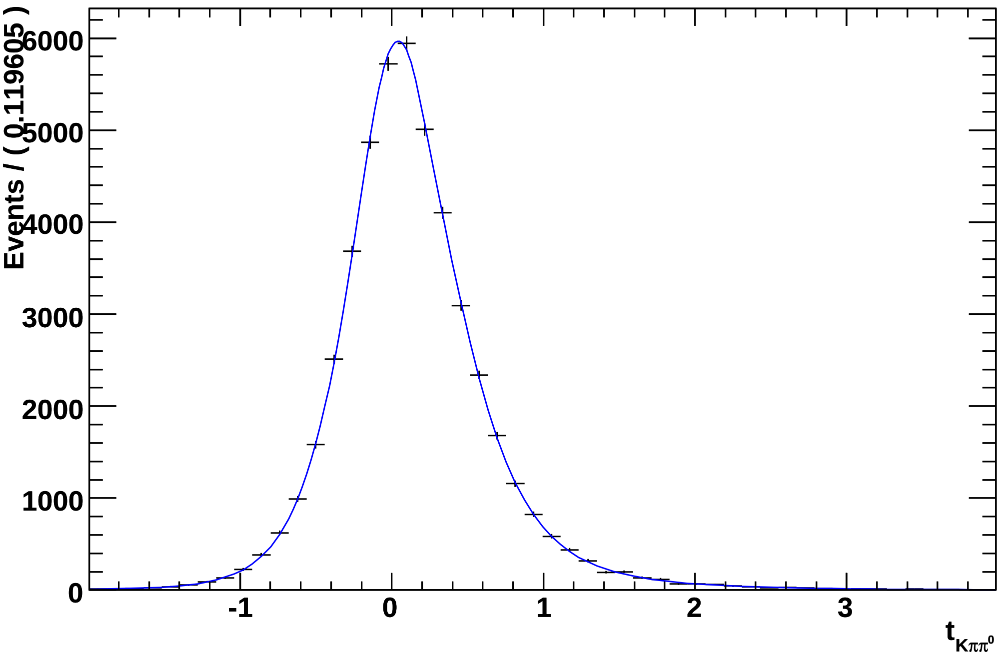

Figure B.2: Data and fit result for the time distribution of the WS background in the sidebands regions of $m_{K\pi\pi^0}$. Dots are data, the blue line is the fit result.

B.3 Dalitz Plot temporal dependence

The background description obtained in Sections B.1 and B.2 assumes that the Dalitz structure of the background does not evolve in time. To test this assumption, we compare the time dependence of three different regions of the Dalitz of the $m_{K\pi\pi^0}$ sidebands. The regions are chosen to be:

- Region **1**: $m^2_{K\pi} < 1\,\mathrm{GeV}/c^2$, which mainly includes the K^{*0} contribution to the Dalitz
- Region **2**: $m^2_{K\pi^0} < 1\,\mathrm{GeV}/c^2$, which includes the K^{*+} contribution
- Region **3**: $m^2_{K\pi} > 1\,\mathrm{GeV}/c^2$ and $m^2_{K\pi^0} > 1\,\mathrm{GeV}/c^2$, essentially the rest of the Dalitz plot.

We took the region 3 D^0 lifetime distribution as a reference, and normalized the distributions of the lifetime of the other two regions to it. The plot of the difference of the lifetime between the regions is shown in Figure B.3. It can be noted that differences in time between the regions selected are visible.

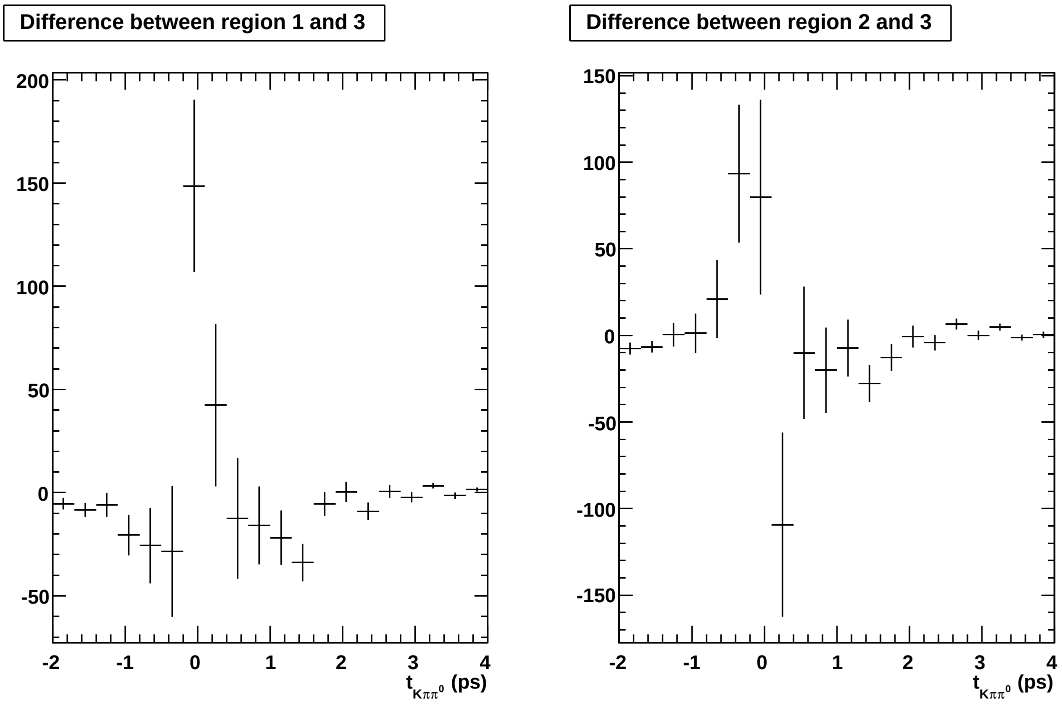

Figure B.3: Difference of D^0 lifetime between three regions of the WS background Dalitz Plot.

Appendix C

Resolution function determination ignoring the background contributions

Since the RS sample is very pure, one can think of determining the resolution function parameters ignoring the background contributions to the D^0 lifetime. This assumption is not adopted in the nominal fit in Section 8.4. However, this simple test gives a good hint of how sensitive are the resolution function parameters to the presence of background, or to a bad characterization of it.

The model used to fit the RS D^0 lifetime signal shape is the same as the nominal one, i.e. a convolution of three gaussians with an exponential decay law. The resolution function can be therefore written as:

$$P_{RS,i}(t) = f_1 \cdot \rho_{1,i} + (1 - f_1) \cdot [f_2 \cdot \rho_{2,i} + (1 - f_2)\rho_{3,i}] \tag{C.1}$$

with

$$\begin{aligned} \rho_{1,i} &= \rho_{RS,i}(t; \tau, k_1) \\ \rho_{2,i} &= \rho_{RS,i}(t; \tau, k_2) \\ \rho_{3,i} &= \rho_{RS,i}(t; \tau, k_3) \end{aligned} \tag{C.2}$$

Since the scale factor parameters k_i and the fraction of each gaussian contribution f_i are strongly correlated, for the comparison we fix the scale factors to the values obtained from the nominal fit. In this way we can better compare the other parameters between the two configurations.

The fit results are reported in Table C.1. As can be noted from the fit result, both the offset and the D^0 lifetime fit results are compatible with the nominal case within the error. This is a good sign, since any mixing sign in the D^0 lifetime distribution could be distorced by an uncorrect knowledge of the resolution function. The fractions of the gaussians seem to be less compatible. This is expected, considering that the fraction of the first and second Gaussians increase with respect to the nominal case. They have an higher scale factor with respect to the third gaussian. This tells us that the fit is trying to compensate the presence of the background underneath the $t \sim 0$ region by enlarging the resolution function contribution.

Parameter	Value
f_1	0.0057 ± 0.0006
f_2	0.221 ± 0.006
t_0	0.0042 ± 0.0008 (ps)
τ	0.4108 ± 0.0009 (ps)
k_1	2.84 (fixed)
k_2	1.36 (fixed)
k_3	0.93 (fixed)

Table C.1: Fit results for the RS time distribution

Appendix D

Validation of the fit procedure using toy-MC studies

In Section D we performed toy-MC studies in order to test the robustness of the fit procedure. In this appendix, we show the plot for the fitted values, errors and pull distributions for the cases we considered in the validation.

D.1 The *no-mixing* scenario

The summary plots for c_1 and c_2 for this generation and fitting mode are in Figure D.1. The distributions for the K^{*0} (892) Dalitz plot parameters are shown in Figure D.2.

D.2 The $c_1 = 0.25$ and $c_2 = 0.18$ scenario

The summary plots for c_1 and c_2 for this generation and fitting mode are in Figure D.3. The distributions for the K^{*0} (892) Dalitz plot parameters are shown in Figure D.4.

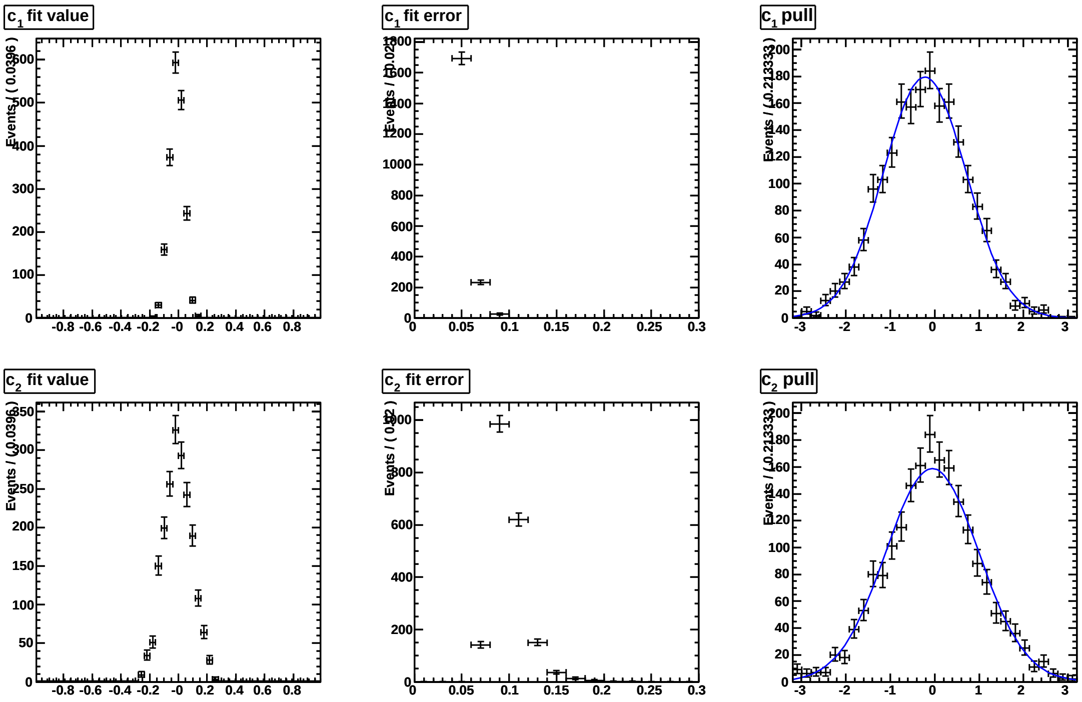

Figure D.1: Summary plot of c_1 and c_2 for the *no-mixing* toy-MC.

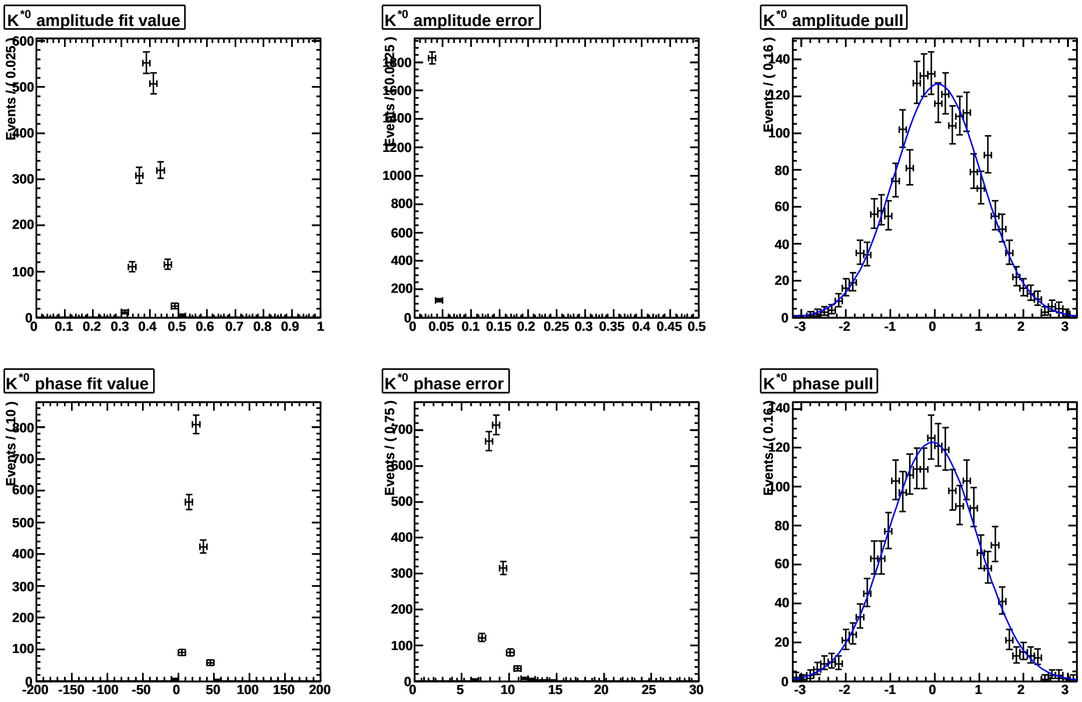

Figure D.2: Summary plot of K^{*0} (892) Dalitz plot parameters for the *no-mixing* toy-MC.

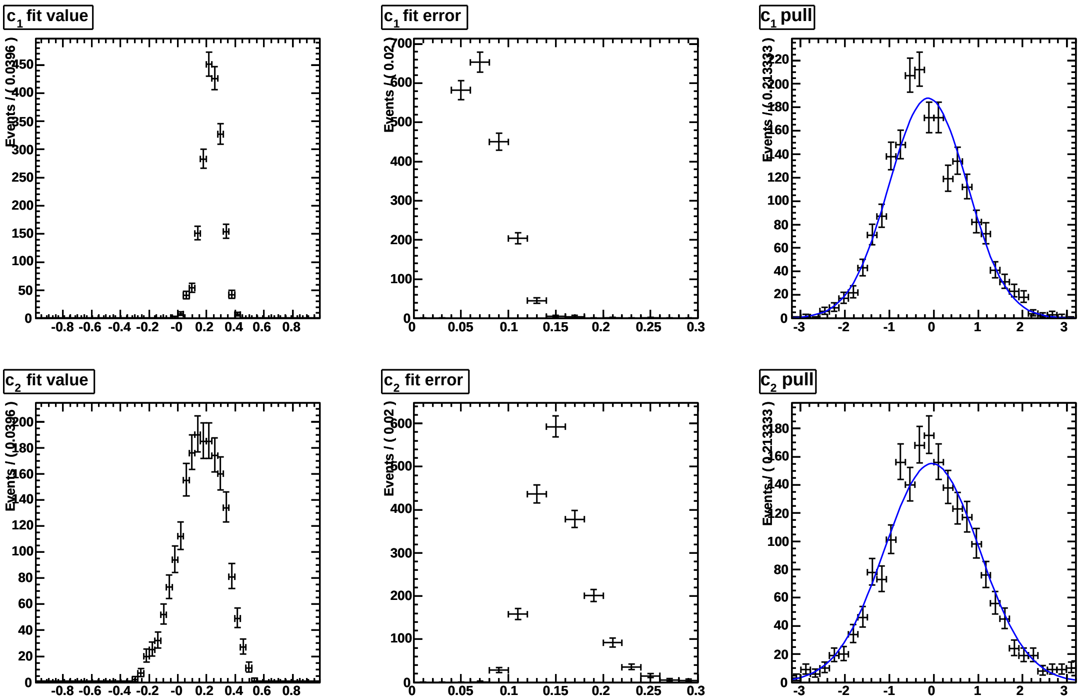

Figure D.3: Summary plot of c_1 and c_2 for the $c_1 = 0.25$ and $c_2 = 0.18$ mixing scenario.

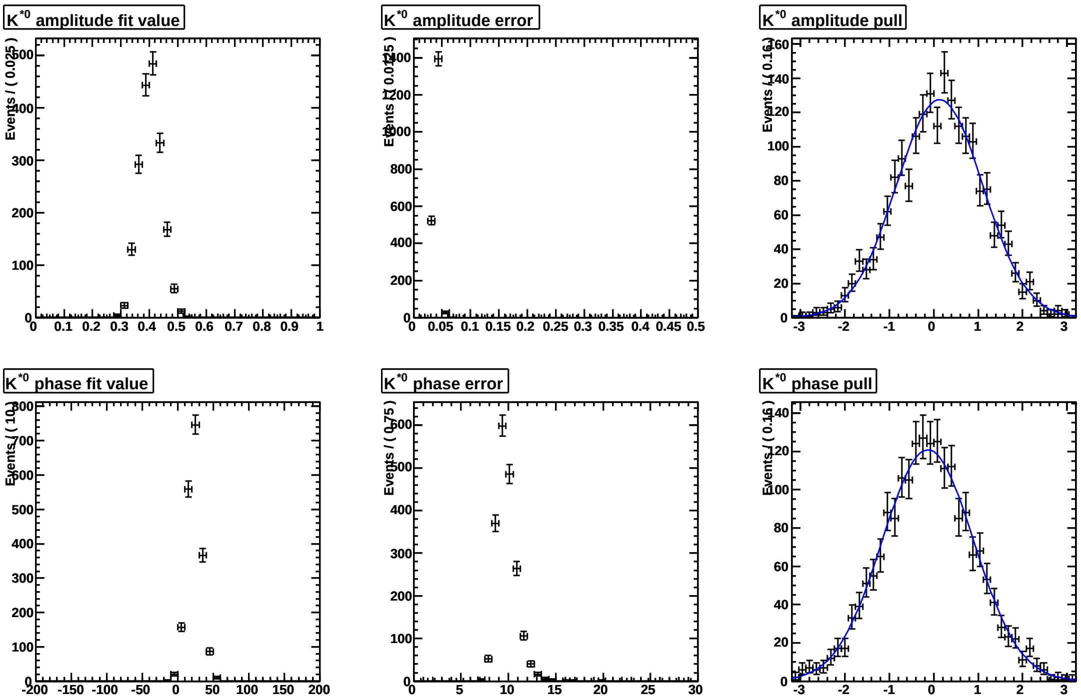

Figure D.4: Summary plot of the $K^{*0}(892)$ Dalitz plot parameters for the $c_1 = 0.25$ and $c_2 = 0.18$ mixing scenario.

Appendix E

Dalitz plot efficiency parametrization using the $K - \pi^0$ pair

To test the systematic effect due to the Dalitz plot efficiency parametrization chosen in Chapter 6, we perform the same procedure using a different choice of pair for the invariant mass and the helicity angle, i.e. $K - \pi^0$. The systematic effect is described in Section 12.3. Here, we report the efficiency parametrization with the $K - \pi^0$ couple along the Dalitz plot (i.e. the equivalent of Figure 6.3) in Figure E.1. As a qualitative comparison between the two choices, we plot the pull distribution, along the Dalitz plot, between the efficiency parametrization using the $K - \pi$ couple and the one using the $K - \pi^0$ couple. This is shown in Figure E.2. As can be noted from the pull distribution, the two parametrizations are reasonably compatible.

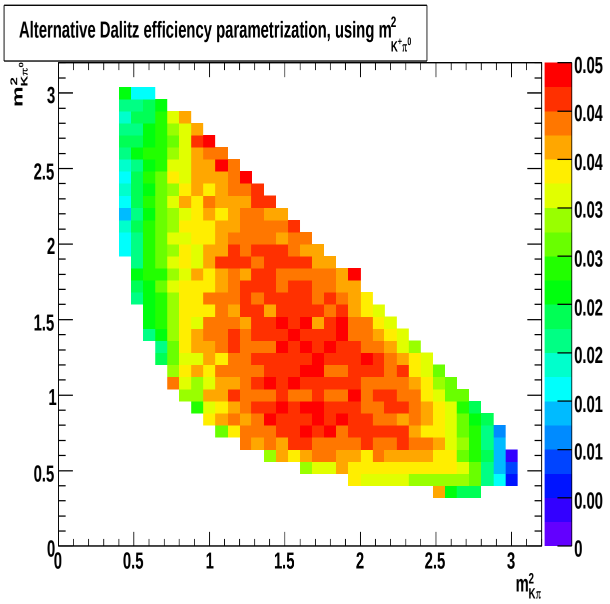

Figure E.1: Dalitz plot efficiency from the fit on the $m^2_{K\pi}$ and $m^2_{K\pi^0}$ plane, using the K-π^0 couple for the parametrization.

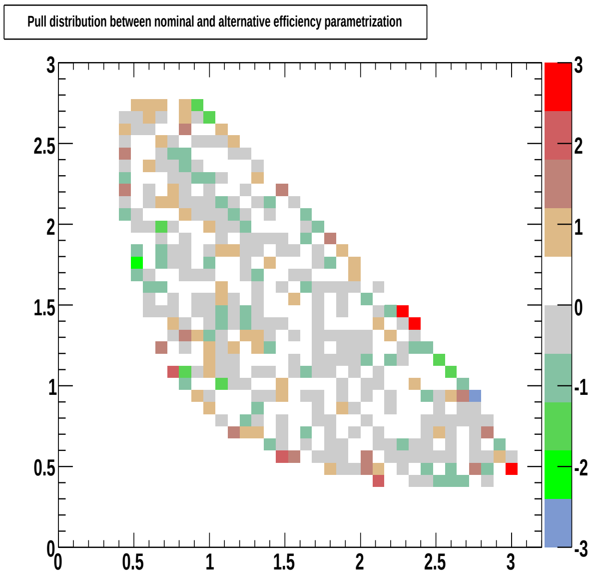

Figure E.2: Pull distribution, along the Dalitz plot, between the efficiency parametrization using the $K-\pi$ invariant mass and helicity angle and the parametrization using the $K-\pi^0$ couple.

Appendix F

Test of the significance coverage

It is necessary to prove that this method to determine the exclusion of the *no-mixing* scenario described in Section 11.1.2 is appropriate. In particular, we have to prove that $-2\Delta Log(\mathcal{L})$ is χ^2 distributed. We consider three points on the $\{c_1, c_2\}$ to test this assumption: the origin, the central value, and a case where both c_1 and c_2 present central values different from zero. The three points are:

$$\{c_1, c_2\} = \{0, 0\} \ , \ \{-0.001966, 0.3535\} \ , \ \{0.15, 0.15\}$$

In each case, we generate 2000 toy-MCs, and fit each experiment both floating the mixing parameters and fixing them to the generated value. We then calculate the $-2\Delta Log(\mathcal{L})$ between the likelihood in the fit where c_1 and c_2 were floating and the likelihood in the fit where the parameters were fixed. Then, we plot the distribution of the probability of the χ^2 for each toy-MC set, assuming two degrees of freedom. If $-2\Delta Log(\mathcal{L})$ is χ^2 distributed, the probability should be flat.

The plots for the three different scenarios are shown in Figures F.1-F.3. For each set, we fitted the probability distribution with a linear polynomial and found it compatible with a flat distribution within the error.

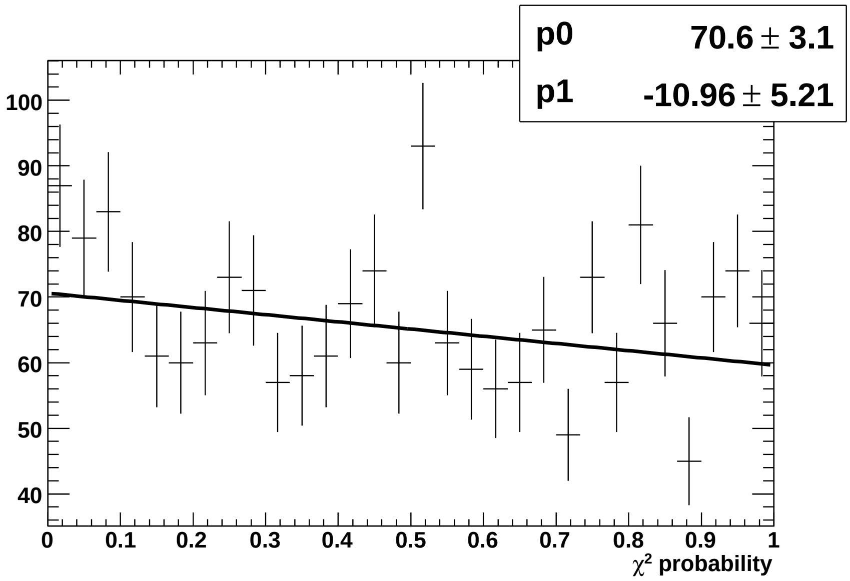

Figure F.1: Distribution of the probability for the χ^2 with two degrees of freedom in the *no-mixing* toy-MC scenario. The probability was fit with a linear distribution $p_0 + p_1 x$.

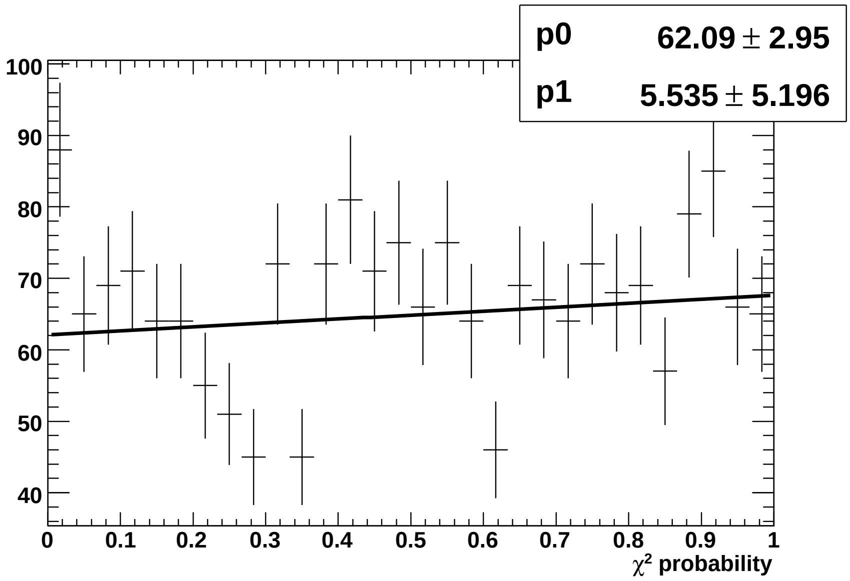

Figure F.2: Distribution of the probability for the χ^2 with two degrees of freedom in the $\{-0.001966, 0.3535\}$ toy-MC scenario. The probability was fit with a linear distribution $p_0 + p_1 x$.

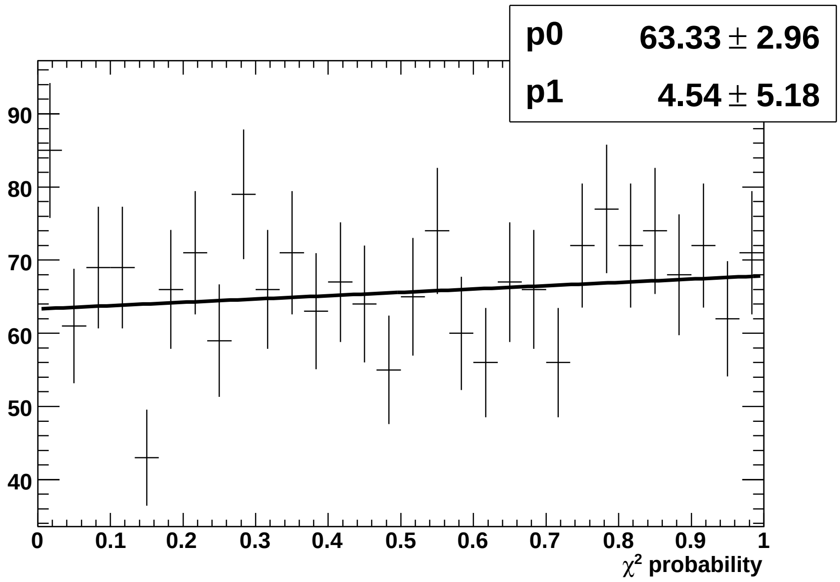

Figure F.3: Distribution of the probability for the χ^2 with two degrees of freedom in the $\{0.15, 0.15\}$ toy-MC scenario. The probability was fit with a linear distribution $p_0 + p_1x$.

Bibliography

[1] N. Cabibbo, "Unitary Symmetry and Leptonic Decays", Phys. Rev. Lett. **10**, 531 (1963).

[2] M. Kobayashi and T. Maskawa, "*CP* Violation In The Renormalizable Theory Of Weak Interaction", Prog. Theor. Phys. **49**, 652 (1973).

[3] S. L. Glashow, J. Iliopoulos and L. Maiani, "Weak Interactions with Lepton-Hadron Symmetry", Phys. Rev. D **2**, 1285 (1970).

[4] H. Georgi, "D^0-$\overline{D}^0$ mixing in heavy quark effective field theory", Phys. Lett. B **297**, 353 (1992) [arXiv:hep-ph/9209291].

[5] A. A. Petrov, "Charm mixing in the standard model and beyond", Int. J. Mod. Phys. A **21**, 5686 (2006) [arXiv:hep-ph/0611361].

[6] A. A. Petrov, "Charm physics: Theoretical review", *In the Proceedings of Flavor Physics and CP Violation (FPCP 2003), Paris, France, 3-6 Jun 2003, pp MEC05* [arXiv:hep-ph/0311371].

[7] A. F. Falk, Y. Grossman, Z. Ligeti and A. A. Petrov, "SU(3) breaking and D^0-$\overline{D}^0$ mixing", Phys. Rev. D **65**, 054034 (2002) [arXiv:hep-ph/0110317].

[8] T. A. Kaeding, "D Meson Mixing In Broken SU(3)", Phys. Lett. B **357**, 151 (1995) [arXiv:hep-ph/9505393].

[9] F. Buccella, M. Lusignoli, G. Mangano, G. Miele, A. Pugliese and P. Santorelli, "*CP* Violating asymmetries in charged D meson decays", Phys. Lett. B **302**, 319 (1993) [arXiv:hep-ph/9212253].

[10] S. P. Martin, "A supersymmetry primer" arXiv:hep-ph/9709356.

[11] M. Ciuchini, E. Franco, D. Guadagnoli, V. Lubicz, M. Pierini, V. Porretti and L. Silvestrini, "D-Dbar mixing and new physics: general considerations and constraints on the MSSM", Phys. Lett. B **655**, 162 (2007) [arXiv:hep-ph/0703204].

[12] B. Aubert *et al.* [BABAR Collaboration], "Evidence for D^0-$\overline{D}^0$ mixing", Phys. Rev. Lett. **98**, 211802 (2007) [arXiv:hep-ex/0703020].

[13] M. Staric *et al.* [Belle Collaboration], "Evidence for D^0-$\overline{D}^0$ Mixing", Phys. Rev. Lett. **98**, 211803 (2007) [arXiv:hep-ex/0703036].

[14] B. Aubert *et al.* [BABAR Collaboration], “Measurement of D^0-$\overline{D}^0$ Mixing using the Ratio of Lifetimes for the Decays $D^0 \to K^- \pi^+$, $K^- K^+$, and $\pi^- \pi^+$”, arXiv:0712.2249 [hep-ex].

[15] B. Aubert *et al.* [BABAR Collaboration], “Measurement of D^0-$\overline{D}^0$ mixing from a time-dependent amplitude analysis of $D^0 \to K^+ \pi^- \pi^0$”, arXiv:0807.4544 [hep-ex].

[16] T. Aaltonen *et al.* [CDF Collaboration], “Evidence for D^0-$\overline{D}^0$ mixing using the CDF II Detector”, Phys. Rev. Lett. **100**, 121802 (2008) arXiv:0712.1567 [hep-ex].

[17] B. Aubert *et al.* [BABAR Collaboration], “Search for D^0-$\overline{D}^0$ mixing using doubly flavor tagged semileptonic decay modes”, Phys. Rev. D **76**, 014018 (2007) arXiv:0705.0704 [hep-ex].

[18] U. Bitenc *et al.* [BELLE Collaboration], “Improved search for D^0 mixing using semileptonic decays at Belle”, Phys. Rev. D **77**, 112003 (2008) arXiv:0802.2952 [hep-ex].

[19] K. Abe *et al.* [BELLE Collaboration], “Measurement of D0-D0bar mixing in D0-¿Ks pi+ pi- decays”, Phys. Rev. Lett. **99**, 131803 (2007) [arXiv:0704.1000 [hep-ex]].

[20] D. M. Asner *et al.* [CLEO Collaboration], “Determination of the D0 -¿ K+pi- Relative Strong Phase Using Quantum-Correlated Measurements in $e^+e^- \to D^0$-$\overline{D}^0$ at CLEO”, Phys. Rev. D **78**, 012001 (2008) [arXiv:0802.2268 [hep-ex]].

[21] H. B. Li and M. Z. Yang, “D^0-$\overline{D}^0$ mixing in $\Upsilon(1S) \to D^0$-$\overline{D}^0$ decay at super-B”, Phys. Rev. D **74**, 094016 (2006) [arXiv:hep-ph/0610073].

[22] A. J. Schwartz, “Measurements of D^0-$\overline{D}^0$ Mixing and Searches for *CP* Violation: HFAG Combination of all Data”, arXiv:0803.0082 [hep-ex].

[23] I. I. Y. Bigi and A. I. Sanda, “CP violation”, Camb. Monogr. Part. Phys. Nucl. Phys. Cosmol. **9**, 1 (2000).

[24] B. Aubert *et al.* [BABAR Collaboration], “Search for D^0-$\overline{D}^0$ mixing and branching-ratio measurement in the decay $D^0 \to K^+\pi^-\pi^0$ ”, Phys. Rev. Lett. **97**, 221803 (2006) [arXiv:hep-ex/0608006].

[25] E. M. Aitala *et al.* [E791 Collaboration], “Dalitz plot analysis of the decay $D^+ \to K^- \pi^+ \pi^+$ and study of the K pi scalar amplitudes” Phys. Rev. Lett. **89**, 121801 (2002) [arXiv:hep-ex/0204018].

[26] J. M. Link *et al.* [FOCUS Collaboration], “Dalitz plot analysis of the $D^+ \to K^- \pi^+ \pi^+$ decay in the FOCUS experiment”, Phys. Lett. B **653**, 1 (2007) [arXiv:0705.2248 [hep-ex]].

[27] B. Aubert *et al.* [BABAR Collaboration], “The BaBar detector”, Nucl. Instrum. Meth. A **479** (2002) 1 [arXiv:hep-ex/0105044].

[28] C. Bozzi *et al.* [*BABAR* Collaboration], Nucl. Instrum. Methods Phys. Res., Sect. A **473** (2001) 7;
C. Bozzi *et al.* [*BABAR* Collaboration], Nucl. Instrum. Methods Phys. Res., Sect. A **461** (2001) 162.

[29] J. Schwiening *et al.* [*BABAR* DIRC Collaboration], Nucl. Instrum. Methods Phys. Res., Sect. A **502** (2003) 67;
I. Adam *et al.*,IEEE Trans. Nucl. Sci. **49** (2002) 1071;
D.W.G. Leith, Nucl. Instrum. Methods Phys. Res., Sect. A **494** (2002) 389;
I. Adam *et al.*, Nucl. Phys. Proc. Suppl. **93** (2001) 340.

[30] F. Anulli *et al.*, "The muon and neutral hadron detector for BaBar", Nucl. Instrum. Meth. A **409**, 542 (1998).

[31] G. Battistoni, E. Iarocci, M. M. Massai, G. Nicoletti and L. Trasatti, 'Operation Of Limited Streamer Tubes", Nucl. Instrum. Meth. **164**, 57 (1979).

[32] R. H. Dalitz, "On the analysis of τ-meson data and the nature of the τ-meson" Phil. Mag. **44**, 1068 (1953).

[33] H. Muramatsu *et al.*, Phys. Rev. Lett. **89**, 251802 (2002), Erratum-ibid: **90**, 059901 (2003).

[34] S. Kopp *et al.* [CLEO Collaboration], "Dalitz analysis of the decay $D^0 \to K^-\pi^+\pi^0$ ", Phys. Rev. D **63**, 092001 (2001) [arXiv:hep-ex/0011065].

[35] D.Aston et al. (LASS), Nucl. Phys. B296, 493 (1988).

[36] B. Aubert *et al.* [BABAR Collaboration], "Branching fraction measurements of $B \to \eta_c K$ decays", Phys. Rev. D **70**, 011101 (2004) [arXiv:hep-ex/0403007].

[37] W. M. Yao *et al.* [Particle Data Group], "Review of particle physics", J. Phys. G **33**, 1 (2006).

[38] J. M. Link *et al.* [FOCUS Collaboration], "Study of the doubly and singly Cabibbo suppressed decays $D^+ \to K^+ \, \pi^+ \, \pi^-$ and $D_s^+ \to K^+ \, \pi^+ \, \pi^-$", Phys. Lett. B **601**, 10 (2004) [arXiv:hep-ex/0407014].

[39] G. Punzi, "Comments on likelihood fits with variable resolution" *In the Proceedings of PHYSTAT2003: Statistical Problems in Particle Physics, Astrophysics, and Cosmology, Menlo Park, California, 8-11 Sep 2003, pp WELT002* [arXiv:physics/0401045].

[40] P.S. Dwyer, "Matrix inversion with the square root method", Technometrics, Vol. 6, No. 2 (May, 1964), pp. 197-213

[41] G. Burdman and I. Shipsey, "D^0-$\overline{D}^0$ mixing and rare charm decays", Ann. Rev. Nucl. Part. Sci. **53**, 431 (2003) [arXiv:hep-ph/0310076].

[42] B. Aubert *et al.* [BaBar Collaboration], "Search for *CP* Violation in the Decays $D^0 \to K^- \, \pi^+$ and $D^0 \to \pi^- \, \pi^+$", Phys. Rev. Lett. **100**, 061803 (2008) [arXiv:0709.2715 [hep-ex]].